THE UNIVERSITY OF CHICAGO

EXPERIMENTAL STUDIES OF NONLINEAR INTEGRABLE OPTICS

A DISSERTATION SUBMITTED TO
THE FACULTY OF THE DIVISION OF THE PHYSICAL SCIENCES
IN CANDIDACY FOR THE DEGREE OF
DOCTOR OF PHILOSOPHY

DEPARTMENT OF PHYSICS

BY
NIKITA KUKLEV

CHICAGO, ILLINOIS
AUGUST 2021

TABLE OF CONTENTS

LIST OF FIGURES

LIST OF TABLES

ACKNOWLEDGMENTS

First and foremost, a big thank you to my Fermilab co-advisor, Alexander Valishev. I had little knowledge of accelerator physics coming in, and your innate grasp of both the theory and the hands-on implementation was inspiring. My experiments have not always gone as expected, but your optimism and support helped me continue to explore further.

I would like to thank my UChicago co-advisor, professor Young-Kee Kim, for her relentless drive in making me document, write, and rigorously quantify my work. You also made sure I had all the resources and support, and could focus on the science.

Many parts of this research were done in collaboration with members of our nonlinear integrable optics group - Sasha Romanov, Sebastian Szustkowski, and Sergei Nagaitsev. Thank you all for advice and ideas. I owe special thanks to Sasha for his expertise in storage ring tuning, and inspiring me to write my own tools.

I am grateful to the Fermilab FAST/IOTA team - Jamie Santucci, Dean Edstrom, Mark Obrycki, and all the support staff. You were always happy to help at any time of day or night, and came through when it counted most.

Thank you to my UChicago groupmates. Stas, you have taught me a lot both about physics and life of physicists. Matt and Lipi, our conference travels, office debates, and sushi dinners were amazing and the best kind of emotional support.

Finally, I owe the opportunity to write this thesis to my family. Their investment into my future and unconditional support is a privilege the value of which I only now understand.

ABSTRACT

State-of-the-art accelerators at energy and intensity frontiers require increasingly bright and powerful particle beams. In conventional linear lattices, intense beams suffer from collective instabilities, resulting in beam losses and maximum beam intensity limits. This thesis presents experimental studies of a novel lattice design concept, the nonlinear integrable optics (NIO), aimed at enhancing beam stability limits with little to no beam dynamics degradation. Single-particle beam dynamics measurements of two NIO devices, the quasi-integrable octupole system and the fully integrable Danilov-Nagaitsev system, were carried out at the purpose-built Integrable Optics Test Accelerator (IOTA) at Fermilab. Their simulation, hardware design, and commissioning process are presented. Extensive model and analysis algorithm development and benchmarking is described. Electron beam data from two scientific runs is analyzed, yielding frequency and phase space dynamics consistent with models. These results demonstrate viability and advantages of the NIO design, providing the groundwork for proton studies in the strong space-charge regime and future integrable accelerators.

CHAPTER 1

INTRODUCTION

Over the past century, particle accelerators have had a profound effect on human society, furthering our understanding of fundamental physics and basic sciences, and finding industrial and medical applications. During that period, accelerator designs have undergone many improvements in efficiency, beam energy, and beam quality to meet the ever increasing demands. Current state of the art machines, like the Large Hadron Collider (LHC) at the energy frontier and Advanced Photon Source upgrade (APS-U) fourth generation light source, push many of the existing approaches to their limits. Next generation of accelerators will require further, novel advances in our understanding of beam dynamics and design strategies. One of key challenges to be solved are the beam instabilities, which limit further power increases. This thesis introduces and experimentally studies a novel class of instability suppression lattices based on the concept of nonlinear integrable optics.

1.1 Overview and history of high energy accelerators

First particle accelerators were motivated by particle physics research into atomic structure. In 1932, within weeks of each other atoms were split by Cockcroft and Walton with an electrostatic linear accelerator and by Ernest Lawrence with a circular resonant accelerator called a cyclotron [1]. Larger and higher energy cyclotrons followed, but quickly reached the relativistic limits of synchronous radio frequency (RF) drive. A new design with variable RF, a synchrocyclotron, was used to push energies further but could only accelerate a single particle bunch at a time. The next evolutionary step was splitting the single large cyclotron bending field into smaller dipole magnets, forming a ring. However, this created significant challenges in confining (*focusing*) the beam transversely and longitudinally. The latter problem was solved with dedicated RF cavities, enabling first synchrotrons. However,

these machine only used the weak transverse 'constant-gradient' focusing integrated within dipoles [2]. They had large beam sizes (i.e. 64cm x 15cm in Cosmotron), and required vast vacuum chambers and large aperture magnets. In 1952, Courant and Snyder proposed a new synchrotron design with dedicated alternating gradient focusing quadrupole elements, the 'strong focusing' concept [3]. Strong focusing revolutionized the field, reducing accelerator costs and enabling a leap in energies. Construction of first particle colliders started shortly thereafter. Since then, the core accelerator lattice design has remained unchanged, and all modern circular machines are alternating gradient synchrotrons.

1.2 Current challenges

While alternating gradient design has persisted to this day, a number of technological improvements have happened - superconducting magnets and accelerating cavities, advanced magnets and RF devices, beam cooling, active feedback systems, numerical simulation tools, and many others. Combined with increasing accelerator sizes, this allowed for continuous increase of collision energies, culminating with the current energy frontier machine, the Large Hadron Collider (LHC), at 27km in length and center of mass energy of 13 TeV [4]. However, accelerator's scientific output depends not only on beam energy but also its intensity and brightness. In colliders, beam brightness determines luminosity - the ratio of the number of events in a certain time to the interaction cross-section. In beam-on-target facilities like spallation neutron sources or neutrino factories, beam intensity corresponds to beam power - the product of particle energy (in electron-volts, eV) and beam *current*. Modern facilities like the Spallation Neutron Source (SNS) are capable of multi-MW beams, and are planning further upgrades.

The most straightforward way to increase beam power is to accelerate more particles while maintaining same focusing. However, high particle densities lead to significant electromagnetic interactions between particles themselves and with the environment. This effect, called

'space charge', complicates beam dynamics significantly. It is usually detrimental, leading to eventual instabilities, beam quality degradation and particle losses. Since accelerator components and enclosures are limited in how much radiation they can absorb ($\sim 1\,\mathrm{W/m}$), space charge driven losses place a limit on maximum beam power. Increasing intensity requires improved control and mitigation of space-charge effects. Many such schemes have been proposed and implemented - multi-level collimation, phase-space painting, active feedback and instability suppression, extensive numerical optimizations, and others. However, these are all incremental improvements and many are reaching fundamental limits. Next generation of accelerators will require further, novel advances in our beam dynamics understanding and design. This thesis studies one such scheme, the nonlinear integrable optics.

1.3 Organization

The work presented in this dissertation consists of design, simulation, construction, and experimental studies of the nonlinear integrable optics concept. To that end, the necessary background theory is introduced in chapter 2, including an brief overview of the more advanced nonlinear and collective motion topics. A description of experimental equipment - magnetic inserts, accelerators, diagnostics, and other devices is given in chapter 3. Simulation and data analysis algorithms are presented in chapter 4 and related to experimentally observable parameters. Simulation results for various ideal, realistic, and perturbed lattices are presented in chapter 5, deriving a set of practical implementation requirements. Finally, experimental commissioning and results are extensively discussed in chapter 6. Thesis concludes with a summary of progress and overview of potential future work in chapter 7.

CHAPTER 2

LINEAR AND NONLINEAR BEAM DYNAMICS

This chapter introduces all the necessary machinery to describe the beam dynamics discussed in this thesis. It begins with a review of standard linear optics in section 2.1, both in the context of single particle motion and for bunched beams. Overview of nonlinear dynamics is given in section 2.2, with focus on practical implications. Finally, the concept of integrable optics is introduced and perturbations discussed in section 2.3.

2.1 Linear beam optics

2.1.1 Charged particle motion

Charged particle motion in an electromagnetic field (consisting of electric field $\vec{E}$ and magnetic field $\vec{B}$) is governed by the Lorentz force law

$$\frac{dp}{dt} = \dot{\vec{p}} = \vec{F} = q(\vec{E} + \vec{v} \times \vec{B}) \tag{2.1}$$

where $\vec{p} = \gamma m \vec{v}$ is the relativistic momentum, q particle charge, m particle mass, and $\vec{v}$ particle velocity vector. It is typical to combine electric and magnetic fields into vector potential $\vec{A}$ and scalar potential ϕ, with $\vec{B} = \nabla \times \vec{A}$. The most general relativistic Hamiltonian for this system is given by

$$H = E_{kinetic} + E_{potential} = \sqrt{\left(\vec{P} - q\vec{A}\right)^2 c^2 + m^2 c^4} + q\phi \tag{2.2}$$

where $\vec{P} = \vec{p} + q\vec{A}$ is the *canonical momentum*. Particle equations of motion can be found by making use of Hamilton's equations (note $p \neq P$)

$$\frac{dx}{dt} = \frac{\partial H}{\partial P}$$
$$\frac{dP_x}{dt} = -\frac{\partial H}{\partial x}$$

and similarly for y-plane (for rest of this chapter, derivations using x also apply to y-plane unless stated otherwise). However, before applying Eq. 2.1.1 it is useful to first transform 2.2 from lab frame Cartesian coordinates (x, y, z) into a more relevant system.

2.1.2 Frenet-Serret coordinate system

Accelerators at their core are collections of devices producing electromagnetic fields that confine particles to the desired path, called *reference orbit*, while also manipulating their position and velocity. Particle motion is usually limited to small deviations around the reference orbit. It is convenient to pick a curvilinear coordinate system that is defined relative to this orbit. This system is called the Frenet-Serret coordinate system, and is shown in Fig. 2.1.

New coordinates (x, y, s) follow the reference orbit, with x and y typically referred to as the transverse coordinates and s, the direction of motion, as the longitudinal coordinate. Particle position is given by $\vec{r} = \vec{r_0} + x\hat{x} + y\hat{y}$, and unit vector transformations are

$$\hat{x} = -\rho\, d\hat{s}/ds \tag{2.3}$$

$$\hat{y} = \hat{x} \times \hat{s} \tag{2.4}$$

$$\hat{s} = d\vec{r}_0/ds \tag{2.5}$$

with ρ the local radius of curvature.

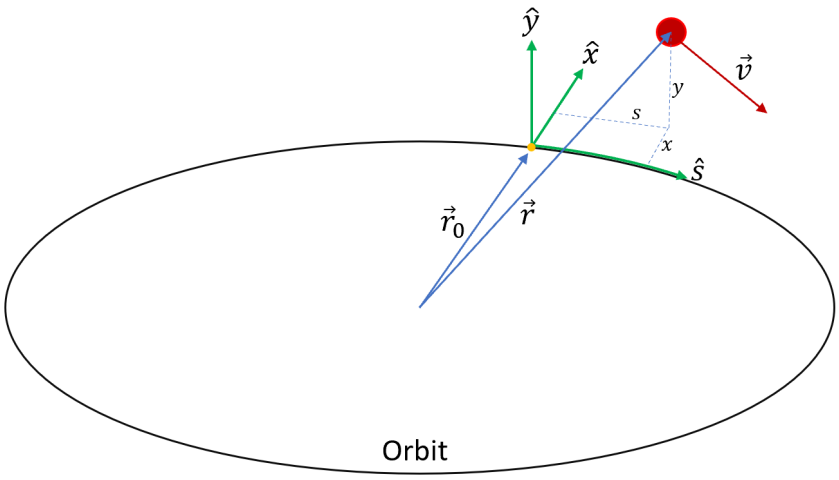

Figure 2.1: Curvilinear coordinate system for particle motion.

2.1.3 Hamiltonian for transverse dynamics

Making use of Frenet-Serret system, and applying several canonical transformations, the standard accelerator physics Hamiltonian for vector potential $\vec{A} = (0, 0, A_s)$ is obtained as

$$H = -(1+hx)A_s - (1+hx)\sqrt{\left(\delta + \frac{1}{\beta_0}\right)^2 - p_x^2 - p_y^2 - \frac{1}{\beta_0^2\gamma_0^2}} + \frac{\delta}{\beta_0} \tag{2.6}$$

where $h = 1/\rho$ is the orbit curvature and $\beta_0 = \frac{v_0}{c}$ and $\gamma_0 = 1/\sqrt{1-\beta_0^2}$ are the standard relativistic factors at design energy. For purposes of linear optics, in the relativistic limit

$$H = -(1+hx)A_s - (1+hx)\sqrt{(\delta+1)^2 - p_x^2 - p_y^2} + (\delta+1) \tag{2.7}$$

Finally, expanding in low orders of p_x and p_y (*paraxial* approximation) we obtain

$$H = -(1+hx)A_s - (1+\delta)hx + \frac{1}{2}\frac{p_x^2 + p_y^2}{1+\delta} \tag{2.8}$$

A detailed derivation of Eq. 2.7 and 2.8 can be found in standard textbooks [5, 6]. Note that the new coordinate system is now $(x, p_x, y, p_y, \Delta z = (s - v_0 t), \delta = \frac{\Delta p}{p})$. Variables p_x and p_y

are referring to dimensionless canonical momenta, and can be related to physical ones with $p_x = P_x/P_0$ and $p_y = P_y/P_0$, where P_0 is the design total momentum. In some calculations and simulation codes, a different choice of momentum coordinates known as slopes (x', y') is made due to historical and computational reasons. In relativistic limit, these values converge since $x' = dx/ds = P_x/P_s \sim P_x/P_0$.

2.1.4 Magnetic elements and multipole field expansion

One of the assumptions made in deriving 2.6 is that most magnetic fields do not vary longitudinally. Using Maxwell's equations, a general description of such 2D fields in terms of cartesian multipoles can be given as ([6] Sec. 1.2):

$$A_s = B_{ref}\,\mathrm{Re}\left[\sum_{n=0}^{\infty}\frac{b_n + ia_n}{(n+1)!}(x+iy)^{n+1}\right] \tag{2.9}$$

$$B_y + iB_x = B_{ref}\sum_{n=0}^{\infty}\frac{(b_n + ia_n)}{n!}(x+iy)^n \tag{2.10}$$

where B_{ref} is a scaling factor and n the order. Coefficients a_n and b_n denote strength of normal and skew n-pole respectively (there are several conventions), and can be found from magnetic field as

$$a_n = \frac{1}{n!B_{ref}}\frac{\partial^n B_x}{\partial x^n}\bigg|_{x=0;y=0} \tag{2.11}$$

$$b_n = \frac{1}{n!B_{ref}}\frac{\partial^n B_y}{\partial x^n}\bigg|_{x=0;y=0} \tag{2.12}$$

In particular, the most common accelerator components are dipoles and quadrupoles, used for beam steering and focusing respectively. Sextupoles and octupoles also have specialized uses, but it is rare to find higher order multipoles except as undesired field errors. The

potentials of these elements are:

$$\text{Drift } A_s = 0 \tag{2.13}$$

$$\text{Dipole } A_s = B(s)x \tag{2.14}$$

$$\text{Quadrupole } A_s = G(s)\frac{x^2 - y^2}{2} \tag{2.15}$$

$$\text{Sextupole } A_s = S(s)\frac{x^3 - 3xy^2}{6} \tag{2.16}$$

$$\text{Octupole } A_s = O(s)\frac{x^4 - 6x^2y^2 + y^4}{24} \tag{2.17}$$

with B, G, S, O the respective position-dependent strengths.

2.1.5 Linear Hamiltonian and Hill's equation

Beam dynamics are divided into *linear* and *nonlinear* parts, with former being significantly easier to treat analytically. Linear dynamics is determined by field-free drifts, as well as dipoles and quadrupoles, since their force on particles is constant or depends linearly on transverse deflection, respectively. By substituting first three potentials of 2.13 into Eq. 2.8, the standard linear optics Hamiltonian is obtained as

$$H = \frac{1}{2}(p_x^2 + p_y^2) + \frac{1}{2}\left(K_x(s)x^2 + K_y(s)y^2\right) \tag{2.18}$$

with

$$K_x(s) = \frac{1}{\rho(s)^2} + eG(s)/P_0 \tag{2.19}$$

$$K_y(s) = -eG(s)/P_0 \tag{2.20}$$

where dipole bending is assumed to occur only in x plane, as is typical in storage rings. The opposite signs of K_x and K_y in quadrupoles (i.e. $K_x(s) = -K_y(s) = k(s)$) explain the

'alternating gradient' name of the strong focusing design - while quadrupoles are focusing in one plane, they defocus in the other, and vice versa. Applying Hamilton's equations 2.1.1, we obtain

$$x'' + \left(\frac{1}{\rho(s)^2} + eG(s)/P_0\right) x = x'' + k(s)x = 0 \tag{2.21}$$

This result is known as Hill's equation, first derived in the context of lunar stability [7]. The challenge in solving Hill's equation comes from $k(s)$, which in general is a piecewise function that varies as the particle passes through various magnetic elements. For rings, this function must satisfy the periodic boundary condition $k(s) = k(s + C)$, where C is ring circumference and reference orbit length. Making use of a Floquet transformation to change from a periodic system into a linear one, the solution has the form

$$x(s) = Aw(s)e^{\pm i\psi(s)} = \sqrt{\epsilon_x \beta_x(s)}e^{\pm i\psi(s)} \tag{2.22}$$

where special functions $\sqrt{\epsilon}$ (amplitude scaling factor), $\sqrt{\beta(s)}$ (amplitude modulation) and $\psi(s)$ (phase modulation) were introduced. In essence, this solution is an oscillating function of variable amplitude - this behavior is called *betatron motion*. The quantity $\beta(s)$, called *betatron function* or just *beta function*, determines beam size along the ring, and together with *emittance* ϵ defines particle motion envelope. Plugging 2.22 back into 2.21, we obtain two further relations:

$$\psi_x' = \frac{1}{\beta_x(s)} \tag{2.23}$$

$$1 = \frac{1}{2}\beta_x\beta_x'' - \frac{1}{4}\beta_x'^2 + k(s)\beta_x^2 \tag{2.24}$$

By convention, the constant factor in the first equation is set to 1, and it can be used to evaluate the phase function $\psi(s)$, while the second relation allows for further simplification of Hill's equation, as will be discussed below.

2.1.6 Linear solution properties

Phase advance

From definition of Eq. 2.23, integration yields phase advance between two locations s_1 and s_2 as

$$\Delta\psi_x = \int_{s_1}^{s_2} \frac{ds}{\beta_x(s)} \tag{2.25}$$

In many cases, lattice longitudinal distance is specified via phase difference.

Tune

Total phase advance around the ring is given a special name, *tune* - it describes the number of oscillations the particle undergoes in a single turn.

$$\nu_x = Q_x = \int_{s_1}^{s_1+C} \frac{ds}{\beta_x(s)} \tag{2.26}$$

Substituting 2.23 back into 2.27 and performing coordinate transformation $q = x(s)/\sqrt{\beta_x}$, $\phi_x = \psi_x/Q_x$, $\dot{\phi_x} = 1/(Q_x\beta_x(s))$, a simplified form of Hill's equation is obtained:

$$\ddot{q} + Q^2 q = 0 \tag{2.27}$$

Equation 2.27 is exactly that of a simple harmonic oscillator with angular frequency Q. Thus, in appropriate coordinates linear lattice dynamics can be reduced to that of a simple harmonic oscillator. As in many other fields, everything is a spring if you look closely enough.

2.1.7 Courant-Snyder Parameters

Transporting a particle through a linear lattice, its (x, p_x) and (y, p_y) motion over several turns will trace out an ellipse regardless of starting position. A parametrization of this

ellipse was proposed by Courant and Snyder [3]. In their description, motion is confined to an invariant surface defined by

$$\epsilon_x = \gamma_x x^2 + 2\alpha_x x x' + \beta_x x'^2 \tag{2.28}$$

with two new function α_x and γ_x (not related to relativistic factors discussed previously) defined as

$$\alpha_x(s) = -\frac{1}{2}\beta_x'(s) \tag{2.29}$$

$$\gamma_x(s) = \frac{1+\alpha_x(s)^2}{\beta_x(s)} \tag{2.30}$$

There is a fundamental connection between emittance preservation and Liouville's theorem, which states that phase space density is invariant under conservative forces. As a consequence, there is no way to 'squeeze' or 'spread out' particles with only magnetic fields. The whole parameter set (β, α, γ) is sometimes referred to as *twiss* or *optical* functions. A visual diagram of CS parametrization is given in Fig. 2.2.

2.1.8 Normalized Courant-Snyder coordinates

It is useful to incorporate Courant-Snyder parameters and compensate for phase space ellipse rotation, resulting in simple harmonic system. This was already done implicitly in 2.27, but we can now make this transformation explicit with generating function

$$F_2(x, p_{x,N}) = p_{x,N}\frac{x}{\sqrt{\beta_x}} + \frac{x^2\alpha_x}{2\beta_x} \tag{2.31}$$

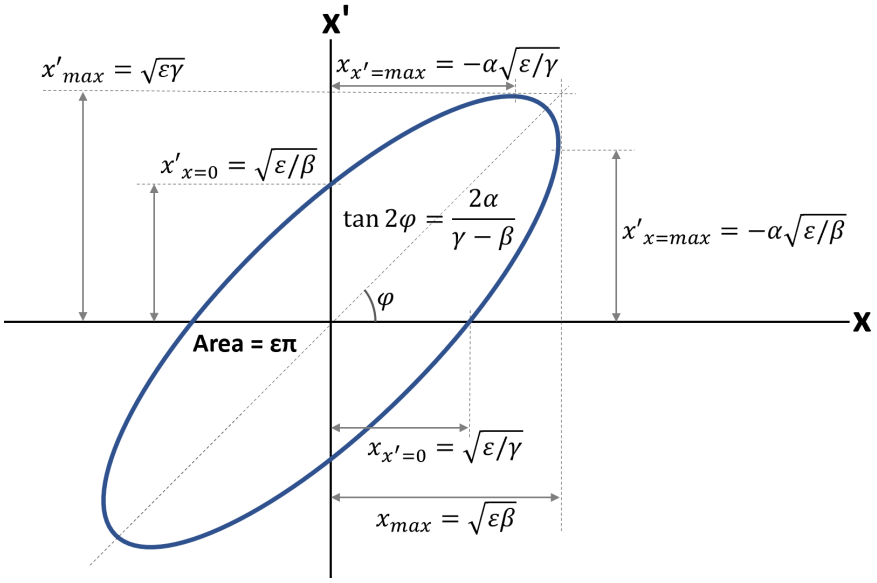

Figure 2.2: Courant-Snyder phase space ellipse parametrization. Emittance defines the area (A=$\epsilon_x\pi$) of phase space that contains all possible particle positions, which is preserved throughout linear motion

which yields

$$x_N = \bar{x} \equiv \frac{x}{\sqrt{\beta_x}} \tag{2.32}$$

$$p_{x,N} = \bar{p}_x \equiv p_x\sqrt{\beta_x} - \frac{\alpha_x x}{\sqrt{\beta_x}} \tag{2.33}$$

This conveniently simplifies the Hamiltonian to

$$H_N = \frac{1}{2}(\bar{p}_x^2 + \bar{x}^2) \tag{2.34}$$

$$H_N = \frac{1}{2}(\bar{p}_x^2 + \bar{p}_y^2) + \frac{1}{2}(\bar{x}^2 + \bar{y}^2) \tag{2.35}$$

which as expected matches that of a simple harmonic oscillator in 2D, or two uncoupled oscillators in 4D.

2.1.9 Transport matrices

For linear elements, it is possible to solve particle motion explicitly and obtain a map of input to output coordinates, which can be expressed as a matrix. For a drift, the Hamiltonian in paraxial approximation becomes

$$H = \frac{1}{2}(p_x^2 + p_y^2) + \frac{\delta}{2\beta_0^2\gamma_0^2} \tag{2.36}$$

where the δ term affect longitudinal coordinates only. The transverse solution can be succinctly expressed by a matrix for length L through 'drift potential' as

$$\begin{pmatrix} x_f \\ p_{x,f} \end{pmatrix} = \vec{x}(L) = \begin{pmatrix} 1 & L \\ 0 & 1 \end{pmatrix} \begin{pmatrix} x \\ p_x \end{pmatrix} = M \begin{pmatrix} x \\ p_x \end{pmatrix} \tag{2.37}$$

The matrix M is called a *transport* matrix, and multiplying such matrices is equivalent to transporting the particle through the elements. A thin quadrupole matrix is given by

$$M_{quad,thin} = \begin{pmatrix} 1 & 0 \\ -1/f & 1 \end{pmatrix} \tag{2.38}$$

where $1/f = kL$ is the integrated focusing strength. Results for other linear elements can be found in reference texts [8]. Note that linear transport is *symplectic*, or area-preserving (recall emittance discussion). A map is symplectic if its Jacobian J satisfies

$$J^T S J = S \tag{2.39}$$

where S is the $2n \times 2n$ antisymmetric matrix

$$S = \begin{pmatrix} 0 & I_n \\ -I_n & 0 \end{pmatrix} \tag{2.40}$$

with I_n denoting the identity matrix of size $n \times n$. In theory, all systems governed by Hamiltonian dynamics are symplectic - after all, Hamiltonian is the generator of canonical transformations describing time evolution [9]. However, in more complex nonlinear cases it may not be feasible to solve the system explicitly. Implications for simulation codes will be discussed further in chapter 4.

Generalizing transport matrices, if we define Courant-Snyder transformation by

$$\mathbf{B}_x^{-1} = \begin{pmatrix} \frac{1}{\sqrt{\beta_x}} & 0 \\ -\frac{\alpha_x}{\sqrt{\beta_x}} & \sqrt{\beta_x} \end{pmatrix} \quad \mathbf{B}_x = \begin{pmatrix} \sqrt{\beta_x} & 0 \\ \frac{\alpha_x}{\sqrt{\beta_x}} & \frac{1}{\sqrt{\beta_x}} \end{pmatrix} \tag{2.41}$$

then linear motion from position s_1 to s_2 with phase advance ψ_x is described by

$$M_{1\to 2} = B_x(s_2) \begin{pmatrix} \cos\psi_x & \sin\psi_x \\ -\sin\psi_x & \cos\psi_x \end{pmatrix} B_x^{-1}(s_1) \tag{2.42}$$

$$= \begin{pmatrix} \sqrt{\frac{\beta_2}{\beta_1}}(\cos\psi_x - \alpha_1 \sin\psi_x) & \sqrt{\beta_2\beta_1}\sin\psi_x \\ \frac{(\alpha_1-\alpha_2)\cos\psi_x - (\alpha_2\alpha_1+1)\sin\psi_x}{\sqrt{\beta_2\beta_1}} & \sqrt{\frac{\beta_1}{\beta_2}}(\cos\psi_x + \alpha_2\sin\psi_x) \end{pmatrix} \tag{2.43}$$

where $\beta_1 \equiv \beta_x(s = s_1)$ and similarly for other variables. Thus, particle motion is a rotation in normalized coordinates with angle given by the phase advance between two locations.

Twiss functions can be 'transported' using

$$\begin{pmatrix} \beta_2 \\ \alpha_2 \\ \gamma_2 \end{pmatrix} = \begin{pmatrix} M_{11}^2 & -2M_{11}M_{12} & M_{12}^2 \\ -M_{11}M_{21} & 1+2M_{12}M_{21} & -M_{12}M_{22} \\ M_{21}^2 & -2M_{21}M_{22} & M_{22}^2 \end{pmatrix} \begin{pmatrix} \beta_1 \\ \alpha_1 \\ \gamma_1 \end{pmatrix} \tag{2.44}$$

where $M_{12}, ...$ are elements of matrix M. If all matrices around the ring are multiplied, Twiss functions return to same values and particles are transported by a *one-turn map* R

$$\begin{pmatrix} x_f \\ p_{x,f} \end{pmatrix} = R \begin{pmatrix} x \\ p_x \end{pmatrix} = \begin{pmatrix} \cos\nu_x + \alpha_x \sin\nu_x & \beta_x \sin\nu_x \\ \gamma_x \sin\nu_x & \cos\nu_x - \alpha_x \sin\nu_x \end{pmatrix} \begin{pmatrix} x \\ p_x \end{pmatrix} \tag{2.45}$$

2.1.10 Coupling

Just as in a system with several linked harmonic oscillators, X and Y optics can become coupled through terms in the Hamiltonian containing both x and y coordinates. In linear optics, linear coupling can occur from misalignments or dedicated skew-quadrupoles. It is possible to parameterize coupled motion by finding a new eigenbasis, in which optics functions can be derived with respect to 'modes' 1 and 2. Two such parameterizations exist - one of Edwards-Teng and one of Mais-Ripken. The algebra is quite involved and can be found in [10]. In strongly coupled systems, all computations would have to be performed in the mode basis. However, in this thesis linear coupling is always avoided as much as possible, and modes $1/2 \equiv$ X/Y. In a coupled system, tunes cannot not be the same, with splitting described by

$$Q_{1,2} = \frac{1}{2}\left(Q_x + Q_y \pm \sqrt{\Delta^2 + |C^-|^2}\right) \tag{2.46}$$

where $\Delta = Q_x - Q_y$ and $\left|C^-\right|$ is the coupling parameter. A simple experimental test for coupling strength is the minimum tune approach - the distance between two observed tunes at equal uncoupled tunes, when $\Delta = Q_x - Q_y = 0$.

2.1.11 Action-angle canonical coordinates

Existence of motion via coordinate rotations suggest another useful set of canonical coordinates. Defining new *action* J_x and *angle* ψ_x variables as

$$J_x = \frac{1}{2}\begin{pmatrix} x & p_x \end{pmatrix}\begin{pmatrix} \beta_x & -\alpha_x \\ -\alpha_x & \gamma_x \end{pmatrix}\begin{pmatrix} x \\ p_x \end{pmatrix} \tag{2.47}$$

$$= \frac{1}{2}\gamma_x x^2 + 2\alpha_x x p_x + \beta_x p_x^2 \tag{2.48}$$

$$\tan(\psi_x) = -\beta_x \frac{p_x}{x} - \alpha_x \tag{2.49}$$

it can be shown that for any linear lattice, J_x remains unchanged even though all of twiss parameters and coordinates do. This constrains values of x and p_x to lie on the invariant ellipse of area $2\pi J_x$. Meanwhile, equation of motion for angle $d\psi_x/ds = 1/\beta_x$ connects the angle variable to the phase introduced previously in Eq. 2.25. Rearranging 2.47, particle motion can be parameterized as

$$x = \sqrt{2\beta_x J_x} cos(\psi_x) \tag{2.50}$$

$$p_x = -\sqrt{\frac{2J_x}{\beta_x}}\left(\sin(\psi_x) + \alpha_x \cos(\psi_x)\right) \tag{2.51}$$

To demonstrate that action-angle coordinates are canonical pair, it is sufficient to do a canonical transformation using generating function [11]

$$F_1(x, \psi_x) = -\frac{x^2}{2\beta_x}(\tan\psi_x + \alpha_x) \tag{2.52}$$

Then,

$$J_x = -\frac{\partial F_1}{\partial \psi_x} = \frac{x^2}{2\beta_x}\sec^2\psi_x \qquad p_x = \frac{\partial F_1}{\partial x} = -\frac{x}{\beta_x}(\tan\psi_x + \alpha_x) \tag{2.53}$$

which after rearranging matches with definitions in Eq. 2.50 and Eq. 2.47

$$\bar{H} = H + \frac{\partial F_1}{\partial s} = \frac{J_x}{\beta_x} \tag{2.54}$$

$$\nu(J) = \frac{\partial H}{\partial J_x} = \nu_0 \tag{2.55}$$

2.1.12 Emittance of a particle bunch

As well as referring to a property of individual particles, emittance can also be defined for a particle bunch, and denotes the phase space area containing a specific fraction of particles (usually ϵ_{rms}, or 1σ). Using action angle parametrization of Eq. 2.50, second moments of a beam distribution can be calculated as

$$\left\langle x^2 \right\rangle = 2\beta_x \left\langle J_x \cos^2 \psi_x \right\rangle = \beta_x \left\langle J_x \right\rangle = \beta_x \epsilon_x \tag{2.56}$$

$$\langle x p_x \rangle = -\alpha_x \epsilon_x \tag{2.57}$$

$$\left\langle p_x^2 \right\rangle = \gamma_x \epsilon_x \tag{2.58}$$

where $\langle \cdot \rangle$ denotes an ensemble average. Thus, RMS bunch emittance is given by

$$\epsilon_{rms} = \sqrt{\left\langle x^2 \right\rangle \left\langle p_x^2 \right\rangle - \langle x p_x \rangle^2} \tag{2.59}$$

For a Gaussian bunch, ϵ_{rms} can be used to find $\sigma_{rms} = 1 \times \sigma_x$, the standard deviation of particle position - an experimentally observable quantity.

2.1.13 Closed orbit and errors

Imperfections in real lattices cause orbit distortions - deviations of the central particle trajectory from reference orbit. This new path is called the *closed orbit*, and is the orbit used

in all simulations and experiments (involuntarily). For a distortion ('kick') $\theta = \frac{\Delta B l}{B\rho}$ created by a field ΔB over length l, the closed orbit periodic condition is

$$R \begin{pmatrix} x \\ p_x \end{pmatrix} + \begin{pmatrix} 0 \\ \theta \end{pmatrix} = \begin{pmatrix} x \\ p_x \end{pmatrix} \tag{2.60}$$

and thus the new closed orbit coordinates are given by

$$\begin{pmatrix} x \\ p_x \end{pmatrix} = (\mathbf{I} - R)^{-1} \begin{pmatrix} 0 \\ \theta \end{pmatrix} \tag{2.61}$$

where it is assumed the one turn map R is known or can be numerically estimated. Solving explicitly for the position at s after kick at s_1,

$$x(s) = \frac{\theta\sqrt{\beta(s)\beta_{s_1}}}{2\sin(\nu_x)} \cos(|\psi(s) - \psi_{s_1}| - \nu_x) \tag{2.62}$$

Thus, a single large distortion can create a closed orbit that oscillates around the reference orbit, with amplitude scaling as a square root of the observer/kicker β functions. Multiple kicks will just be linear superpositions of individual contributions. Analytically finding closed orbit in full 6D is challenging. Most accelerator codes implement an iterative minimization algorithm, convergence of which is ensured in all simulations. Experimentally, single turn dipole *pings* by a rapidly ramped electrostatic or magnetic device called 'kicker' are used to excite the beam into *free* oscillation (in essence, briefly shifting closed orbit back and forth). Subsequent observations of beam motion can then be used to deduce linear and nonlinear dynamics.

2.1.14 Energy-dependent effects

So far, our discussion has focused on transverse motion under implicit assumption of no energy deviation, $\frac{\Delta p}{p_0} = \delta = 0$. However, real bunched beams will always have an energy spread, determined by the lattice and RF cavities. Two key effects emerge when considering slight deviations from design momentum.

Dispersion

In the presence of dipole magnets, particle orbit will vary with energy deviation. More energetic particles will be bent and focused less, and conversely for less energetic ones. The instantaneous particle trajectory relative to on-momentum x_0 is given by

$$x = x_0(s) + \eta_x \delta + \eta_x^{(2)} \delta^2 + ... \simeq x_0(s) + \eta_x(s)\delta \tag{2.63}$$

where a new lattice function η_x is introduced, called *dispersion*, as well as its higher order terms (second order dispersion $\eta_x^{(2)}$, etc.). Purely linear lattices do not have higher order dispersion, but it can naturally arise from nonlinearities in real rings. Linear dispersion can be obtained by modifying Hill's equation as

$$x''(s) + k(s)x = \frac{1}{\rho}\delta \tag{2.64}$$

$$\eta_x'' + k(s)\eta_x = \frac{1}{\rho} \tag{2.65}$$

which yields an ODE for dispersion that can be solved by similar methods as for on-energy case. Dispersion increases apparent beam size by

$$\sigma_x = \sqrt{\epsilon_x \beta_x + \eta_x^2 \sigma_\delta^2} \tag{2.66}$$

where σ_δ is the rms fractional energy spread. This effect can be important when considering beam pipe apertures and various measurements at location with nonzero dispersion. Dispersion function can be propagated using matrix formalism, same as other twiss functions - exact solutions can be found in [8]. Finally, the effect of dispersion on path length is described by the *momentum compaction factor* α_c (not to be confused with the twiss function $\alpha_x(s)$):

$$\frac{\Delta C}{C} = \alpha_c \frac{\Delta p}{p_0} \rightarrow \alpha_c = \frac{1}{C} \oint \frac{\eta_x(s)}{\rho} ds \approx \frac{1}{\nu_x^2} \tag{2.67}$$

Eq. 2.67 is useful in relating a change in path length ΔC as enforced by RF cavity frequency to the change in particle energy.

Chromaticity

Now, we consider the impact of momentum deviation on the quadrupoles. Similar to dipoles, particles with $\delta > 0$ will experience less focusing, and hence less phase advance, and lower tune. This tune change is called *chromaticity*, by analogy to light optics. The overall tune shift can be expressed as

$$\nu_x = \nu_{x,0} + \left.\frac{\partial \nu}{\partial \delta}\right|_{\delta=0} \delta + ... = \nu_{x,0} + \xi_x \delta + \xi_x^{(2)} \delta^2 + ... \tag{2.68}$$

Since linear chromaticity is often corrected to small values to suppress head-tail instabilities, second order chromaticity $\xi_x^{(2)}$ often has significant impact on beam dynamics. Evaluating linear chromaticity contributions from linear elements, called *natural* chromaticity, is straightforward:

$$\xi_{x,nat} = -\frac{1}{4\pi} \oint \beta_x(s) k(s) ds \tag{2.69}$$

For alternating gradient lattices, β-function is generally higher in regions of positive focusing strength $k(s)$, and hence natural chromaticity is negative, increasingly so for longer rings. However, in what is the beginning of the downfall for the linear lattice concept, natural

chromaticity correction usually (but not always [12]) requires the use of nonlinear elements, intentionally breaking system integrability.

Chromaticity also affects Twiss functions, since tune shift is effectively a phase advance perturbation. The chromatic $\beta, \alpha, ...$ functions vary around the ring, and importantly are not minimized globally if the tune chromaticity is. In other words, while overall phase $\psi = \int 1/\beta$ might be constant for a ring with corrected linear chromaticity, the β function itself is different, with deviations that cancel upon integration. Chromatic optics evaluation can be done by explicitly expanding linear matrices for energy $(1 + \delta)$, or through particle tracking with energy offset, and is implemented in standard simulation codes.

2.1.15 Equilibrium emittance

Equilibrium emittance of lepton rings is determined by a balance of several non-symplectic processes. First is synchrotron radiation damping - the emission of EM radiation by particles undergoing acceleration in an EM field, such as one in dipoles. Photons are emitted in a $1/\gamma_0$ cone in front of the particle, dissipating some amount of both transverse and longitudinal momentum. The total energy loss per turn is given by

$$U_0 = \frac{e^2}{2\epsilon_0} \frac{\beta_0^3 \gamma_0^4}{\rho} \tag{2.70}$$

Because of the steep γ_0 dependence (γ_0 here is again the Lorentz factor, not be confused with twiss function γ_x), hadron machines emit very little SR. There is an observable effect on a timescale of hours at very high energies [13], but in general hadron machines rely on low starting emittance at injection, and careful control of any emittance growth sources.

The second non-conservative process is acceleration in the RF cavities, which restores lost longitudinal energy. On average, SR and RF processes damp transverse oscillations and decrease bunch emittance.

The final effect is quantum excitation, which describes particle recoil from photon emission. If recoil happens in a dispersive location, it will induce particle oscillations (since particles are set on an off-energy closed orbit), increasing bunch emittance.

The equilibrium balance of SR, RF, and quantum excitation determines minimum possible, or *natural*, transverse and longitudinal emittances. This relationship is usually expressed through synchrotron integrals $(I_1, ..., I_5)$, which are properties of linear lattice only, as

$$\epsilon_0 \propto \gamma_0^2 \frac{I_5}{I_2} = \gamma_0^2 \frac{\oint (\gamma_x \eta_x^2 + 2\alpha_x \eta_x \eta_{p_x} + \beta_x \eta_{p_x})/\rho^3 \, ds}{\oint 1/\rho^2 \, ds} \tag{2.71}$$

To get lower emittance, as desired in light sources and current work, dispersion within bending elements ($\rho \neq \infty$) needs to be minimized, energy maximized, and overall ring size increased.

Actual operational emittance is often larger than natural one. An effect relevant to this thesis is Intra Beam Scattering (IBS), a process that couples and increases all three emittances through multiple particle scattering within a bunch. IBS results in a current-dependent equilibrium emittance with scattering strength that scales as $1/\gamma_0^4$. Exact analytical treatment is quite involved [14], so most codes perform numerical IBS evaluation, such as with completely integrated modified Piwinski approximation [15].

2.1.16 Stability of linear systems

The general question of stability or conversely of chaotic behavior of classical systems is very broad and beyond the scope of this thesis. A useful result is that for a system with N degrees of freedom, motion can be guaranteed to be regular and stable everywhere if there are N isolating integrals of motion. An isolating, or 'first' integral, is a function of phase space variables which is constant along a phase space trajectory. A sufficient condition to be isolating is that the integral I_i is in involution with all others, that is, $[I_i, I_j] = 0$ and

$[I_i, H] = 0$ where $[f, g]$ denotes Poisson bracket.

In case of linear systems, the isolating integral of motion is the Hamiltonian itself, which was shown in 2.54 to be a time-independent function of action. In general however, finding isolating integrals is a difficult and open problem, as is proving non-integrability.

Stability of integrable systems under perturbation $H_p = H + \epsilon f(J, \psi)$ was studied by Nekhoroshev [16]. He found that to insure stability of a near-integrable Hamiltonian system over exponentially long times, H needs to meet two conditions - steepness and complex-analyticity [17]. Linear Hamiltonian is not steep, and thus any nonlinear perturbations can make particle motion unstable.

2.2 Nonlinear beam dynamics

In the linear analysis presented above, beam dynamics was well behaved and life was good - motion was regular and stable everywhere, and analytically tractable. Unfortunately, purely linear systems are not possible due to operational requirements, magnet misalignments, and field errors. This section presents some of the issues and advantages of nonlinear effects.

2.2.1 Nonlinear elements

Multipoles above $n = 2$ do not affect linear dynamics, but play an important role in beam stabilization. Sextupoles are used to change natural chromaticity, usually such that the total magnitude is small. This suppresses a class of head-tail instabilities [18], a necessary requirement for high intensity operation. Sextupolar chromaticity contribution can be found by expanding the Hamiltonian for an off-momentum particle and keeping lowest order terms

[5], giving

$$\xi_{x,sext} = \frac{1}{4\pi} \oint \beta_x(s)\eta_x(s)k_2(s)ds \tag{2.72}$$

$$\xi_{y,sext} = -\frac{1}{4\pi} \oint \beta_y(s)\eta_y(s)k_2(s)ds \tag{2.73}$$

Note that this effect requires dispersion - sextupoles located in non-zero dispersion regions are referred to as *chromatic*, and those without dispersion as *harmonic*. The latter are important since they still produce higher order beam kicks and can be used to cancel out the detrimental abberations of the chromatic elements.

The primary use of octupoles is in generation of amplitude-dependent tune shift for beam stabilization purposes, as will be discussed below. For octupole strength $k_3 = 6O(s)/B\rho$, first order detuning can be found by substituting action-angle parameterized coordinates of Eq. 2.50 into octupolar Hamiltonian as

$$\Delta Q_x = \left[\oint \frac{k_3\beta_x^2}{16\pi}ds\right] J_x - \left[\oint \frac{k_3\beta_x\beta_y}{8\pi}ds\right] J_y \tag{2.74}$$

$$\Delta Q_y = \left[\oint \frac{k_3\beta_y^2}{16\pi}ds\right] J_y - \left[\oint \frac{k_3\beta_x\beta_y}{8\pi}ds\right] J_x \tag{2.75}$$

Octupoles also contribute to second order chromaticity and multiple higher order effects. Note that sextupoles also produce a tune shift, but it is a second order effect ($\propto k_2^2$) and has no simple formula, being highly dependent on lattice tunes and phase advances.

In the presence of multipoles, Hamiltonian generally no longer has any invariants - the resulting system is not stable at all amplitudes, and exhibits irregular, chaotic motion. Phase space trajectories get modified and distorted, as shown in Poincaré map of Fig. 2.3. Detailed study of nonlinear beam dynamics proceeds through normal form analysis and Lie algebra formalism, which are (roughly) the generalizations of Courant-Snyder normalization and matrix maps, respectively. An interesting overview can be found in [19], and experimental

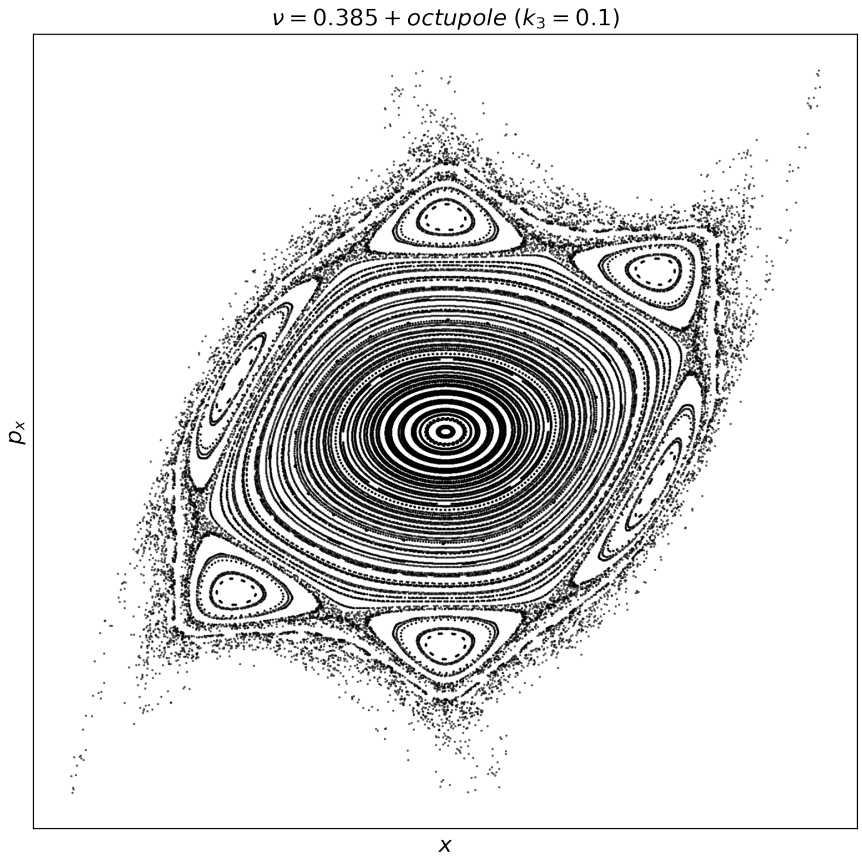

Figure 2.3: Phase space $x - p_x$ of Henon-Heiles 2D system - a linear cell with single thin octupole. Empty outside areas are unstable, with lost particles. Inner circular region is stable, and is called dynamic aperture. In between, various resonant and chaotic motion occurs.

measurements in [20]. One important conclusion of such analysis is determination of invariant *smear*, or *jitter* - the variation of linear invariants (or amplitudes, A) over many turns

$$S_x(\phi) = \frac{\sigma_{J_x}}{< J_x >} = \sqrt{\frac{< (\delta A_x)^2 >}{A_x^2}} \tag{2.76}$$

Analytic results of [21] show that smear will depend on the strengths of nonlinearities, their phases, and measurement location. However, smear amplitude will only change at the nonlinear elements. So, if the accelerator has a single dominant nonlinear region, equal smear levels would be expected at all other points.

2.2.2 Resonances

The term 'resonance' in the context of particle accelerators refers to any perturbation which drives particle motion at a frequency related to linear tunes by an integer ratio:

$$m\nu_x + n\nu_y = r \qquad (m, n, r) \in \mathbb{Z} \tag{2.77}$$

The resonance *order* is the sum $|m| + |n|$, and reflects the types of fields and elements that can contribute to it (although a multipole of matching order is *not* required [22]). Since linear optics tunes are invariant, resonances can result in unbounded betatron amplitude growth and eventual particle loss. For example, dipoles produce resonances $(0, 1)$ and $(1, 0)$, which can be understood as beam getting kicked at the same phase every time it passes around the ring. In reality, resonance conditions are not exact - some are not harmful while others have varying widths, called stopbands. Since more elements contribute to lower order resonances, those have the largest stopbands and are avoided.

The operational accelerator tune is called the *working point*, and is placed in a region with as few harmful resonances as possible. Typically that is along the diagonal of the tune diagram, near the difference resonance $\nu_x - \nu_y = n$. Tune diagram is a plot in ν_x/ν_y space, and will be used frequently in this thesis. An example with up to 8th order resonances is given in Fig. 2.4.

Beam dynamics in the vicinity of a specific resonance can be studied though a canonical transformation via perturbation theory [23], and leads to resonant driving term [24] formalism of nonlinear beam motion.

2.2.3 Space charge

In this thesis, all measurements were done with electron beams, which have negligible space-charge effects at relativistic energies. However, is it important to explain why these effects are

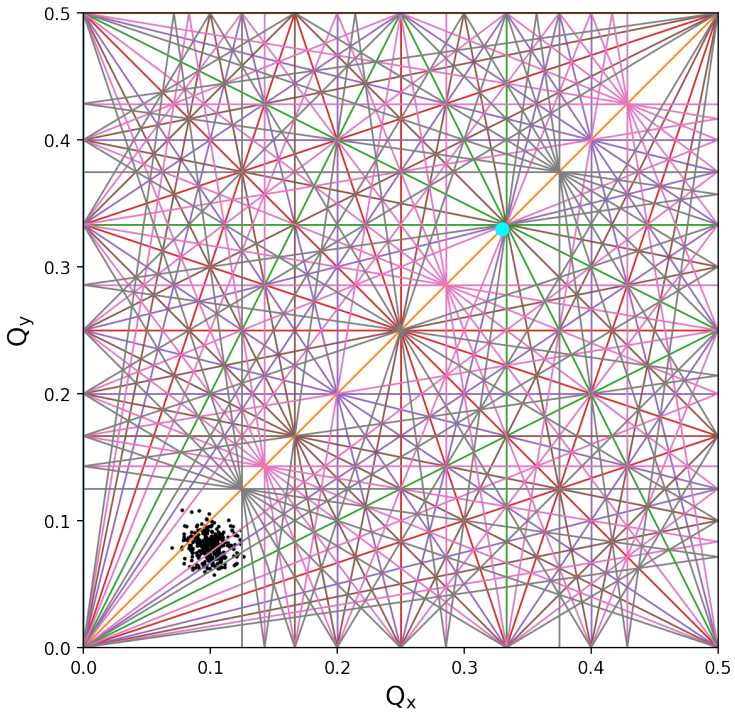

Figure 2.4: Resonance lines up to 8th order. Black dots denote tunes of a collection of particles with tune spread, while cyan a point-like tune of an ideal linear optics bunch.

detrimental - space-charge forces produce a current and distribution dependent incoherent and coherent tune shifts, as well as collective oscillations. The coherent linear tune shift is negative (particles defocus each other), and can be corrected. Variable incoherent tune shift depends on particle location and bunch distribution, and increases beam tune footprint. If tune spread becomes too large, as for the black points in Fig 2.4, some particles will be pushed onto a resonance and lost [25]. The last effect, collective motion, results in a variety of transverse, longitudinal, or coupled instability modes with varying causes, thresholds, and resonance conditions [26]. In high intensity machines, the latter is most problematic and difficult to analyze. The goal of strongly nonlinear lattices such as one studied in this thesis is to suppress collective instabilities through nonlinear decoherence and Landau damping.

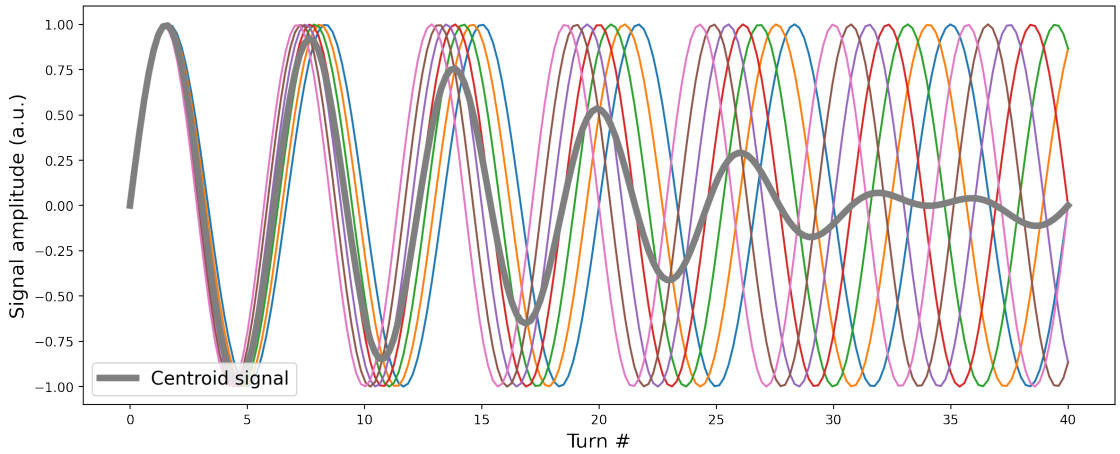

Figure 2.5: Decoherence of centroid motion for particles with a large tune spread.

2.2.4 Decoherence

An important practical effect of tune spread, such as that caused by octupoles and non-zero chromaticity with energy spread, is particle (nonlinear) decoherence after an excitation, also known as phase space *filamentation*. This effect can stabilize resonantly exited particles by shifting their tunes off the resonance once their amplitude slightly increases. Decoherence strength depends only on the lattice design, and not on collective beam behavior - a practical advantage over Landau damping (discussed below). However, decoherence also presents a practical problem - devices that measure bunch centroids have a limited time window to observe beam dynamics evolution after a perturbation, even though the individual particles are still oscillating at full amplitude. This problem is shown in Fig. 2.5. In chapter 4, explicit formulas will be derived for the envelope shape of several decoherence effects and correction schemes discussed. Note that decoherence should not be confused with damping, specifically synchrotron damping, where individual particles do experience a true decrease in individual oscillation amplitudes.

2.2.5 Landau damping

Landau damping is a mechanism of collective instability suppression first studied in the context of plasma confinement [27]. It is a common approach for controlling space-charge, impedance, and other beam instabilities and is actively employed at virtually all hadron facilities, for example SIS100 [28] and LHC [29]. Producing strong Landau damping is the eventual goal of nonlinear systems being studied in this thesis, but full analytic treatment (through Vlasov equation formalism and dispersion relation [30, 31]) is highly involved - only a brief summary is given here.

Landau damping describes a process of energy transfer from coherent to incoherent particle motion within a bunch such that any coherent instability formation is suppressed. Energy is not dissipated during this process, but redistributed such that no collective motion occurs. The strength of Landau damping depends on the amount of tune spread, but it is not a sufficient condition. Unlike nonlinear decoherence, Landau damping is a property of the particle ensemble [32], and has two additional requirements [33]. First is that the coherent mode frequency must be within the range of tune spread, enabling nearby (in tune) particles to interact with it. Second is that this coherent mode be on the downward slope of the frequency distribution (more particles nearby with a lower frequency), such that energy is on average extracted from the collective wave. This is true for bunches with higher phase space density at lower amplitudes and standard multipole detuning, but other collective effect can cause Landau damping loss. In practice, last two conditions can usually be satisfied at operational parameters through careful lattice design, and so the relevant figure of merit for Landau damping strength is the maximum available detuning.

2.3 Nonlinear integrable optics

The unavoidable complications of nonlinear imperfections, avoiding resonances, and suppressing instabilities significantly degrade the nominal performance of alternating gradient

linear lattices. The standard mitigation strategy is to correct parameters so as to return close to the linear, integrable baseline. In the case of nonlinear requirements like Landau damping and chromaticity correction, nonlinear strengths are reduced to the bare minimum and undesired higher order contributions canceled out with careful element placement. As beam intensity requirements grow, finding acceptable tradeoffs is becoming harder and more expensive to implement.

However, there is no fundamental requirement that integrable lattices be linear - their popularity is the result of model simplicity and historical familiarity. The goal of nonlinear integrable optics (NIO) is to study explicitly nonlinear integrable lattices. As will be demonstrated in this section, they do exist and have a built-in advantage - strong detuning with amplitude, which through nonlinear decoherence suppresses resonant losses and halo formation without a reduction in dynamics aperture [32, 34, 35]. Furthermore, thanks to KAM theorem such lattices are more tolerant to perturbations than linear ones. In this section, we follow the work of Danilov [36] and Nagaitsev [37] in deriving several types of NIO lattices, and discuss their properties.

2.3.1 Nonlinear Hamiltonian

We start with the linear Hamiltonian of Eq. 2.18 and add an arbitrary nonlinear potential $V(x, y, s)$ to obtain

$$H = \frac{1}{2}(p_x^2 + p_y^2) + \frac{1}{2}\left(K_x(s)x^2 + K_y(s)y^2\right) + V(x, y, s) \tag{2.78}$$

$$= \frac{1}{2}(p_x^2 + p_y^2) + \frac{1}{2}K_x\left(x^2 + y^2\right) + V(x, y, s) \tag{2.79}$$

Several assumption have been made here, and it is helpful to state them explicitly:

- The optics is symmetric, $\beta_x = \beta_y$ (and hence $K_x = K_y$)
- The particle has no energy deviation, $\delta = 0$

- There is no dispersion, $\eta = 0$, or chromaticity, $\xi = 0$
- Orbit is straight, $1/\rho = 0$

These assumptions will be important when designing an actual ring lattice. As in section 2.1.8, a canonical transformation to normalized coordinates is made

$$H_N = \frac{1}{2}(\bar{p}_x^2 + \bar{p}_y^2 + \bar{x}^2 + \bar{y}^2) + \beta(s)V(\bar{x}\sqrt{\beta(s)}, \bar{y}\sqrt{\beta(s)}, s) \tag{2.80}$$

$$= \frac{1}{2}(\bar{p}_x^2 + \bar{p}_y^2 + \bar{x}^2 + \bar{y}^2) + U(\bar{x}, \bar{y}, s) \tag{2.81}$$

where substitution for U is done to match DN notation.

2.3.2 Henon-Heiles or quasi-integrable lattice

The Danilov/Nagaitsev approach is to seek solutions for U that yield two isolating invariants of motion. First invariant could be the Hamiltonian itself, if it were possible to make $U(\bar{x}, \bar{y}, s)$ time independent, i.e. $U(\bar{x}, \bar{y})$. From the multipole expansion $V \propto \sum z^{n+1}$ (where z is x, y, or their cross terms), it is clear that the required scaling correction is $\beta^{-\frac{(n+1)}{2}-1}$. For example, given normal octupole potential ($n = 3$)

$$V(x, y, s) = \frac{1}{24}(x^4 + y^4 - 6y^2x^2) \tag{2.82}$$

the normalized potential is

$$U(\bar{x}, \bar{y}) = V(\bar{x}\sqrt{\beta(s)}, \bar{y}\sqrt{\beta(s)}, s)\frac{1}{\beta(s)^3} = \frac{1}{24}(\bar{x}^4 + \bar{y}^4 - 6\bar{y}^2\bar{x}^2) \tag{2.83}$$

Adding a strength scaling constant κ, the final Hamiltonian is

$$H_N = \frac{1}{2}(\bar{p}_x^2 + \bar{p}_y^2 + \bar{x}^2 + \bar{y}^2) + \frac{\kappa}{4}(\bar{x}^4 + \bar{y}^4 - 6\bar{y}^2\bar{x}^2) \tag{2.84}$$

Note that many other multipole potentials would also be valid with appropriate scaling [38], and sextupoles were studied theoretically in [39]. However, octupoles have a natural advantage in terms of beam dynamics and are a stepping stone to the fully integrable case. Because this system only has a single invariant, it is referred to as 'quasi-integrable' (QI). Another common name for it is 'octupole Hénon-Heiles type system', due to similarity with the well studied Hénon-Heiles map [40]. A consequence of quasi-integrability is that the region of stable motion has an upper limit, determined by locations of the hyperbolic fixed points at $(\bar{x}, \bar{y}) = (\pm\sqrt{1/2\kappa}, \pm\sqrt{1/2\kappa})$ [32]. This is easily visualized by plotting the invariant contours, as in done in Fig. 2.6a. Thus, to ensure stability of a particle with emittance ϵ^*, octupole strength must be $\kappa < 1/4\epsilon^*$. A simple simulation with exact maps shows ideal dynamic aperture to be slightly lower, at $0.6/\sqrt{\kappa}$, due chaotic but bounded motion near the separatrix [41].

In essence, QI system is a nonlinear system with 1 invariant that has a fundamental hard upper detuning strength limit due not being fully integrable. Nonetheless, it is a significant improvement on the completely non-integrable alternatives, and combined with robustness to perturbations (studied in chapter 5) is a great candidate for experimental studies.

2.3.3 Danilov-Nagaitsev fully integrable lattice

While the majority of this thesis is focused on exploring the QI system, some measurements of DN system were also performed. As such, we also present the more involved derivation of the second isolating integral of motion. Starting with Hamiltonian in Eq. 2.84, we search for the most general quadratic second integral of motion of the form

$$I = Ap_x^2 + Bp_xp_y + Cp_y^2 + D = (ay^2 + c^2)p_x^2 + (-2axy)p_xp_y + (ax^2)p_y^2 + D \qquad (2.85)$$

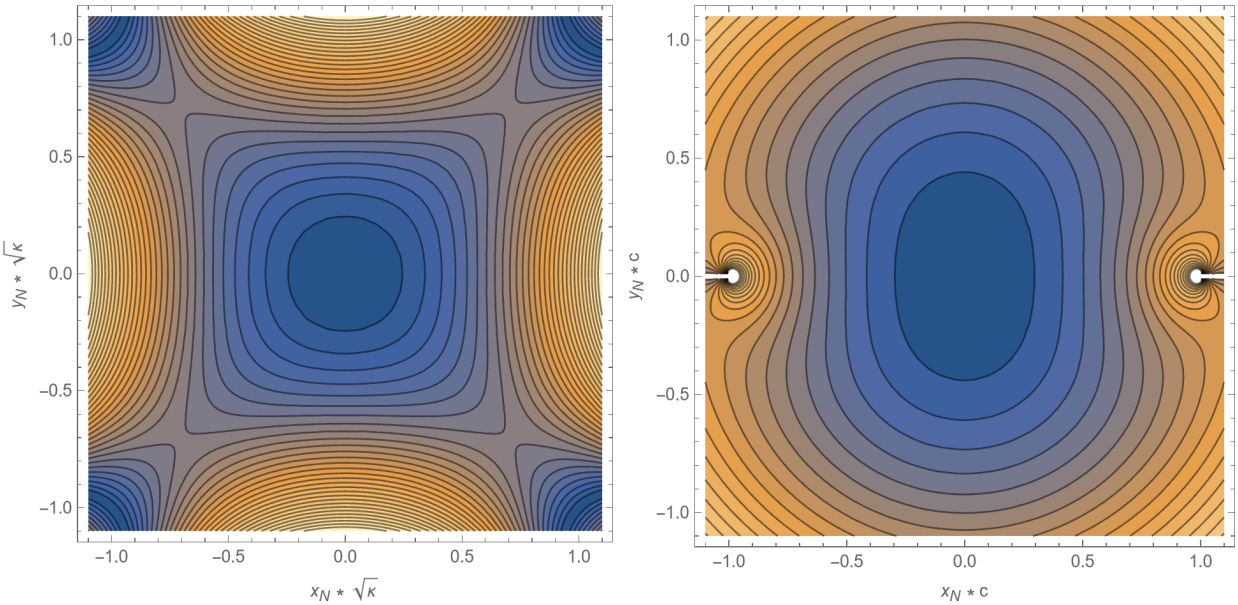

(a) QI system Hamiltonian contours (b) DN system Hamiltonian contours

Figure 2.6: NIO systems.

where the bars above normalized variables were dropped for brevity. Choosing $a = 1$ and $c \neq 0$, the classical Bertrand-Darboux PDE [42] is obtained

$$xy(U_{xx} - U_{yy}) + (y^2 - x^2 + c^2)U_{xy} + 3yU_x - 3xU_y = 0 \tag{2.86}$$

where $U_{xx} \equiv \partial^2 U/\partial x^2$, etc. The solution is given by

$$U(x, y) = \frac{f(\xi) + g(\eta)}{\xi^2 - \eta^2} \tag{2.87}$$

for arbitrary f and g, and with elliptical coordinates for foci $\pm c$ given by

$$\xi = \frac{\sqrt{(x+c)^2 + y^2} + \sqrt{(x-c)^2 + y^2}}{2c} \qquad \eta = \frac{\sqrt{(x+c)^2 + y^2} - \sqrt{(x-c)^2 + y^2}}{2c} \tag{2.88}$$

Finally, the second invariant is then obtained as

$$I(x,y) = (xp_y - yp_x)^2 + c^2 p_x^2 + 2c^2 \frac{f(\xi)\eta^2 + g(\eta)\xi^2}{\xi^2 - \eta^2} \tag{2.89}$$

and Hamiltonian is

$$H_N = \frac{1}{2}(p_x^2 + p_y^2 + x^2 + y^2) + \frac{f_2(\xi) + g_2(\eta)}{\xi^2 - \eta^2} \tag{2.90}$$

with

$$f_2 = \xi\sqrt{\xi^2 - 1}(d + t\cosh(\xi)) \tag{2.91}$$

$$g_2 = \eta\sqrt{1 - \eta^2}(b + t\cos(\eta)) \tag{2.92}$$

where constants d, b, and t are arbitrary, with choice of $d = 0$ and $b = -t\pi/2$ motivated by practical factors. Note that implementing DN potential of Eq. 2.90 in tracking codes is difficult due numerical instability of the small denominator. A new parametrization in complex plane ($\zeta = x + iy$) was introduced in [43], and is the preferred approach that is used in this thesis

$$H_N = \frac{1}{2}(p_x^2 + p_y^2 + x^2 + y^2) + t\,\mathrm{Re}\left(\frac{\zeta}{\sqrt{1 - \zeta^2}}\arcsin(\zeta)\right) \tag{2.93}$$

Note how constant t is the strength scaling factor of the nonlinear potential. Unlike QI system, for DN there is no stability boundary - the system is fully integrable in 4D (Fig. 2.6). However, there are practical and topological considerations [44] which limit experimentally accessible regions to those away from singularities at $x = \pm c$

2.3.4 Connection between DN and QI systems

Complex DN potential of Eq. 2.93 has a multipole expansion (valid inside $r = \sqrt{x^2 + y^2} < c$) of

$$U(x, y) = t \,\mathrm{Re}\left[(x + iy)^2 + \frac{2}{3c^2}(x + iy)^4 + \frac{8}{15c^4}(x + iy)^6 + ...\right] \tag{2.94}$$

where first term is quadrupolar ($\propto z^2$), second octupolar, etc. By truncating the expansion at the first nonlinear (amplitude detuning capable) order, and dropping linear contributions, the quasi-integrable octupole system potential is recovered. The conversion from t to κ notation is

$$\kappa = \frac{8}{3}\frac{t}{c^2} \tag{2.95}$$

and the octupole strength k_3 (before scaling by magnet/insert length) given by

$$k_3 = \frac{16}{\beta^3}\frac{t}{c^2} \tag{2.96}$$

Typical design values are $c^2 = 0.01\,\mathrm{cm}$ (fixed geometric parameter, also expressed as $c = 0.01\,\mathrm{m}^{1/2}$) and $t = 0$ to $t = 0.5$ (variable strength parameter).

2.3.5 NIO perturbations

In above derivations, several simplifying assumptions were made. Of special interest is adding back momentum deviation, as was done for the linear case. Using Lie operator formalism methods, in [45] a Hamiltonian was derived with off-momentum terms as

$$H = \mu_0 \left[(1 - \xi_x(\delta))\frac{x^2 + p_x^2}{2} + (1 - \xi_y(\delta))\frac{y^2 + p_y^2}{2} + \nu_0 t U(x, y)\right] + \text{h.o.t.} \tag{2.97}$$

where μ_0 is total phase advance and ν_0 phase advance across the insert. There is a clear effect of chromaticity on the invariant, in that it is no longer conserved. However, if chromaticities

are made equal (but non-zero), ignoring higher order terms, this can be simplified to

$$H = \frac{1}{2}\left(1 - \frac{\mu_0 \xi(\delta)}{\nu_0}\right)(x^2 + p_x^2 + y^2 + p_y^2) + tU(x, y) \tag{2.98}$$

which for on-momentum particle matches previous results. In other words, integrability is broken for off-momentum particles, but can be restored to lowest order if the chromaticities are made equal. Practically then, off-momentum effects can be compensated with relatively modest sextupole corrections.

Using similar approach, effects of synchrotron motion were analyzed in [46], and new 'stroboscopic' invariants were shown to be preserved over many periods, suggesting that the system remains integrable. Treatment of other perturbations, such as field error and misalignments, is not tractable analytically and will rely on extensive numerical simulations.

CHAPTER 3

EXPERIMENTAL DESIGN

This chapter presents the implementation of NIO concepts introduced in Chapter 2. Section 3.1 discusses the properties of nonlinear and linear regions, and the consequences for ring design. The Integrable Optics Test Accelerator (IOTA) ring history and lattice are presented in section 3.2. Sections 3.3 and 3.4 discuss the specifications and manufacturing of the two nonlinear inserts.

3.1 Implementation of QI and DN potentials

3.1.1 T-insert design

In deriving the ideal Hamiltonians of Eqs. 2.84 and 2.93, a key assumption was made that the linear optics is symmetric, $\beta_x = \beta_y$. However, both dipoles and quadrupoles perturb twiss functions asymmetrically, and thus cannot be placed anywhere in a contiguous nonlinear region. This leaves only one possible solution, a drift - if a symmetric beam is placed at the start of the drift, the evolution of β (dropping x/y subscripts) in a drift is given by

$$\beta(s) = \beta(s=0) - 2s\alpha(s=0) + s^2\gamma(s=0) \tag{3.1}$$

where all initial twiss parameters are specified at the start $s = 0$. Beta functions will evolve parabolically and maintain symmetry, but this drift on its own is useful for only a single pass. In a ring, it is necessary to maintain beam focusing - an element is required to bring the beam back to the start of the nonlinear drift with the same parameters as before the first pass. Ideally, this should be done transparently, so that the effective system Hamiltonian remains unchanged. Expressed as a single matrix, the element that accomplished this is an

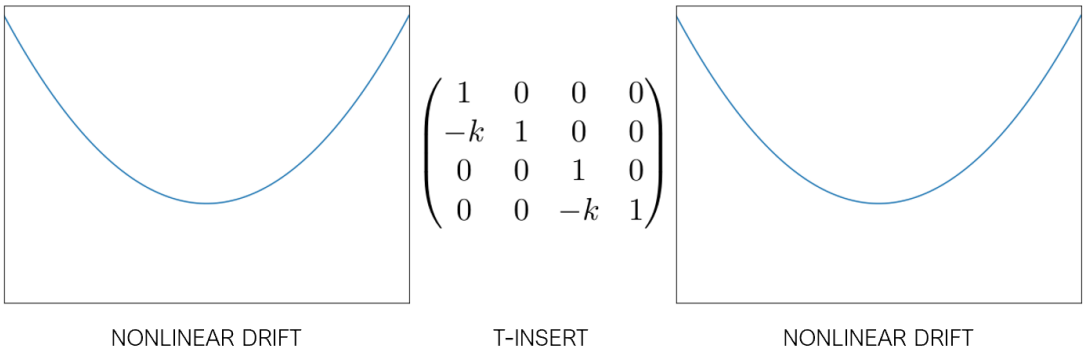

Figure 3.1: T-insert design with drift and focusing regions.

axially symmetric thin lens ('T-insert'), with transfer matrix of

$$M_T = \begin{pmatrix} 1 & 0 & 0 & 0 \\ -k & 1 & 0 & 0 \\ 0 & 0 & 1 & 0 \\ 0 & 0 & -k & 1 \end{pmatrix} \tag{3.2}$$

where $k = 1/f$ is the integrated focusing strength and inverse of focal length. With a drift + T-insert arrangement, particle ends up in a periodic FOFO... (focus-drift-focus-drift-...) lattice, as shown in Fig. 3.1.

3.1.2 Lattice parametrization

T-insert optics is mirror symmetric around the drift midpoint, which sets $\alpha(s = 0) = -\alpha(s = L)$ and $\gamma(s = 0) = \gamma(s = L)$. Thus, $\beta(s)$ can be re-expressed as only a function of distance s as

$$\beta(s) = \frac{L - sk(L - s)}{\sqrt{1 - \left(1 - \frac{Lk}{2}\right)^2}} \tag{3.3}$$

where L is the total drift length. The minimum value of β occurs in the middle of the drift, and is called β^*. A useful relation is

$$\beta(s) = \beta^* + \frac{(s - s^*)^2}{\beta^*} \tag{3.4}$$

where s^* is location of β^*. Overall, nonlinear drift only has two free parameters - the drift length L and focusing strength k. However, since T-insert phase advance is $n\pi$, the fractional tune of the whole ring is exactly that of the nonlinear drift (or 0.5 plus the drift). So, it is more convenient to parameterize the system by the drift phase advance $0 < \mu < \pi$. Namely,

$$\beta^* = \frac{L}{2}\cot(\mu) \tag{3.5}$$

$$\beta(s) = \beta^* \left[1 + \left(\frac{2s}{L}\right)^2 \tan^2(\mu/2)\right] \tag{3.6}$$

$$f = 1/k = \frac{L}{4}\csc(\mu/2)^2 \tag{3.7}$$

The general relationship (Fig. 3.2) is that if phase advance is increased, more focusing is required, β^* is reduced, while β_{edge} is increased (in region $\pi/2 < \mu < \pi$). In colliders, this approach is used to increase luminosity by squeezing the beams at the collision point. The disadvantage is that large β_{edge} requires large aperture quadrupoles, very strong focusing, and also introduces significant chromatic perturbations.

For the nonlinear lattice, on paper it is desirable to have a high phase advance so as to produce larger tune spread. However, this presents a significant implementation challenge - a large variation in β implies large range of required nonlinear field strengths ($1/\beta^3$), making an implementation with acceptable field errors more difficult. A more detailed discussion of performance considerations will be given in chapter 5 and section 3.3.

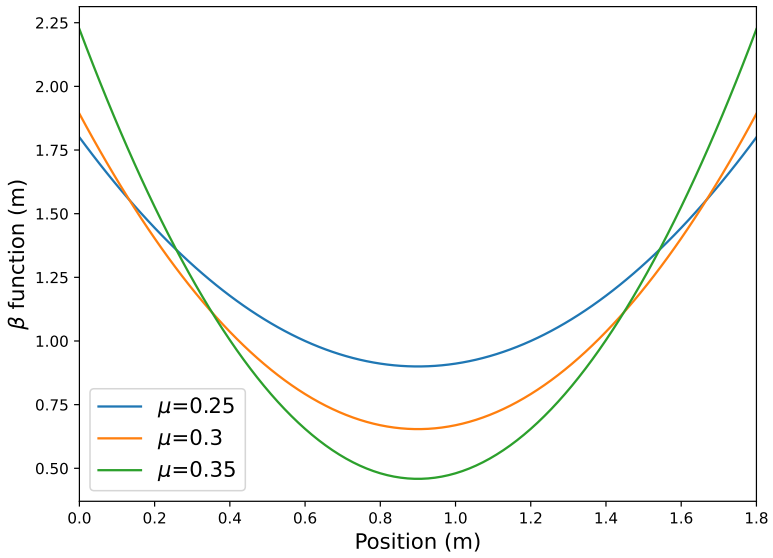

Figure 3.2: A drift space with varying phase advances.

3.1.3 Effect of DN magnet

Because of the quadrupole field component, DN magnet affects linear optics. The resulting tune shift with strength is given by

$$Q_x = Q_0\sqrt{1+2t} \tag{3.8}$$

$$Q_y = Q_0\sqrt{1-2t} \tag{3.9}$$

Twiss functions also become distorted, but remain symmetric:

$$\beta_x = \beta_0\sqrt{\frac{1}{1+2t}} \tag{3.10}$$

$$\beta_y = \beta_0\sqrt{\frac{1}{1-2t}} \tag{3.11}$$

$$\alpha_x = 0 \tag{3.12}$$

$$\alpha_y = 0 \tag{3.13}$$

For IOTA, 0.3/0.3 working point implies interception of $Q_y = 5.0$ integer resonance at around $Q_x = 0.42$ (Fig 3.3). The above detuning formulas will not be valid past $t = 0.5$, and a new two-orbit topology will develop. More theoretical details can be found in [44].

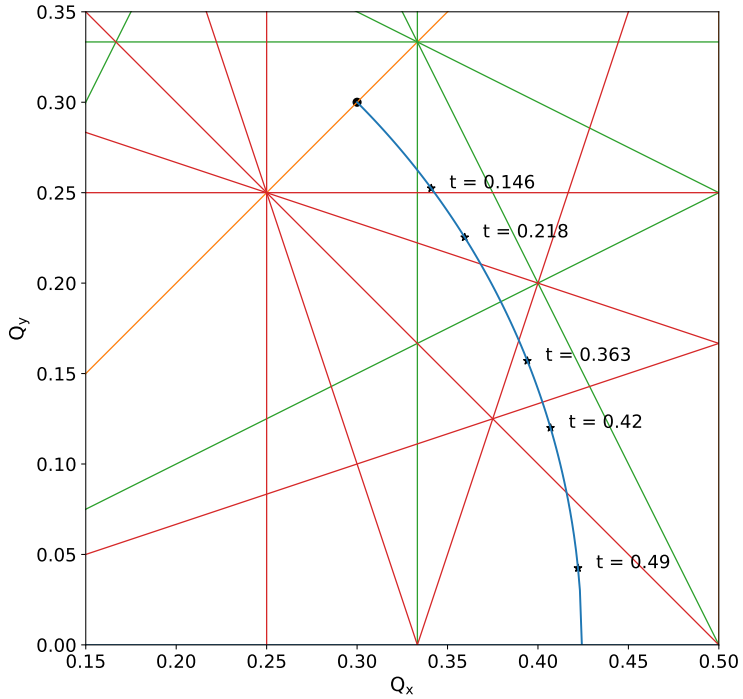

Figure 3.3: Linear tune of DN insert system.

3.2 The Integrable Optics Test Accelerator (IOTA) ring

Due to the unique T-insert design requirements, modification of existing rings to accommodate NIO lattices is either impossible or not practical. As such, a new dedicated facility was necessary. At Fermilab, first plans to build an integrable ring started in 2008, stimulated by the advancement of theory [36]. Simultaneously, construction of a superconducting linac to be used as the International Linear Collider (ILC) test facility was set in motion. As part of that facility, a linac tunnel extension and a small cave were built for a potential low energy research ring. First IOTA lattices had 4 cell symmetry, with integrable optics and optical stochastic cooling as the two flagship experiments [47]. This design underwent several

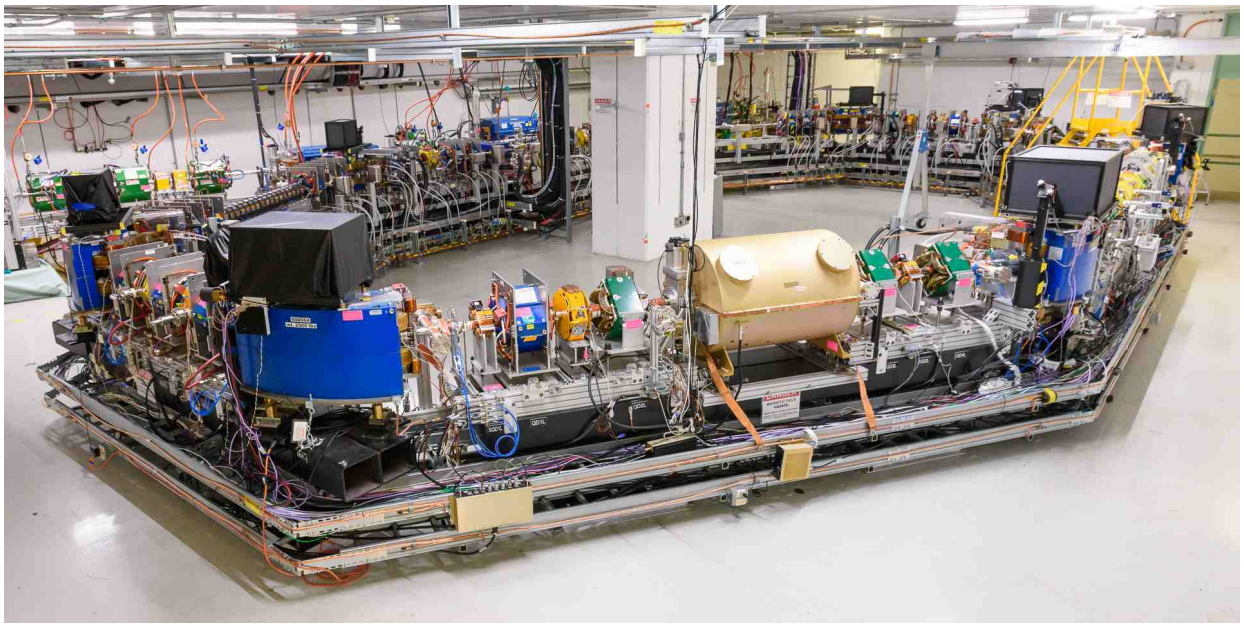

Figure 3.4: Panoramic picture of IOTA ring. The nonlinear inserts can be seen in the background left and right. Image by G.Stancari/Fermilab.

iterations to accommodate the growing list of potential users, but construction was limited by funding availability. In 2014, the Particle Physics Project and Prioritization Panel (P5) report was released, setting the neutrino program as priority for domestic accelerator-based high energy physics [48]. These experiments would necessitate significant upgrades to Fermilab linac (Proton Improvement Plan - II) and Booster (replaced by a new rapid cycling synchrotron) so as to produce multi-MW proton beams [49]. Combined with ILC future becoming uncertain, a new mission of the test facility was set - to be the testbed for advanced beam dynamics concepts in support of the neutrino program and other high intensity/high brightness machines. With single-cryomodule linac completion in 2017 (now called FAST linac), focus finally shifted to IOTA. Ring construction was completed in summer of 2018. An image of IOTA is shown in Fig. 3.4 and the block schematic in Fig. 3.5.

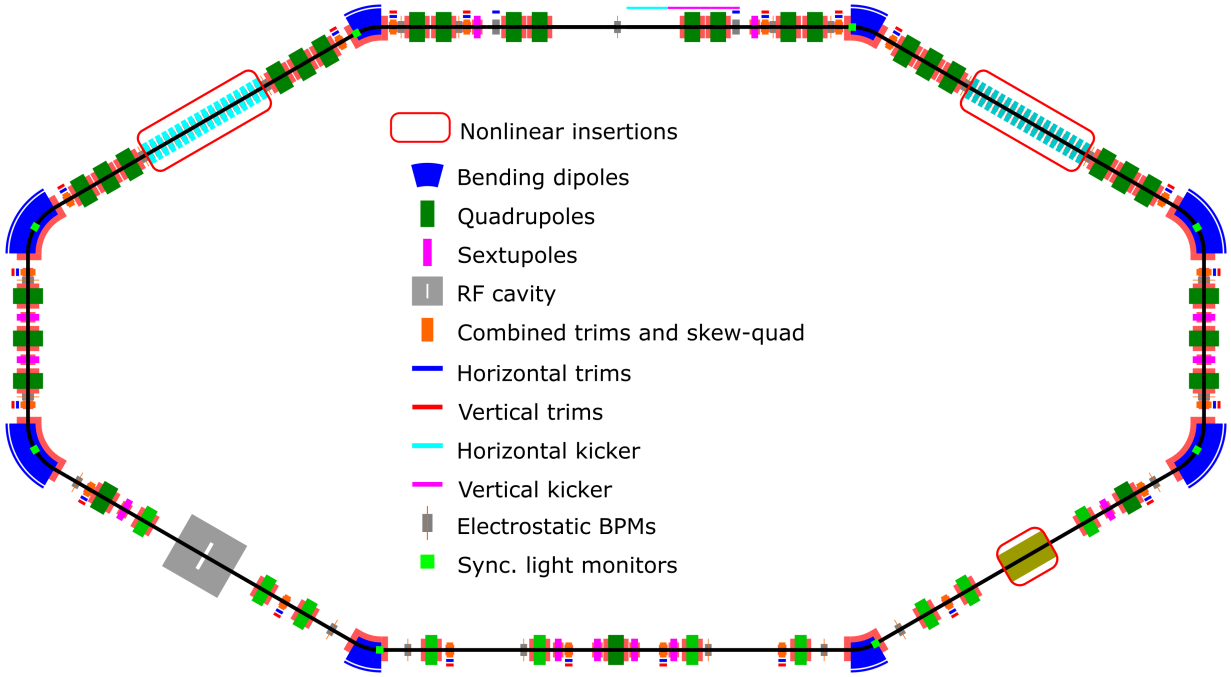

Figure 3.5: Schematic block diagram of the IOTA ring in as-designed run 2 configuration.

3.2.1 IOTA NIO program

Being one of flagship IOTA experiments, NIO program has three overarching goals spanning almost a decade of preparation and studies. First is to demonstrate viability of the NIO design - whether it offers practical benefits, and also to study some of the more academic questions of stability and integrability. Second goal is to establish NIO limits of applicability, such as required magnet and other tolerances and possible modes of operation. Third is to put it all together and develop practical, experimental, data-driven solutions for larger machines. The leading option for the latter goal is a booster upgrade at Fermilab to a rapid cycling synchrotron, the recent design studies of which (including NIO option) can be found in [50, 51].

These three goals are to be accomplished in two phases, first with electron beams (2018-2021) and then with proton beams (2021-2023). The reasons for this separation are both logistical, in that the proton injector will not be ready until end of 2021, but also because

of the fundamentally different beam properties. For protons, emittance is expected to be large, and there is no synchrotron damping. Given the low energy and high intensity of beam provided by the injector, significant space-charge effects will be present. These beam parameters mimic high energy and intensity machines, and so it can directly probe various collective instabilities and resonances, quantifying the suppression strength of NIO systems. However, for studying certain aspects of beam dynamics protons are a poor choice - they emit no SR, decohere extremely quickly, and because of space-charge are very hard to measure reproducibly at same current. Thus, for initial beam dynamics studies, electron beam is the preferred choice - it can be placed at various points in phase space, and serves as a probe of local single-particle dynamics. This allows for accurately measuring the tune and dynamical aperture, and reconstructing phase space (Poincaré surfaces). As a side benefit, electrons are easier to commission and tune lattice with due to additional SR-based beam diagnostic, and were available for injection starting in 2017 upon completion of FAST linac.

In this thesis, the results of electron beam NIO studies are presented covering phase I of NIO program. In that period, IOTA has performed two scientific runs - run 1 (fall 2018 - spring 2019) and run 2 (fall 2019 - spring 2020, cut short by mandatory COVID-19 shutdown), both involving long commissioning and frantic data collection intervals.

3.2.2 IOTA NIO lattice

Majority of IOTA lattice design was done by Fermilab staff scientists A. Valishev and A. Romanov. Most of this process was never published and instead disseminated through personal communication and training in the control room. I was not involved in the design until about a year before completion, and just summarize here some of the considerations and constraints that had to be accommodated, as well as final nominal parameters.

Optics

The limitations imposed by the available space in the machine hall, the desired beam energy, and the length of experimental straight sections determined the machine layout and circumference. To allow for maximum space for experimental insertion devices, IOTA was designed as a mirror-symmetric ring with two regions for nonlinear inserts (unlike most other machines which have periodic arcs, 'cells'). To implement a symmetric ring, it is necessary to ensure optical function derivatives (β' and η') vanish at the symmetry point. On top of this the optics, dispersion, and phase advance requirements of NIO inserts are added (potentially with both inserts used simultaneously).

The final loose requirements is that beam sizes outside nonlinear inserts should be kept small (low $\beta_{x,y}^{max}$). This relaxes magnet and alignment tolerances and ensures that large beam oscillations can be accommodated everywhere. The maximum possible particle action that can fit in a ring is called the *acceptance*.

Together, above requirements necessitated the use of at least 14 reasonably spaced quadrupoles between each nonlinear section - two triplets and four doublets [52]. This is precisely the number used in the upper injection section of IOTA (edges of figure 3.6). In the bottom section, extra elements were placed so as to enable chromaticity correction and installation of other devices including RF cavity, OSC, and an electron lens.

In terms of acceptance, low $\beta_{x,y}^{max}$ relative to the available physical aperture ensured that acceptance is determined completely by the aperture of DN insert, to be discussed in 3.4. For that reason, in the following chapters amplitudes are often compared and plotted by their value in the middle of DN insert, at a marker called 'IOR'. There is a symmetric marker in the middle of QI insert called 'IOL'.

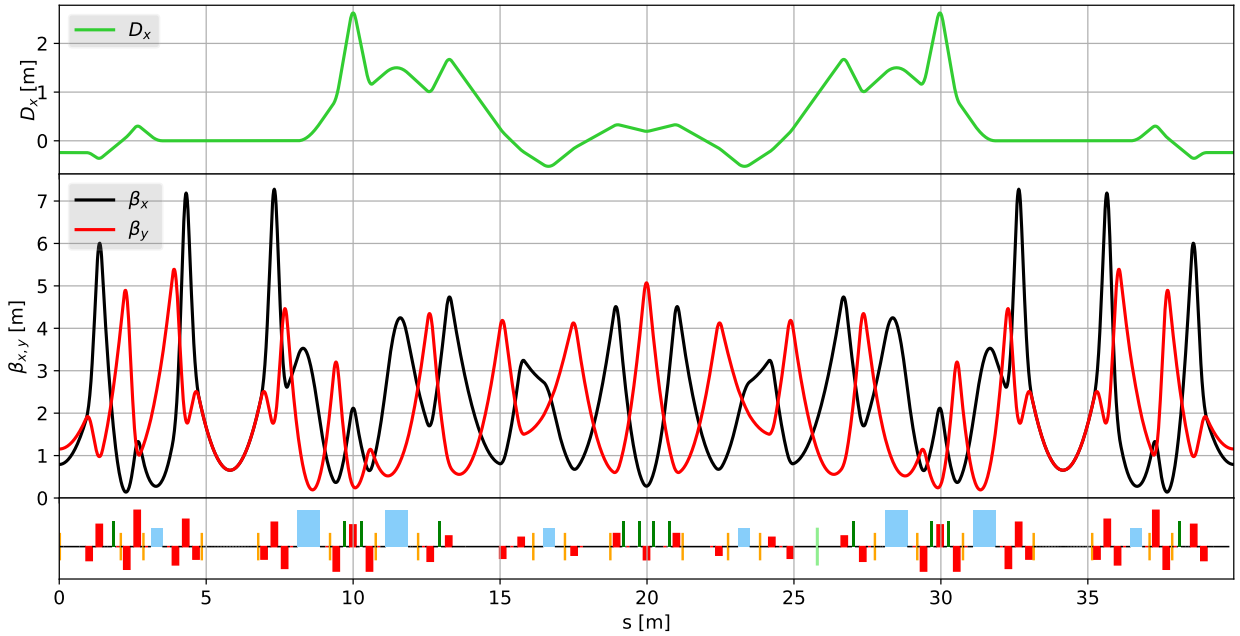

Figure 3.6: Optical functions of the IOTA NIO lattice.

Injection

Modern light sources are often constrained by the injection requirements, since incoming bunches are both bigger than equilibrium emittance (needing larger DA) and must be inserted without disrupting other bunch trains. These considerations are not relevant to IOTA, and so the main constraints of injection scheme were space requirements and physical aperture clearance. An on-axis kicker scheme was chosen together with a 4-corrector injection bump, and has performed well experimentally. Some discussion on specialized Lambertson magnet design can be found in [53].

Nominal parameters

In table 3.1, IOTA parameters are given in three configurations. First is design 150MeV, which was the original goal of the program and what all the early simulations targeted. The second configuration is design 100MeV one, which was adopted for all simulations in this thesis when the 150MeV was not achieved experimentally. In addition to low energy, a lower

Parameter	Design 150MeV	Design 100MeV	Observed (run 2)
Length	39.97 m	39.97 m	39.9616 m
Beam energy	150 MeV	100 MeV	96.4 ± 1 MeV [54]
Beam current avg	10^9, 1.2mA	1.2mA	up to 4mA
Beam current max	4mA	4mA	4mA
Emittance ϵ_x/ϵ_y	13/13nm	13/13nm	60/60nm (@1mA)
Tunes ν_x/ν_y	5.3/5.3	5.3/5.3	5.3/5.3
Bunch length	11cm	11cm	$\sim$ 25 cm (@1mA)
Mom. compaction α_c	0.072	0.071	n/a
RF voltage	1kV	340kV	$\sim$ 340 kV [55]
RF harmonic	4	4	4
Energy spread σ_{delta}	1.4×10^{-4}	1×10^{-4} (8.71×10^{-5})	2.28×10^{-4} @1mA
Aperture[1]	50mm	50mm	$>$ 40 mm
Damping time x/y/s	0.92/0.92/0.23	3.51/3.54/0.84 (coupled)	$\sim$ 5s/5s/(n/a)

Table 3.1: IOTA ring design and scientific run 2 experimental parameters. Values taken from specified references, simulation code results, and experimental estimates.

RF voltage was used as well due to RF system limitations. The final configuration uses best experimental estimates observed during scientific run 2, and is used for experimental data benchmarking.

For simulation purposes, a set of expected misalignments and field errors was defined and is shown in Table 3.2. While some magnets had significantly larger deviations in practice, design rms values were useful for simulation purposes. In following the tactic of [56], errors were scaled until the optics perturbations (tune, coupling, etc.) had same magnitude as residual errors observed after experimental tuning. This bypassed the need to implement most correction algorithms inside simulation codes while maintaining relevant perturbations. Expected maximum optical errors, as obtained in [57] and [58], are summarized in Table 3.3. Also provided are some typical values used in modern light source design and commissioning studies [59, 60]. The expected final optics errors after correction are given in table 3.3.

Parameter	IOTA	Typical light source
Dipole tilt	1 mrad	0.5 mrad
Dipole x/y	100 um	100 um
Dipole FSE	1e-3	1e-3
Quad tilt	1.7 mrad	0.2 mrad
Quad x/y	250 um	30 um
Quad FSE $\Delta k_1/k_1$	1%	5e-4
Sextupole x/y	250 um	30 um
Sextupole roll	1.7 mrad	0.2 mrad
Octupole x/y	200 um	n/a
Octupole roll	5 mrad	n/a
BPM calibration	4%	5%
BPM tilt	35 mrad	1 mrad

Table 3.2: Expected errors prior to commissioning for IOTA and for a typical light source. FSE stands for fractional strength error.

Parameter	Max error
β_{drift} error	1%
Overall β-beat	3%
Dispersion deviation η_{drift}	1cm
Closed orbit distortion through drift	0.05mm
μ_{ring}, phase advance error outside drift	0.001

Table 3.3: Expected final optics errors for IOTA lattice after correction.

3.2.3 Instrumentation

IOTA ring is equipped with several types of beam diagnostics devices. For position measurements, two systems were used - the electrostatic beam position monitors (BPMs) and the visible spectrum synchrotron light monitors (SLMs) (Fig. 3.7). SLM system was also capable of beam profile measurements, and its initial design and commissioning was led by myself in collaboration with A. Romanov as one of the first IOTA projects. Longitudinal beam profiles were acquired with a wall current monitor, and absolute current readings with a direct current-current transformer. Beam excitations were produced with a pair of electrostatic kickers. A detailed description of all of the above devices is given in appendix A.

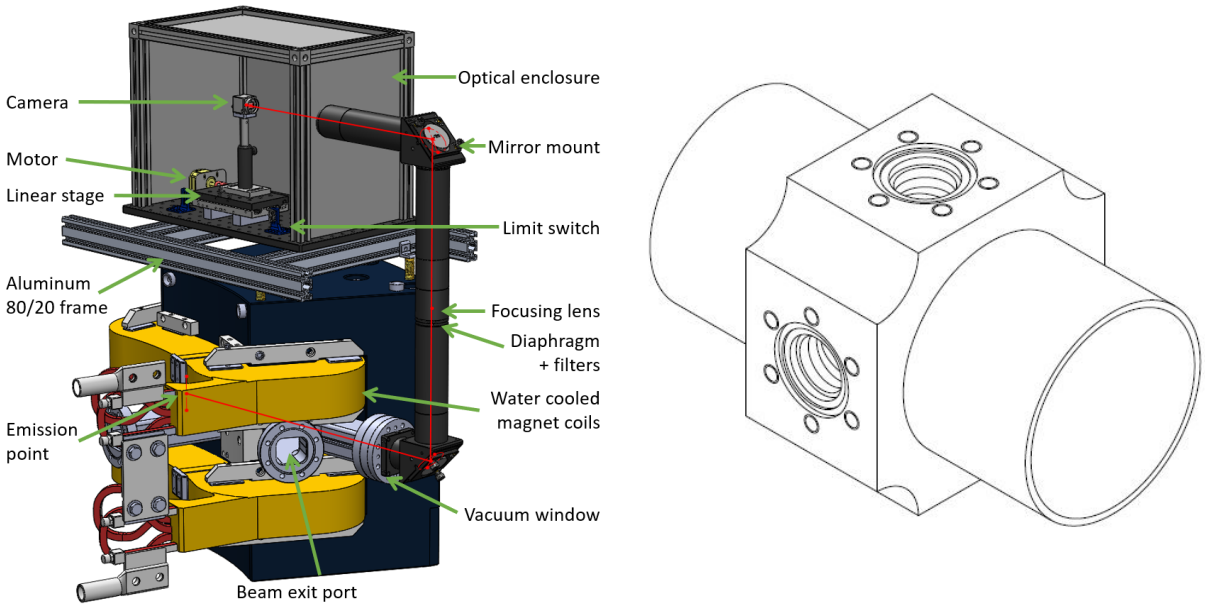

Figure 3.7: CAD drawing of SLM (left) and BPM (right).

Parameter	Design value
Magnets	18
Overall insert length	1.8m
Magnet length	7cm
Effective length	7.5cm
Max gradient k_3	$1.4\,\mathrm{kG/cm^3}$ @2.0A
Max field error	$< \%1$
Max current	2A continuous, 6A periodic

Table 3.4: QI insert parameters

3.3 QI insert

3.3.1 History and parameters

The octupole QI insert is comprised of 18 (17 in run 2) equidistant air-cooled iron yoke octupoles spanning the 'BL' 1.8m nonlinear insert drift. The choice in number of magnets was determined by balancing manufacturing and assembly cost with preserving the intended integrable beam dynamics, as will be discussed in chapter 5. Majority of prototype magnet design and testing was performed by Fermilab Technical Division and S. Antipov in 2015-2016 [61, 62]. I took over QI project in 2017, after the serial production parts were already manufactured but before final assembly. The design QI specifications are given in table 3.4. Beyond cost considerations, primary requirement was acceptable field quality and octupole gradient sufficient to reduce dynamic aperture to below physical one (thus achieving maximum possible tune spread). A CAD drawing of one of the octupoles is shown in Fig. 3.8.

3.3.2 Rework

Soon after assembly started, a manufacturing flaw was discovered - the pole length was dimensioned incorrectly, resulting in excess 0.052" of length. While seemingly a small error, this meant the insert was incompatible with the 1" beam pipe and would have a distorted

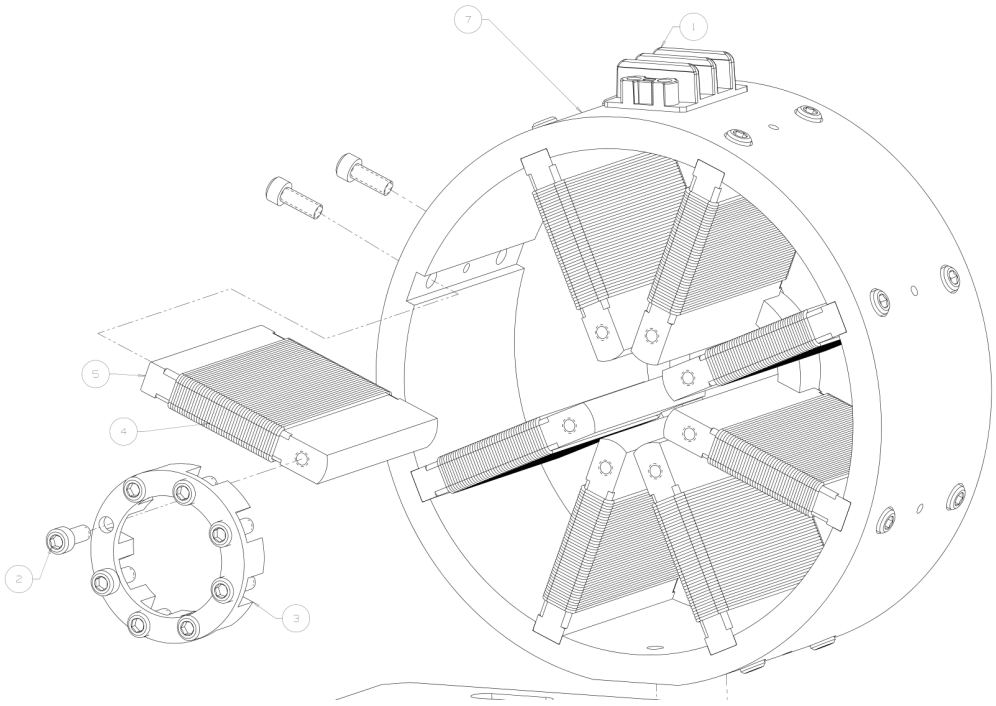

Figure 3.8: Initial CAD model of single QI octupole.

field shape. Since poles were already wound, individual rework would be problematic and imprecise - it was decided to attempt an in place fix on the complete magnet assembly. The procedure was to use wire electrical discharge machining to reference (touch) outside yoke, find geometrical center, and then feed wire through the bore and remove pole material. This process is shown in Fig. 3.9. Because of exquisite EDM precision ($< 10\,\text{um}$), good final pole shape accuracy was expected, and verified using gauge blocks. EDM work was performed at Fermilab machine shop. To cross-check results, independent 2D simulations were done using FEMM to ensure new profile was correct and had acceptable field quality - results are shown in Fig. 3.9. The corresponding field gradient derived from cubic fit ($k_3 = \frac{1}{3!}\frac{\partial^3 B_x}{\partial y^3}\frac{1}{B\rho}$) was consistent with previous COMSOL simulations. Due to schedule pressure, no time was available for magnetic testing before run 1, and so insert was assembled without field measurements.

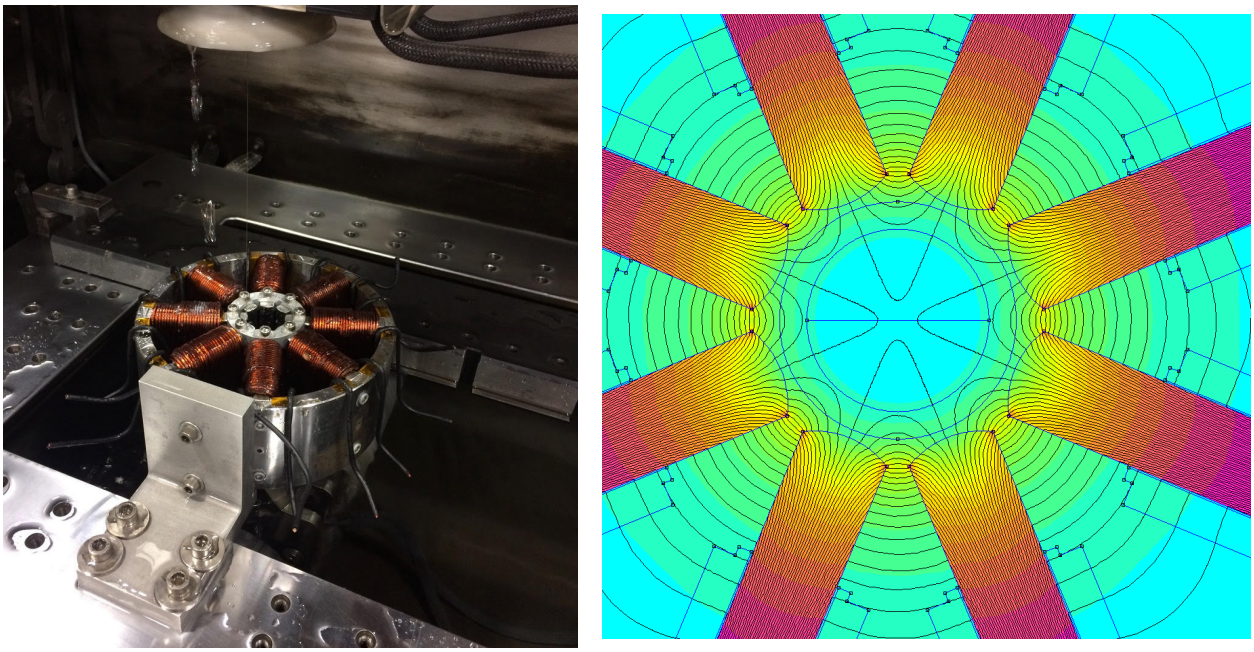

Figure 3.9: Octupole rework. Left - wire EDM machine with octupole prepared for pole cutting. Right - FEMM 2D simulation of corrected octupole model.

3.3.3 Rotating coil measurements

Between scientific runs 1 and 2, QI insert was disassembled and moved to Fermilab technical division for proper rotating coil measurements. In this process, a PCB with multiple traces is rotated inside the bore and the induced currents measured. After compensation of undesired fields, contributions of various harmonics can be extracted and field quality evaluated [63]. For octupoles, measurements were performed by Joe DiMarco and staff technicians, with my contributions as a pack mule and in final data analysis. Overall, measurements showed good field quality, meeting design specifications. In Fig. 3.10, a detailed breakdown is shown. When reassembling the insert for run 2, magnets with lowest extraneous harmonic strength were placed closer to drift center (highest current region), and those with worst field quality on the outside.

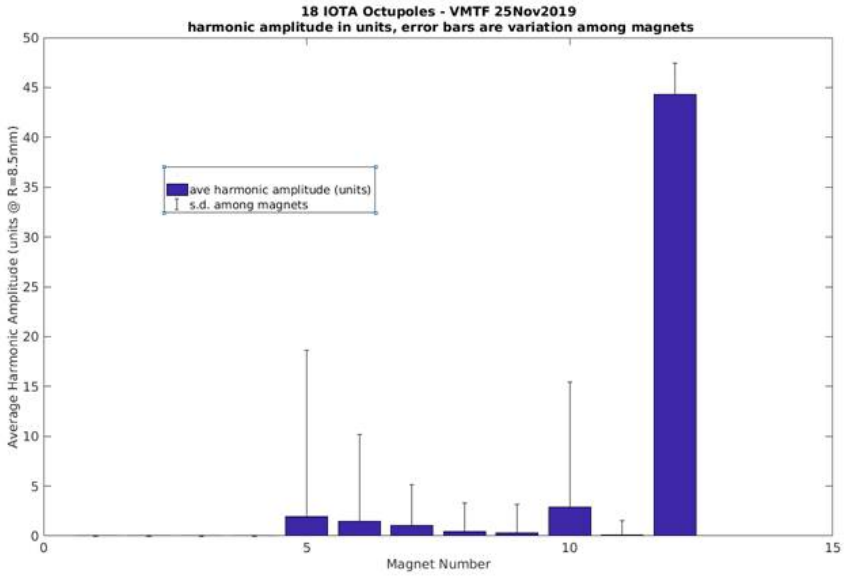

Figure 3.10: Statistics of higher order multipole content in IOTA octupoles. Note that 12-pole is the first allowed harmonic and is expected to be strong. Image by Joe DiMarco/Fermilab.

3.3.4 Alignment

Due to time and cost pressures it was desirable to align the magnets without vibrating wire station or individual referencing and individual laser tracker alignment. Our approach was to modify the retention disk ('crown') with tiny pinholes of $200-800$ um diameter, with the intention of using either lasers or fine beryllium wire to align octupoles relative to each other on a single girder. Then, only alignment of girder to the ring drift axis would be necessary, and could be accomplished during overall ring survey and followed up with beam-based closed orbit adjustments. The octupole girder in shown in Fig. 3.12, and pinhole crown in figure 3.11. Laser tracker and beam-based measurements are discussed in chapter 6.

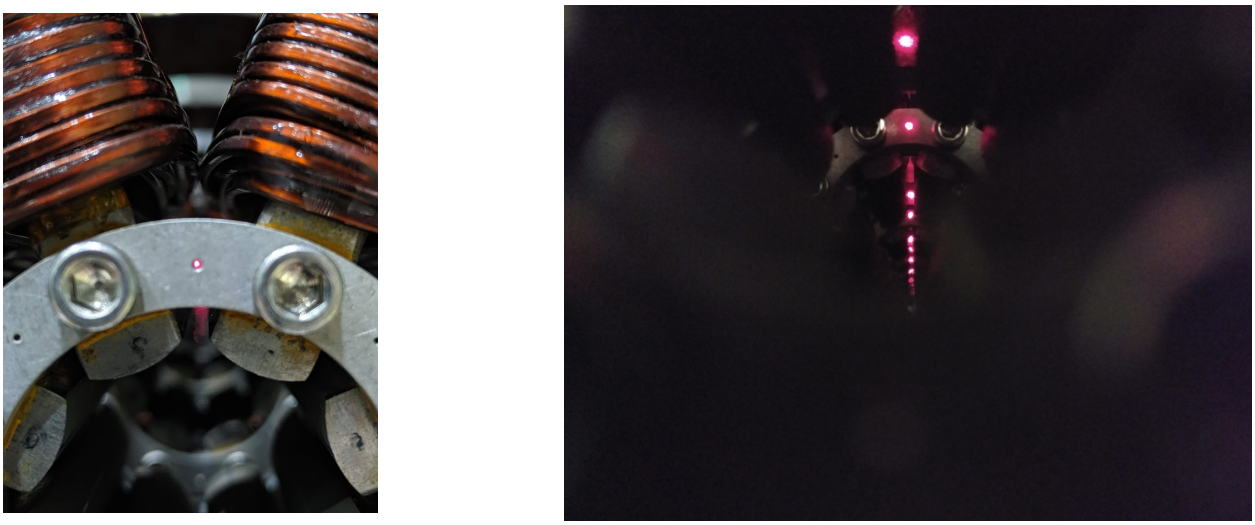

Figure 3.11: Octupole alignment. Left - laser shining through the one of the crown pinholes. Right - resulting alignment path along the insert.

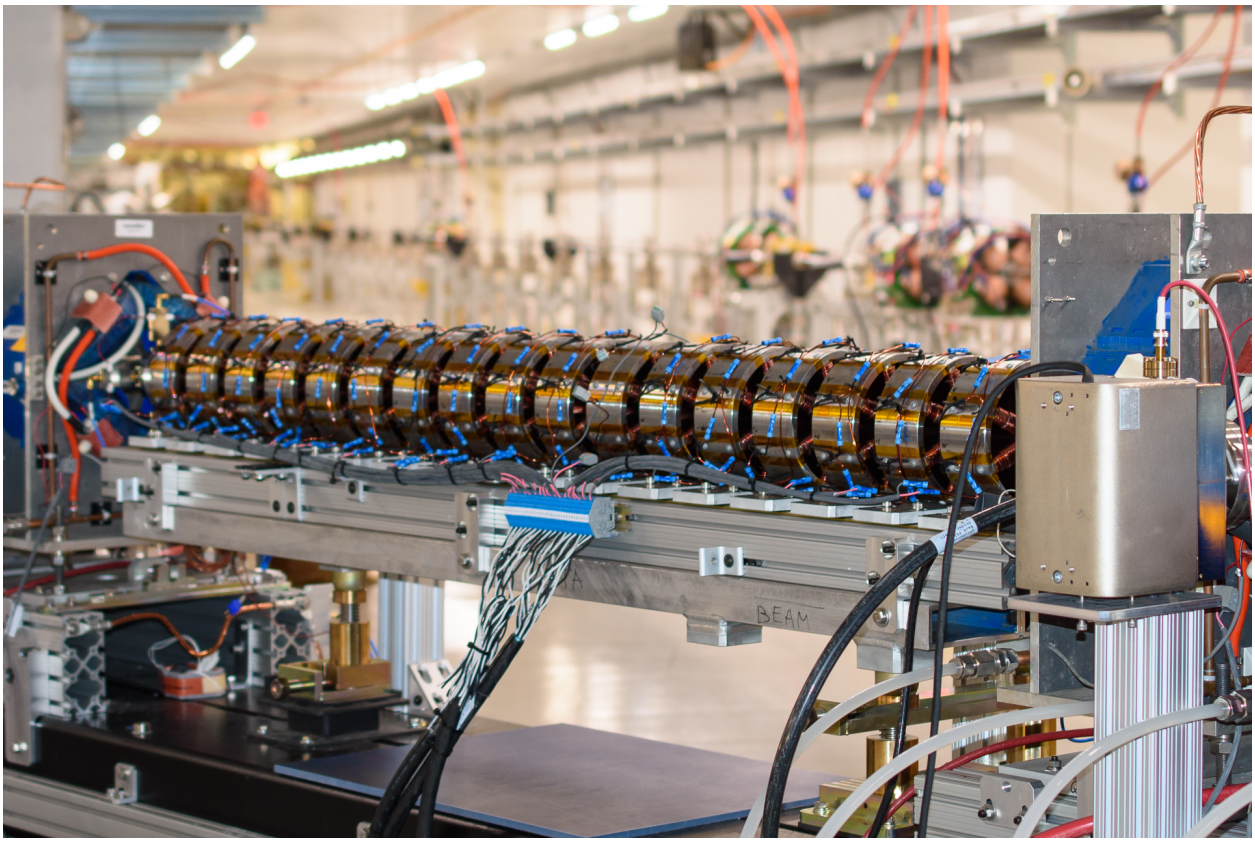

Figure 3.12: Octupole girder during run 2. Image by G.Stancari/Fermilab.

3.4 DN insert

3.4.1 History and parameters

The mechanical design and manufacture of the more complicated DN insert was done by an outside company, RadiaBeam, as a phase I and phase II Small Business Innovation Research (SBIR) project. Description of prototype and main magnet design and manufacture can be found in [64–66]. Overall, DN insert has same length and number of magnet as QI, driven by similar performance considerations and tradeoffs [67]. Specifications are given in table 3.5, and a picture of the girder in Fig. 3.13.

Parameter	Design value
Magnets	18
Overall insert length	1.8m
Magnet length	6.5cm
Geometric parameter c	0.0081 $m^{1/2}$
Strength parameter t	0.0 - 0.9

Table 3.5: DN magnet parameters.

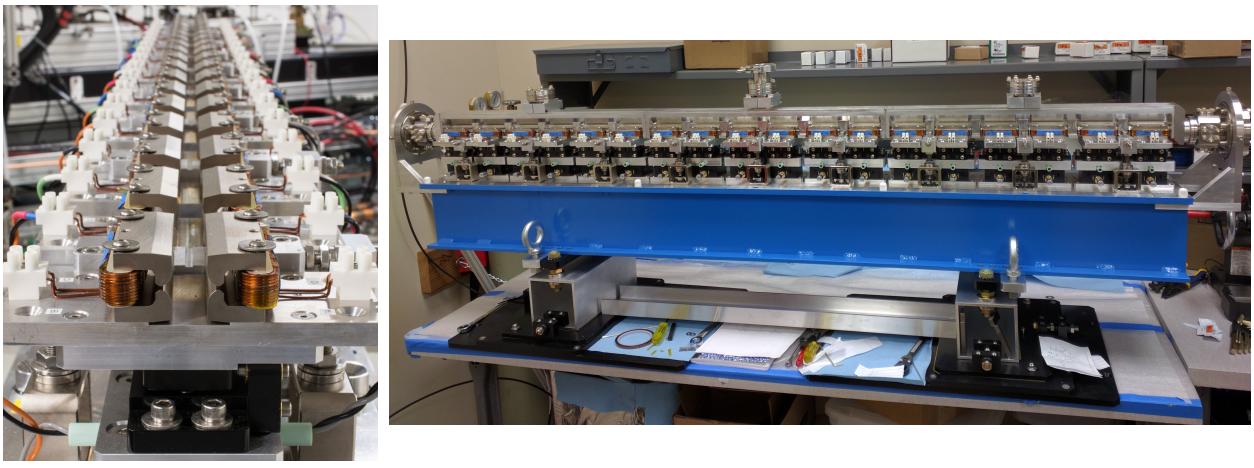

Figure 3.13: DN insert. Left - nonlinear poles. Right - girder with installed vacuum chamber.

The biggest challenge of DN system is the linear scaling ($c_{lab} = c * \sqrt{\beta}$) of pole distance within the insert, with the smallest spacing in the middle of the drift. In order to preserve as

much of physical aperture as possible and not create pumping restrictions, vacuum chamber was carefully 3D shaped to be thin and nearly touch magnet poles. Resulting aperture (at β^*) was an ellipse of $2 * 3.94\,\text{mm} \times 2 * 5.26\,\text{mm}$ (width $\times$ height). Even accounting for the small β, this point is the limiting aperture for the whole ring in both planes, and made orbit correction through DN insert critical.

3.4.2 Alignment

Because of schedule pressure, no field mapping was performed after assembly. Based on coordinate measuring machine (CMM) data (surface deviation $< 10\,\text{um}$), no significant field error were expected. Individual magnet pieces were relatively aligned on girder by Fermilab TD using a stretched wire measurement station. Details of this methods can be found in [68] and the Fermilab implementation in [69]. For the DN magnet parameters, a transverse precision of $\sim 50\,\text{um}$ rms was predicted. Beam-based measurements are discussed in chapter 6.

3.5 Summary

This chapter introduced the requirements and strategies of implementing integrable nonlinear systems. Properties of the drift + T-insert approach were presented, and parametrization defined. The exotic NIO requirements motivated the necessity to construct a dedicated NIO research ring.

The history, design considerations, and final lattice properties of the Fermilab IOTA research ring were presented. Brief description of the relevant beam diagnostics was given. Parameters and construction challenges of the two nonlinear inserts, QI and DN, were discussed.

CHAPTER 4

ANALYSIS AND SIMULATION ALGORITHMS

This chapter presents the methodology for simulation and measurement of tune, integrability, dynamic aperture, and other figures of merit. In section 4.1, various analysis methods and their experimental implementations are discussed. The types of simulations used in this thesis are presented in section 4.2. Chapter concludes by describing the common IOTA configurations used for evaluating ring performance in section 4.3.

4.1 Beam dynamics analysis

4.1.1 Spectral analysis and tune measurement

Spectral analysis of beam motion is a critical experimental and simulation tool for studying both linear and nonlinear beam dynamics, as well as for day to day operations. To maintain the correct tune working point, virtually all machines implement some form of tune measurement device or diagnostic [70], and often several at the same time [71] tied into beam feedback and machine safety systems. In IOTA, the only available method is through analysis of TBT BPM data.

Fourier transform of betatron motion

Discrete Fourier transform (DFT), by analogy to its well known continuous version, transforms data sampled at discrete time intervals to frequency space. For a signal of length N,

$$X_k = \sum_{n=0}^{N-1} x_n e^{-i2\pi kn/N} \tag{4.1}$$

with $x_n = x_0, x_1, ..., x_{N-1}$. If DFT is applied to linear betatron motion of Eq. 2.50 for ring with tune Q_{full}, the frequency spectrum is given by

$$X_k = \sum_{n=0}^{N-1} x_n e^{-i2\pi Q_{full} n/N} = \sum_{n=0}^{N-1} x_n e^{-i2\pi Q n/N} \tag{4.2}$$

where $x_n = x(s = n \times C)$ is position at turn n. Due to $2n\pi$ periodicity of the exponential term, only the fractional part of Q_{full} contributes to DFT. This means a single BPM is only sensitive to the fractional tune $Q \equiv Q_{full} \mod 2\pi$. Moreover, due to DFT properties there is an ambiguity between Q and $1 - Q$, sometimes referred to as aliasing or spectral folding. In practice, it is not a big issue and can be resolved by using model priors or observing direction of tune line shifts with focusing changes. In IOTA, all NIO studies are done in $5.25 - 5.50$ tune region for both planes.

Tune measurements

Tune measurement convergence is important for many analysis techniques, since simulation time and/or number of turns with signal can be limited. In general, average tune error scales with number of turns N as

$$\epsilon(N) = |Q(N) - Q_0| \propto \frac{1}{N^l} \tag{4.3}$$

where l is the scaling exponent. In the case of simple DFT followed by maximum amplitude bin selection, resolution scales as $1/N$ ($l = 1$) [72]. This can be intuitively understood by considering that frequency space signal has $N/2$ unique points (for real-valued time series) spread over frequency range $0 \rightarrow f_{sampling}/2$ (Nyquist criterion). Thus, for $f_{sampling} = 1$ (every turn), distance between signal bins scales as $1/N$. If BPM measurement error σ for signal of amplitude A is incorporated into the analysis, FFT uncertainties for tune,

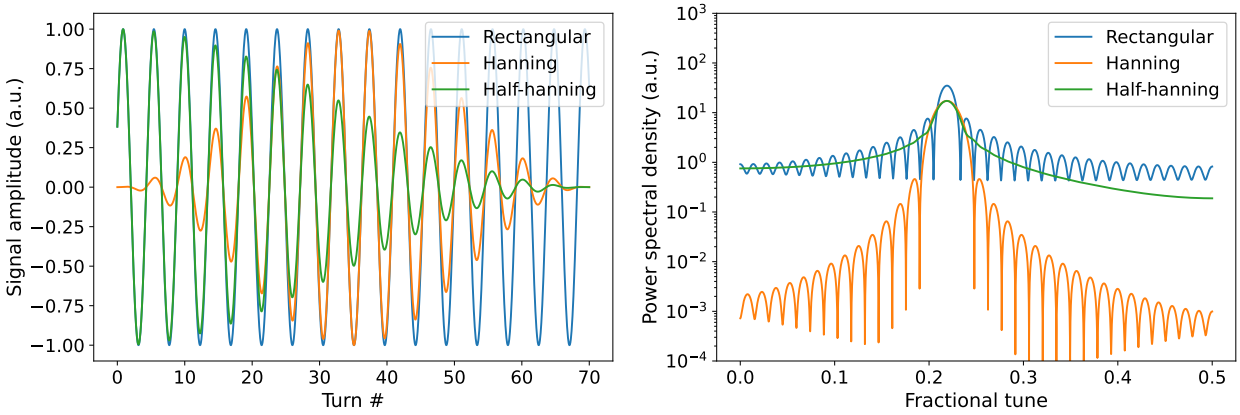

Figure 4.1: Effect of various windows on FFT spectrum.

amplitude, and phase are given by

$$\sigma_Q \leq \frac{1}{2N} \qquad \sigma_A \approx \sqrt{\frac{2}{N}}\sigma \qquad \sigma_\phi \approx \sqrt{\frac{2}{N}}\frac{\sigma}{A} \tag{4.4}$$

Several standard techniques can be used to improve this result. One example are interpolation formulas, like Jacobsen method [73] or those of [74]. Their derivation relies on evaluation of windowing effects. In Eq. 4.5 an implicit rectangular window $w(n)$ (1 everywhere with signal present, 0 otherwise) was used to multiply the (theoretically assumed to be infinite) signal:

$$X_k = \sum_{n=0}^{N-1} x_n w(n) e^{-i2\pi Qn/N} \tag{4.5}$$

According to convolution theorem, multiplication in time domain is equal to convolution in frequency domain. A pure sine wave then has a spectrum that is a convolution of single true peak and the Fourier transform of the rectangular window, as shown in Fig. 4.1. Knowing the two or three largest peak values, interpolation formulas get a better true peak estimate, improving error scaling to $\epsilon(N) \propto 1/N^2$.

Note that choosing a different window, such as the popular Hann or Hamming ones, does not by itself improve tune resolution. These windows suppress sidelobes (the oscillations away from main peak in Fig. 4.1) at the cost of widening the main lobe, and in fact lower

frequency resolution. Windowing also biases spectral power measurements if signal changes with time. However, windows are often necessary to separate signals with multiple strong nearby tunes.

Numerical Analysis of Fundamental Frequencies (NAFF)

Iteratively refined frequency analysis methods are a better but more computationally intensive alternative to interpolation formulas, the latter being susceptible to noise and systematic errors. One of the most popular such method in accelerator physics is Numerical Analysis of Fundamental Frequencies (NAFF), introduced by Laskar in the context of planetary dynamics [75]. Starting from FFT tune estimate, it seeks to maximize the correlation amplitude of the signal $f(t)$ and a sinusoidal tone $g(w,t) = e^{-iwt}$

$$\Psi(w) = \langle f(t), g(t) \rangle = \frac{1}{2T} \int_{-T}^{T} f(t) \bar{g}(w,t) w(t) dt \tag{4.6}$$

where w is windowing function as before. The iterative part comes from seeking $\max \Psi(w)$ through minimization methods, like Brent's line search in Laskar's implementation, or more modern simplex and gradient descent algorithms. NAFF precision without windowing is $1/N^2$ [76]. Application of Hann window of power p improves resolution further to

$$\epsilon(N) \propto \frac{1}{N^{2p+2}} \tag{4.7}$$

but only works well on near-noiseless signals, degrading back to $\sim O(1/N^2)$ for typical experimental data [76, 77]. Numerical evaluation of Eq. 4.6 can be done with standard discrete integration methods, such as trapezoidal or Newton-Cotes formulas. To reduce number of iterative evaluations, signal is zero-padded (i.e. to $2^{13} = 8192$) before initial DFT. This is equivalent to interpolating the frequency spectrum (Fig. 4.2), but has only a small performance cost thanks to highly efficient Fast Fourier transform (FFT) algorithms.

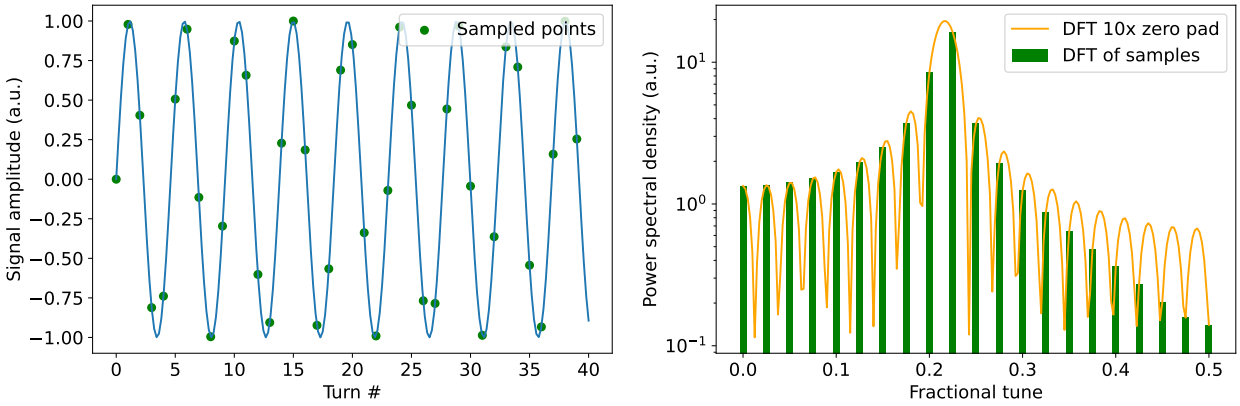

Figure 4.2: Effect of zero-padding FFT with no windowing

Another trick is wrapping the signal so as to eliminate discontinuity of data at $t = 0$ - this shifts the phase reference point from start of signal to middle, reducing phase offset errors (as long as signal amplitude is roughly uniform, sadly not the case for IOTA).

Direct fitting

For simple signals, it is possible to perform direct least-squares fitting of betatron oscillations, either at a single BPM over multiple turns or at all BPMs if Nyquist criterion is met, thereby reconstructing the betatron motion. Direct fit is useful when only a few turns of data are available. However, it becomes unstable and slow for long or complicated signals, and introduces significant systematics if the model is inadequate.

Augmentations and experimental caveats

Analysis of accelerator experimental data introduces yet another layer of complexity into the picture. However, this is not necessarily bad - for example, one of advantages of rings with supersymmetry (periodic repeating lattice cells) is ability to do combined BPM measurements [76, 78] where BPM signals add coherently and improve tune resolution. Unfortunately, IOTA lattice is mirror symmetric and poorly suited for this approach. The disadvantages of real machines are numerous - decoherence, noise, analog frontend systematics, and all the

other usual joys of experimental physics. Some of these will be discussed further below and in chapter 6.

Connection to beam optics

Spectral information can be directly used for fitting optical functions. As shown in [79], the amplitude of first order tune-line for normalized position is

$$|H(1,0)_0| = \frac{\sqrt{2J_x}}{2} \tag{4.8}$$

where $H(1,0)$ denotes the tune line as that of horizontal spectrum at $X_k(Q_x) \equiv 1 \times Q_x + 0 \times Q_y$. Any error c in signal calibration would propagate as

$$|H(1,0)| = \frac{1}{\sqrt{c}} \frac{\sqrt{2J_x}}{2} \tag{4.9}$$

By fitting the ideal Courant-Snyder parameters (β_{model},ψ_{model}) to the experimental data so as to minimize tune-line amplitude variation, quadrupole-like errors can be corrected and removed from further spectral analysis. Remaining tune-like errors can be shown to consist of only oscillatory terms. As such, with sufficient number of turns and BPMs in the ring, overall action can be estimated as

$$\sqrt{2J_x} \simeq \frac{2}{N} \sum_{n=1}^{N} |H(1,0)|_n \tag{4.10}$$

and residual beta-beat is then given by

$$\beta_{x1,n}^{corr} = \left(\frac{|H(1,0)|}{\langle |H(1,0)| \rangle} \right)^2 \beta_{x1,n}^{model} \tag{4.11}$$

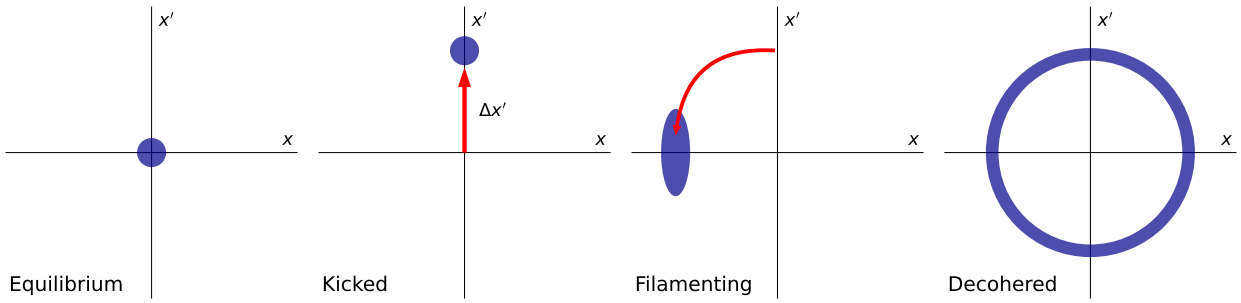

Figure 4.3: Kicked bunch filamentation.

The above treatment serves to establish a link between spectral analysis, which is typically then extended to look at nonlinear dynamics/resonance driving terms, and the more conventional optics correction algorithms that work on parameters like betatron amplitude and phase. These approaches are equivalent, but one may be more convenient to integrate into the analysis pipeline than the other.

4.1.2 Beam decoherence

Oscillation envelopes

Both linear and nonlinear decoherence present significant experimental issues that dominate the resolution of our measurements. A simple diagram of filamented bunch after kick is shown in figure 4.3. The root cause of decoherence is breakdown of single-particle assumptions, and its treatment necessitates working with density distributions instead. Inside a distribution, position of particle i at turn n is described by

$$\bar{x}^i(n) = \sqrt{2J_x}\cos(\mu^i(n)) + \eta_x\delta^i = \sqrt{2J_x}\cos(2\pi n\nu_{x,0} + \Delta\psi^i + \phi^i) \tag{4.12}$$

where $\cos(n\nu_{x,0})$ is linear small amplitude tune, ϕ^i individual phase offset, and $\Delta\psi^i$ the individual detuning (phase advance modification)

$$\Delta\psi^i = \xi_x\delta^i + \frac{1}{2}\xi_x^{(2)}(\delta^i)^2 + ... + k_{xx}J_x + k_{xy}J_y + ... \tag{4.13}$$

For IOTA the lowest order terms, linear chromaticity ξ_x and first order detuning k_{xx} and k_{xy} (produced by octupoles), are dominant detuning sources.

The experimental observable of bunch motion is the beam centroid. To find centroid 'equation of motion', a kick is introduced as an instantaneous change in actions $\vec{I}$ of all particles, such that total action is now $(J_x, J_y, \delta) = \vec{J} \to \vec{I} + \vec{J}$. Then, centroid position is an integral over the particle density distribution ρ:

$$\left\langle \bar{x}^i(n) \right\rangle = \int \rho(\vec{I}, \vec{\phi})\ \bar{x}^i(n, \vec{J} + \vec{I}, \vec{\phi})\ d\vec{\phi}\ d\vec{I} \tag{4.14}$$

The difficulty comes in knowing the real bunch distribution and it being sufficiently simple to have a closed form solution. In case of IOTA, beam profiles are expected to be close to Gaussian even with nonlinear inserts (as has been verified experimentally with SLM system). Derivations for a Gaussian bunch can be found in [80, 81] for 2D and linear chromatic cases, in [82, 83] for second order chromaticity and 4D, and in action-angle form in [84]. In this thesis, a 4D solution for a kick of $\vec{I} = (I_x \propto A_x^2 \equiv \beta_x\Delta x', I_y \propto A_y^2 \equiv \beta_y\Delta y', 0)$ starting from equilibrium closed orbit is used, which is the most general of relevant forms. Centroid position is given by

$$\left\langle \bar{x}^i(n) \right\rangle = -\sqrt{I_x}F_{xx}F_{xy}F_\delta \sin\left[2\pi\nu_{x,0} + \phi_x(n)\right] \tag{4.15}$$

with

$$\phi_x(n) = \left[2\tan^{-1}(\theta_{xx}) + 2\tan^{-1}(\theta_{xy}) + \frac{I_x}{2\sigma_x^2}\frac{\theta_{xx}}{1+\theta_{xx}} + \frac{I_y}{2\sigma_y^2}\frac{\theta_{xy}}{1+\theta_{xy}} \right] \tag{4.16}$$

and

$$F_\delta = \exp(-\alpha^2/2) \qquad \alpha = \frac{2\xi_x\sigma_\delta sin(\pi n\nu_s)}{\nu_s} \tag{4.17}$$

$$F_{xx} = \frac{1}{1+\theta_{xx}}\exp\left(-\frac{I_x}{2\sigma_x^2}\frac{\theta_{xx}}{1+\theta_{xx}}\right) \qquad \theta_{xx} = 4\pi k_{xx}\sigma_x^2 n \tag{4.18}$$

$$F_{xy} = \frac{1}{1+\theta_{xy}}\exp\left(-\frac{I_y}{2\sigma_y^2}\frac{\theta_{xy}}{1+\theta_{xy}}\right) \qquad \theta_{xy} = 4\pi k_{xy}\sigma_y^2 n \tag{4.19}$$

For $< y >$, solution has same form with all x and y indices swapped.

Experimental impact

Beam decoherence contains a lot of information about lattice conditions, and can serve as a diagnostic. For example, the synchrotron sidebands of signal FFT can be used to fit for chromaticity [85], and longitudinal momentum distribution can be reconstructed if several BPMs are used [86]. However, as far as beam dynamics goes, decoherence is the main obstacle for high fidelity measurements. Of the three envelopes, only chromatic one is an oscillatory function that returns to full amplitude, as would be expected from linear tune shift. Meanwhile, both transverse terms decrease monotonically. Experimentally, the overall decoherence envelope needs to be as large (long) as possible. Nonlinear systems will produce strong detuning by design, meaning k_{xx} and k_{yy} cannot be reduced. Chromaticity can be corrected with sextupoles to small values at the cost of DA size, but beam size (i.e. emittance) is strongly constrained by the need to maintain sufficient current for BPM TBT mode. Thus, except for lattice changes to reduce IBS and equilibrium emittance, there is little freedom to optimize decoherence envelope parameters.

Similar challenges were previously observed in measurements of crab-cavities at SPS [87], where it was necessary to avoid high intensity bunches due to electron cloud tune shift. Their solution was to use trains of low intensity bunches, maximizing overall current, and then normalizing obtained data with fitted exponential damping curves. Unfortunately IOTA does not support multiple bunches. For applications only requiring spectral measurements, decoherence can be ignored on a short timescale, as was done in [83], or worked around with repeat acquisitions [88]. However, in this work we are interested in quantitative phase space values as well as tunes.

To better understand the impact for IOTA, visualization of individual envelope components for several chromaticity and nonlinear detuning values is shown in Fig. 4.4. A moderate kick of $J_x = (1\,\text{mrad})^2$ was used, bunch rms size was set to 100 um, and octupole detuning normalized as $2k_{xx}(t = 0.3) = -k_{xy}(t = 0.3) \equiv 1$.

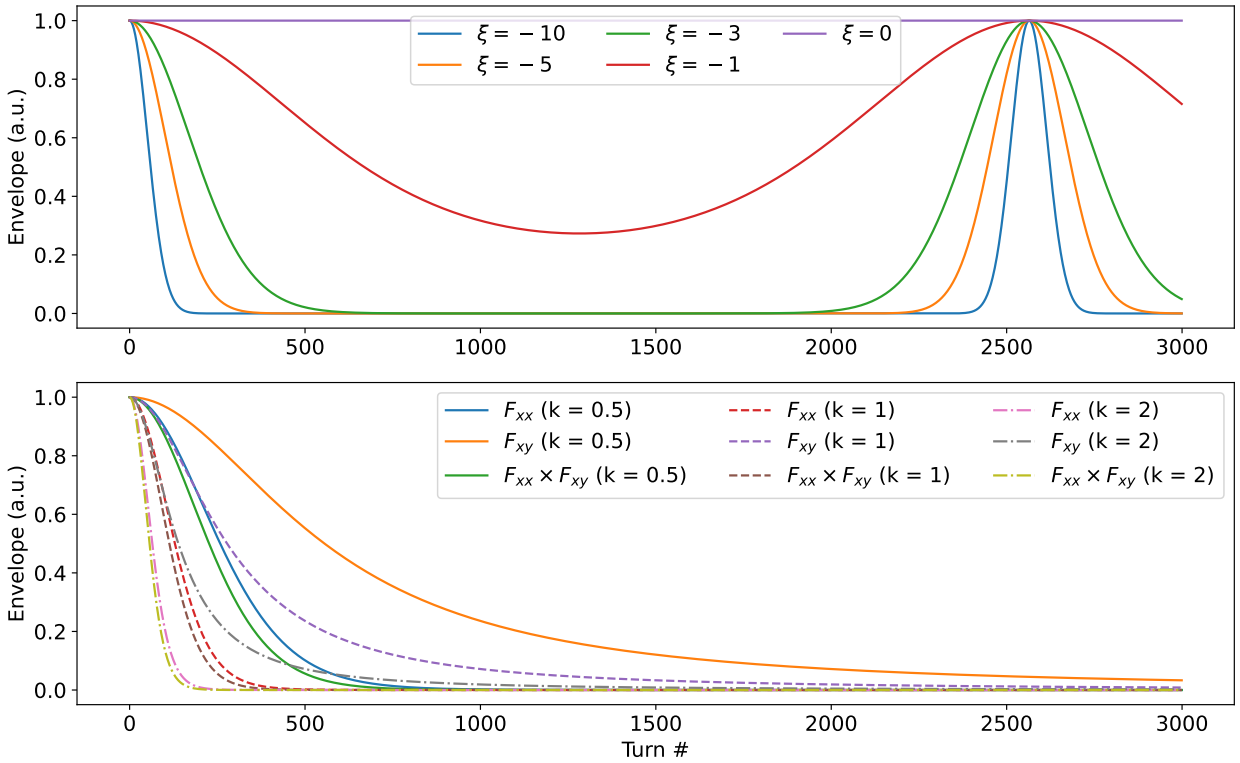

Figure 4.4: Chromatic (top) and nonlinear (bottom) decoherence envelopes.

Even with 150MeV design numbers, uncorrected chromaticity (~ -10) has an immense impact. Nonlinear terms at nominal strength have a moderate impact, and are approximately matched by a partial chromaticity correction to $\xi = -5$. Note that nonlinear envelope will shrink at stronger kicks, whereas chromatic one remains the same. Overall, fast signal decoherence within first 100-300 turns is expected for IOTA parameters and partial chromaticity correction will be needed to increase the number of observable turns.

In addition to signal damping, finite beam size also affects the observed tune, both because the tune average of the bunch is not same as that of the central particle (quadratic detuning asymmetry) and due to decoherence which is in effect a forced data window of the real oscillation signals. From Fourier transform of 4.15, for $\theta << 1$ the observed tune is

$$\nu_{x,obs} = \frac{1}{2\pi}\frac{\partial \phi_x}{\partial n} \approx \nu_{x,0} + k_{xx}(I_x + 4\sigma_x^2) + k_{xy}(I_y + 4\sigma_y^2) + \xi_x^{(2)}\sigma_\delta^2 \tag{4.20}$$

where second-order chromaticity term from derivation of Ref. [82] is applicable if first order chromaticity is corrected close to 0, as is the case for many rings. Shortly after the kick, amplitude modulation is Gaussian, and so is the spectral peak. A long time after the kick, modulation is a power law and spectrum is exponential. The exact tune shift is plotted in Fig 4.5, and shows that for strong kicks an observed shift of $\sim$ 1e-3 can be expected within the first 200 turns. Given the fast nonlinear decoherence (red line), only 200 turns would be visible experimentally. Thus, NAFF resolution would also be around 1e-3 - 1e-4, and tune shift effect would be hard to distinguish. Overall, time-varying tune peak location combined with peak shape evolution limit the effectiveness of methods like NAFF, making them usable only on short intervals. Simultaneously, decoherence limits number of available turns, and together these set a hard experimental resolution limit.

If the above 4D model was sufficient to fully describe observed signals, corrected values could be produced by first fitting the parameters and then applying transforms to amplitude and phase data. However, because of higher order effects, coupling, experimental systematic,

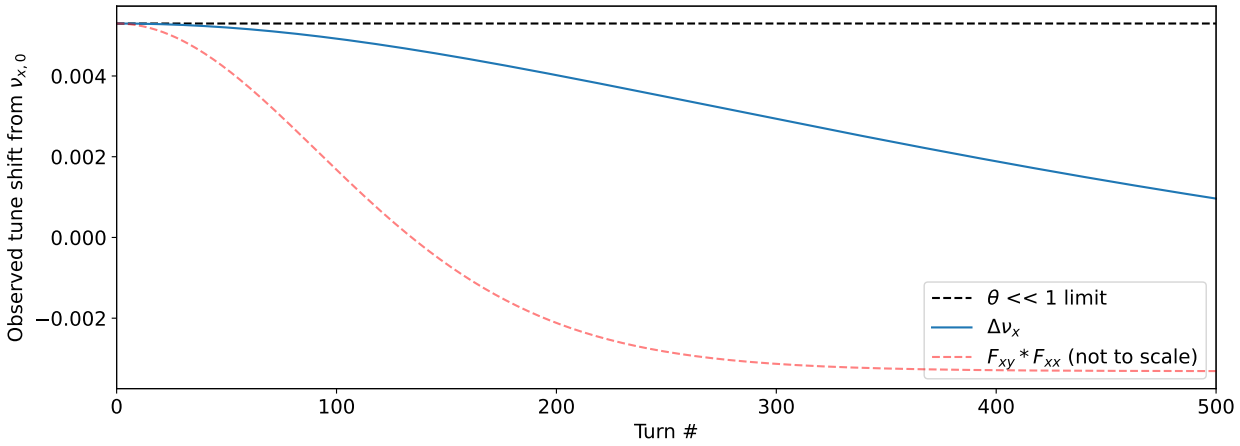

Figure 4.5: Observed tune shift as a function of turn number.

and many other reasons, this will only work for a moderate number of turns. Assuming reasonable recovery, outputs can then be used to compute 'undecohered' phase space. Error analysis on simulated signals is performed in chapter 5.

4.1.3 Optics

Note on error propagation

A key part of optics measurements and analysis is understanding the resolution and systematics of algorithms and data. To compute statistical error propagation, recall that any function f of variables $x_0, x_1, ..., x_i$ can be Taylor expanded as

$$f \approx f_0 + \sum_i \frac{\partial f}{\partial x_i} \Delta x_i + ... \tag{4.21}$$

and the corresponding uncertainty of its value is given by

$$\sigma_f^2 = \mathbf{J}\boldsymbol{\Sigma}\mathbf{J}^T = \begin{pmatrix} \frac{\partial f}{\partial x_1} & \frac{\partial f}{\partial x_2} & \cdots \end{pmatrix} \cdot \begin{pmatrix} \sigma_1^2 & \sigma_{12} & \cdots \\ \sigma_{21} & \sigma_2^2 & \cdots \\ \vdots & \vdots & \ddots \end{pmatrix} \begin{pmatrix} \frac{\partial f}{\partial x_1} \\ \frac{\partial f}{\partial x_2} \\ \vdots \end{pmatrix} \tag{4.22}$$

$$\sigma_f^2 = \sum_i \left(\frac{\partial f}{\partial x_i} \right)^2 \sigma_i^2 \quad \text{(no covariance)} \tag{4.23}$$

with $\mathbf{J}$ being the function Jacobian. The second case of no covariance corresponds to the standard sum of squares uncertainty formula.

Twiss functions

Experimentally, it is of interest to recover optics parameters based on observables. Since amplitude of oscillations is proportional to $\sqrt{\beta}$, a direct measurement of β functions is possible. However, this approach suffers from BPM calibration uncertainty, which is often of same magnitude, a couple %, as the β function error. However, by fitting all BPM amplitudes around the ring to the model simultaneously, this calibration can be canceled out (if all BPMs share calibration) or at least minimized. This method is called 'beta from amplitude', and if large number of BPMs are present (not the case for IOTA), performs quite well.

It is desirable to find some way to avoid calibration factor errors, which requires removing dependence on position data and relying only on phase. If phase differences of 3 nearby BPMs $\phi_{1\to2}, \phi_{1\to3}, \phi_{2\to3}$ are known, they can be plugged into optics transport matrices of Eq. 2.44. With model values β^m and ϕ^m, the system can be solved for experimental $\beta_{1,2,3}$. Central value β_2 is given by

$$\beta_2 = \beta_2^m \frac{\cot\phi_{1\to2} + \cot\phi_{2\to3}}{\cot\phi_{1\to2}^m + \cot\phi_{2\to3}^m} \tag{4.24}$$

This method is referred to as 3-BPM 'beta from phase', and because of exquisite phase precision afforded by spectral methods like NAFF, is the standard method for TBT data analysis. Error propagation and formulas for other β and α functions can be found in [89], where it is shown that relative error ϵ_{β_2} is minimized for $\phi^m_{1\to2} = \phi^m_{2\to3} = 45^o$ while average error at all 3 locations is smallest with $\phi^m_{1\to2} = \phi^m_{2\to3} = 60^o$. Part of lattice design is optimizing BPM phases/positions so as to improve optics measurement accuracy. In IOTA, placement was limited by other design considerations, with consequences discussed later in this chapter. Note that above formulas are valid for free betatron oscillations (only type possible in IOTA), with AC dipole data requiring correction factors [90].

Linear Optics from Closed Orbit

Linear Optics from Closed Orbit (LOCO) is another approach to recover linear optics that requires only knowledge of closed orbit shifts. The principle behind LOCO is that of an orbit response matrix - a matrix which describes the change of beam position at BPMs for a particular change in corrector or off-axis quadrupole magnet, $\Delta x_{1,2,3} = \mathbf{R}_M \Delta\theta_{1,2,3}$, with θ being the kick from closed orbit discussion of Eq. 2.61. With a sufficient number of measurements, response matrix can be inverted, and used to calculate corrective currents and kicks so as to get a better model fit. By iterating the data collection and correction procedures, overall fit to the model, and hence optics errors, are improved. A detailed description of the process can be found in [24, 91].

According to a recent benchmark of LOCO vs TBT methods [92], LOCO has slightly better performance and advantages in highly nonlinear rings, but comes at the cost of long acquisition times (minutes) and susceptibility to systematic drifts. Because of significantly higher BPM accuracy in orbit mode ($\sim 1\,\mathrm{um}$), LOCO is the primary commissioning and tuning algorithm for IOTA (used by the optics expert of the group, A. Romanov).

Phase space

Phase space reconstruction essentially means obtaining coordinates (p_x, p_y) just from position data (x, y). The best case for such a measurement are two BPMs separated by a drift, giving

$$p_x \approx x_1' = \frac{x_2 - x_1}{\Delta s} \tag{4.25}$$

where x_i is position measurement at BPM i. In IOTA, only 1 such drift is available (the opposite insert from active one). A more general formula for any two BPMs is obtained using transport matrix of Eq. 2.42 - the momentum at BPM 1 in a purely linear lattice is given by

$$x_1' = \frac{x_2 - M_{11}x_1}{M_{12}} \tag{4.26}$$

The caveat is that no nonlinear effects can be present between the two BPMs. In IOTA, nonlinear inserts are the dominant nonlinearities and so it is hoped that everywhere in T-insert is close enough to linear. This is not true in practice due to large dipoles and strong sextupoles, but nonetheless sections of 3-6 BPMs can be identified with only quads and correctors in between.

To incorporate multiple BPMs, additional indices are required. Suppose there are N_{bpm} BPMs (Fig. 4.6), which form $m = N_{bpm} - 1$ pairs denoted by index $l \equiv (i, j)$ (with $(i, j) \equiv (j, i)$):

$$m = (N_{bpm} - 1) \tag{4.27}$$

$$l = [1, 2, ..., m] \tag{4.28}$$

Plugging in general matrix element definition of Eq. 2.42, momentum of l-th BPM pair (i, j) is given by

$$p_l = p_{(i,j)} = \frac{x_j}{\sqrt{\beta_i \beta_j}\sin\phi_{i,j}} - \frac{\cot\phi_{i,j}x_i}{\beta_i} - \frac{\alpha_i x_i}{\beta_i} \tag{4.29}$$

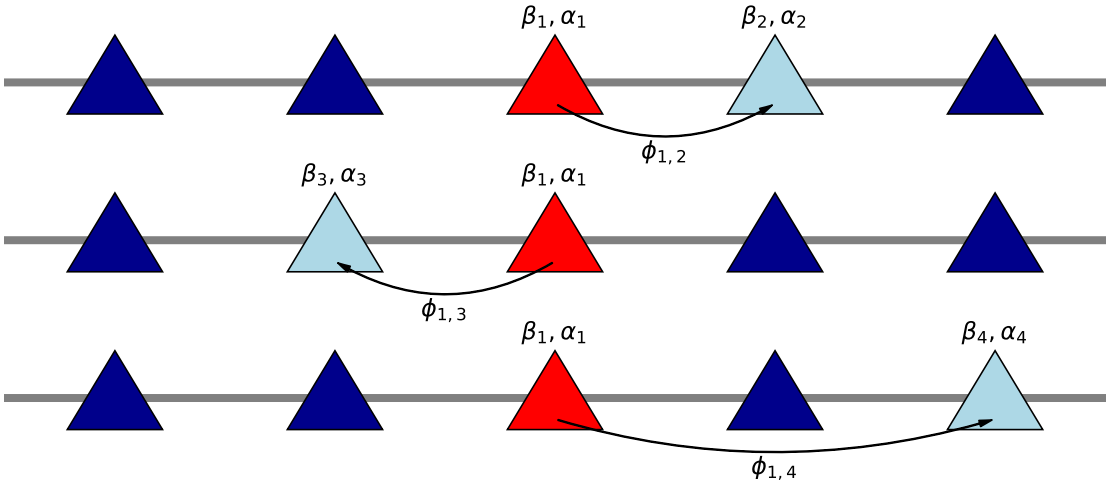

Figure 4.6: Several possible pairs of BPMs for momentum measurement.

and thus normalized momentum is

$$\bar{p}_l = \bar{p}_{(i,j)} = -\frac{x_i}{\sqrt{\beta_i}} \cot \phi_{i,j} + \frac{x_j}{\sqrt{\beta_j}} \csc \phi_{i,j} \tag{4.30}$$

Weighted estimate of all measurements at location j is given by

$$\tilde{p}_j = \sum_{i=1,\neq j}^{m} w_i p_{(i,j)} \tag{4.31}$$

where w_i is the normalized weight of each individual pair computation. Naturally, it is desired to pick the best possible set of weights. This problem is equivalent to finding a best estimator in least squares sense, also known as generalized least squares (GLS). GLS requires knowledge of the covariance matrix $\mathbf{V}$, which can be separated into systematic and statistical parts as

$$\mathbf{V} = \mathbf{V}_{\text{stat}} + \mathbf{V}_{\text{sys}} \tag{4.32}$$

Looking first at the statistical part,

$$\mathbf{V}_{\text{stat}} = \mathbf{J}\mathbf{M}\mathbf{J}^{\text{T}} \tag{4.33}$$

where $\mathbf{M}$ is the matrix of independent errors for various measured parameters - positions x_i, phases $\phi_{i,j}$, optical functions, etc. Focusing only on position and phase errors,

$$\mathbf{M} = \begin{pmatrix} \sigma_{x_1}^2 & 0 & \cdots & 0 \\ 0 & \sigma_{x_2}^2 & \cdots & 0 \\ \vdots & \vdots & \ddots & \vdots \\ 0 & 0 & \cdots & \sigma_{\phi_{1,m+1}}^2 \end{pmatrix}$$

Matrix $\mathbf{J}$ is the Jacobian of Eq. 4.30, given by

$$\mathbf{J} = (\mathbf{J}^{x_i}\mathbf{J}^{\phi_{ij}}) = \begin{pmatrix} \frac{\partial \bar{p}_1}{\partial x_1} & \frac{\partial \bar{p}_1}{\partial x_2} & \cdots & \frac{\partial \bar{p}_1}{\partial \phi_{1,2}} & \cdots & \frac{\partial \bar{p}_1}{\partial \phi_{1,m+1}} \\ \frac{\partial \bar{p}_2}{\partial x_1} & \frac{\partial \bar{p}_2}{\partial x_2} & \cdots & \frac{\partial \bar{p}_2}{\partial \phi_{1,2}} & \cdots & \frac{\partial \bar{p}_2}{\partial \phi_{1,m+1}} \\ \vdots & \vdots & \ddots & \vdots & \ddots & \vdots \\ \frac{\partial \bar{p}_m}{\partial x_1} & \frac{\partial \bar{p}_m}{\partial x_2} & \cdots & \frac{\partial \bar{p}_m}{\partial \phi_{1,2}} & \cdots & \frac{\partial \bar{p}_m}{\partial \phi_{1,m+1}} \end{pmatrix}$$

where the partial derivatives are

$$\frac{\partial \bar{p}_{(i,j)}}{\partial x_i} = -\frac{\cot(\phi_{i,j})}{\sqrt{\beta_i}} \tag{4.34}$$

$$\frac{\partial \bar{p}_{(i,j)}}{\partial x_i} = -\frac{\csc(\phi_{i,j})}{\sqrt{\beta_j}} \tag{4.35}$$

$$\frac{\partial \bar{p}_{(i,j)}}{\partial \phi_{i,j}} = \csc(\phi_{i,j}) \left(-\frac{x_j \cot(\phi_{i,j})}{\sqrt{\beta_j}} + \frac{x_i \csc(\phi_{i,j})}{\sqrt{\beta_i}} \right) \tag{4.36}$$

Unlike statistical part, systematic covariance is harder to define analytically and so is usually estimated via Monte Carlo with several thousand error realizations on best available

ring model. Once the final matrix $\mathbf{V}$ is known, weight are computed as

$$w_i = \frac{\sum_{k=1}^{m} V_{ik}^{-1}}{\sum_{k=1}^{m}\sum_{j=1}^{m} V_{jk}^{-1}} \tag{4.37}$$

This procedure is called the 'N-BPM' method. It was introduced as an extension of the 3-BPM method for β function measurement in 2016 [93], and an analytic extension of systematic covariance computation was recently proposed in [94]. To our best knowledge it has not been extended to momentum/phase space applications until now. Since momentum measurement depends on position as well as phase, N-BPM momentum method introduces a number of complications (BPM calibration factors, amplitude dependence of covariance matrices, etc.). As a simplification, in this work we focus only on position and phase errors. Note that N-BPM method reduces to a simple variance weighted average if measurements are uncorrelated, which can be used as a fall back if model systematics do not appear to match experimental results. Another interesting detail is the phase uncertainty in above equations - it is that of phase difference, which is not the same as uncertainty of individual phase measurements. The relationship can be shown to scale as $\sigma_{\phi_i}^2 = \sigma_{\phi_{i,j}}^2 \left(1 + \beta_i/\beta_j\right)^{-1}$ [95].

Model independent methods

Another approach to optics analysis are the model independent methods, which rely on properties of beam motion and various decompositions to obtain optics function without knowledge of model values. A detailed overview can be found in [96]. One of simplest methods for MIA is singular value decomposition (SVD). To establish the connection with betatron motion, consider a beam history matrix $B_{M\times P}$. Each row of length P is a vector of turn by turn data at BPM M. For linear motion, matrix elements are given by

$$B_{m,p} = \sqrt{2J_p\beta_m}\cos(\phi_p + \psi_m) \tag{4.38}$$

If this matrix is decomposed with SVD, then

$$B = USV^T = \sum \sigma_i \vec{u}_i \vec{v}_i^T \tag{4.39}$$

By computing the eigenmodes, it can be shown that with sufficient number of randomly distributed BPMs the decomposition requires only two [97]:

$$B \equiv \frac{1}{\sqrt{P}} B_{m,p} = \sigma_+ \vec{u}_+ \vec{v}_+^T + \sigma_- \vec{u}_- \vec{v}_-^T \tag{4.40}$$

where σ are called singular values, and

$$u_+ = \frac{1}{\sigma_+} \sqrt{\langle J \rangle \, \beta_m} \cos(\phi_0 - \psi_m) \tag{4.41}$$

$$u_- = \frac{1}{\sigma_-} \sqrt{\langle J \rangle \, \beta_m} \sin(\phi_0 - \psi_m) \tag{4.42}$$

$$v_+ = \sqrt{\frac{2J_p}{P \langle J \rangle}} \cos(\phi_p - \phi_0) \tag{4.43}$$

$$v_- = \sqrt{\frac{2J_p}{P \langle J \rangle}} \sin(\phi_p - \phi_0) \tag{4.44}$$

with $p = 1...P$, $m = 1...M$, ψ_m the individual BPM phase advances from start, and ϕ_0 the angle coordinate offset. The vectors u are called spatial components, since they describe how much each principal component (eigenmode) contributes to a particular BPM. Vectors v are called temporal, and describe the sine/cosine components of linear motion in normalized coordinates. This property is very powerful - by just applying SVD to (purely linear) BPM data, normalized Courant-Snyder coordinates are obtained as the principal components of SVD decomposition without any knowledge of the lattice. As with momentum formulas above, any nonlinearities between BPMs invalidate SVD analysis. Uncorrelated measurement errors can be incorporated into SVD by scaling the individual signals prior to decomposition. BPM phase can be computed from the angle of sine/cosine spatial vectors

as

$$\psi = \tan^{-1}\left(\frac{\sigma_- u_-}{\sigma_+ u_+}\right) \tag{4.45}$$

Relative amplitudes are also straightforward to extract, but to obtain absolute Twiss functions a fit for scaling factor, the average action $< J >$, is required

$$\beta = \langle J \rangle^{-1}\left(\sqrt{\sigma_+} u_+^2 + \sqrt{\sigma_-} u_-^2\right) \tag{4.46}$$

SVD errors can be roughly estimated by

$$\sigma_\psi \sim \frac{1}{\sqrt{P}} \frac{\sigma_x}{\sigma_{signal}} = \frac{\sqrt{2}}{\sqrt{P}} \frac{\sigma_x}{A} \tag{4.47}$$

$$\sigma_{\Delta\beta/\beta} \sim 2\sigma_\psi \tag{4.48}$$

More advanced decompositions are possible, such as the Independent Component Analysis (ICA) for nonlinear problems and mode unmixing for coupled motion [98–100]. Applications of these methods were explored for NIO experimental analysis with mixed results depending on signal quality and hyperparameter tuning. No advanced decompositions were used in the final analysis, but in all cases SVD was applied to raw data to reconstruct the signals with only top few singular values - this removed small uncorrelated noises while keeping important signal information.

4.2 Simulation techniques

4.2.1 Codes

Accelerator physics simulations aim to numerically approximate particle motion in an electromagnetic field subject to performance and accuracy constraints. While the system is fully described by the equations of motion and the Hamiltonian, analytic solutions exist for only

the simplest of cases. Given the complexity or sometimes impossibility of an analytical treatment, numerical simulations have played a crucial role in understanding the performance and limitations of IOTA ring and NIO inserts.

In general, to perform a numeric simulation some sort of integration of the equations of motion is required, with considerations of symplecticity and other constraints. Many types of codes and beam dynamics indicators have been developed, but there is no one simulation code to rule them all - each project is specialized for the needs of their respective facility, with varying degrees of performance, physics fidelity, and modification flexibility. The codes used in this thesis (MAD-X, OCELOT, ELEGANT, 6DSim), and my own custom-made pyIOTA accelerator control and analysis framework are described in appendix B.

4.2.2 Simulation types

Several standard simulation studies/types were used in this thesis. This section summarizes them, and discusses possible pitfalls in comparisons with experimental data.

Linear optics

Linear optics simulations were performed in OCELOT and cross-checked with elegant and MAD-X. Internally, these codes use equations of section 2.1 to find periodic Twiss functions and propagate them to points of interest. For misalignments, appropriate feed-down effects are added to linear matrices up to octupolar order.

Tracking

The fundamental building block of simulation tools is tracking - transporting the particle through lattice using some set of maps. Along the path, particle position can be recorded and various effects applied - apertures, kicks, etc. Since the dynamical behavior of integrable systems is being studied, it is imperative to use symplectic methods - they ensure preservation

of energy and other invariants up to some order in step size. Symplecticity restricts the choice of element maps to either linear matrices or full numeric integrators. Whenever possible, the latter was used, either in elegant or MAD-X PTC. Number of kicks was increased until no further changes were observed in the output.

Chromaticity

For brevity, linear chromaticity will be referred to as just chromaticity. In simulations, it can be derived from analysis of second/third order transport matrices or by particle tracking. The latter method can be easily extended to higher order chromaticities (by tracking more momentum offsets and fitting tune shift curve), and is in general more accurate at a slight performance cost. MAD-X and elegant are capable of both algorithms, and both were added to pyIOTA as well. For IOTA lattice, these approaches yield similar results.

Dynamic aperture

Dynamic aperture was introduced in Chapter 2 as the region of phase space around reference orbit with perpetually stable motion. It is expressed either in physical coordinates or in units of beam σ, the latter being useful for hadron machines. In simulation studies, DA is evaluated at the point of interest, such as the injection location. In this thesis, all DA and related simulations are performed from the middle of nonlinear drift BR, since that is the dominant aperture restriction in the ring, and also a location shared between the various conceptual and experimental lattices (discussed in section 4.3). Since $\alpha_x = \alpha_y = 0$, this location also has no phase space tilt and thus a round (or elliptical for DN) beam distribution is implicitly a matched one.

Computationally, true DA has to be estimated by tracking a limited number of particles/turns. Analytical descriptions and speed-ups of this process have been the subject of much research. In hadron machines, models based on Nekhoroshev theorem have shown

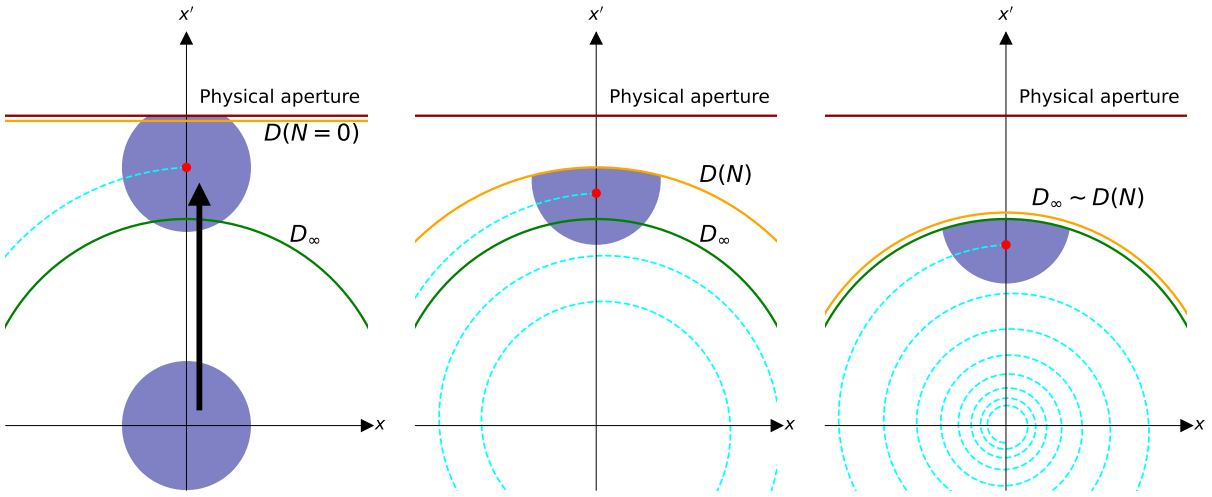

Figure 4.7: Interplay of synchrotron damping and effective dynamic aperture reduction with number of turns. Left image is just after a bunch is kicked, central after some time has passed, and right after particle losses have stopped.

good accuracy [101, 102]. Nonetheless, it is still necessary to track a significant number of turns - $10^5 - 10^6$ turns are used in LHC simulations [103]. High energy lepton machines have strong synchrotron damping, and so require only enough turns so as to have noticeable amplitude decay, on the order of $0.25 \times \tau_s \approx 10^3$ turns [60]. IOTA is a special case of a low energy lepton machine, with transverse damping times of seconds (millions of turns at 7.5MHz), which implies the need for $> 10^5$ turns. The various particle loss causes and effects of synchrotron damping on a particle bunch are shown in Fig. 4.7.

To avoid such computationally intensive simulations, a short study was performed to evaluate DA scaling, and results suggest that even the small energy loss helps particles explore phase space faster - over 95% are lost in the first 10^4 turns and the loss scaling is smooth. As such, for relative comparisons $10^3 - 10^4$ turns are used in all tracking studies. As for the initial distribution, as shown in [104], it is sufficient to use a grid in transverse coordinates, Cartesian $(x,\ y)$ or polar $(x = r\cos\theta, y = r\sin\theta,\ 0 \leq \theta \leq \pi/2)$, with no momenta $(p_x = p_y = 0)$. This is because over many turns particles will eventually explore

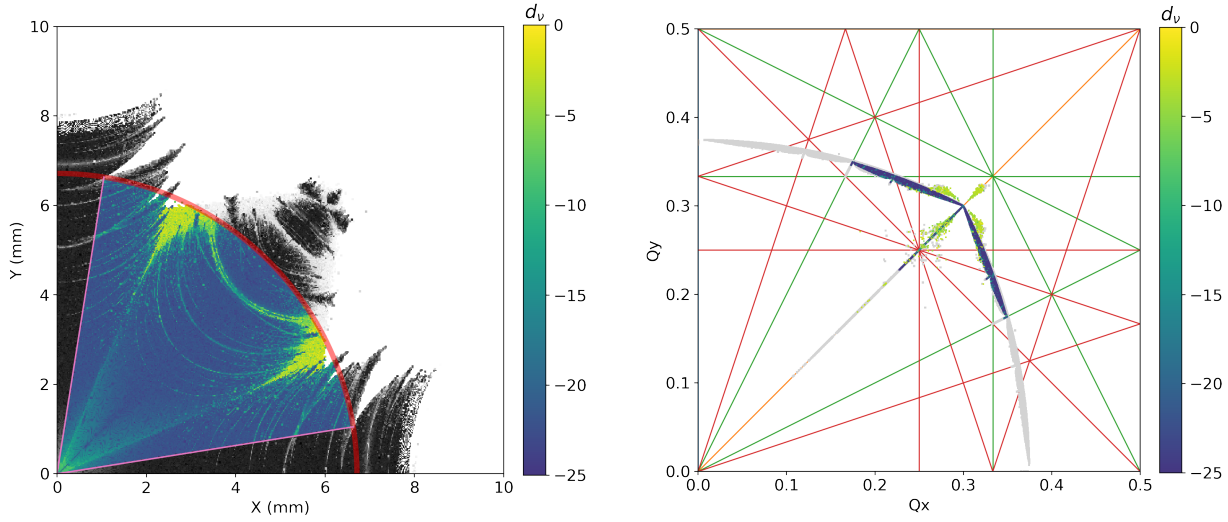

Figure 4.8: Dynamic aperture evaluation for typical NIO asymmetric profile. Left - DA with active 99% survival area highlighted. Right - corresponding FMA.

all possible phases. Note also that just a single quadrant $+x, +y$ is evaluated - while there is a $\pm x$ asymmetry in some machines, it is not an issue in IOTA since we are interested in kicks/DA from reference orbit and not injection.

A practical question arises in evaluating the size of dynamic aperture. Simple count of all surviving particles is a bad solution, since it does not consider possible DA asymmetry or discontinuous resonant islands. In [105], the largest possible radius where all particles survive was used as measure of DA. A similar concept of boundary clipping was used in [56], where DA profile was cut so as to be convex at each step (i.e. no protrusions allowed). In our simulations, radius approach was used since it made most sense in terms of experimental observations - a kicked bunch will rotate around and eventually explore all angles. However, radius calculation was enhanced with robust thresholds so as to reject stochastic noise/particle losses. Namely, DA was defined as largest radius within $\pi/20 < \theta < \pi/2 - \pi/20$ segment in which less that 1% of particles were lost. This is shown in Fig. 4.8. For DN magnet, aperture was rescaled based on the perturbed optics functions.

Momentum aperture

Local momentum aperture (LMA) describes the dynamic aperture of an off-momentum particle. It is typically smaller than on-momentum one, and vanishes at momentum error equal to the energy acceptance of the ring. LMA varies with longitudinal position, since an energy change has different trajectory impact depending on the local dispersion. LMA determines Touschek lifetime, a scattering effect that is the primary beam loss mechanism in lepton machines. However, for NIO experiments lifetime was not an operational concern. LMA also affects beam dynamics since high amplitude kicks produce a path length change, and start synchrotron oscillations. For the time scales measurable with BPMs, < 500 turns ($< 0.25\tau_s$), this effect was not significant.

Frequency map analysis

Frequency map analysis (FMA) is one of the primary tools for studying the impact of nonlinear effects on beam dynamics. Its use in accelerators was pioneered by J. Laskar [106], after he used it extensively in analyzing the stability of solar systems [107]. Since then, FMA has been used in machine design [108], beam-beam effects [109], and other studies, effectively becoming a standard tool and being incorporated in many accelerator codes.

A good recent review is given in [110], which we summarize here. The goal of nonlinear beam dynamics optimization is to estimate and correct nonlinear effects so as to increase the dynamic aperture. While the most straightforward simulation benchmark is to track particles and evaluate beam losses, this is computationally expensive and not scalable for modern machines. On the other hand, fast chaos indicators like the Lyapunov exponent, while efficient, do not provide the global phase space structure. FMA serves to bridge these two extremes. It relies on detecting changes in particle tune as indicator of chaos onset, since according to KAM theory tune is an invariant of stable quasi-periodic motion [111]. By measuring the difference in tune of successive tracking increments, a picture can be built

that demonstrates the width, strength, and interplay of the various resonances. The standard FMA figure of merit is diffusion, defined as $d\nu = |\nu_1 - \nu_2|$. For completely quasi-periodic particles, $d\nu \to 0$. Typically, $\log_{10} d\nu$ is plotted due to the immense dynamic range of this indicator.

For FMA implementation, particles are tracked like in DA, their position recorded, and tunes extracted. In this thesis, internal elegant FMA module was used for most studies, but unfortunately was prone to spurious frequency peak reordering in highly nonlinear conditions. As such, for some simulation the data was stored as raw tracks and then analyzed with the NAFF algorithm in pyIOTA. For a more precise diffusion measurement, original 2-part algorithm was extended to a sliding window $\sigma_{d\nu}$ calculation (for example, 4096 turns overall, 1024 turn window, 256 step size), with diffusion defined by

$$d_{\nu,j} = \log_{10}(\max(|Q_{i,j} - \bar{Q_j}|)), \quad j = x, y, s, \quad i = [1...N_{samples}] \tag{4.49}$$

$$d_\nu = (d_{\nu,x} + d_{\nu,y})/2 \tag{4.50}$$

To evaluate the RMS and maximum detuning, same stable area radius cutoff criterion was used as for DA.

4.3 IOTA simulation configurations

Simulations in this thesis serve two key purposes. First is to guide and validate designs for the nonlinear inserts, quantifying theoretical and expected performance, as well as requirements and limitations. Second is to provide an 'in the loop virtual accelerator' for development and optimization of analysis algorithms. To that end, a common set of configurations and benchmarks was established. Thanks to pyIOTA, most of the codebase could then be reused for all simulation and experimental data. The three nonlinear insert configurations were

- Ideal insert - a gapless continuous sequence of 500 symplectic octupoles, each a 4-step

integrator

- Design insert - 18 magnets in ideal design arrangement
- Perturbed insert - same as design, but with errors applied

and the four T-insert configurations (rest of the ring) were

- Matrix - the ideal T-insert linear matrix
- Perturbed matrix - perturbed linear matrix with tune and/or dispersion errors
- Ideal ring - linear ring lattice (matrix-based), but including the limiting apertures
- Full ring - full symplectic integration ring model

Finally, in terms of longitudinal dynamics, two settings were available:

- 5D - no synchrotron damping, no RF, coasting bunch but still 6D tracking
- 6D - synchrotron damping, RF on, phase adjusted to have 6D closed orbit at $\Delta t = 0$ (in other words, reference particle experiences acceleration to exactly compensate for energy loss in 1 turn with no synchrotron oscillations)

Where applicable, chromatic correction could be enabled with either all 12 design or only 4 available sextupoles. Errors could be applied at either design and close-to-experimental levels, plus ad hoc corrections from experimental experience. Three combinations were typically used in simulations. Namely, ideal/matrix/5D, which represented the best theoretical NIO case, design/full ring/6D as the configuration that guided initial insert optimization, and the maximally realistic perturbed/full ring/6D/errors used for experimental benchmarking. In the following section, these configurations are referred to as ideal NIO, ideal/clean ring, and realistic/full ring.

4.3.1 Particle distribution and matching

When simulating particle bunches and not individual particles, *matched* distributions are used. In lepton machines, equilibrium distribution after damping will be a matched one.

However, in case of strongly nonlinear potentials, linear matching suggested by Courant-Snyder parameters is not correct. A general procedure was proposed in [112] - to obtain a matched KV (Kapchinskij-Vladimirskij)-like distribution, particles should be placed randomly on the 4D shell defined by $H_{QI/DN} = E$, where E is the energy or emittance of the bunch. This procedure has been used successfully in proton studies. However, in case of electrons, Hamiltonian-matched distribution competes with synchrotron damping. For parameters used in IOTA, the equilibrium electron bunch shape is very close to that of a Gaussian. As such, for all simulations a linear matched distribution was used.

4.4 Summary

This chapter introduced analysis and simulation techniques for studying beam dynamics and performance of accelerator lattices.

Spectral methods were described for determination of tune and phase of the betatron oscillations. Effects of data windowing and zero padding were demonstrated, and tradeoffs discussed. An iterative frequency refinement method called NAFF was introduced as the standard algorithm to be used in this thesis, and its uncertainties estimated. Derivation of Twiss functions from spectral line amplitudes was explained. For the types of signals expected in IOTA, NAFF with Hanning window used over first 100-200 turns is expected to have 10^{-3} - 10^{-4} tune precision.

Decoherence of bunch centroid motion was analyzed for linear chromatic and quadratic nonlinear transverse detuning terms. The former produces an oscillatory envelope that recoheres at each synchrotron oscillation, while the latter permanently smears out the signal. Large kicks are affected more strongly by the nonlinear terms, while chromatic effects are unchanged. IOTA lattice parameters suggest at least partial chromaticity correction to $-5/-5$ will be necessary to increase the number of turns available for experimental analysis. Observed bunch tune deviation from single-particle value is expected to be of same magnitude

as NAFF resolution, and should not have a significant effect given the low observable number of turns.

Lattice function measurement algorithms were discussed, including orbit-based LOCO and TBT-based betatron amplitude, betatron phase, and model independent beam history matrix methods. Their connection to linear optics of chapter 2 was established, and experimental caveats highlighted. Error propagation and optimized N-BPM measurement averaging based on generalized least squares approach was explained. For the expected IOTA signals, SVD and N-BPM method applied to linear regions are expected to have best performance.

In second part of this chapter, various types of simulations were described in terms of their algorithms and physical significance. Of particular relevance for IOTA were the FMA and tracking simulations, which can be used to measure DA, detect unstable regions through diffusion, and analyze the smear of the invariants.

All of the above analyses and simulations will be used in the next two chapters to quantitatively study NIO systems.

CHAPTER 5

SIMULATION RESULTS

This chapter presents the simulation and optimization results for several nonlinear integrable systems, starting from ideal QI/DN toy models and clean IOTA lattice all the way to IOTA run 2 configuration. Impact of misalignments, optics errors, collective behavior, and other factors is studied. It is demonstrated that if design specifications are met, IOTA ring is capable of satisfying integrable optics requirements, and that this will be observable experimentally.

5.1 Quasi-integrable octupole system

5.1.1 Ideal system overview

To begin the simulation section, it is useful to point out salient features of the QI system with some pretty pictures of Fig. 5.1, which contain high resolution FMA data in various projections. Looking at the diffusion map (top left), a plethora of different kinds of resonances are present as bright lines within the stable region. However, most do not appear harmful until very large amplitudes. The speckled sections at the x and y maxima are indicative of strongly chaotic motion that confuses the tune detection algorithm. The tune maps of Figs. 5.1b and 5.1c visualize the expected tune shifts and have three distinct sectors, referred to as vertical, diagonal, and horizontal. The experimental goal is to observe greatest possible detuning - for that, kicks should be aimed between sector boundaries. Finally, the tune footprint in 5.1d shows the huge extent of theoretically possible tune spread. Resonant capture is evident on many resonance lines, and footprint narrows close to those areas. Experimentally, it is unlikely that these will be accessible.

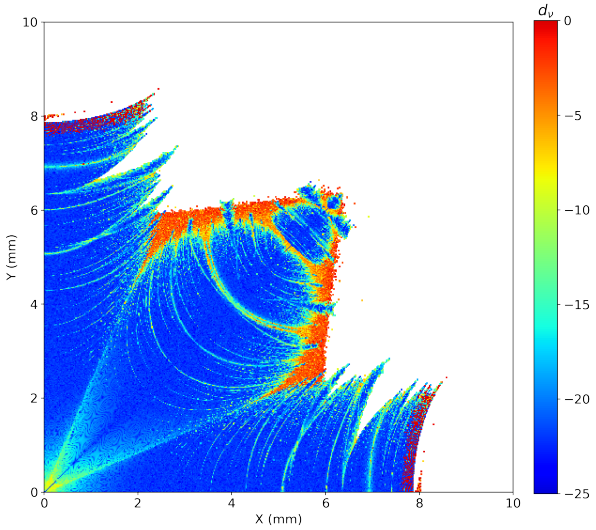

(a) Tune diffusion

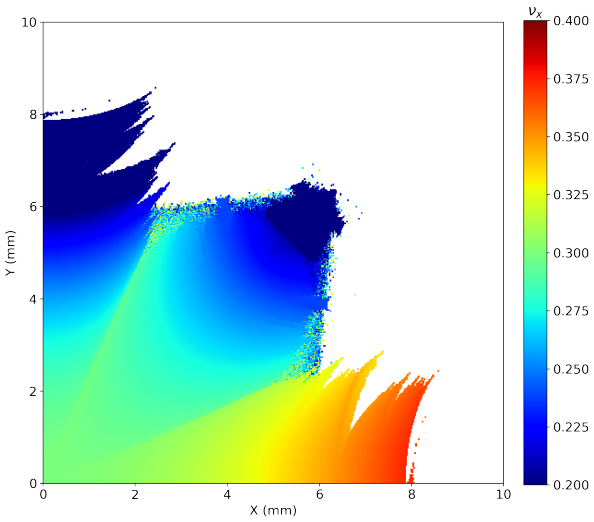

(b) ν_x distribution

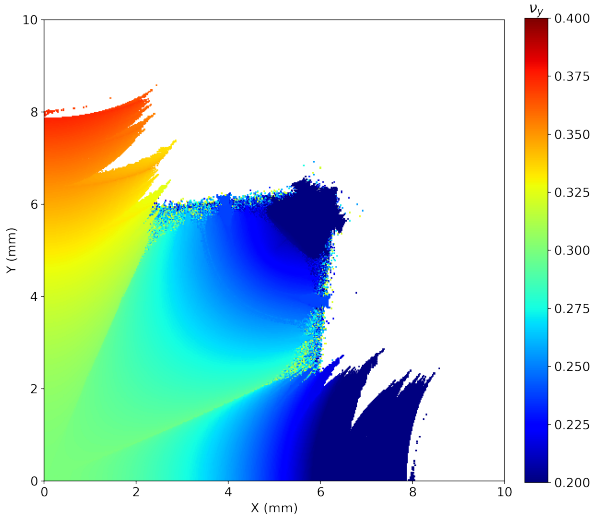

(c) ν_y distribution

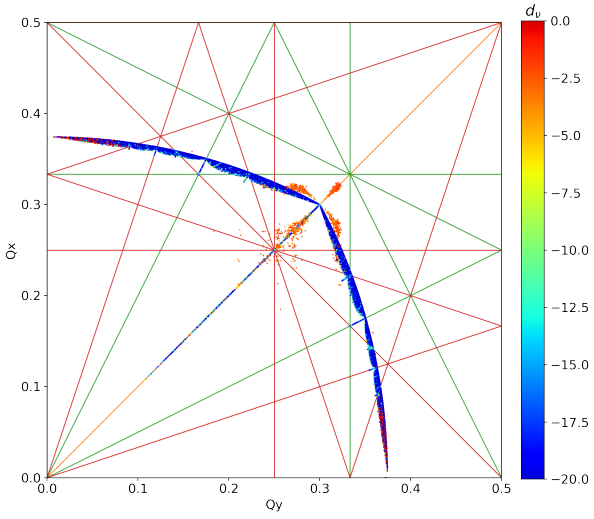

(d) Tune map with resonances up to 4th order

Figure 5.1: High resolution FMA of ideal QI system.

5.1.2 Nonlinear potential discretization

QI and DN insert designs rely on approximating the ideal NIO potential with a set of piecewise constant magnetic elements, which inevitably perturbs the Hamiltonian. This section studies resulting impact on performance using the ideal QI lattice.

Detuning impact

During insert design, an implicit assumption was made that uniform slicing is the optimal way to maintain integrability for given number of elements. However, recent work has shown that one can position elements to specifically cancel out certain low order perturbation errors by analogy with numeric integration schemes [113]. This solution requires precise longitudinal element positioning and was considered too risky to switch to as main configuration. Nonetheless, even with equidistant magnets, it is important to consider the actual impact on detuning integrals to ensure a fair comparison. In Eq. 2.74, octupole detuning was given as an integral

$$\Delta Q_x = \left[\oint \frac{k_3 \beta_x^2}{16\pi} ds\right] J_x - \left[\oint \frac{k_3 \beta_x \beta_y}{8\pi} ds\right] J_y \tag{5.1}$$

For QI insert, $k_3 \propto 1/\beta^3$ and hence

$$\Delta Q_x = \left[\int \frac{k_3}{16\pi\beta} ds\right] J_x - \left[\int \frac{k_3}{8\pi\beta} ds\right] J_y \tag{5.2}$$

$$= \frac{16t}{c^2} \frac{\nu_{drift}}{8\pi} \left[J_x - 2J_y\right] \tag{5.3}$$

The simulated detuning with action along X and Y axes (Fig. 5.2) confirms this results - it has the expected 2:1 ratio for small amplitudes, but begins to diverge at large actions due to higher order effects. Analytical detuning can be used to compute a reference strength for each (t, c) setting pair, and then scale all discrete element configurations to same strength.

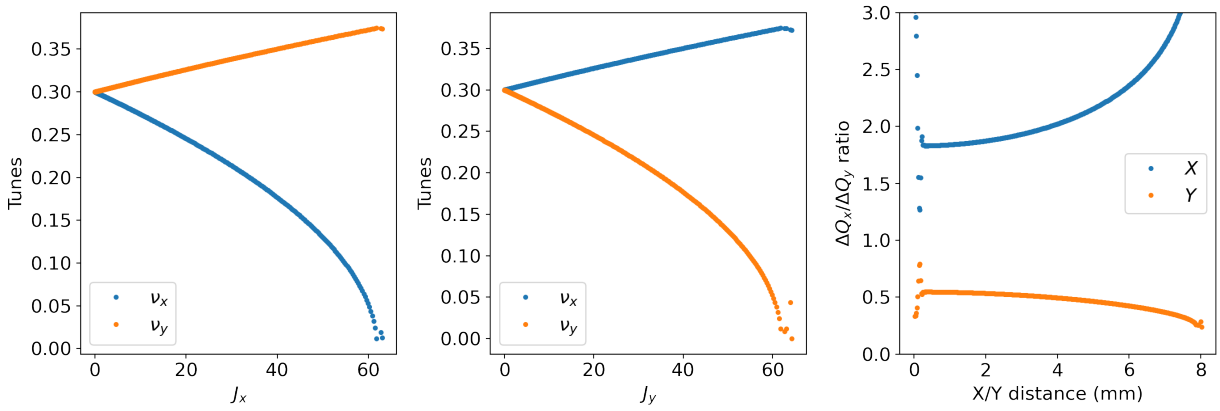

Figure 5.2: Tune shift with amplitude for QI system.

This is done in all subsequent simulations. Central and corrected strengths are visualized in Fig. 5.3.

DA impact

To measure DA impact, a scan is performed over the number of octupole slices, with results shown in Fig. 5.4. Beyond 10-15 elements, the ideal system experiences no further DA increase. In fact a tiny decrease is observed at very high counts - this is likely a consequence of the stochastic nature of tracking simulations, where depending on slight numerical effects and errors (which happen faster with more elements), particles can become unstable.

A more sensitive indicator of beam dynamics can be obtained through average diffusion as shown in Fig. 5.5. Diffusion shows a continuous improvement of beam dynamics all the way to $>$ 100 octupoles. However, it is largely academic - without improvements in DA, the maximum detuning remains similar beyond 15 elements. For all subsequent simulation in this chapter, we will focus on dynamic aperture and detuning as the two most relevant performance parameters.

The next effect to consider is that of gaps in the potential. From discussion in section 3.3, fringe fields fall off sufficiently quickly ($< 0.5cm$) that any practical magnet arrangement will

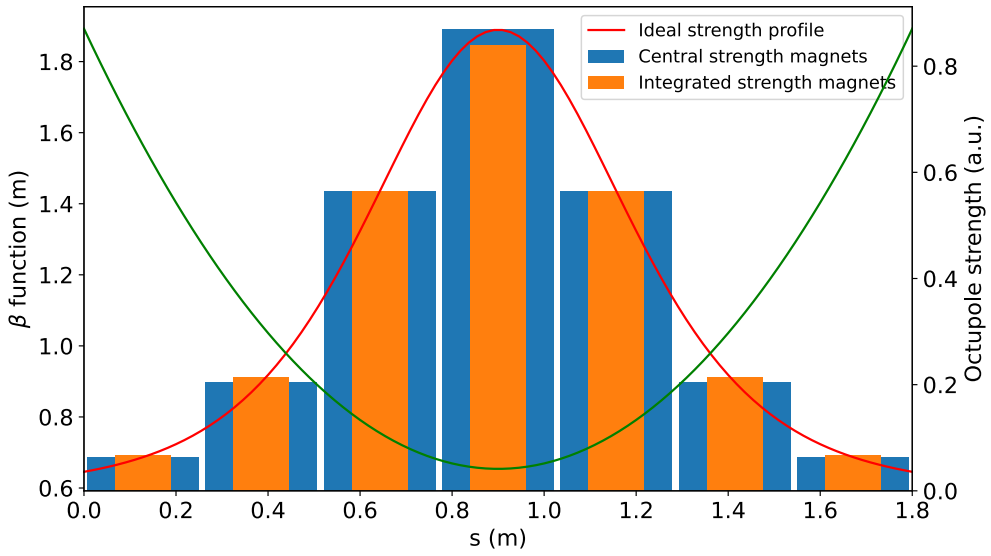

Figure 5.3: Discretization errors introduced by using only central potential strength. Note how blue bars do not match needed integrated strength in areas fast slope change.

require more clearance. Thus, it is reasonable to ignore fringe field interactions and model octupoles as hard edge elements with an effective magnetic length. By changing the fraction of empty space in the drift, a span of systems from a continuous QI potential all the way to thin kick elements is explored. Note that magnet centers need to be positioned such that the gap between any two is the same, including across the T-insert (i.e. half-gap from each end). This ensures an optimal approximation of the potential. The results are shown in Fig. 5.6 for an 18 element insert.

Only a small impact is observed for all the metrics, with the slight disadvantage of thick elements (low gap factor) caused by the loss of a few particles at key grid locations. For an ideal lattice of reasonable n, it is acceptable to use any magnet length. Experimentally, short magnets are difficult due to iron saturation and heating concerns, so a larger, mechanically convenient length should be chosen.

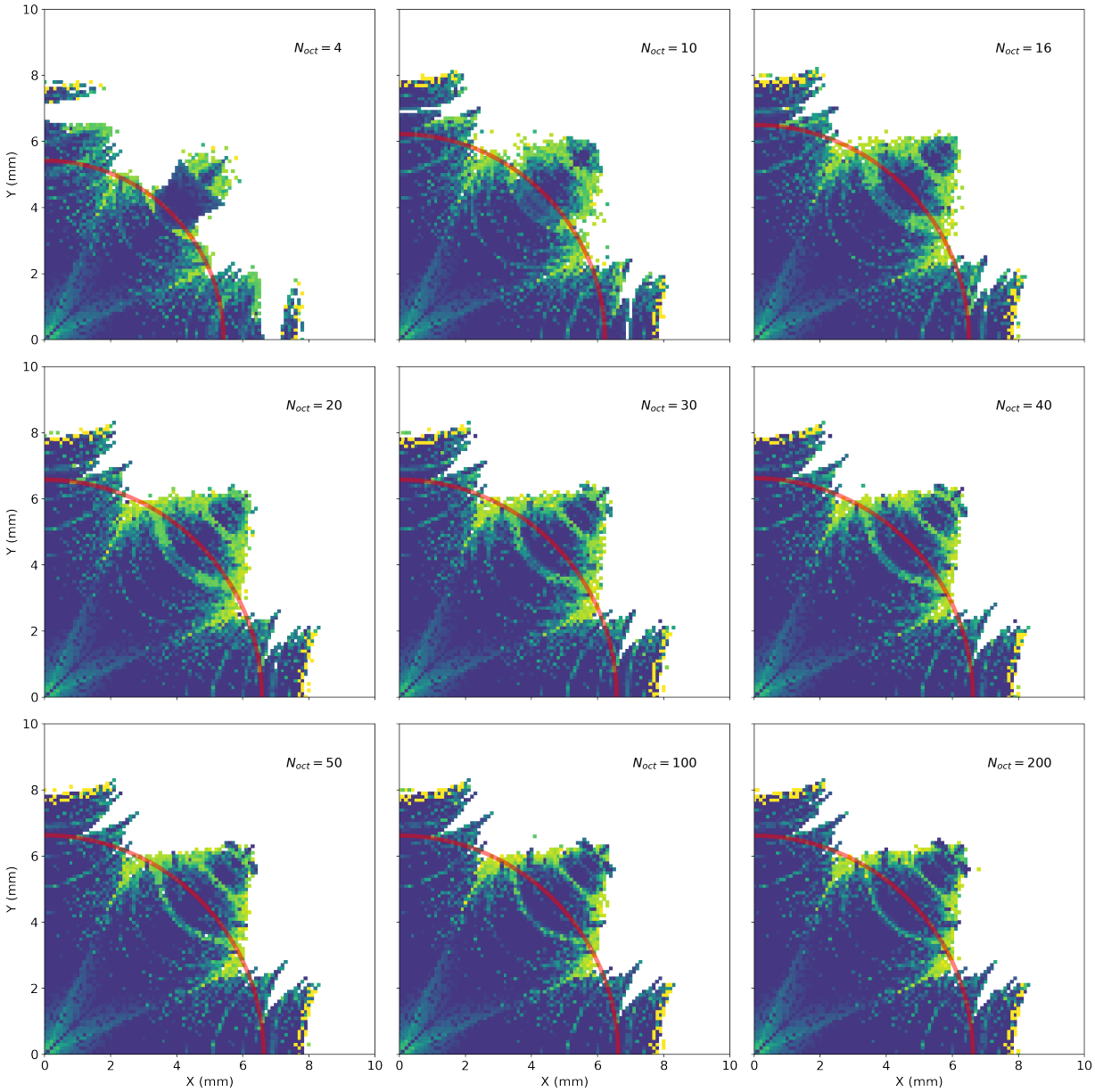

Figure 5.4: Scan of number of octupole slices in ideal QI system, with DA limit denoted in red.

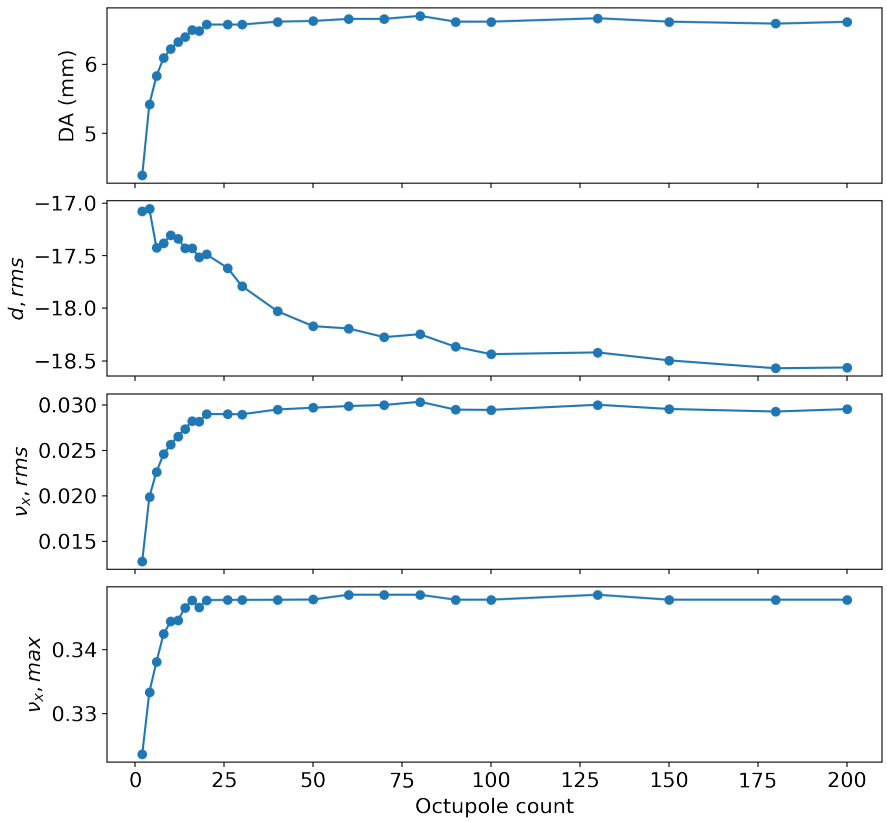

Figure 5.5: Scaling of dynamic aperture, detuning, and diffusion with number of elements.

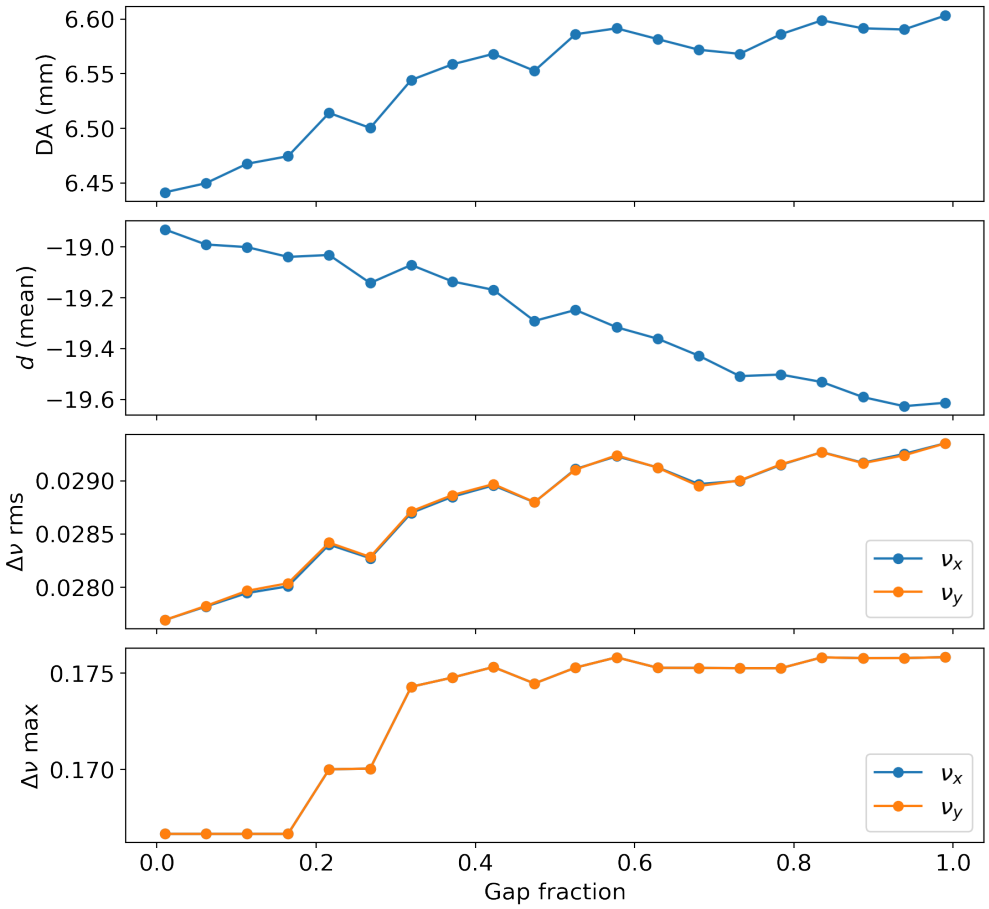

Figure 5.6: Various QI performance metrics as functions of the amount of empty space in the insert at constant detuning.

5.2 Danilov-Nagaitsev system

Same as with QI system, ideal DN tune footprints are shown in figure 5.7 for several t-strength values. The footprint shape does not only scale with increasing strength, but is distorted because of changing linear optics functions. For very high amplitude particles, DN detuning can force them over the integer tune ($Q_y < 5$), aliasing the frequency - for visualization purposes, those particles were removed. A dynamic aperture boundary is observed close to the $\pm c$ singularities, where truly ideal DN motion should have remained stable. This is due to perturbations of ideal Hamiltonian by finite integrator steps and magnet discretization, which manifest quickly near the singularities. Results of discretization and gap fraction scans (not shown) are comparable to those of QI system, with little benefit for > 20 magnets and minor impact of magnet length.

5.3 IOTA

This section presents simulations of IOTA ring without nonlinear inserts, establishing baseline lattice features.

Natural detuning

By design IOTA lattice has the required linear T-insert transfer matrix, but in practice this condition is satisfied only for very small amplitudes. Because of fewer total elements, small ring dipoles end up with very tight bending radii and large angles, producing *geometric* nonlinearities. Detailed analysis of dipole Hamiltonian shows that dipole resonance strengths are proportional to $1/\rho$ [114], while the sextupolar-like potential itself scales as $1/\rho^3$ [115]. In IOTA, tracking results (Fig. 5.8) show detuning in $\sim 10^{-4}$ range within the available physical aperture - noticeable but significantly below that of NIO inserts. Clean lattice DA radius is in excess of 30mm, several times larger than the physical aperture.

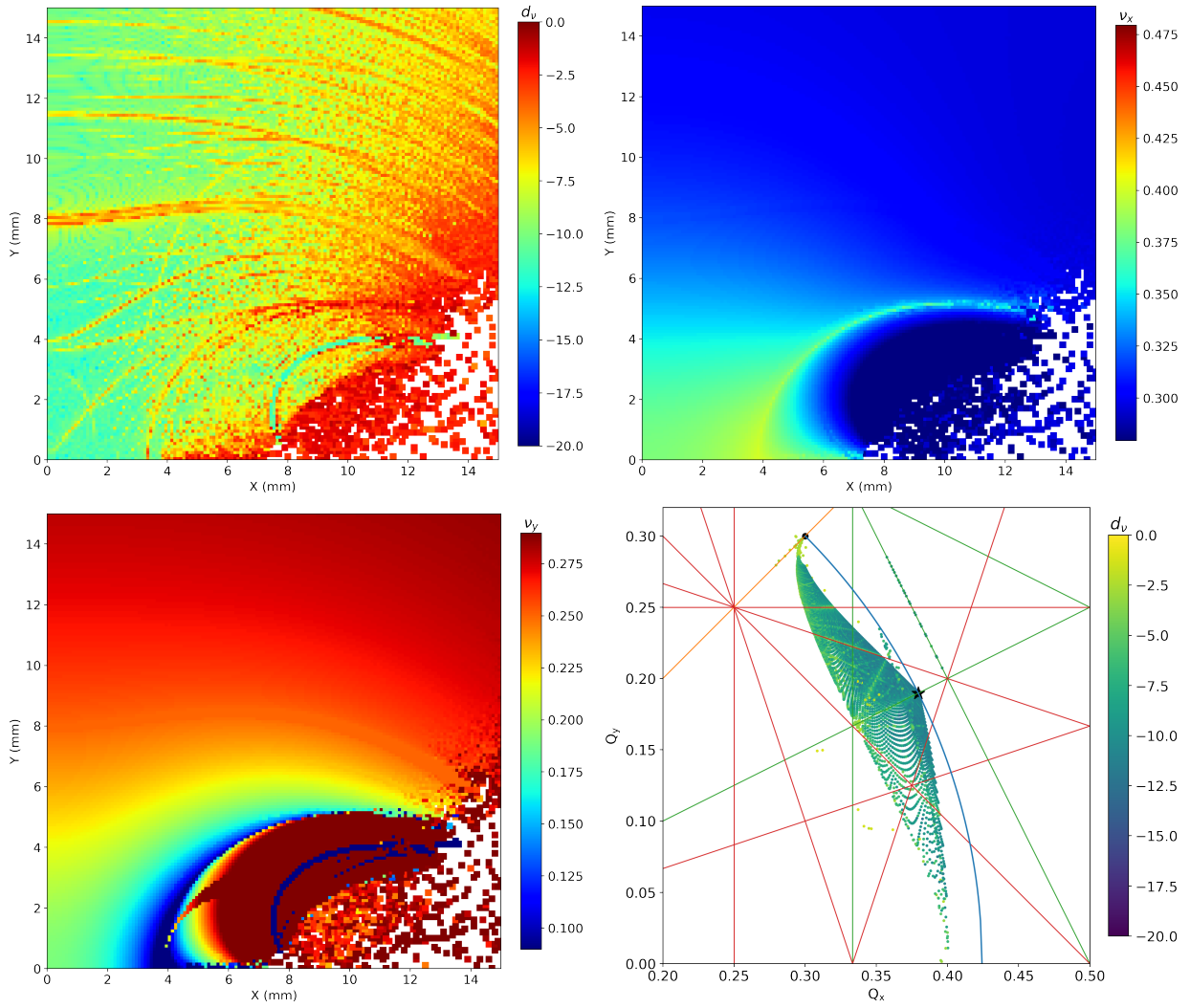

Figure 5.7: High resolution FMA of DN system at $t = 0.3$.

Chromaticity correction

Largest lattice adjustment needed for NIO is the chromaticity correction. As described in chapter 3, IOTA design has 6 sextupole families with two chromatic ones and four (mostly) harmonic ones. The following simulations use the experimental configuration with only two families. Since two families only have a single solution that satisfies specific ξ_x/ξ_y (two constraints and two 'knobs'), no optimization is possible. Sextupole strengths are derived directly from inverse chromaticity response matrix (several iterations) and applied to clean IOTA lattice. A scan in ξ_x/ξ_y parameter space is given in Fig. 5.9a. For NIO, operation

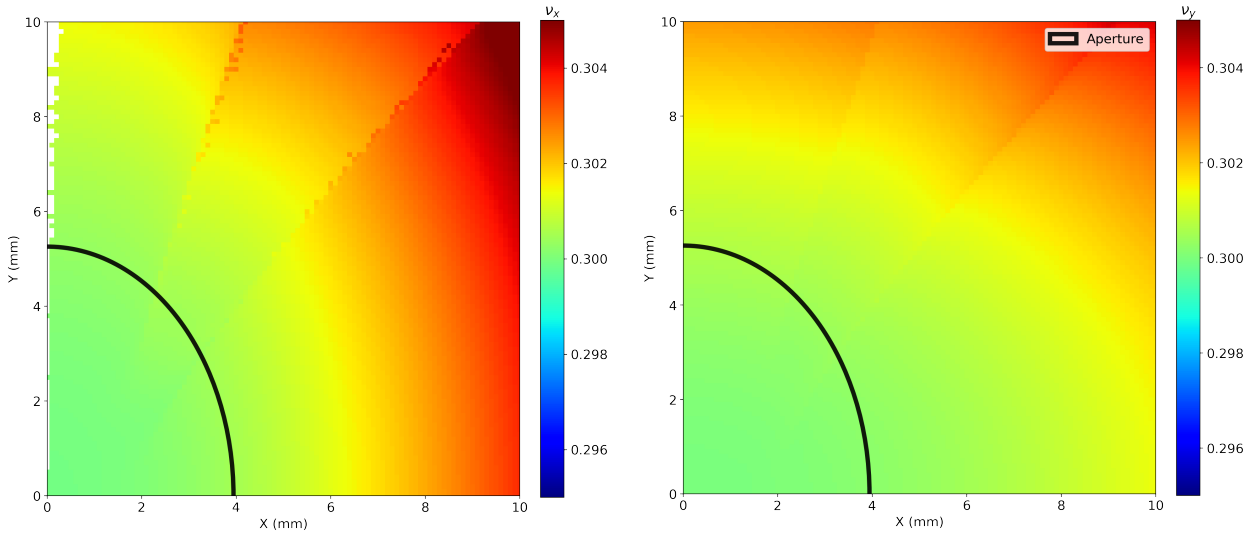

(a) ν_x distribution

(b) ν_y distribution

Figure 5.8: Clean IOTA lattice 5D FMA.

along $\xi_x = \xi_y$ is expected to yield best performance, as denoted by a dotted line.

Overall, any application of sextupoles results in DA reduction, consistent with expectations. For corrections towards 0/0, there is a very significant decrease in DA down to $\sim$ 5 mm at full correction - FMA of this case is shown in Fig. 5.9b. Inspection of individual FMA plots (not shown) indicates that a few configurations exhibit resonant capture (stable resonant islands), and others significant DA asymmetry with larger vertical sizes. Near the equal chromaticity line however, aperture boundary is smooth and it degrades predictably. The sextupole detuning within physical aperture region is significant as well, up to $\Delta\nu_{max} \approx +0.005$ at the edge. This positive shift occurs for both horizontal and vertical directions, and will affect NIO insert tune footprints.

5.4 IOTA with NIO inserts

Combining IOTA and NIO inserts produces significant interactions of various nonlinearities. Performance of this configuration places an upper bound on the possible experimental detuning, and any further perturbations can be compared against this level.

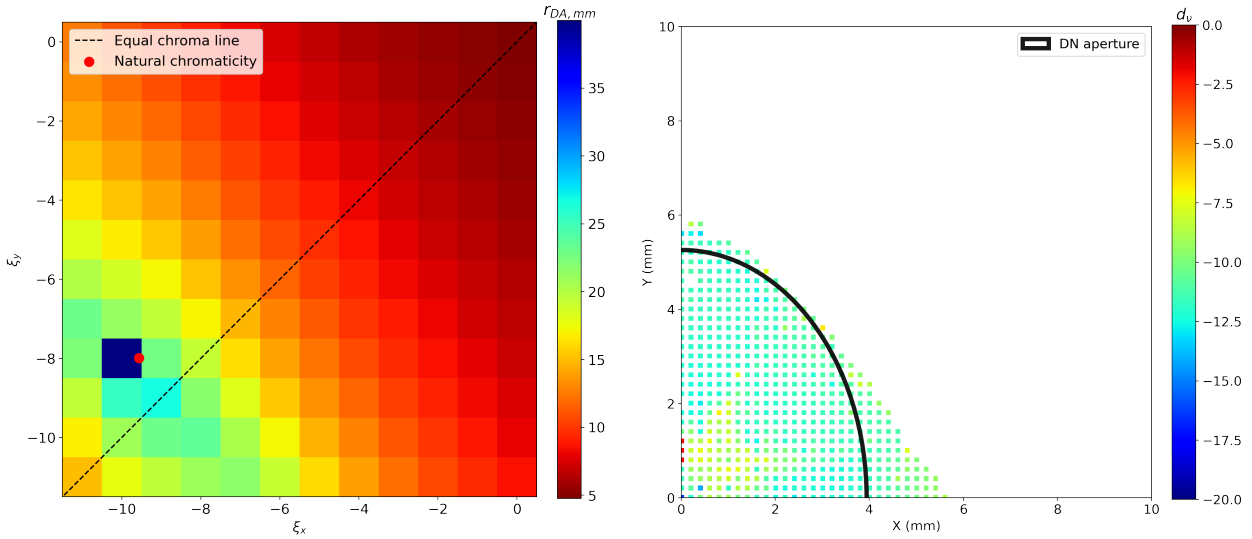

(a) Chromaticity scan

(b) FMA of fully corrected lattice

Figure 5.9: 6D FMA of clean IOTA lattice chromaticity correction.

FMA

The combined IOTA+NIO FMA (Fig. 5.10a) exhibits clear resonant island behavior - the region along x-axis of is completely separated from main DA area. It remains stable for 10^5 turns, and particle tunes inside are all the same ($Q_x = 1/3$), consistent with resonant motion. Note that full island formation occurs at strong sextupole correction levels - both octupoles and sextupoles are required to produce them. However even without dedicated sextupoles, DA is starting to have deep resonances around the island region (Fig. 5.10b), suggesting a sufficient effect from dipole kinematic terms.

Resonant islands have a detrimental effect on experimental studies, since some particles will end up getting captured and produce non-decohering resonant signals. Surprisingly, there is a use for these resonant islands in lepton machines - to form transverse resonance island buckets and provide a single pulse with 1 bunch of a bunch train for specific light source users [116]. In IOTA however, these have no use and should be avoided (but admittedly look very pretty on SLMs).

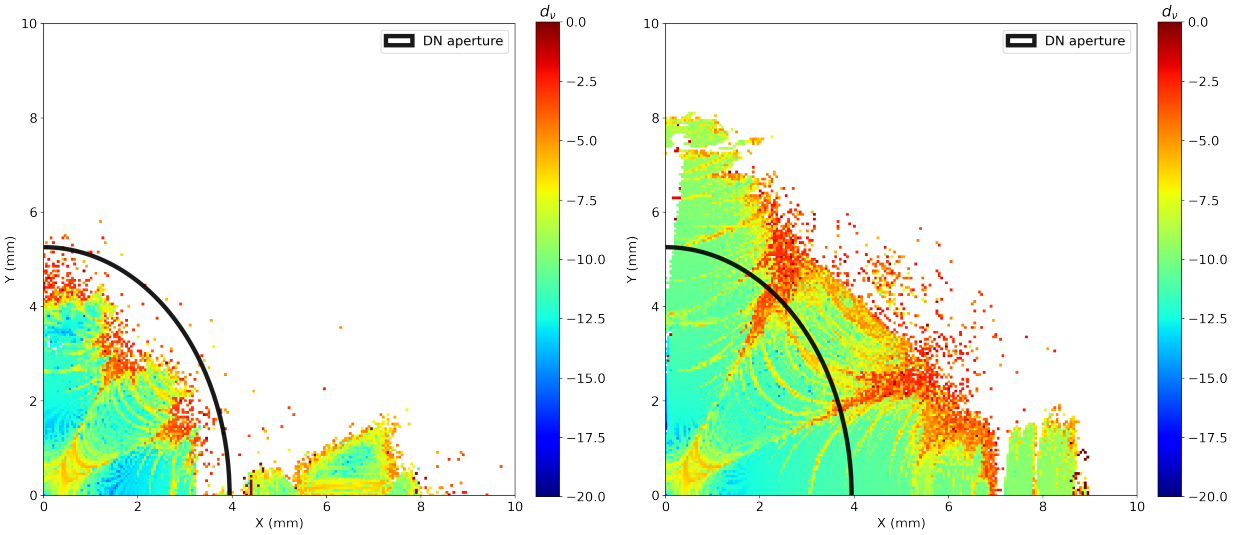

(a) Chromaticity $\xi_x/\xi_y = -2.0$ and $t = 0.27$ (b) Natural chromaticity and $t = 0.27$

Figure 5.10: FMA of IOTA with QI insert at natural and corrected chromaticities.

Chromaticity correction

As with clean IOTA lattice of previous sections, a chromaticity scan is performed at fixed QI strength (Fig. 5.11). Theoretical results suggest a sweet spot along equal chromaticity line, but there is only a slight preference for equal chromaticities in terms DA size. It seems equal chromaticity condition can be broken if necessary. No preference for x or y chromaticity is observed.

To understand which nonlinearity dominates DA size, a scan of octupole strength vs equal chromaticity correction is made in Fig. 5.12. Results show that any major chromaticity correction reduces available DA, with strengths of up to $t \sim 0.2$ being amenable to half the full correction with $r > 5\,\text{mm}$. However, looking at the rms detuning value presents a more hopeful view, with a broad region of parameter space having comparable performance. Past $t > 0.22$ at natural chromaticity, there is very little further gain, indicating QI dominates DA size. As QI strength continues to increase, stronger chromatic correction becomes possible as well. One thing not captured by average detuning metric is distortion of tune footprint (Fig. 5.13) - as expected from sextupole FMA, a positive shift in x and y is added, making

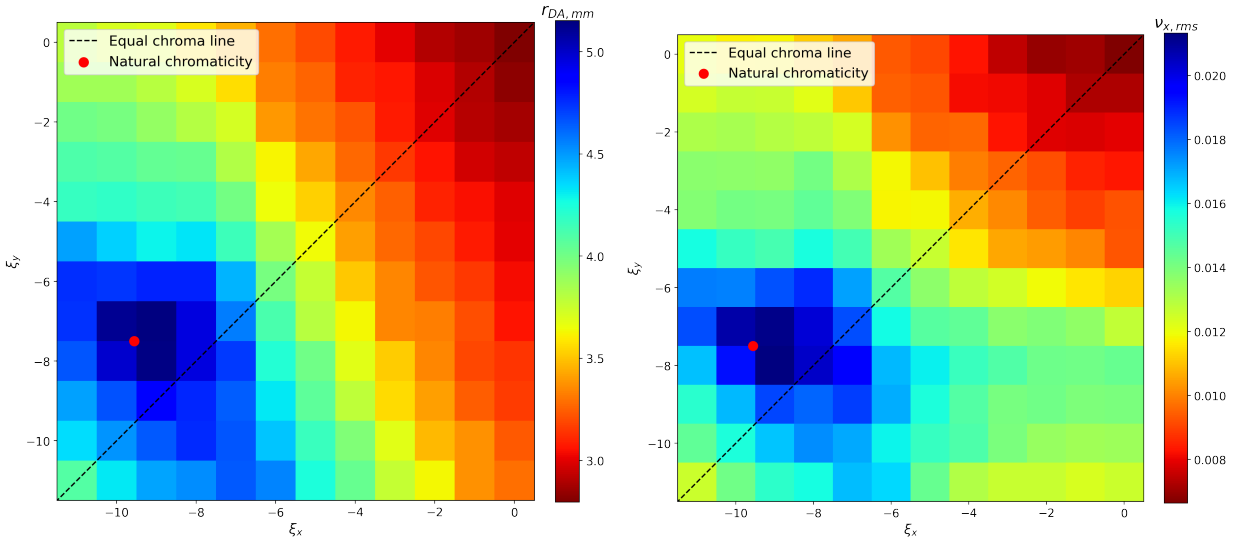

(a) DA size colormap

(b) RMS X detuning colormap

Figure 5.11: Scan of x and y chromaticities for fixed QI $t = 0.3$.

overall slope deviate from 1/2 and 2/1 in left and right arms respectively. This slope change might allow for an indirect chromaticity measurement using QI detuning data.

Overall, IOTA with QI insert performs best at near-natural chromaticity, showing only a weak preference for them being equal. There is a steep performance degradation with stronger chromaticity correction in terms of dynamic aperture size, but rms detuning shows a broader parameter space area with comparable performance. Larger QI strengths permit stronger correction.

DN magnet linear optics distortion

Quadrupole component of the DN potential distorts linear optics, increasing average β_y while decreasing β_x (Fig. 5.14). These changes must be accounted for during optics calculations. While limiting aperture remains at IOR for low strength values, near $t = 0.5$ the beta functions in focusing triplets grow to over 20m, resulting in $\sqrt{20/6} \sim 2$x increase in beam size at these locations. Note that linear optics stability breaks down completely at $t = 0.5$ - reference orbit becomes an unstable saddle point, and any analysis beyond this strength

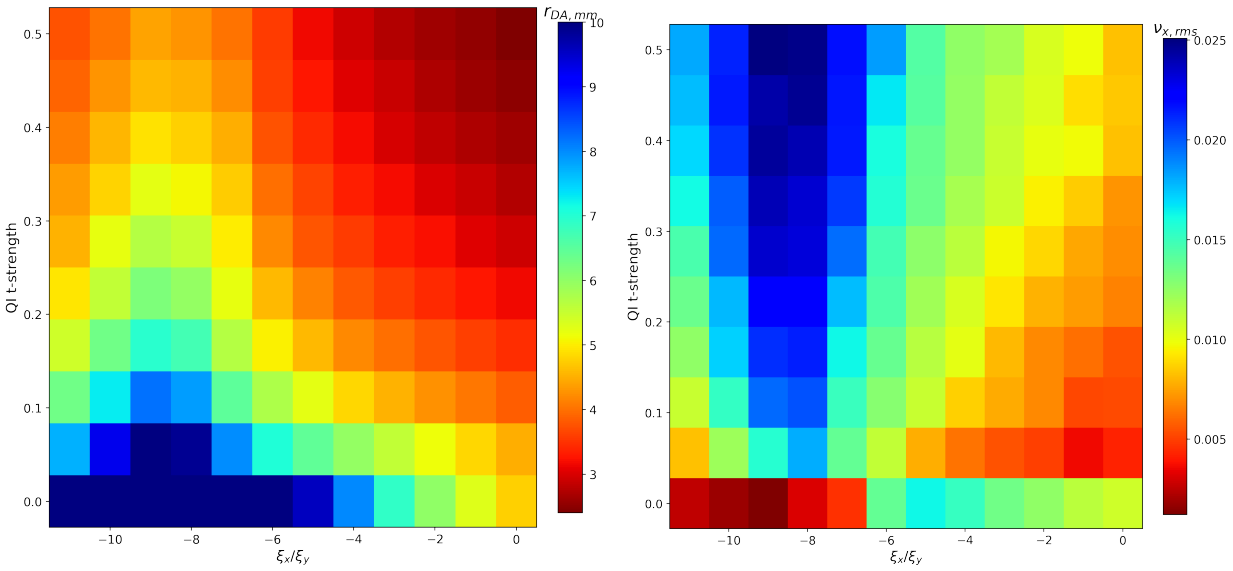

(a) DA size colormap

(b) RMS X detuning colormap

Figure 5.12: Scan of equal corrected chromaticities and octupole insert strength.

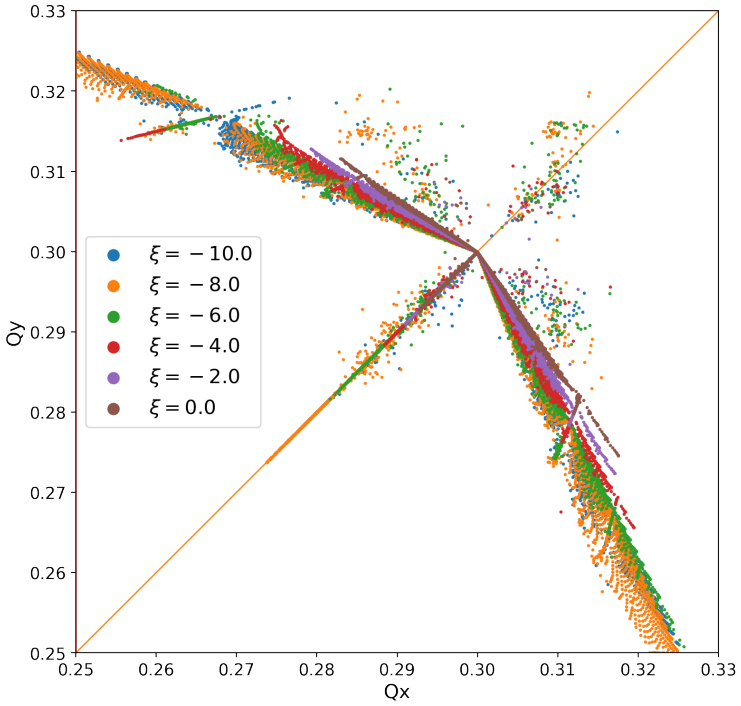

Figure 5.13: FMA of IOTA with QI at t=0.3 and varying equal chromaticities.

requires a different formalism. No good kick data beyond $t = 0.5$ was collected, and this is not the intended operational configuration, so no simulation studies were performed in this

region.

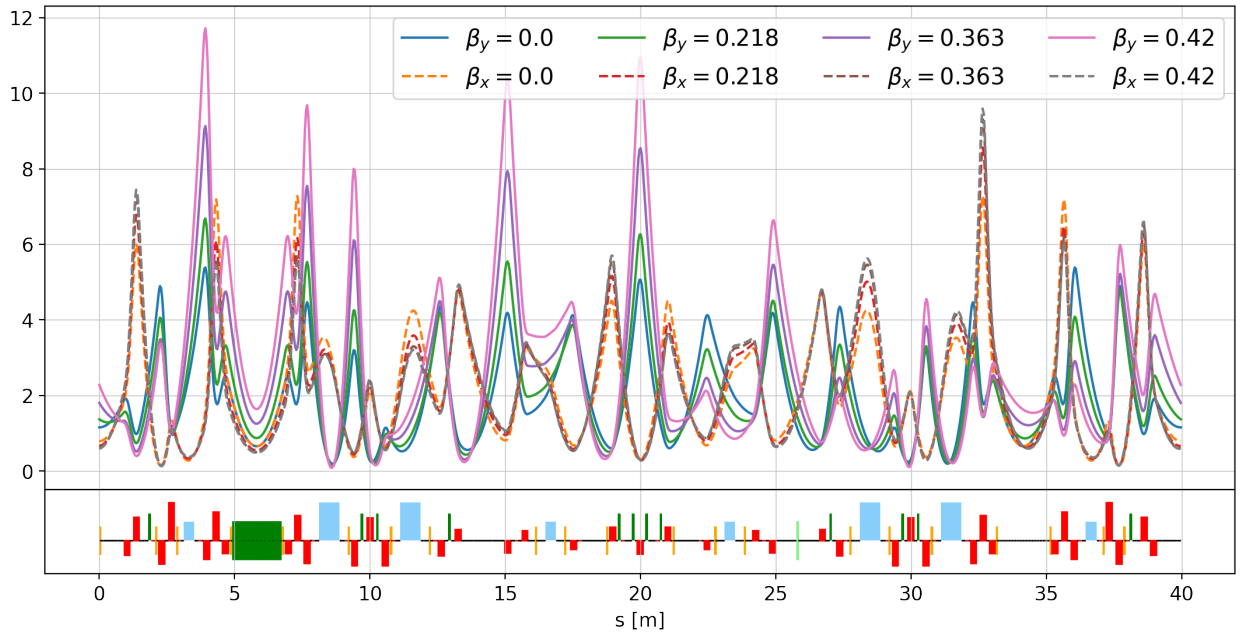

Figure 5.14: Optics distortions of DN magnet lattice at three commonly used strengths.

5.5 IOTA and NIO perturbations

The final ingredient in predicting experimental performance is addition of various perturbations. This task can be approached in two ways - the experimentally relevant way is aiming for a specific level of optical distortions (beta-beat, dispersion deviation, etc.). This method will be used in making final experimental data predictions. The other way to scan the various possible errors independently so at to determine their importance. This approach is useful, but computationally expensive and somewhat hard to interpret, since so many of the misalignments have significant covariance. Focusing on just the inserts reduces the number of parameters and makes this error scan appropriate.

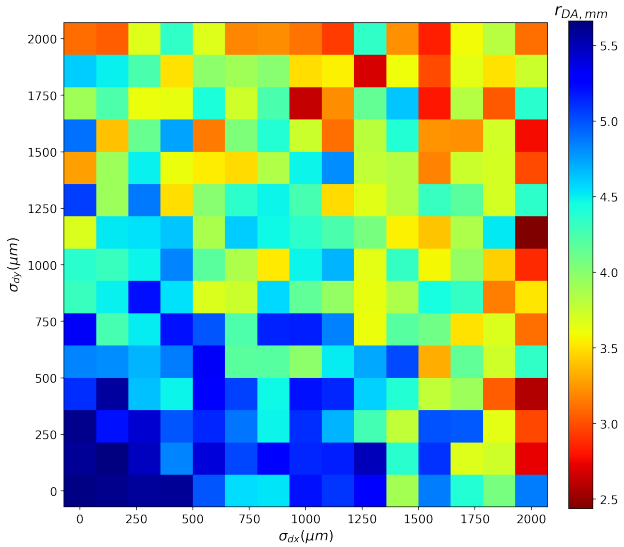

Figure 5.15: Scan of QI DA for octupole misalignments in x and y (single seed).

Insert errors

To fully specify QI insert errors, 6 parameters are necessary - x/y/tilt/s sigmas, a global longitudinal offset, and a strength error. For simplicity, transverse errors will be constrained to have same magnitude (they technically have different feed-downs, but are likely to scale together during the laser-based alignment). This rough parity was also verified with a separate simulation (Fig. 5.15), where symmetric performance degradation was observed. Since octupole strength error has close to same effect as a longitudinal misalignment, those parameters can also be treated together. A significant global offset is unlikely given the hard mechanical constraints of the drift. This leaves three parameters - σ_{xy}, FSE, and tilt. A 3D scan is performed over them, and results in various planes are shown in Fig. 5.16. For left heatmaps, values of $t = 0.3$ and $\xi_x/\xi_y = 0.0$ chromaticity correction were used to ensure all effects and interactions can be observed. For right heatmaps, sextupoles were turned off.

For corrected chromaticity case perturbations of up to 0.1 in fractional strength, 20mrad tilt, and misalignment at 0.8mm rms do not affect DA beyond approximately 10%. These results slightly exceed tolerances seen in preliminary studies [41] - the likely culprit is inclusion of full IOTA model and chromaticity, since latter dominates DA size so much that

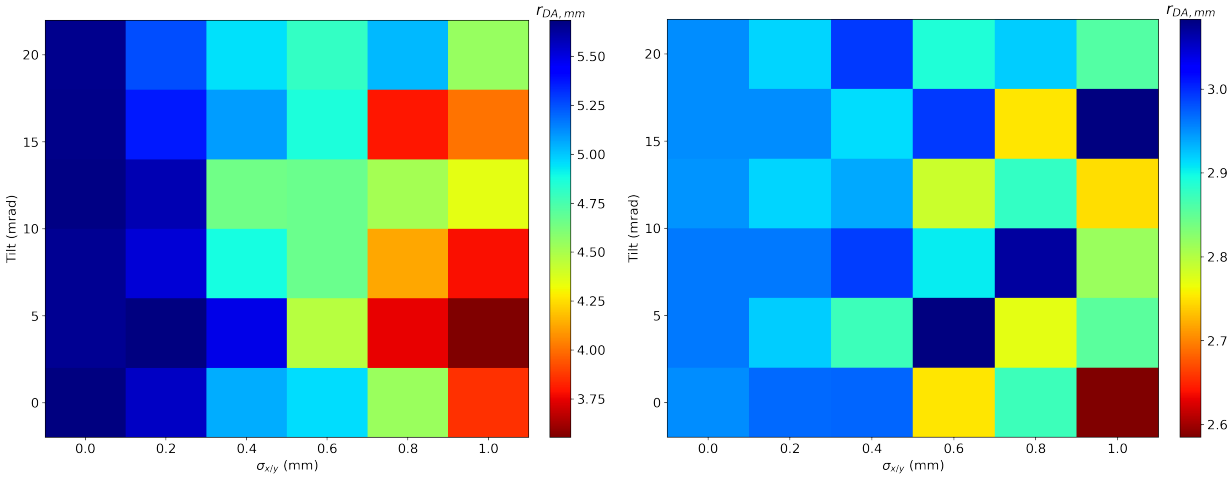

(a) Shift vs tilt at $\xi_x/\xi_y = 0.0$ and $t = 0.3$

(b) Shift vs tilt at natural ξ_x/ξ_y and $t = 0.3$

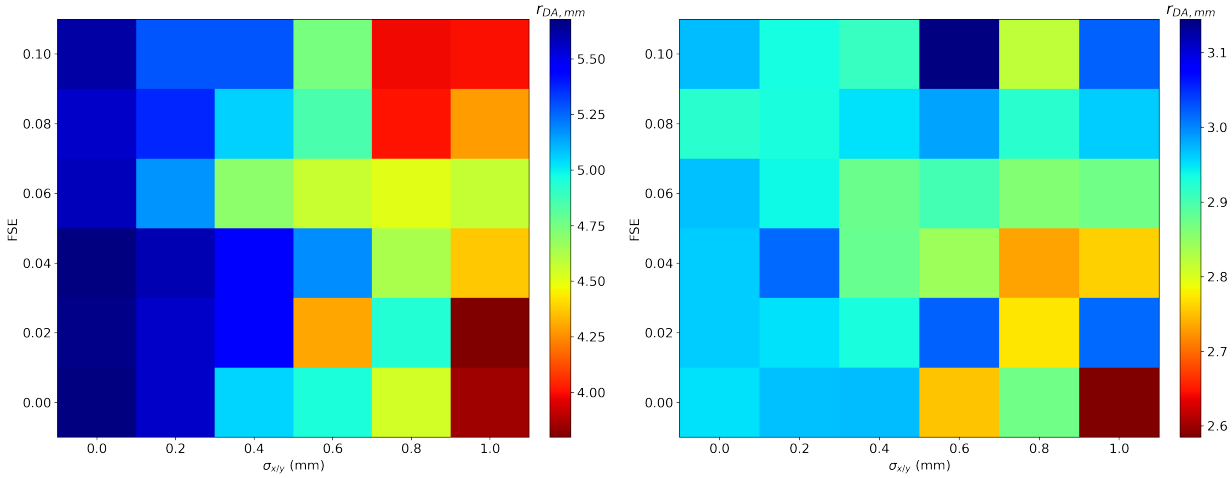

(c) Shift vs FSE at $\xi_x/\xi_y = 0.0$ and $t = 0.3$

(d) Shift vs FSE at natural ξ_x/ξ_y and $t = 0.3$

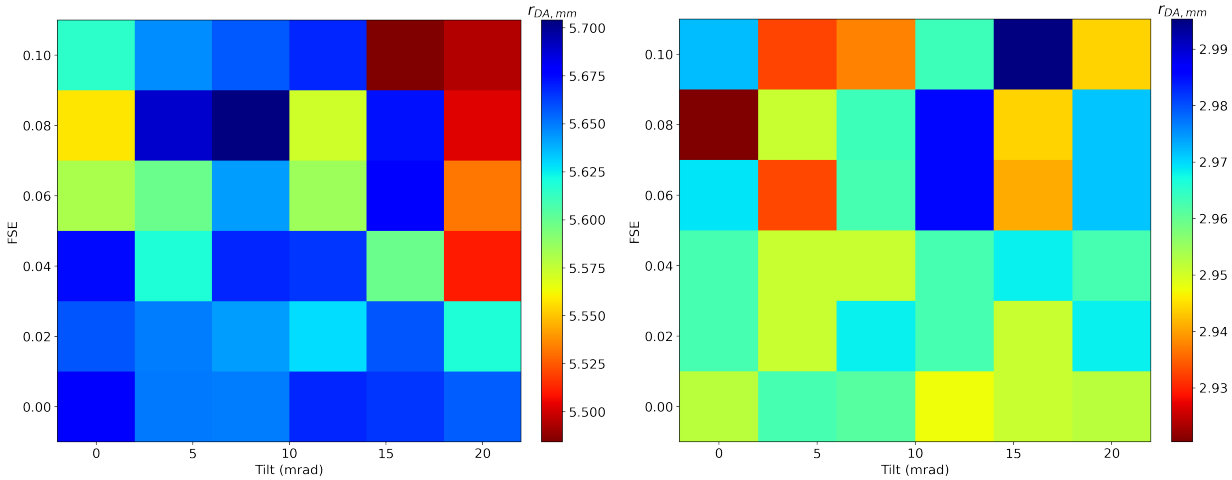

(e) Tilt vs FSE at $\xi_x/\xi_y = 0.0$ and $t = 0.3$

(f) Tilt vs FSE at natural ξ_x/ξ_y and $t = 0.3$

Figure 5.16: Dynamic aperture of perturbed QI insert (3 error seeds/point).

any additional octupole imperfections are less impactful. This is supported by natural chromaticity scans (the right 3 pictures in Fig. 5.16), where a significantly higher impact could be observed for magnet misalignments, but not the other two parameters. The sharp drop in performance occurs between 400 and 600 um shift, suggesting that 200-300um alignment specification is required to achieve full performance. Nonetheless, above result clearly demonstrate the robustness of QI system under both sets of conditions.

Linear optics errors

To first order, the exact source of optics errors within the T-insert is not important, only its effects on the transfer matrix. In fact, one can implement any such error as modification of tune and twiss parameters in the one-turn map of Eq. 2.45. A more advanced version of this concept is incorporation of chromaticity and other energy and amplitude dependent detuning effects individually for each particle, such as in LIFETRAC and elegant ILMATRIX elements. However, these do not capture the ring kinematic nonlinearities fully.

The approach used in this thesis is to designate a basis of independent optics perturbations, which can then be produced both in simulations and with experimental knobs derived from fitted optics model. Since drift of fixed length is parameterized by phase advance, that is one natural 'unit vector' choice. Other independent parameters are phase advance in the ring, the location of β^* within the drift, and dispersion. Accounting for both planes, these make a set of 8 knobs. To obtain numeric solutions, DN and QI inserts were moved to same BL drift (this gives freedom to break integrability in BR), and then simplex or genetic algorithm optimizers (when cost function had local minima) were used on the 39 quadrupole knobs. Automatically generated constraints held all parameters except one of interest constant. Full convergence was not always possible (this is not a true orthogonal basis), but in all cases the dominant perturbation was the desired one. Symmetry of all solutions was enforced where applicable, and large quadrupole changes penalized. The modified

beta functions within the drift for a few of the knobs are plotted in Fig. 5.17.

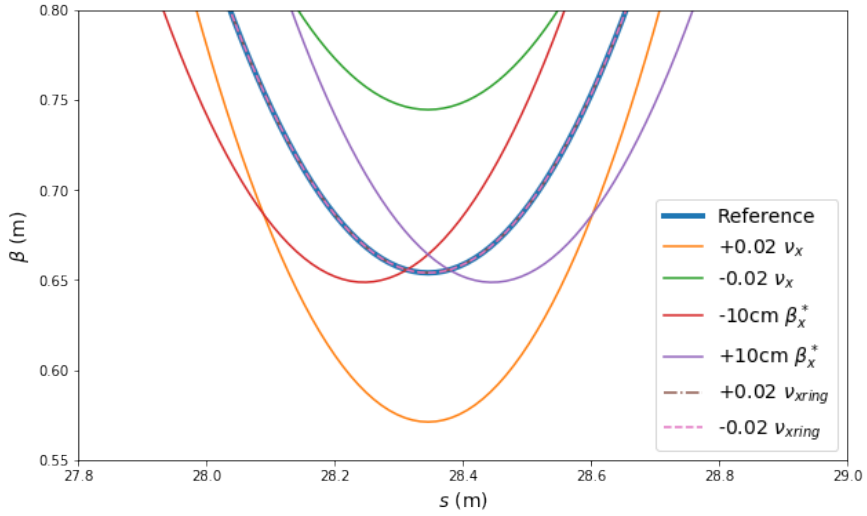

Figure 5.17: Effect of optical error knobs on β_x within nonlinear drift.

Using above knobs and linear interpolation (knobs were derived at maximum scan amplitude), scans of same lattice configuration as for the previous QI misalignment study were performed. Due to high dimensionality only a pair of parameters were varied at a time. Results for some are shown in Fig 5.18 as pairs of dynamic aperture size and detuning heatmaps.

For phase advances within the insert, dynamic aperture and rms detuning are maximized close to the nominal tune values consistent with the integrability conditions. A valley of optimum performance is formed for ν_x and ν_y errors being equal but of opposite sign, with no clear theoretical explanation. Overall, phase advance errors of 0.002-0.003 appear to not reduce DA below 90% of nominal value.

If chromatic correction is added, the area of good performance shifts to the negative range (phase advance decrease) for all 4 parameters. There is an apparent preference for equal magnitude and equal sign of ν_x and ν_y errors, potentially suggesting the QI system is more capable of fighting against sextupole perturbations when the integrability conditions is satisfied in both plane or perturbed equally. Note that optics scan in presence of sextupoles

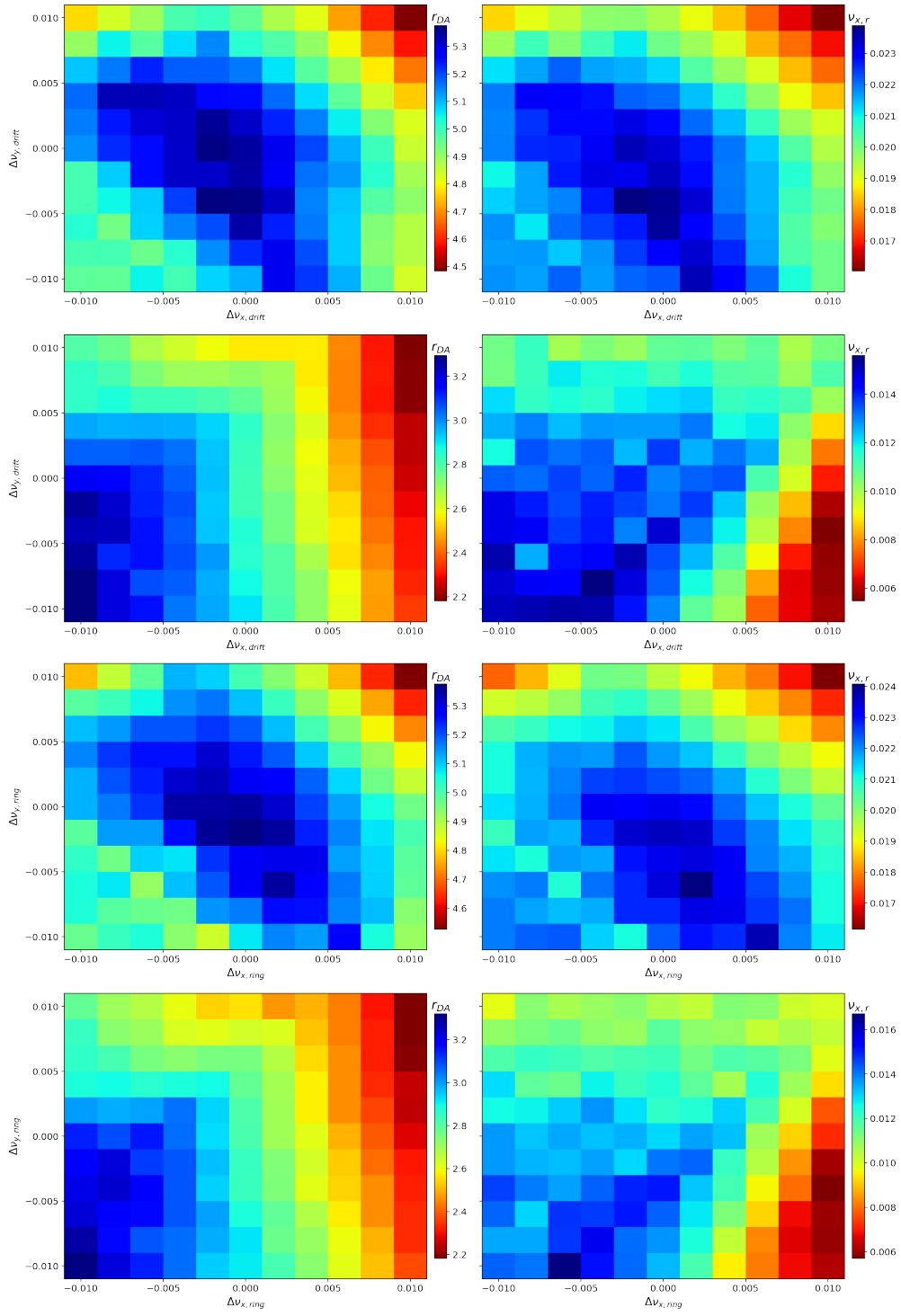

Figure 5.18: Optics perturbations of QI insert. From top, tune advance in the insert without chromaticity correction, tune advance in the insert with full correction, tune advance in the ring without correction, and tune advance in the ring with correction.

has a systematic - since error knobs perturb optics functions in the ring, they have a direct effect on the sextupole strengths, which in turn have to be adjusted to obtain the desired chromaticity. A more advanced knob set that also holds sextupole dispersion and optics functions constant would be better suited for the scan, but no such solution was found for current NIO lattice.

Coupling

The last linear parameter not covered by above scans is the coupling, both in a global sense and locally near the NIO insert. Coupling can have an effect on nonlinear observables, beam instabilities [117], and directly change the nonlinear detuning [118].

In IOTA, coupling determines the closest tune approach at working point and ensures the beam is round prior to any kicks. Because of this, it is closely monitored and corrected very accurately. In simulations, several skew-quad magnets were enabled at very low current so as to get $|C^-| = 0.001 \approx \Delta Q_{min}$. However, no significant effects were observed on QI performance.

5.6 Bunched beam simulations

In this section, the behavior of particle bunches placed into previously discussed lattices is presented. Of special interest are equilibrium distributions, and the expected BPM signals of centroid motion.

5.6.1 IBS

Formulas for evaluating equilibrium emittance with and without IBS or coupling were discussed in section 2.1.15. Using elegant IBSCATTER element, it is possible to verify the expected values with extremely long (>1e6 turn) simulations. Of special interest, and not

covered by standard formulas, are the possible effects of NIO inserts on the equilibrium distributions. Because of immense computational cost (20 nodes * 28 cores * 36 hours), IBS simulations were performed starting with rough parameter estimates for equilibrium values and not the zero-current ones. Results for case with QI on are shown in Fig. 5.19. Starting distribution was taken from a fully uncoupled bunch IBS simulation result with a huge emittance ratio (150nm/6nm x/y), and thus the redistribution into 'rounder' shape is due to octupolar effects. Constant decrease in longitudinal emittance suggests that 30cm/3e-4 was a slight overestimate of length/energy spread respectively. When bunch was started in a coupled case (50/50nm round shape + skew-quads, not shown), no octupole effects were observed and distribution remained roughly Gaussian. The latter situation is more reflective of experimental conditions, and validates the use of round Gaussian distributions for simulations.

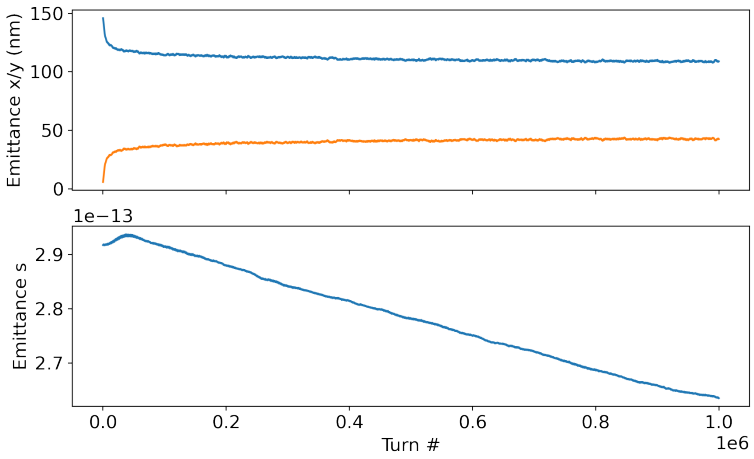

Figure 5.19: Evolution of bunch emittances for clean IOTA lattice and QI turned on to t=0.3, starting at large flat beam of a purely linear lattice.

5.6.2 *Kicked beam motion*

To simulate bunch decoherence, offset matched distributions of 10000 particles were generated and tracked for 2 synchrotron periods. Ideal lattice results are shown in Fig. 5.20. As expected from the envelope formulas, centroid signal decoheres quickly and then recoheres after a synchrotron period (denoted by black dotted line). However, inherent IOTA nonlinearities serve to both delay and suppress the recoherence signal at higher amplitudes, consistent with FMA predictions.

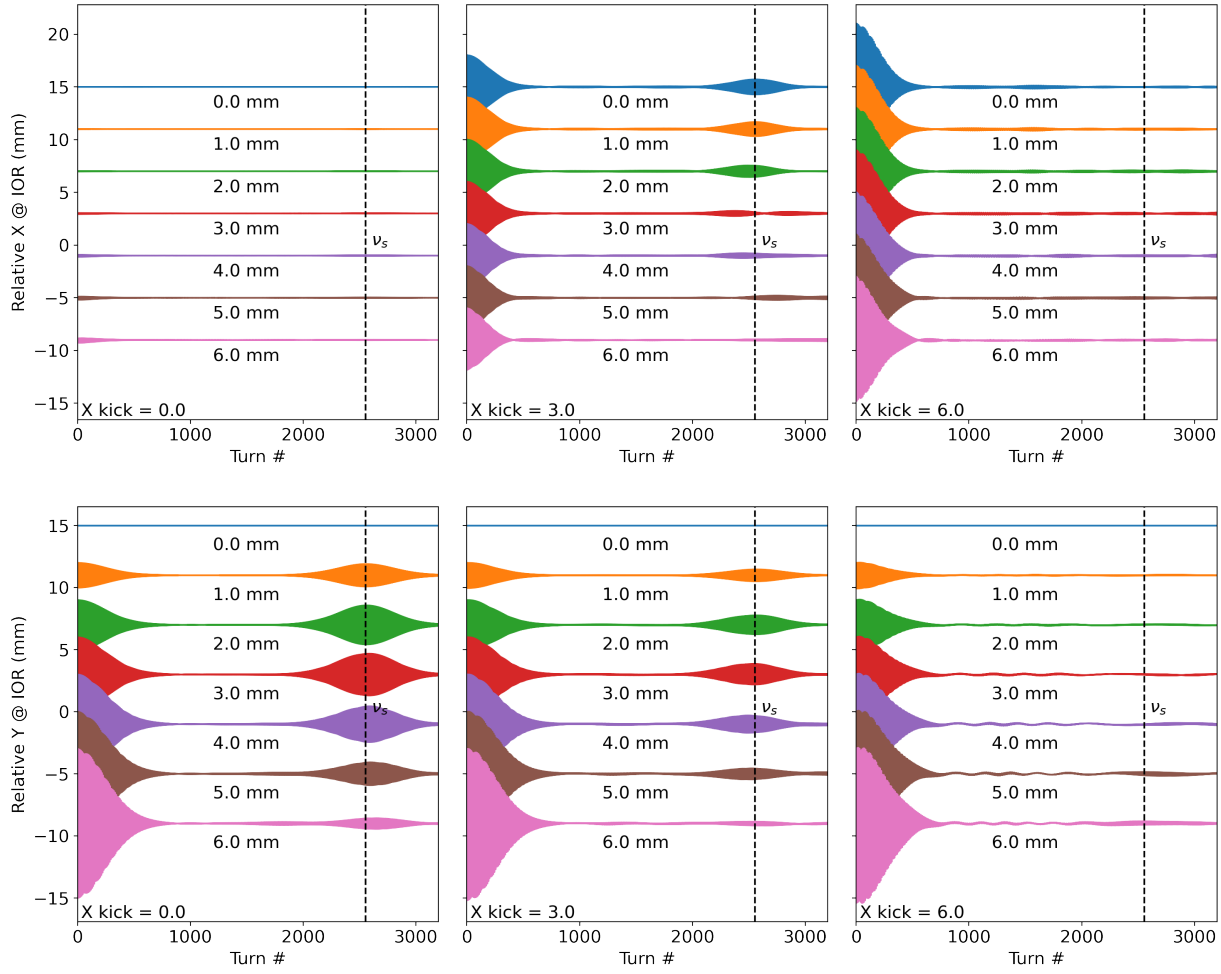

Figure 5.20: Kicks of increasing amplitude in X/Y planes in clean IOTA lattice. Columns denote varying X amplitude of excitation, and lower kicks in each plot have stronger Y excitations as denoted by text labels.

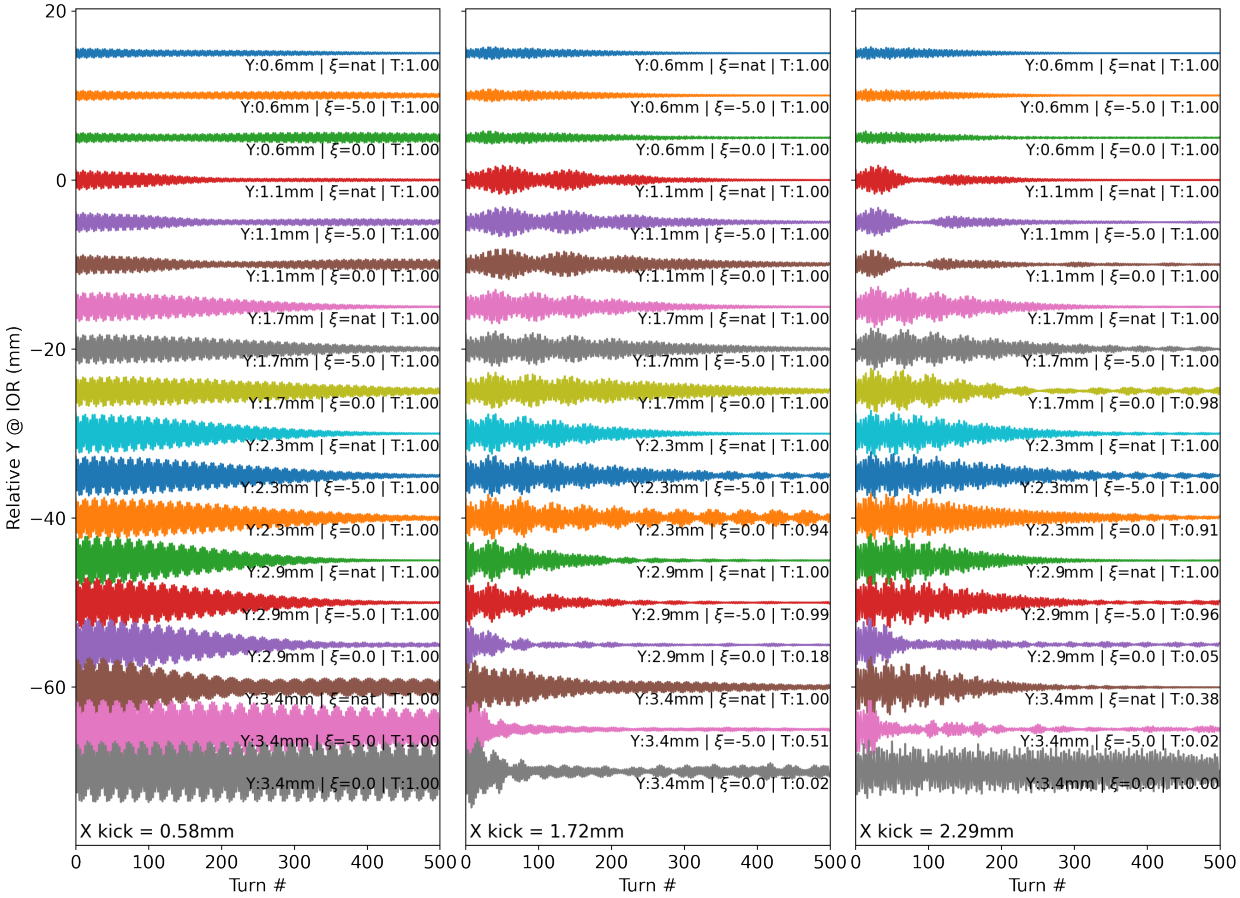

Figure 5.21: Y centroid data of kicks with aperture, QI, and sextupoles. Text of each kick denotes amplitude of excitation in Y plane, the chromaticity, and the fraction of particles transmitted for the full 500 turns. Amplitude of X plane is denote at the bottom of each column.

Addition of apertures, sextupoles, and the nonlinear inserts has a large impact (QI at $t = 0.3$ in Fig. 5.21). In addition to nonlinear detuning, beam is scraped at higher amplitudes, changing its distribution, observed tunes, and future decoherence rates. There is also resonant capture at some amplitudes (bottom left), nonlinear coupling (fast wavy oscillations), and other effects.

Experimentally, it is useful to be able to distinguish physical aperture losses from DA ones. Current profiles of several bunches are shown in Fig. 5.22. In ideal IOTA lattice, physical aperture scraping is near instant. With QI and chromatic corrections added, the

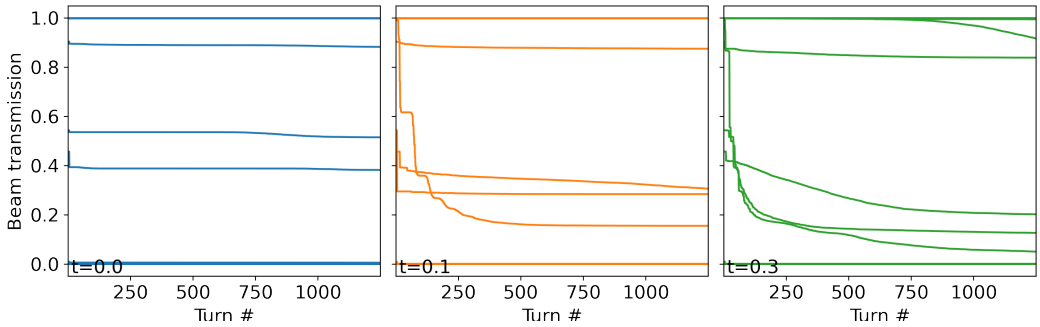

Figure 5.22: Normalized beam losses of kicked bunches for increasing QI strength.

behavior is more involved, with a wide variety of slow and fast losses. Anything past turn $\sim$ 50 is attributable to dynamic aperture effects. While 8000 turns of experimentally accessible data capture most losses, DCCT measurements are still needed for the slower resonant effects.

5.7 Accuracy of analysis algorithms

In this section, performance of analysis algorithms is studied for simulated signals with varying levels of noise corruption.

5.7.1 Tunes

Stationary signals

For a stationary signal with no tune change, such as single particle in FMA simulation or a sine wave, adaptive NAFF convergence follows the expected $1/N^4$ trend (Fig. 5.23), and degrades to $1/N^{1.5} - 1/N^2$ in presence of even 0.1% noise. This confirms correct NAFF implementation.

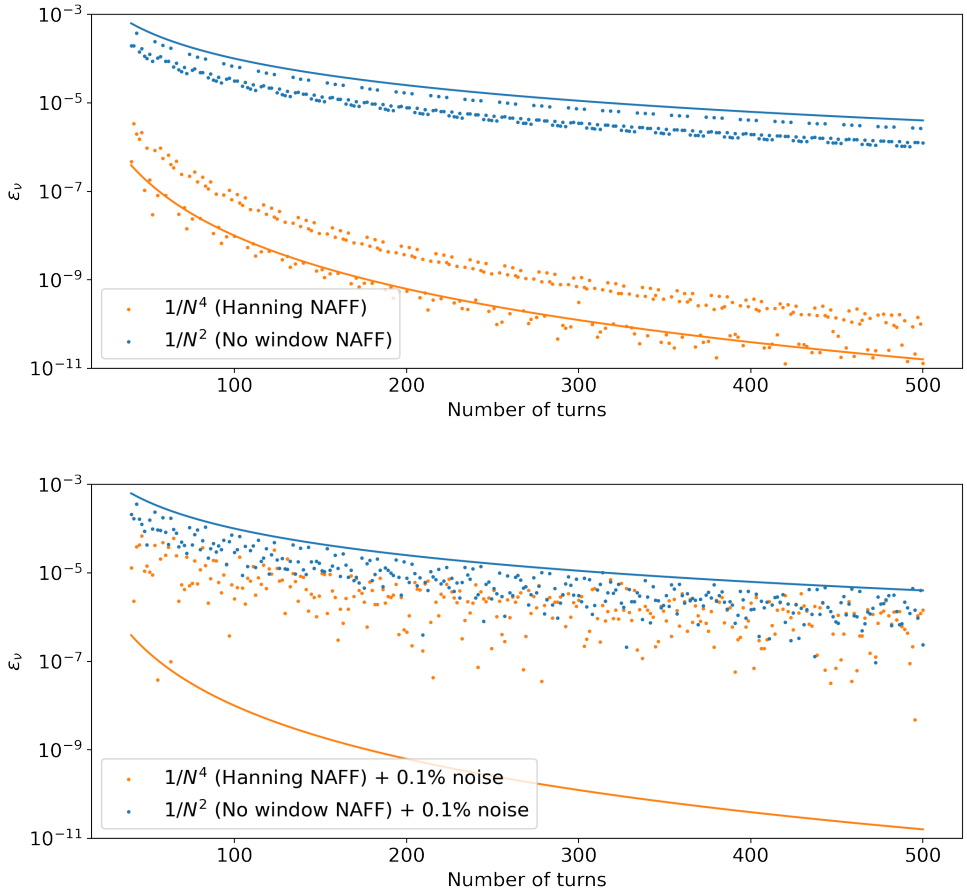

Figure 5.23: Accuracy of NAFF algorithm without noise (top) and small amount of noise (bottom) for synthetic sine wave signals.

Decohering signals

An example of decohering and almost stationary signal is that of a clean IOTA lattice kick. Using previous data of figure 5.20, NAFF is applied to the signal (Fig. 5.24a) with two full length windows (Hanning and half-Hanning), as well as with a 50 turn sliding Hanning window. The latter gives an idea of the local tune in a specific signal region. Clean data indicates the expected positive tune shift, although the amount is quite high for a clean lattice. The full and half-Hanning windows do not agree fully, but are close for first 100 turns. Later, the disagreement grows as the full window starts suppressing early signals and thus average tune shifts upwards faster.

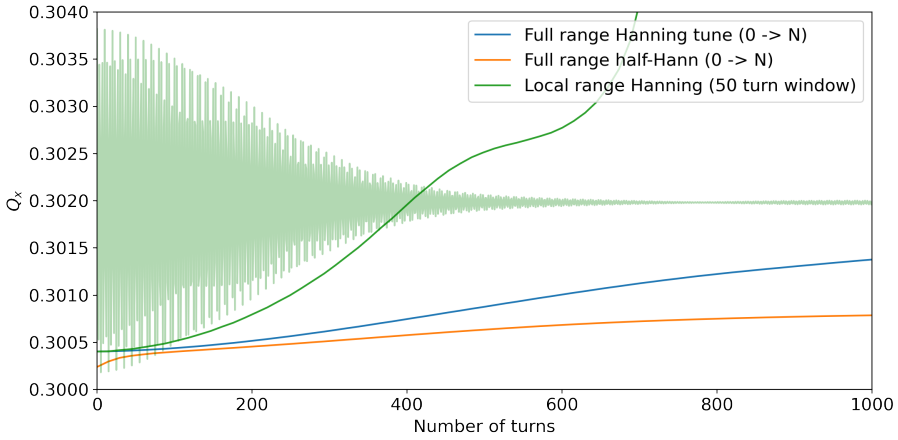

(a) Clean signal NAFF with various growing and sliding windows.

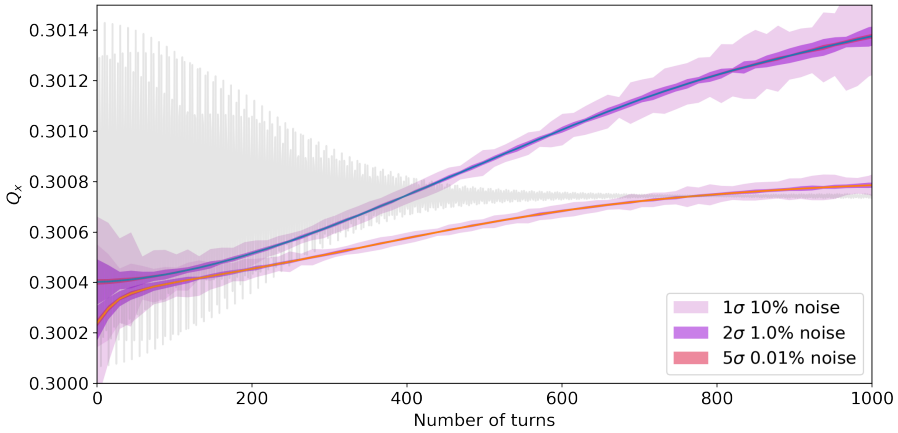

(b) Performance with increasing noise

Figure 5.24: Performance of NAFF on clean IOTA lattice signals. Confidence bands on bottom plot were increased from standard 1σ for legibility, as denoted in the legend,

Discarding the local tune method, and rerunning analysis with increasing levels of noise (5.24b) shows superior performance of full Hanning window at very low number of turns, since the signal essentially has no decoherence. However, the disadvantage of suppressing early data again becomes clear as the error spread increases with number of turns once signal is fully decohered. Overall, there is an optimum around $\sim$ 100 turns where both methods perform well, and without much tune shift bias.

Realistic signals

Same NAFF procedure is applied to IOTA lattice with $t = 0.3$ QI insert. Figure 5.25 shows an equal kick in x and y (tune shift is along the coupling resonance). Fast coupling oscillations can be seen, with signals exchanging planes over around 100 turns. This suggest the actual X/Y detuning is not equal, likely because of sextupolar contributions, and some bias of the frequency measurement is thus expected depending on the number of turns used.

When tunes are split, such as for kicks predominantly along a single plane, the situation is much better. In Fig. 5.26, a well decoupled kick with stronger Y excitation produces stable tune estimate over range of 50 to 200 turns, with comparable errors for either windowing method. Experimentally then, it is desired to produce maximum kicks in vertical and horizontal planes - simulations indicate very little tune drift or coupling issues, and best possible detuning measurement accuracy.

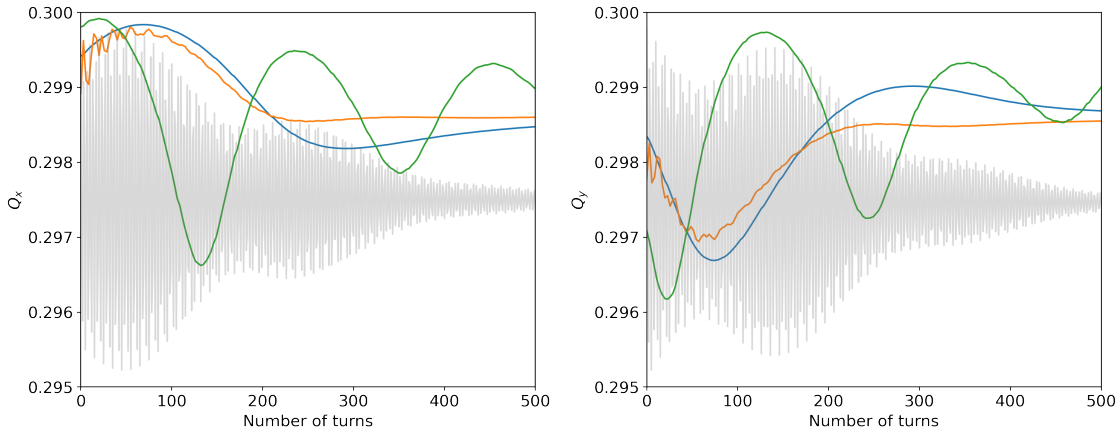

Figure 5.25: NAFF performance on QI signal for beam excited diagonally. Colors denote same analysis algorithms as in figure 5.24a

.

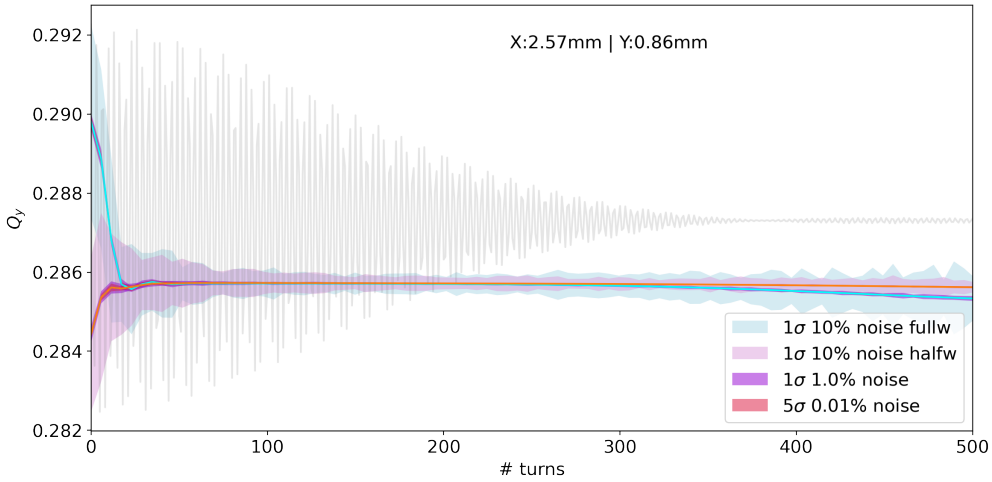

Figure 5.26: NAFF performance on QI signal at split tunes.

5.7.2 Phase space

Momentum

Accuracy of momentum and phase space measurements depends on the phase advance between BPMs, with values close to $\pi/2$ being ideal. In figure 5.27, all BPM phase advances around the ring are computed and plotted as a heatmap.

While there is no hard phase advance cutoff, even for advanced approached like covariance weighting it is prudent to remove combinations too close to $n\pi$ due to numerical issues. Given the small weighting such pairs would receive in any case, little if any useful data is lost. In order to compute not just Courant-Snyder invariants but H and I for NIO systems, both planes have to satisfy phase advance criterion. In figure 5.28, a cutoff $\epsilon < 0.1 \times 2\pi$ is applied and a locality constraint is added (4 nearest neighbors) as denoted by green band.

To evaluate phase and invariant recovery algorithms, an example region of 6 BPMs was used, and single particle and bunch motion simulated. Table 5.1 lists the BPMs and their phase advances relative to BPM B1R, which is where the phase space reconstruction is desired in this example. Note that 4 of the 5 pairs pass the phase check, but C1R phase advance is very close to π. This is reflected by its extremely poor naive weight (1/variance),

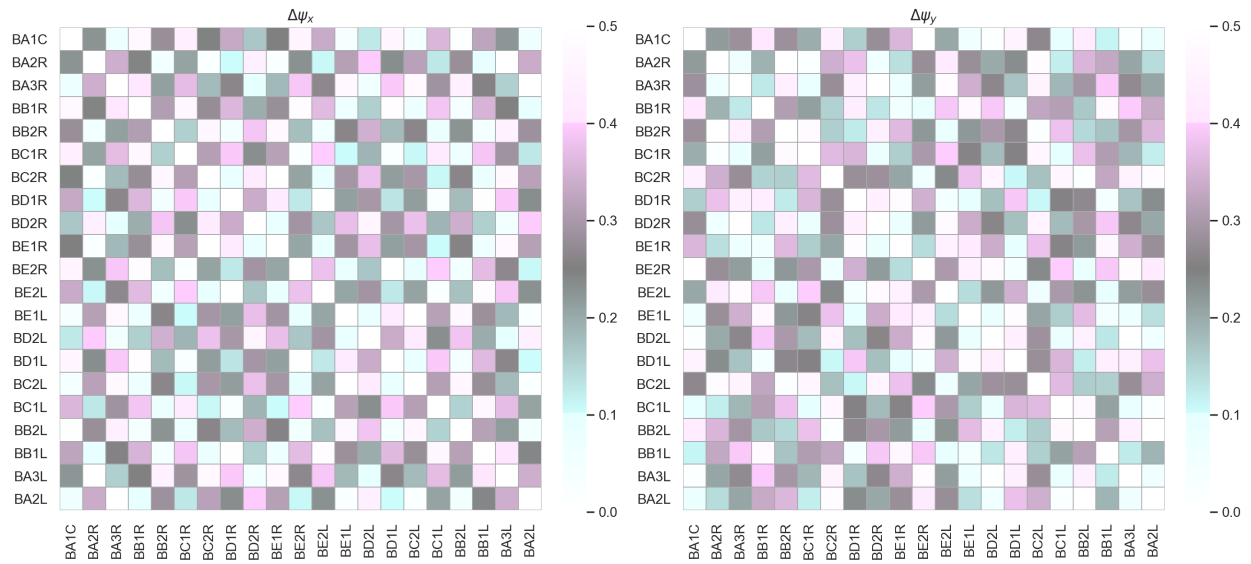

Figure 5.27: Phase advances between all BPM pairs.

BPM1	BPM2	$\beta_{2,x}$	Delta from $\pi/2$ (deg)	Phase to B1R (deg)	Naive weight
B1R	B2R	2.05	21.47	68.52	0.481
B1R	A2R	0.40	2.42	87.57	0.125
B1R	A3R	0.85	-55.07	-34.92	0.067
B1R	C1R	0.62	77.37	12.62	0.007
B1R	C2R	1.09	9.68	80.31	0.320

Table 5.1: BPM data for momentum recovery.

and as discussed above this pair is immediately rejected.

The remaining 4 pairs are used in a benchmark where increasing levels of white noise corruption are applied, and momentum calculated. The methods benchmarked are single pair (B1R-B2R), simple average of all pairs, variance weighted average, covariance weighted (statistical only) and finally the optimized covariance method, where MC contributions are added and a weight optimization pass is done. Results are shown in figure 5.29, and demonstrate good gains until variance weighting. Addition of statistical covariance produces only a little gain, and full covariance no further changes. This is expected, since the ideal simulation optics contain no systematics. For typical MC seeds in line with previously discussed optics errors, the advantage was up to 5-10% but highly dependent on the exact error distributions

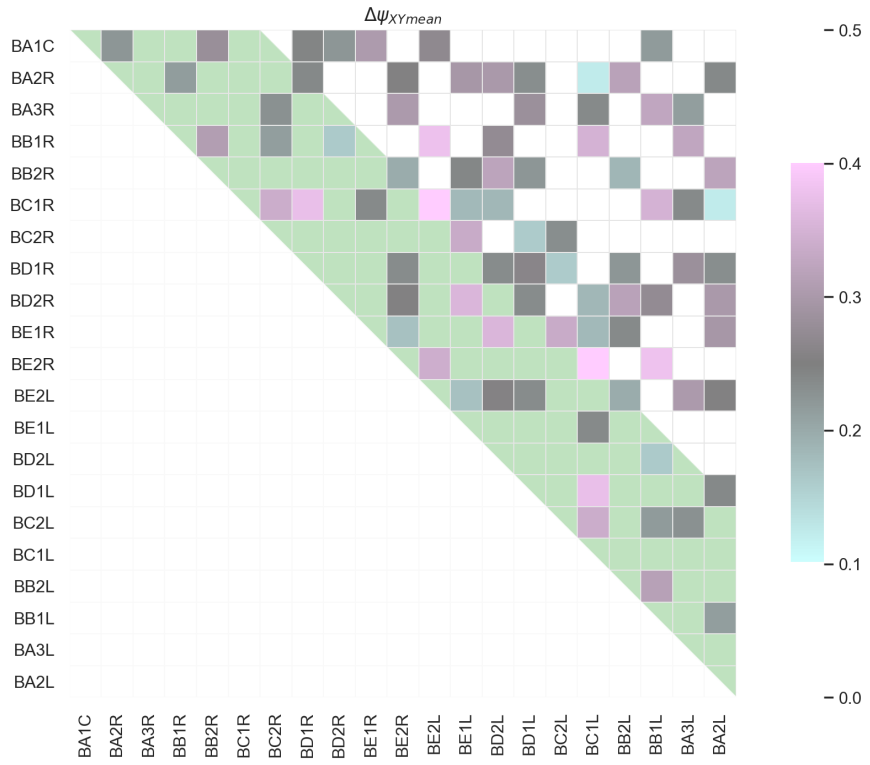

Figure 5.28: BPM pairs suitable for X/Y momentum measurement.

and seeds used.

Invariants

Using above momenta, CS invariants were calculated for a simulation with clean IOTA lattice. The goal is to estimate the (constant) invariant with least smear, and unlike for localized momentum measurement, now SVD methods can be used. Results (Fig. 5.30) indicate SVD to perform noticeably better at higher noise levels where its statistical use of all signals allows it to beat down noise, but worse at low noise levels where covariance information is most useful. Note that the comparison with localized B1R momenta/invariants is not completely fair - a proper value to calculate would be the weighted average of the 5 CS invariant measurements from the 5 reconstructed momenta. Proper error propagation would require multiple variable transformations to form the final generalized least squares covari-

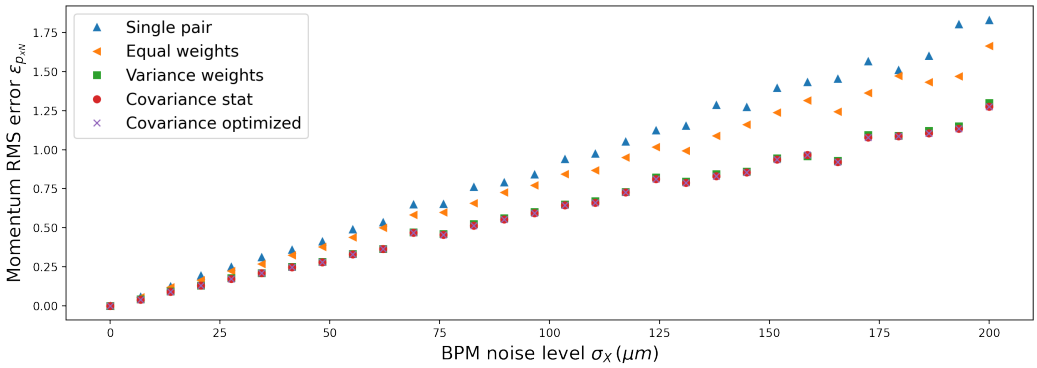

Figure 5.29: Momentum recovery error of various algorithms.

ance matrix, but this level of sophistication was found unnecessary and variance weighting used instead.

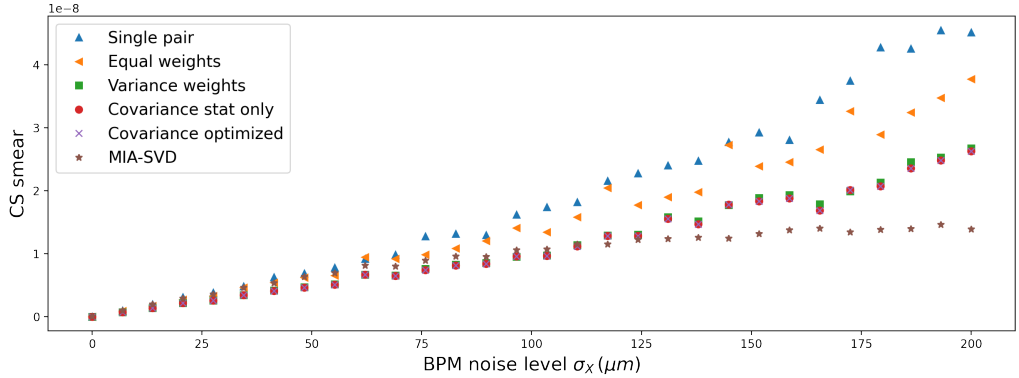

Figure 5.30: CS smear for linear motion with BPM noise.

Invariants of centroid motion

Invariant recovery from centroid motion requires fitting of the decoherence envelopes (Eq. 4.15). A sample fit of a well decoupled QI signal is shown in Fig. 5.31, with good agreement between model and fitted envelope parameters for the strong vertical signal, and marginally worse fit for the weak horizontal one. Note how Hilbert transform is used to obtain an approximation of the signal envelope. It can also be used to find instantaneous frequency,

albeit with poor resolution. Another method, reversed cumulative maximum value scan, was also explored but had larger systematics and was not suitable for coupled signals. Recovered phase space is shown in Fig. 5.32.

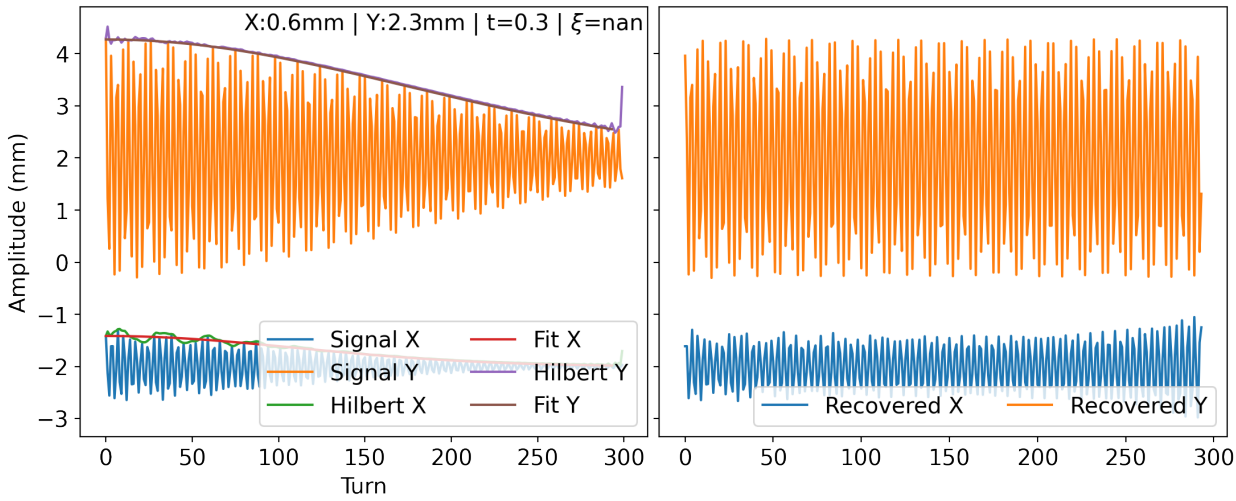

Figure 5.31: Envelope fit of vertical QI kick signal with split tunes.

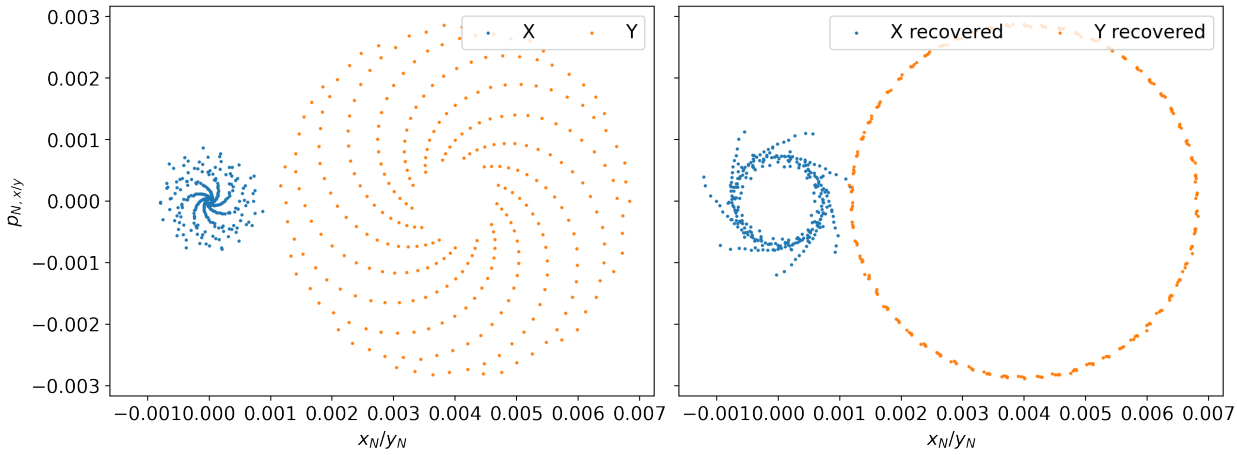

Figure 5.32: Phase space for split tune signal before (left) and after (right) envelope compensation.

As seen above, nonlinear coupling is a significant effect for some kicks - this situation is shown in Fig 5.33. Since coupling in not considered in the decoherence envelopes, signal beating can cause slight issues when fitting. In literature, several approaches for unmixing linearly coupled motion have been proposed based on spectral [119] or model independent

methods like SVD and ICA [100]. They were not suitable for strongly nonlinear motion, performing poorly in simulations. Moreover, as long as envelope fitting is unbiased, unmixing is unnecessary - the main quantity of interest, the invariant, already accounts for the coupling (while the betatron modes are obscured). Results of invariant reconstruction on clean signal are shown in Fig. 5.34. A scan of invariant jitter as function of strength κ produces a minimum precisely in location expected from the potential, confirming good invariant recovery.

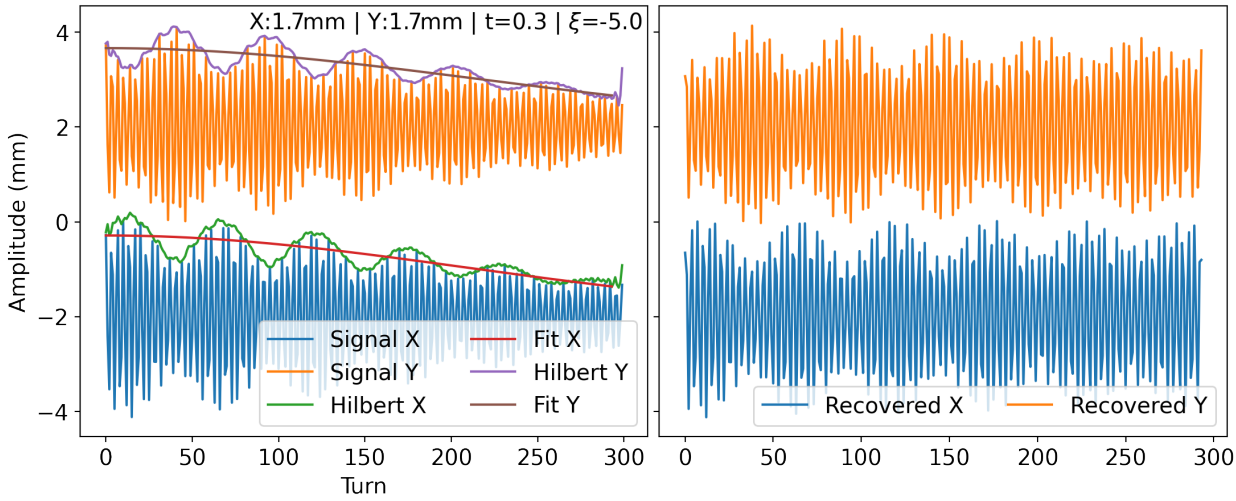

Figure 5.33: Envelope fit of diagonal QI kick signal with significant nonlinear coupling.

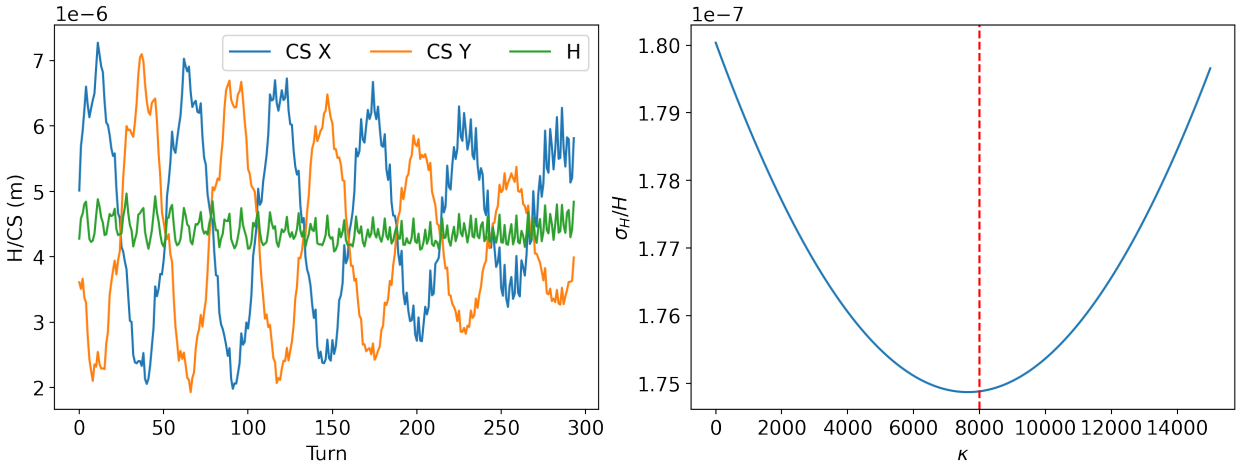

Figure 5.34: Recovered invariants and scan of nonlinear strength parameter for diagonal QI kick. Courant-Snyder (CS) amplitude decrease due to decreasing coupling oscillations, not decoherence.

Parameter	Design value	Experimental value
Energy	150MeV	96.4 ± 1 MeV
Chromaticity corrected x/y	0/0	$\sim 0/+1$
Chromaticity uncorrected x/y	-9.5/-8	$\sim -5/-7.5$ (X chroma source unknown)
Energy spread	8.7e-5	$\sim$ 2.3e-4 @1mA
Bunch length	11cm	~ 25 cm @1mA
Emittance x/y	12nm/12nm	60nm/60nm @1mA - 80nm/80nm @2mA

Table 5.2: Key run 2 experimental parameter deviations.

5.8 Experimental predictions

To conclude this chapter, key simulations are redone with the beam parameters observed during run 2 and applicable for most of the collected data. These were listed in Table 3.1, and key ones are summarized in Table 5.2 below. As will be seen in the next chapter, the overall situation is that collection parameters were degraded from design values due to low energy, resulting IBS, and poorly understood chromaticity. Together, these reduced the resolution and sensitivity of the measurements. Note that the unidentified chromaticity is modeled as if it was corrected to those values by sextupoles. This is a convenient simulation approach but does not properly simulate the actual sources, since those would have different optics and RDTs and thus will impact DA differently.

5.8.1 Dynamic aperture and tune footprint

Using 30 error seeds, probabilistic DA contours were computed (Fig. 5.35) and show same result as in previous sections - chromaticity and octupoles are almost equal in DA impact, with full correction tipping the scales. The difference between natural and -5 values is significantly smaller. The associated tune footprints are shown in Fig. 5.36, and are also similar to those seen previously. One interesting observation is occasional asymmetry of the branches, with almost complete loss of one or the other. Exploring the reasons for poor performance of these seeds would be an interesting study.

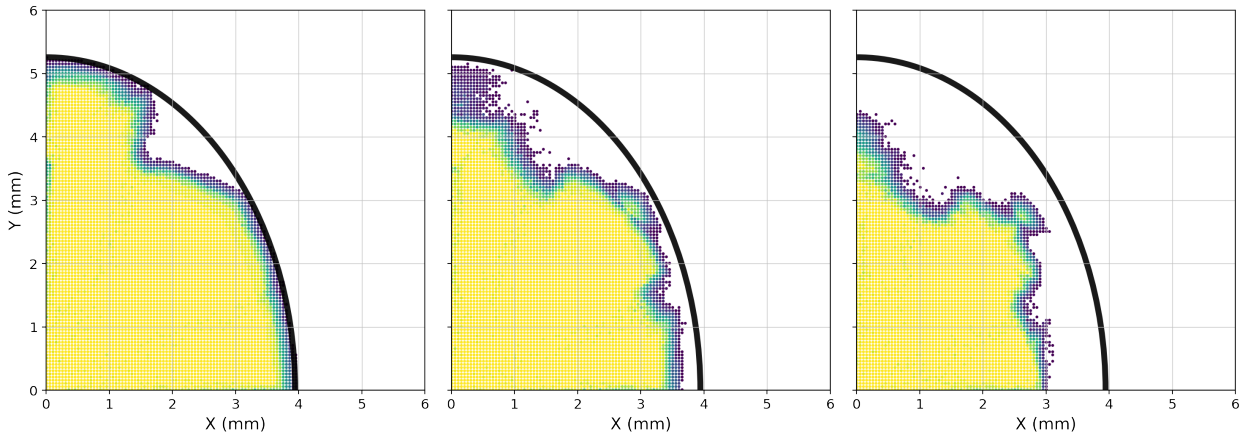

Figure 5.35: Dynamical aperture with fully corrected chromaticity (left), -5 (middle), and natural (right).

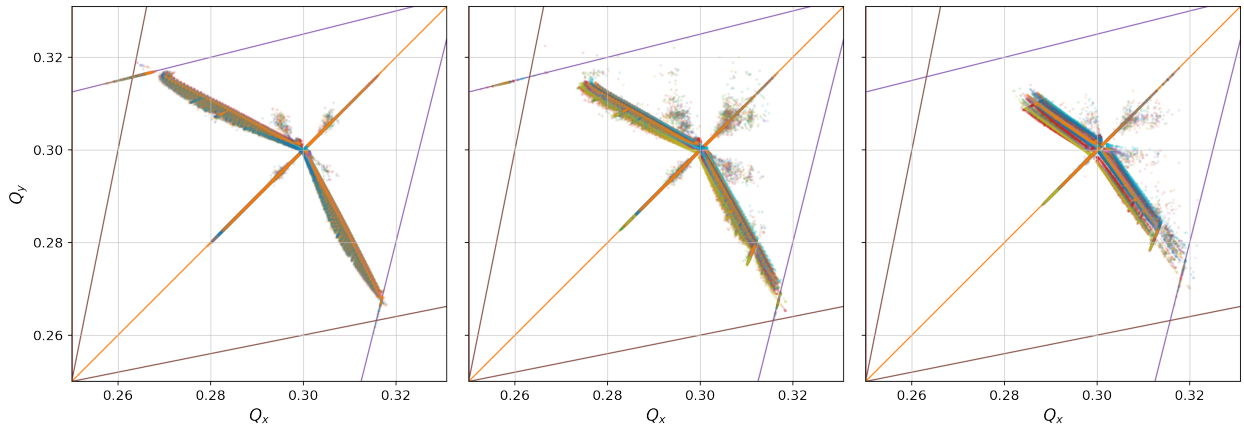

Figure 5.36: Tune footprint with seeds for fully corrected chromaticity (left), -5 (middle), and natural (right).

5.8.2 Bunched beam signals

Bunch centroids, NAFF tunes (blue), and beam intensity (cyan) from kicks along x, y, and diagonal planes are shown in figures 5.37, 5.38, and 5.39 respectively. QI strength of $t = 0.25$ ($\approx$ 1.0A), no errors, and fully corrected chromaticity were used for lattice configuration. As expected, increased beam emittance leads to faster signal decoherence, with usable data in only the first 200 turns. There is also a clearer slow beam loss behavior near dynamic aperture edge, since beam halo now extends significantly further. For tune measurements, NAFF performance without noise is stable at $>$ 50 turns. Consistent with previous simulations

there is little tune peak shift at low amplitudes, but for high V amplitudes an apparent resonance capture is observed - signal decoherence is reduced, and NAFF is locked onto a peculiar 0.263/0.318 tune line that did not change for two kicks. By inspecting QI tune footprint produced by running the bunch data through the frequency analysis pipeline (Fig. 5.40), this tune recognized as the intersection of 5th and 6th order resonance lines in the upper left quadrant. Since few particles are captured there in FMA, experimentally complete loss of resonant particles is expected. An interesting observation is that FMA detuning predicts only a small beam fraction will be captured, and yet bunch motion is dominated by those particles, highlighting the potential issues and incorrect tune estimates when probing around such resonances.

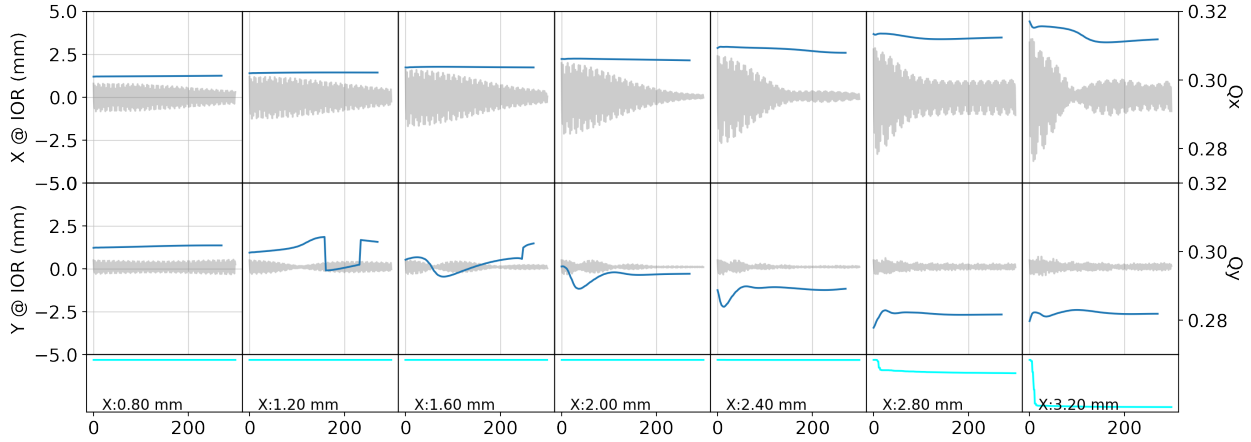

Figure 5.37: Signal prediction along H.

5.9 Summary

In this chapter, simulations of NIO systems and IOTA ring were performed. Theoretical maximum performance was determined, and impact of unavoidable implementation imperfections studied. Little to no benefit was found in using more than 15 magnets, validating the chosen insert design. Individual magnet length had no significant impact.

Effects of chromatic correction, magnet misalignment, and aggregate optics errors were

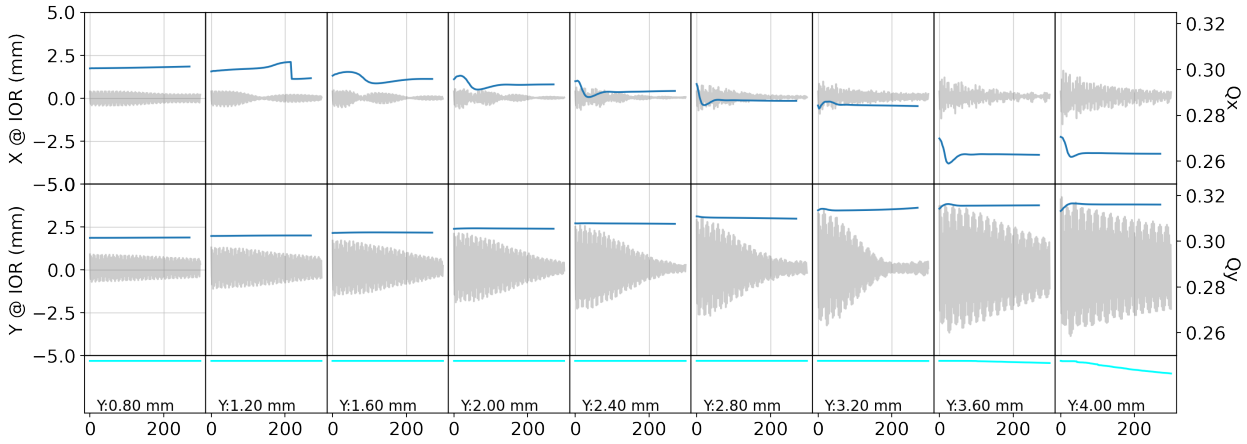

Figure 5.38: Signal prediction along V.

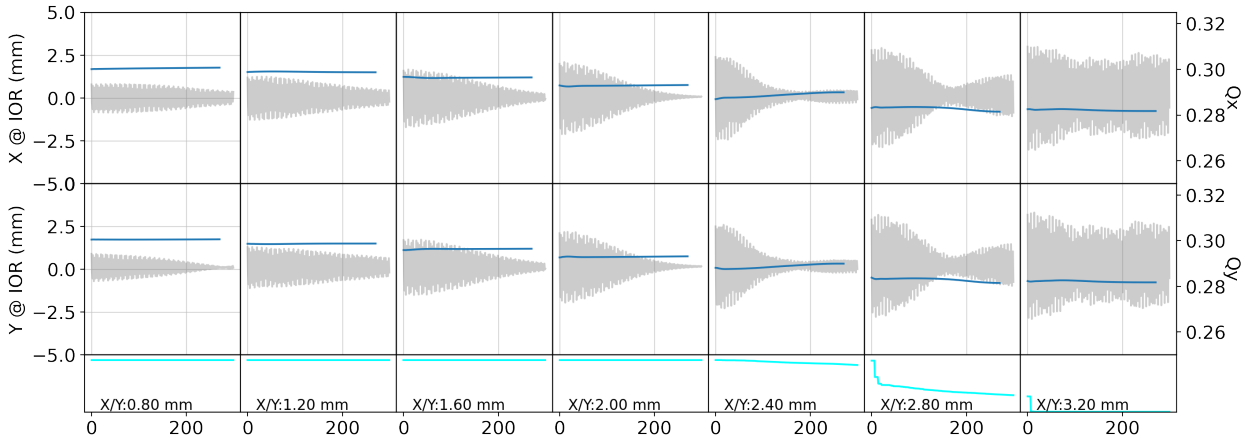

Figure 5.39: Signal prediction along equal kick line (diagonal).

checked. With strong chromaticity correction, sextupoles were found to dominate dynamic aperture while QI perturbations had a relatively low impact. At partial correction values, the trade-offs were comparable, with break-even point around $\xi = -5$. At natural chromaticity, QI performance scaling agreed with theoretical predictions and more integrable configurations had larger detuning. Large hardware errors, such as up to 400um transverse misalignments, did not decrease dynamic aperture to below 90%. Sensitivity to optics errors was found to be consistent with integrability conditions at natural chromaticity, but with full correction a complicated pattern with best results for equal tune errors was observed. Phase advance deviations of up to 0.005 were tolerable with little performance loss. Overall,

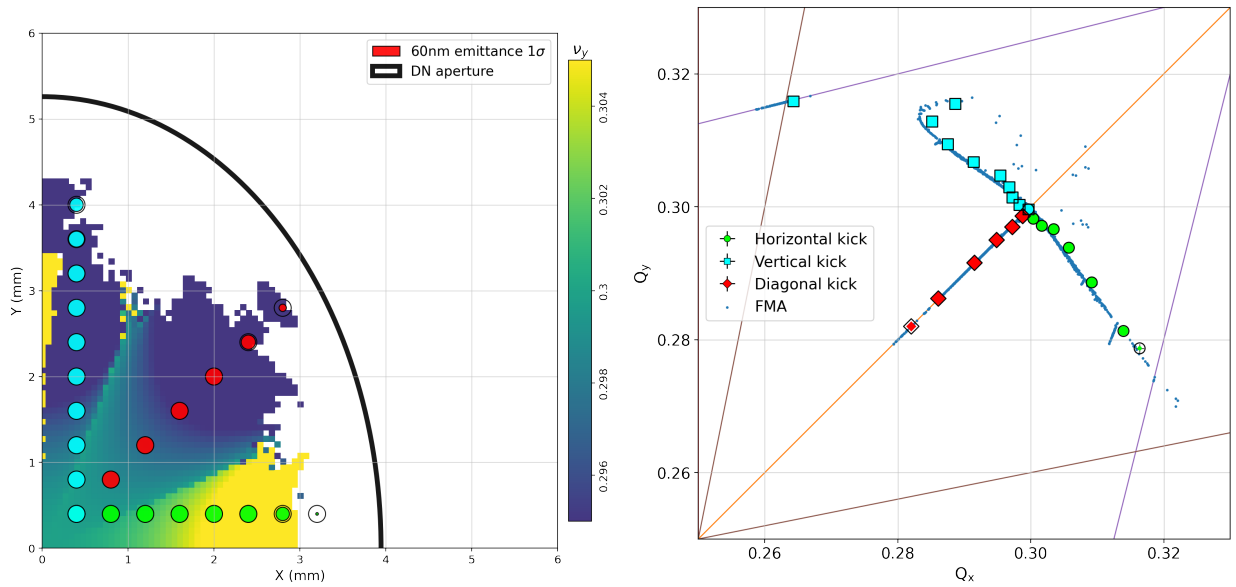

Figure 5.40: FMA of kicked experimental sized bunches. Left plot shows amplitude space with 1σ contours of initial positions, and right the corresponding tune analysis results.

QI system was demonstrated to have high resilience to optics and mechanical perturbations.

Bunch simulations exhibited a complicated interplay of oscillation coupling and decoherence that resulted in shift of tune measurements with number of turns. For well split tunes however, this shift was small relative to the detuning amount. Phase algorithm benchmarks indicated good performance of SVD and N-BPM methods when used with small groups of BPMs. Benefit of using systematic corrections was not clear, with simple variance weighting achieving nearly same performance. In terms of invariants, decoherence compensation should be sufficient to observe the integrability of QI system. For both tune and phase space, decoherence limited the algorithms to first few hundred turns, and should be optimized for more precise measurements.

Simulations using experimental parameters indicated dynamic aperture reduction to below physical one, especially with sextupoles. Within the aperture, sufficient signal will be available for high fidelity tune measurements until certain resonances are encountered. For high amplitude kicks, less than 150 turns of usable data will be available for phase space analysis.

CHAPTER 6

EXPERIMENTAL RESULTS

In this chapter, experimental results are presented. Section 6.1 gives an overview of ring commissioning and the performance of some subsystems. Commissioning and results for QI and DN inserts are discussed in sections 6.2 and 6.3 respectively, along with implications and possible improvements.

6.1 IOTA commissioning

Prior to starting NIO experiments, extensive work was done to commission the ring, especially during initial startup of run 1. During this period, I performed a variety of tasks - analyzing logger data to find magnet anomalies, designing and performing orbit bumps to scan aperture, calibrating BPM and SL systems, and others. These studies were extremely useful as a way of gaining control room experience. Unfortunately, most of collected data is unpublished and not publicly accessible [120]. A good overview of the timeline and difficulties encountered can be found in IOTA collaboration/retreat meeting presentations of runs 1 [121] and 2 [122, 123]. In this section experimental measurements of three subsystems with direct NIO impact as well as those of lattice optics are presented.

6.1.1 BPM system

Low noise and linearity of the BPM system are key to accurate nonlinear optics measurements, and major effort was placed on its commissioning. During run 1, system experienced major software and analog processing issues, with malfunctions, timeouts, and hangs. Upon testing the linearity and current dependence, significant issues were found. Of particular relevance for LOCO, above 1.2mA, linearity deviated by $> 5\%$, making long data acquisitions without reinjection impossible. A set of pre-amplifiers were installed for counteract this, but

those only became unsaturated at 0.2mA and had high noise floor. Run 1 BPM issues were traced to the poor choice of RF envelope tracking analog front-end, and required a complete overhaul to fix [124]. This remedial work was done in time for run 2, making all TBT data from run 1 significantly inferior. As such, all TBT data analyzed in this thesis is from run 2.

To quantify BPM performance, two types of studies were performed. In first, a corrector magnet was toggled on and off while beam was left to coast and decay, periodically changing closed orbit. Data collection in TBT mode was triggered every 20 seconds, and mean and noise calculated. Since no current dependent orbit shifts are expected in IOTA, any change of measured distance would indicate a current nonlinearity. Moreover, because of different beta functions and phases, the orbit distortion amplitude was different for each BPM. By analyzing if the response scaled as expected, position nonlinearity was estimated. Typical output from a BPM can be found in appendix Figure A.2, and linearity details in Figure A.3.

Unfortunately, in the final week of run 2 BPM system was damaged - a power wire was shorted across data pins of front-end FPGA board crate. This fried all boards and disabled our ability to control BPM attenuation and gain, resulting in a fallback solution at high fixed attenuation of 18dB. Noise measurements were (Fig. 6.1) redone, and indicated acceptable performance, but linearity data had to be inferred (Fig. A.4) since bump response checks were not repeated. The overall conclusions of BPM commissioning were:

- Linearity of 4% within $0 - 6\,\text{mm}$ of BPM center
- Linearity of $< 2\%$ for currents of $0.4\,\text{mA}$ to $3.0\,\text{mA}$
- RMS noise of $100\,\text{um}$ for 0.8mA beam current
- Smooth degradation of all parameters with current
- Poor calibration of special BPM A1C (it was removed from further analysis)

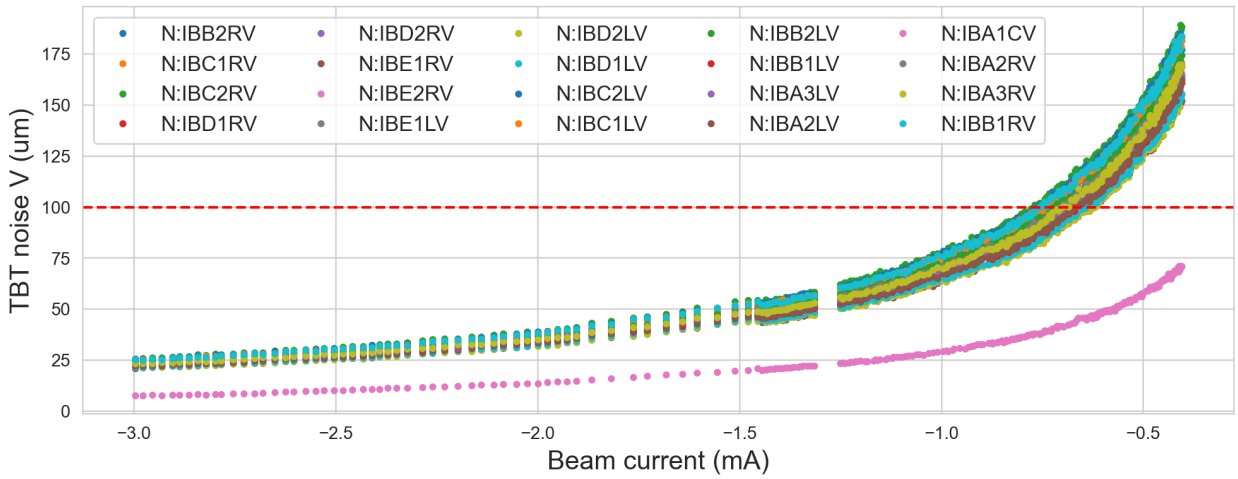

Figure 6.1: BPM TBT noise at high attenuation as a function of current.

6.1.2 Miscellaneous issues

Aperture

During run 1, it was noticed that physical aperture size does not match with the model predicted by DN magnet restriction. Based on localized bumps around the ring, DR region was found to contain a problem. Further examination showed the culprit to be a pipe of 1in diameter that was installed for a small undulator midway through the run. Attempts to shift it around were not successful, and disassembly after the run showed that the whole section was bowed into an arch shape. This defect reduced physical aperture, but since exact distortion could not be measured, it was hard to account for in the model. Estimates from linear lattice kicks were used as a proxy, but reproducibility was poor. The DR section was fixed in run 2.

Multibunch injection

While not designed to operate with multiple bunches, IOTA can inadvertently capture up to four buckets (since RF operates at 4th harmonic). This phenomenon was noticed by the fact that very strong kicks were not able to completely lose the beam, and then confirmed

with WCM. Extra bunches were problematic, since they broke single-bunch assumptions of BPM and other systems and introduced extra RF load/noise, while not being beneficial to the quality of collected data. For all experiments in run 2, linac energy was constantly tuned to avoid multiple injections as much as possible.

Kicker variability

Brief testing with repeated kicks at same voltage settings showed amplitude variability of 5% on the vertical kicker and 2% on the horizontal kicker. Given the good performance of BPM system in run 2, this was considered acceptable - amplitudes and actions were extracted directly from the TBT data of first few turns.

Noise in RF and power supplies

Comparison of data between nominally identical kicks during both run 1 and run 2 indicated large random variability beyond just amplitude, especially in terms of beam losses. At the same time, beam shape on SLMs was seen to oscillate between fully round and slightly squished profiles, suggesting time varying optics and coupling changes. Because the lattice was on difference resonance and with minimized coupling, beam profile was extremely sensitive to any tune movement/split. The practical impact of this variability was that depending on kick timing, σ_x and σ_y were different and so was the decoherence and beam loss profile.

Sources of noise were searched using high frequency live and low frequency historical logger data. For example, spectrum of beam current readout is given in Fig. 6.2, and shows a number of harmonics from power supply switching frequency at 720Hz, and other unexplained peaks.

Several quadrupoles were also found to oscillate in current, which was traced to poor magnet connections. However, even after manual inspection of all elements, some beam oscillations persisted. In data presented below, this is usually the reason for disagreement of

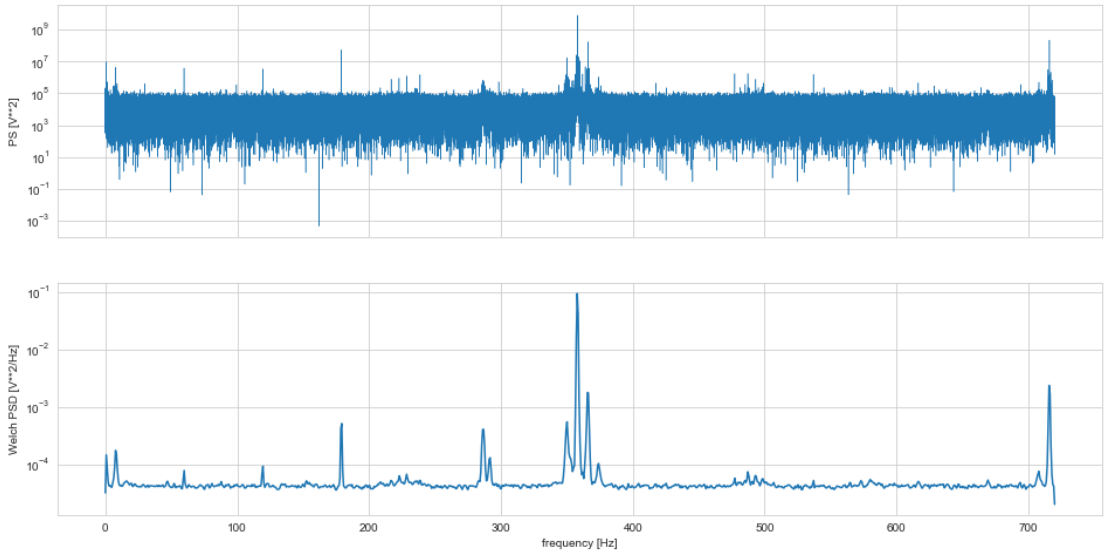

Figure 6.2: FFT and Welch PSD of main bend power supply readback N:IBEND, showing various noises in the ring.

duplicate measurements, and necessitated analyzing each kick independently.

6.1.3 Lattice

In both runs 1 and 2 IOTA was used at 100MeV energy, below the original 150MeV design goal. This was driven by several considerations - time requirements to commission 150MeV (during run 2), the need for a transformer tap switch in bending dipole power supply to enable sufficient current, and preferences of other experiments. This had a significant detrimental effect on NIO studies. As mentioned previously, all benchmarks and simulations were performed at the new lower energy.

Optics from LOCO

Multiple rounds of LOCO were performed by A. Romanov with 6dsim tool to fit and adjust the lattice. Unfortunately, it was difficult to convert LOCO results into quantitative error estimates, since the error metric of the fit, χ^2, was dominated by systematics and stopped decreasing after several LOCO iterations. However, fitted parameters can still be interpreted

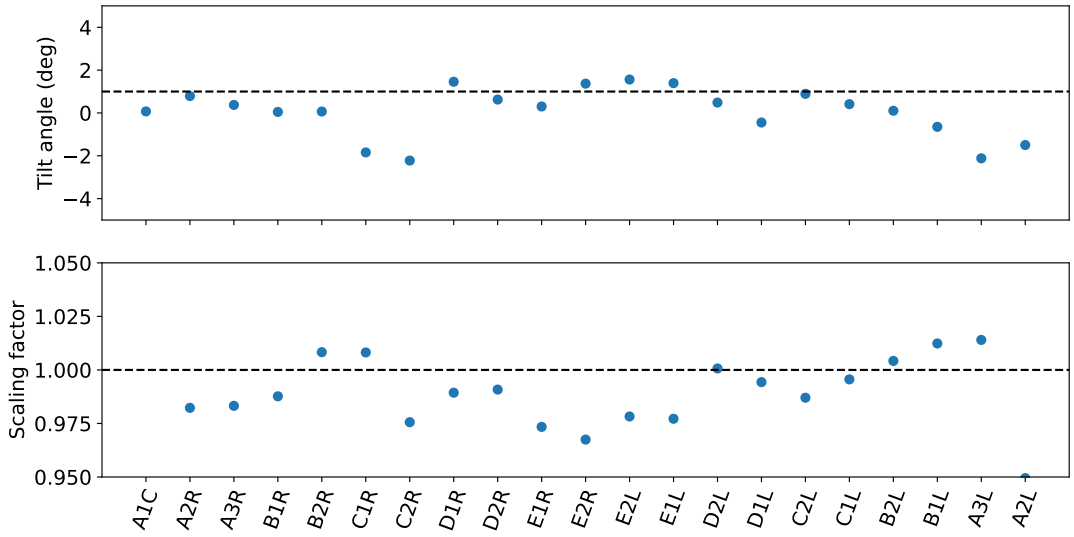

Figure 6.3: Calibrations and tilts of electrostatic BPMs based on LOCO fit.

Parameter	Error estimate
β in drift	$< 2\%$
β-beat	$< 5\%$
η in drift	$< 1\,\mathrm{cm}$
Phase error in ring	0.002
Phase error in drift	0.001
Coupling $\lvert C^- \rvert$	< 0.001

Table 6.1: LOCO-based optics errors.

as relative weights, and used as calibration for devices like BPMs. The results for '8.6.1.4' lattice, the final version used in run 2, are given in Fig. 6.3. A note about lattice versions - while no major changes were physically done to the ring during run 2, the presence of systematics stimulated slight redistribution of dipole and dipole field corrector strengths and hence angles in lattice files, creating many similar versions. For all simulations and experimental analysis, 8.6.1.4 lattice was used.

Rough tuning estimates by A. Romanov based on his extensive personal experience with IOTA and other rings are summarized in table 6.1.

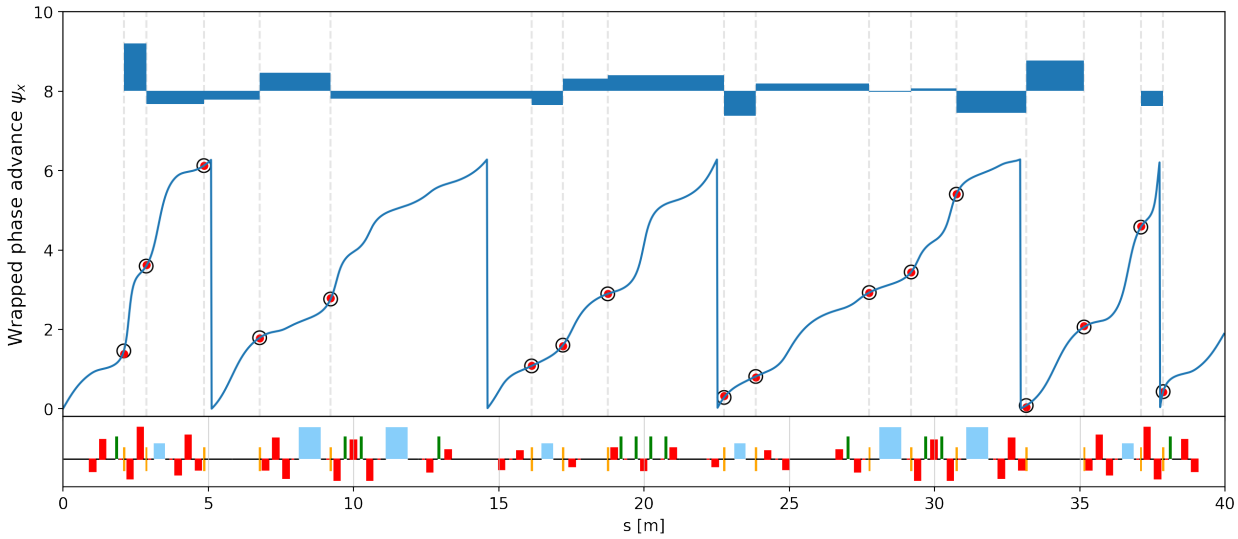

Figure 6.4: Wrapped phase of calibration kick vs model. Top bar graph denotes amount of phase lost or gained between BPMs vs expected.

Overall, these results meet QI requirements but were a factor of 2-3 off from those required by DN magnet. Nonetheless, this was a significant achievement of many months of work, and placed IOTA in the ballpark of optics accuracy of latest generation production machines [125].

Optics from TBT

An independent method of optics measurement is with TBT data. Using formulas of section 4.1.3, calibration kicks were analyzed with three algorithms - beta from amplitude, beta from MIA, and 3-BPM beta from phase (via NAFF, Fig 6.4). In all cases, data was preprocessed as with regular kicks, bad BPMs removed, and then algorithm output fitted to the model.

Results for a representative kick (Fig. 6.5) show amplitude method to have significant systematics due to noise and calibrations, while both SVD and NAFF produce good results, the latter performing somewhat more consistently. However, beta beat from SVD also suffers from several anomalies with deviations of above 10%. These anomalies were systematic between many kicks and are associated with only a few BPMs. The exact reasons are not

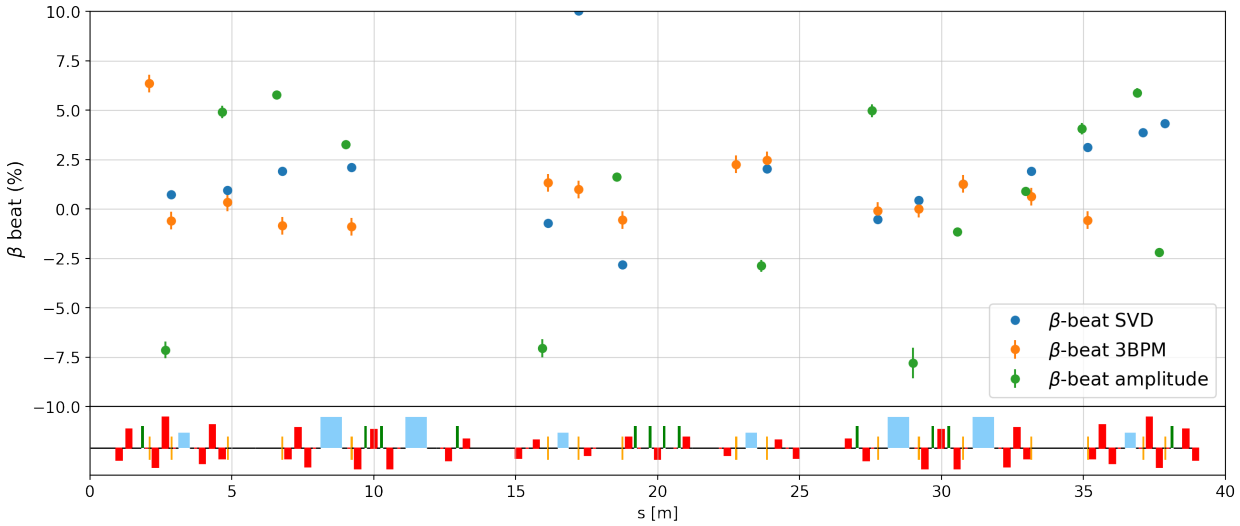

Figure 6.5: Estimates of beta-beat with three different methods. Some amplitude method point are beyond axis limits.

clear - one correlation was high level of noise, but it cleanly separated out in SVD, and preprocessed data appeared no different from other BPMs.

Since calibration kicks were performed at each reinjection (see section 6.2.3), a continuous lattice accuracy measurement was possible. Results of several hundred kicks are shown in Fig 6.6. As with single kick analysis, MIA and amplitude values have outliers which cause rms beta-beat to be higher. All methods agree on the trends however, with regions near 8AM and 11:30AM experiencing changes in rms errors. Those were times when significant lattice perturbations were introduced on purpose. Admittedly, the 8AM decrease in beta-beat is unexpected - one possible reason is that split tunes allowed for better NAFF convergence, and also that this particular perturbation counteracted some of the inherent optics errors. The raw phase error data follows same trends as beta-beat, consistent with theory. For both beta and phase beat, y-plane results (not shown) had same trends, but reconstruction accuracy was higher.

Overall, TBT data provided sufficiently accurate measure of phases and betas to claim achieving design optics with $< 3-5\%$ beta-beat in x, $2-4\%$ beta-beat in y, and phase advance errors inside/outside the insert of $< 0.002-0.003$. Total ring tune was monitored

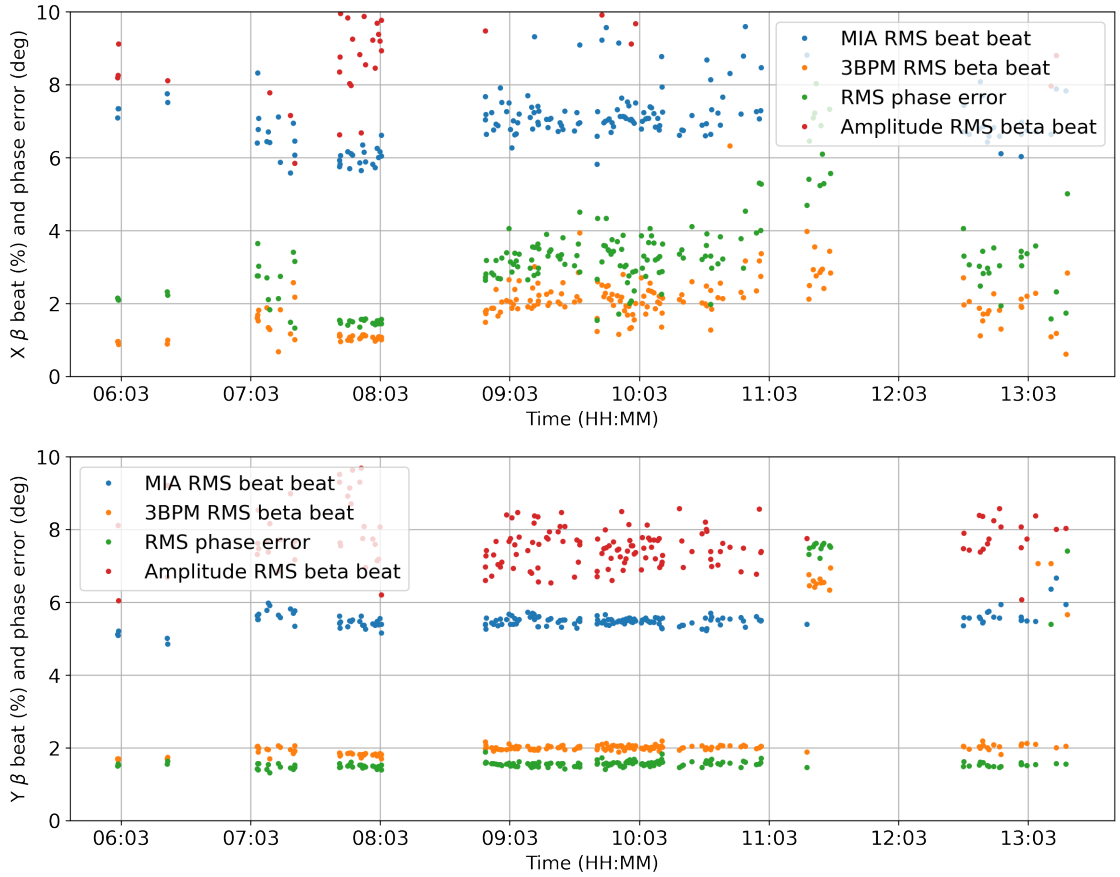

Figure 6.6: Beta-beat and phase variation in X and Y over several same-day collection runs.

independently during operations and kept to minimum tune distance $\Delta Q \leq 0.001$ (Fig. 6.7), as determined by residual coupling.

Emittance and bunch length

A separate experiment performed during run 2 looked into beam length and emittance in both coupled (but split tune) and uncoupled regimes [126]. Since NIO lattice was used with minor perturbations, their results are directly applicable to NIO experiments. Significant IBS effects were observed with a strong current dependence of beam size and length, with unexplained systematic deviations from model in terms of beam lifetime and emittance. Measured emittance estimates ranged from 55-75nm (unnormalized rms) for beam current

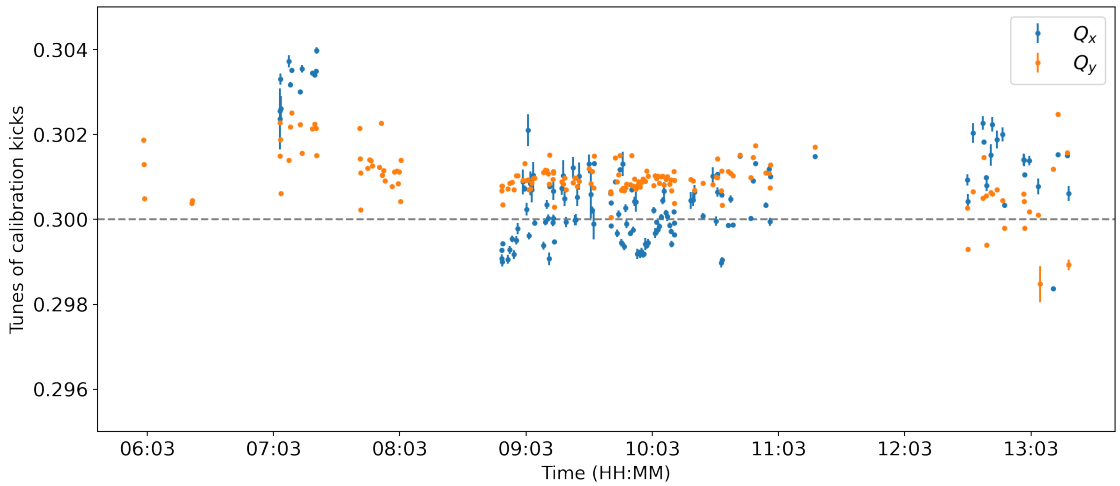

Figure 6.7: Tunes of calibration kicks over several same-day collection runs showing consistently small tune distance.

of 1mA to 90-105nm at 3mA. They also observed slight deviations from the ideal Gaussian bunch profile both transversely and longitudinally, with suspected large halos. Impact on experimental tune and centroid measurements was expected to be minor. In benchmark simulations, 3σ cutoffs were used to better model the tails.

Chromaticity

Only four sextupoles were installed in time for run 2, the SC1 and SC2 families. Because of control board limitations, they could not be turned off easily or reliably, and only accepted current commands of 0.1A and up. All 'no sextupole' measurements were done with this low sextupole setting. To determine and correct chromaticity, tunes were slightly split so as to better separate the peaks, and RF cavity offset scanned. Low sextupole data (Fig. 6.8) exhibited the expected chromatic recoherence at synchrotron tune in the vertical plane. However, horizontal plane only had a small recoherence - this suggested a nonlinear detuning at least an order of magnitude larger than that of the vertical plane. From simulations of 5.6, a smaller horizontal signal and eventual disappearance was expected, but at amplitudes $> 3mm$ IOR, not $1mm * \sqrt{0.65/2.05} = 0.55mm$. No specific nonlinearity source could be

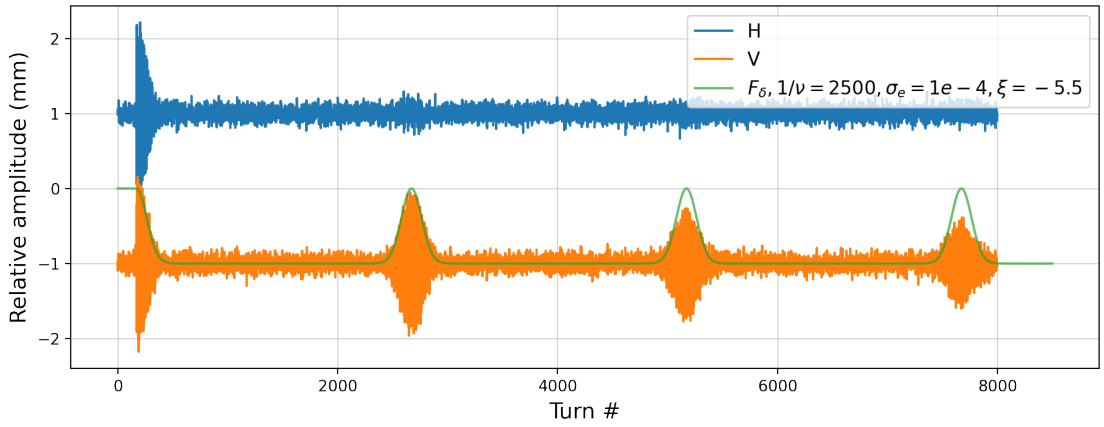

Figure 6.8: TBT signal at B2R after H/V ping with low sextupole settings.

identified.

The observed chromaticity values, $\xi_x = -5.2$ and $\xi_y = -6.8$ (calculated with model momentum compaction factor), also did not agree with the model in horizontal plane. The expected values, given sextupole currents, were $\xi_x = -9.2$ and $\xi_y = -7.2$.

Based on manual tuning, near full correction settings were found at SC1=0.902A, SC2=-1.004A (again in large disagreement with model). A detailed scan a few weeks later (Fig. 6.9) showed this to still be a near perfect correction in x, but a slight overcorrection in y. No significant second order chromaticity was observed, consistent with the model. It was speculated that closed orbit changes combined with small ring effects resulted in chromaticity drift that depended on specific fine tuning adjustments used during a shift. No source for the unexpected low x chromaticity was found, with suspicion of complex interplay of dipole edge field correctors and internal dipole field roll-off that was not accounted for in the model. In benchmark simulations, the intended low/full correction chromaticity was used as if produced by sextupoles, and long-term drift ignored.

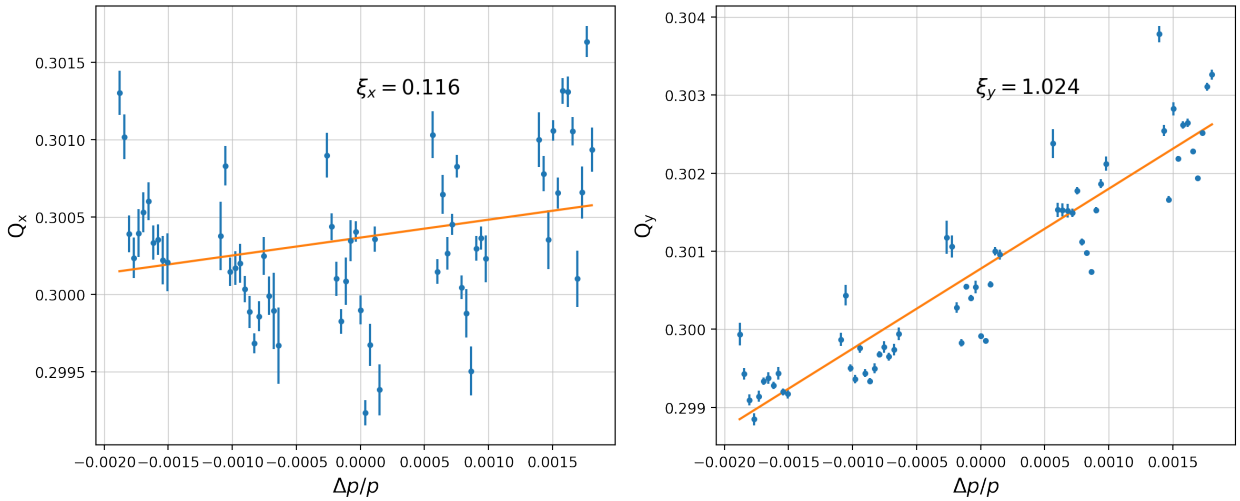

Figure 6.9: X/Y linear chromaticity measurement at full correction settings. Signal oscillations and gaps are due to BPM timing system fluctuations that were caused by RF frequency changes.

6.1.4 Summary

IOTA ring linear and nonlinear optics has been commissioned. Based on LOCO data, beta-beat was estimated at $< 5\%$, and all BPMs calibration corrections were below 2.5% (gain) and 2 degrees (tilt). Analysis of TBT calibration kicks over a typical 8 hour shift found poor performance of amplitude-based methods, reasonable SVD performance, and good 3/N-NPM method performance. Using latter two methods, beta-beat was found to be $3-5\%$ in x, in agreement with LOCO, and about $2-4\%$ in y. Phase advance errors inside and outside the nonlinear inserts were below 0.003, with overall tune split kept under 0.001 as limited by residual linear coupling.

Emittance measurements with SLMs showed strong IBS current dependence, with round beam emittances approaching 100nm at a high current of 3mA, and operational values of 50-60nm at 1mA. Corresponding bunch length increase to 25-30cm was also observed. These observations imply faster centroid decoherence than expected from simulations, and thus worse analysis algorithm accuracy.

Chromaticity measurements were performed and found an anomalously low horizontal

value with near perfect agreement on vertical one. No definitive source could be identified. Current setpoints were found for full chromaticity correction and $\sim -5/-5$ partial equal chromaticity.

Overall, IOTA ring has not met energy design specifications, but achieved optics accuracy sufficient for QI insert. DN design specifications were not fully met. Large emittance values caused by IBS were observed, worsening data quality for both inserts.

6.2 QI measurements

6.2.1 Commissioning

Quasi-integrable insert design, hardware testing, assembly, and initial alignment procedures were presented in 3.3. This section discussed the issues encountered in verifying expected QI mechanical alignment.

Laser tracker alignment

Upon being moved into the ring, insert was measured with a laser tracker by Fermilab alignment crew (Fig. 6.10a). The raw output of this process was retroreflector position as it was moved along magnet edge. Using about 10 points, 5 per face, a cylinder was then fitted and 3D magnet orientation determined. Tracker precision at such close distances is $\sim$ .001in.

Processed output showed that longitudinal alignment (Fig. A.11) was good, with a global shift of 0.5 mm and magnet-to-magnet spacing error of ~ 100 um. Transversely, considerable vertical sag of octupole axis was observed (Fig. A.10), which however was expected since the support columns for the girder were hand-aligned. Based on tracker data, far end was raised closer to central axis, with the expectation that fine tuning will be done via orbit steering. Once the average trend is subtracted with a linear fit, remaining spread is quite

(a) Laser tracker measurement

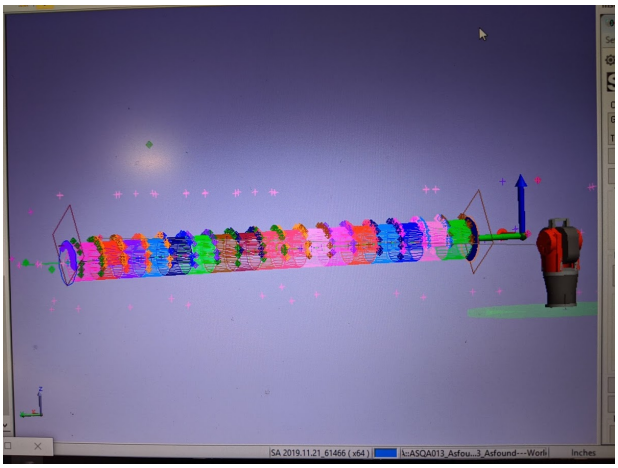

(b) Laser tracker cylinder fit of octupoles

Figure 6.10: Alignment of QI insert.

Parameter	Value
σ_s (relative)	133 um
σ_s offset	-500 um
σ_x rms	180 um
σ_y rms	202 um

Table 6.2: Summary of QI mechanical alignment survey results.

small and matches the design specifications. Results are summarized in Table 6.2. Overall, tracker data indicated that all alignment goals were achieved, with exceptional longitudinal and acceptable transverse accuracy.

Given the good laser tracker results, beam-based alignment was expected to also go well. However, measurements indicated issues. Some, like reversed polarity, were quickly mitigated, whereas others persisted. Namely, octupole #5 was exhibiting a recurring short to ground that could be fixed temporarily by jiggling the wires, and some octupoles had very large transverse offsets - up to 0.8mm. To verify that beam-based method performed reasonably, orbit in the drift was shifted by 1mm and measurement repeated. Results are shown in the appendix Figure A.13a, and were consistent, showing 1mm offset change.

Based on this data, it was decided to attempt to move the magnets. A number of tunnel

Parameter	Value
σ_s (relative)	200 um
σ_s offset	N/A
σ_x rms	300 um
σ_y rms	300 um

Table 6.3: QI alignment accuracy estimates after attempted fixes.

accesses were made, but it was discovered that some of the required shifts were so large that they would collide with the vacuum pipe. Moreover, after modifications the beam-based positions did not shift as much as expected, casting suspicion on beam-based algorithm and further confusing the situation.

Several electrical sanity checks were done (section A.4.4), including measuring resistance, inductance, and currents, with no outliers detected. Another hypothesis was potential permanent magnetization after high current rotating coil test. However, magnetic probe measurements showed residual magnetization of around 10G, and running a magnet at 10A did not cause any significant permanent residual fields.

Above results suggested that whatever the problem was, it was small electrically (at most a couple coils) and should not have a drastic effect on the beam, in contradiction with beam-based measurements. However, beam-based measurements are a tried and true method and performed well on other magnets. Given the time pressures, a final decision was made to restore the octupole alignment to optically guided one *in situ* (Fig. A.12b), guaranteeing a reasonable mechanical alignment level as defined by pinholes, and proceed with experiments. The corresponding final beam-based alignment results are shown in Fig. A.13b.

For simulation purposes, errors in excess of those observed mechanically were set for the full ring simulations, and are shown in Table 6.3.

Configuration	Nominal value	Perturbation values
Nominal	N/A	N/A
Phase advance drift x	0.30	+0.01, +0.03, +0.1
Phase advance drift y	0.30	+0.01, +0.03, -0.03, +0.1
Phase advance ring x	5.00	+0.01, +0.03, +0.1
Phase advance ring y	5.00	+0.01
β_x^*	0.9m (middle)	+10cm along s
β_y^*	0.9m (middle)	+10cm along s
Current	1.0A	0.5A, 0.75A, 1.25A , -1.0A
Current profile phase	mu=0.3	0.31, 0.29
Flat current profile	N/A	0.25A, 0.35A
Dispersion x	0.0	+10cm
Low sextupoles	0/0	-5/-7 @ 0.75A, 1.00A, 1.25A, -1.00A

Table 6.4: Summary of QI configurations explored during run 2.

6.2.2 Collected data summary

QI insert was studied in both runs 1 and 2, with various minor changes in lattice and hardware performance within each run. The results presented here were mostly collected during run 2 due to better BPM performance. The QI kick data spans approximately 3000 kicks in 40 configurations, some of which are summarized in table 6.4. Majority of this data was collected in the last two weeks prior to COVID-19 mandated shutdown, and has comparable lattice and equipment state (except accidental damage of BPM system).

An important choice was made to collect all perturbation data at the fully corrected chromaticity settings. The justification being that because full correction required significantly less sextupole strength than expected, almost at $-5/-5$ model levels, the resulting DA size would be acceptable. With full chromaticity correction, more turns could be observed, clawing back some of the lost analysis accuracy. Data at other chromaticities was collected only for nominal settings and a couple select perturbations.

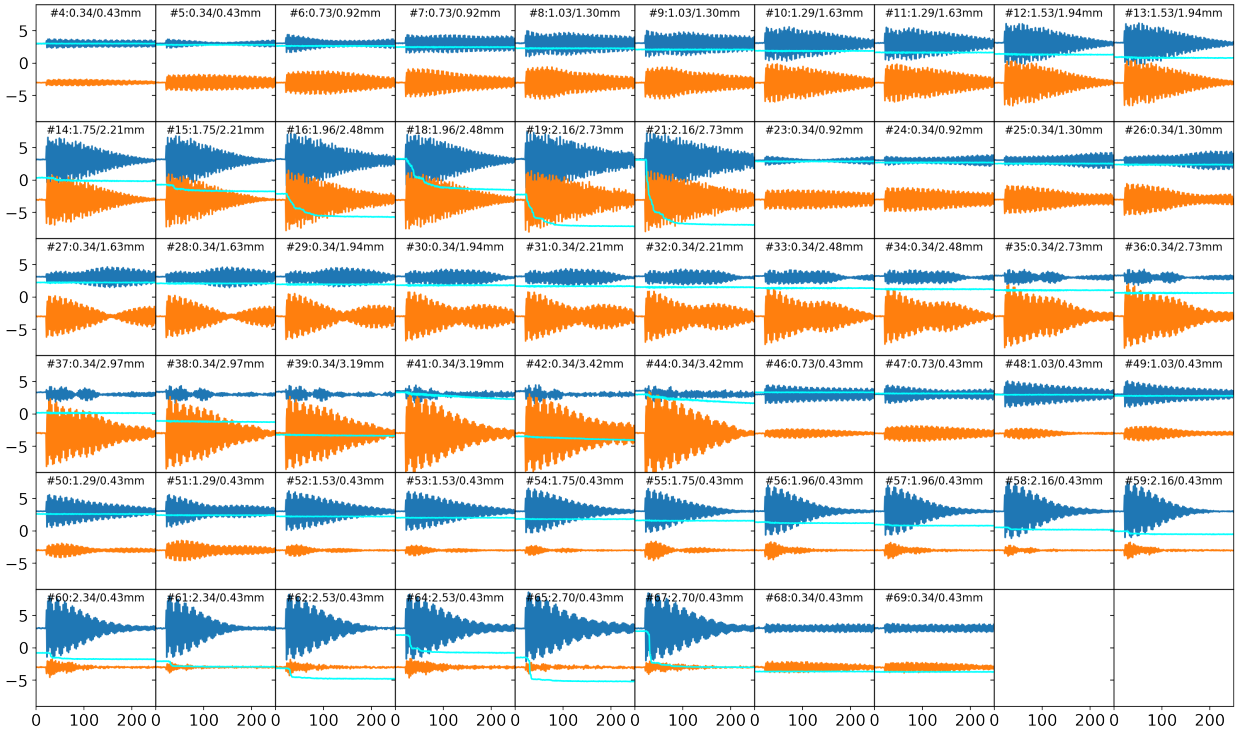

Figure 6.11: H (orange), V (blue), and Sum (cyan) data for all kicks of a typical kick sequence. Sum signal scale is approximately 150k to 0, with 20k corresponding to near complete beam loss. H/V signals in mm at B1L BPM. Text labels denote kick number and max amplitude (H/V) at IOR.

6.2.3 Data exploration

It is infeasible to present the analysis of all the sets individually, so in this section a single representative set is analyzed and discussed. Specifically, a QI system at 1.0A central current with perturbed $+0.003Q_{x,ring}$ optics was selected. The raw data is shown in Figure 6.11 and serves as a great demonstration of the complex beam dynamics being captured by free betatron oscillations - various decoherence lengths, couplings, beam losses, and many other factors change with amplitude to produce the final centroid signals. Of particular interest is the beam loss behavior at strong kicks, with distinct fast and slow jumps.

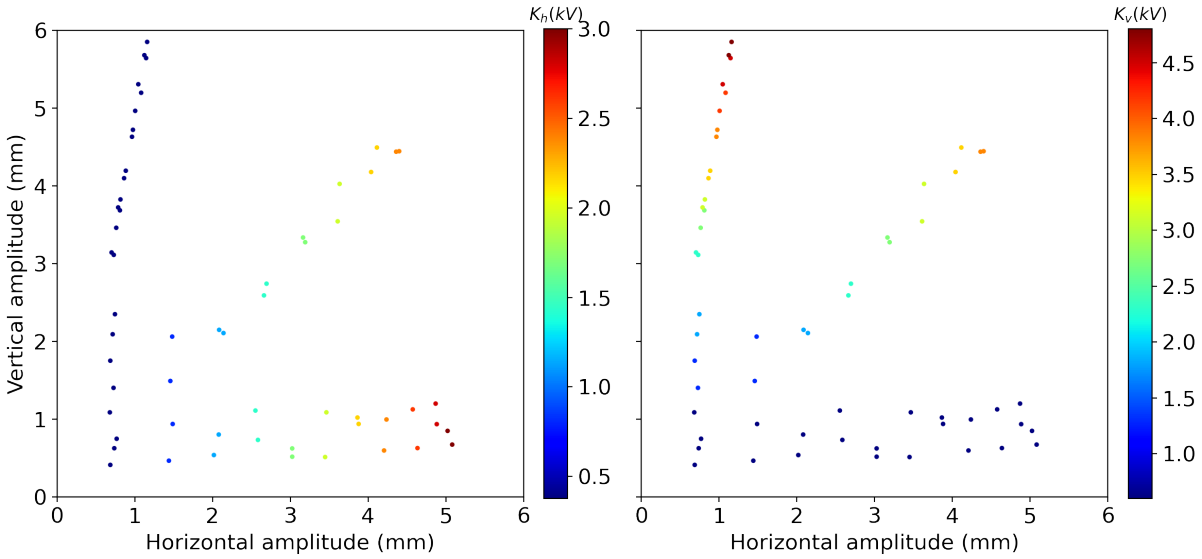

Figure 6.12: Amplitude of kicks as derived from top 2 measurements in first 20 turns.

Amplitudes

As one of sanity checks during preprocessing, kick amplitudes (Fig. 6.12) are plotted and compared to the requested kick strength. In this particular case, no suspicious outliers are obvious, but some sequences have multiple kick failures or timing issues. Deflection of vertical amplitude line at higher amplitudes is consistent with simulations, and occurs due to very fast kick signal coupling into horizontal plane. A comparison of amplitudes at symmetric locations (Figure 6.13) was another check used to detect major issues. In this case, some deviation for diagonal kicks was observed but other signals matched, indicating acceptable optics.

Tunes

Before applying NAFF a visual inspection of the FFT spectra is performed so as to better adjust the analysis hyperparameters. It is especially important to intelligently pick the region of interest so at to maximize the number of turns and yet not let the dominant kick completely

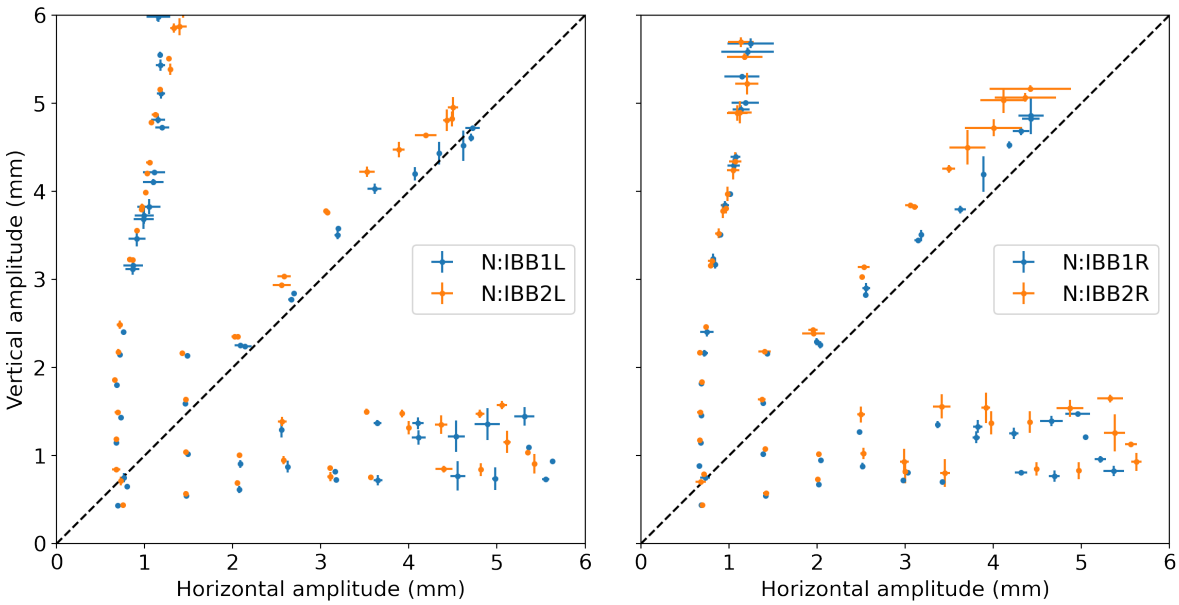

Figure 6.13: Comparison of kick amplitudes between nominally identical optical locations.

mask the weaker signal. In Fig. 6.14, FFT power spectrum is plotted for a few data ranges with and without windowing. Consistent with discussion of chapter 4, windowing helped to suppress sidelobes and distinguish the nearby peaks at the cost of broadening overall shape.

For bulk analysis, selection of appropriate span and window is handled automatically based on heuristics, signal to noise, and amplitude ratio threshold in both planes, with tuning knobs and limits set manually. This helps to minimize spurious signals that can confuse the algorithm. The results of applying ROI heuristic are shown in Fig. 6.15.

As a small aside, the case presented in Fig. 6.14 is quite challenging even for NAFF because of a combination of small number of turns and very close tunes (but they are truly distinct and not on the difference resonance). While it is a good scenario to test code against, in practice this does not matter - peak detuning at high amplitudes is what determines system performance. To avoid any confusion (unreasonably large error bars, etc.), in most tune footprints the small amplitude points are masked until they are sufficiently resolved to ensure consistent NAFF performance. The exception to this are of course the small amplitude calibration kicks, which determine the linear starting point.

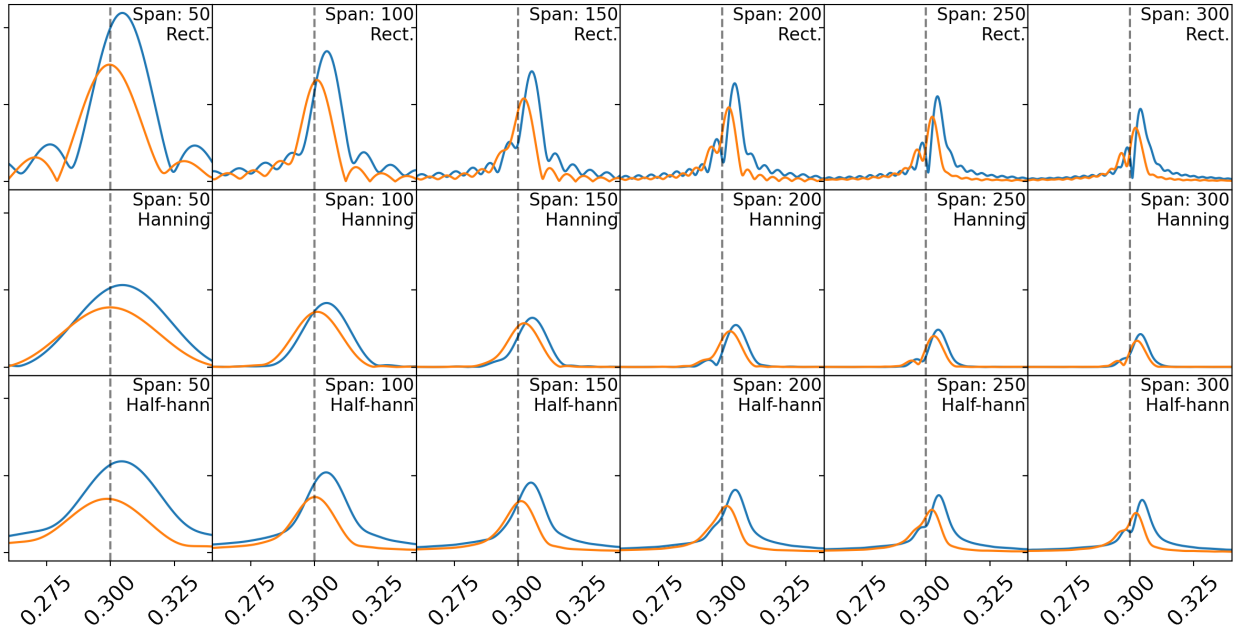

Figure 6.14: Various FFT windows and spans applied to challenging experimental kick data.

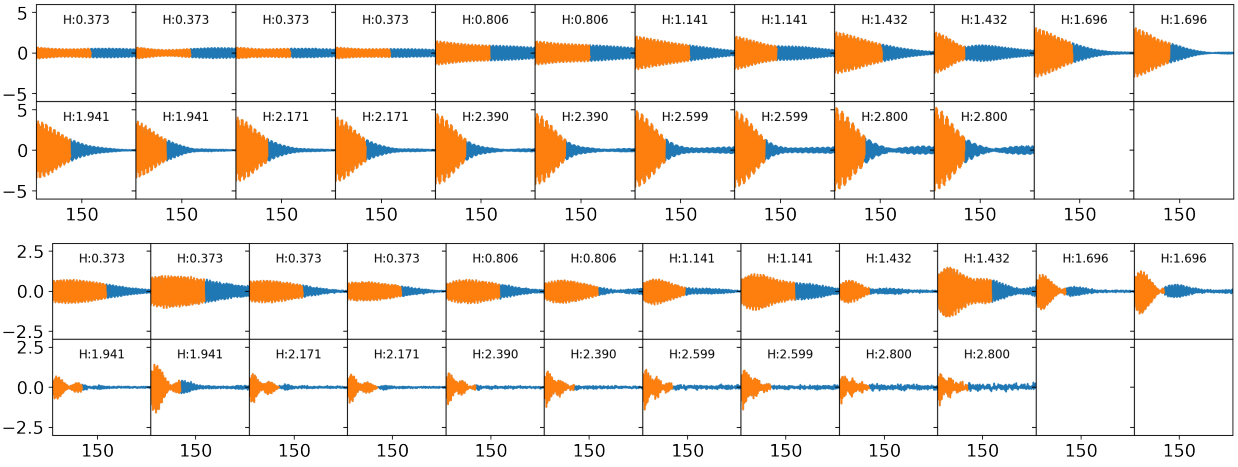

Figure 6.15: Region of interest selection for increasing horizontal kick strength. Top plot is horizontal signal, bottom plot vertical, y-axis units in mm.

After suitable ROI is identified applying NAFF to each kick gives a more refined tune measurement. These can be fitted as functions of action (from amplitude and optics model) to determine amplitude detuning terms, or drawn as a tune footprint (FMA) as in Fig. 6.16.

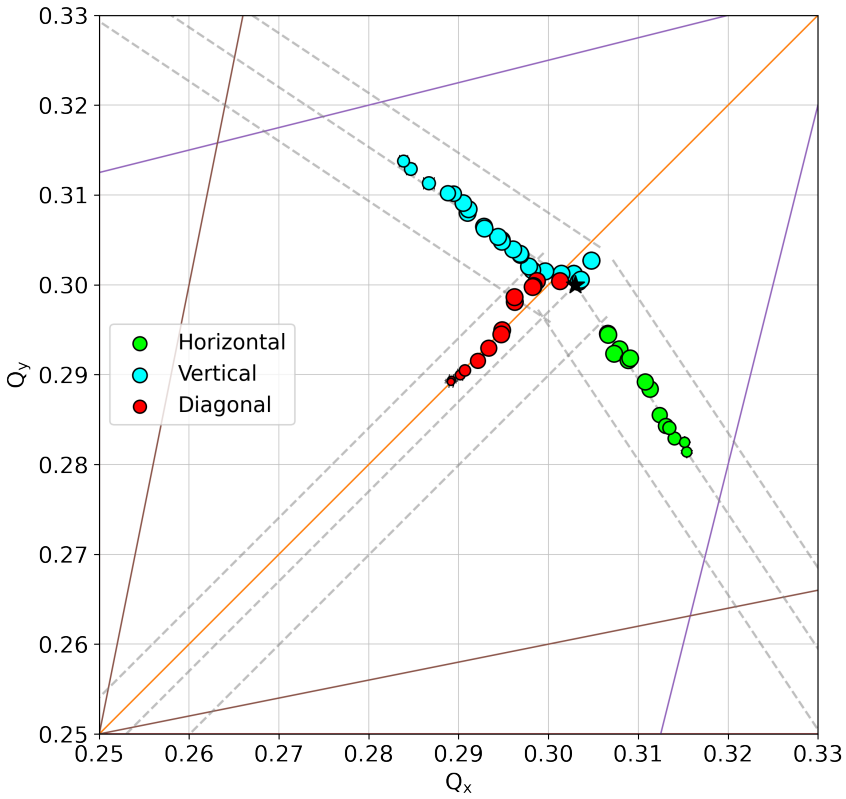

Figure 6.16: QI FMA for +0.003 phase advance error in the ring. Marker size, if less than standard, indicates that beam loss has occurred. Error bars are present but too small to be seen behind the markers. Dotted gray lines are hints for expected tune location regions, used in the peak selection and clustering algorithm.

Phase space

A process similar to that of section 5.7.2 was applied to the diagonal kicks at maximum amplitude without beam losses or suspicious signals. To ensure unbiased fitting, envelope parameter optimization was performed in ensemble mode - error of fit was calculated on all BPMs simultaneously, with global physics parameters like action and detuning same in all

envelopes. Only amplitudes and small offsets were specific to each BPM. Initially, the error sum contributions of each BPM were scaled by signal amplitude to normalize their impact on the fit, but better performance was achieved without this normalization, possibly due to better signal quality at higher amplitudes.

Decoherence fits and fitting residuals for kick at 1.3/1.6mm IOR amplitude are shown in Figures 6.17 and 6.18. As in simulations, an exchange of oscillation amplitudes is observed and is not accounted for by the envelopes. There is also another type of oscillation with very fast period of ~ 10 turns, the origin of which is unclear. Possibly, it is just an artifact of the Hilbert envelope detection - applying Savitzky–Golay smoothing removed this oscillation, but did not affect the final fit. An alternative explanation is a complex interaction of linear and nonlinear coupling at the particular tunes of this kick. Kicks at lower amplitudes had lower relative amplitude of these fine oscillations, but they were present in all diagonal kicks.

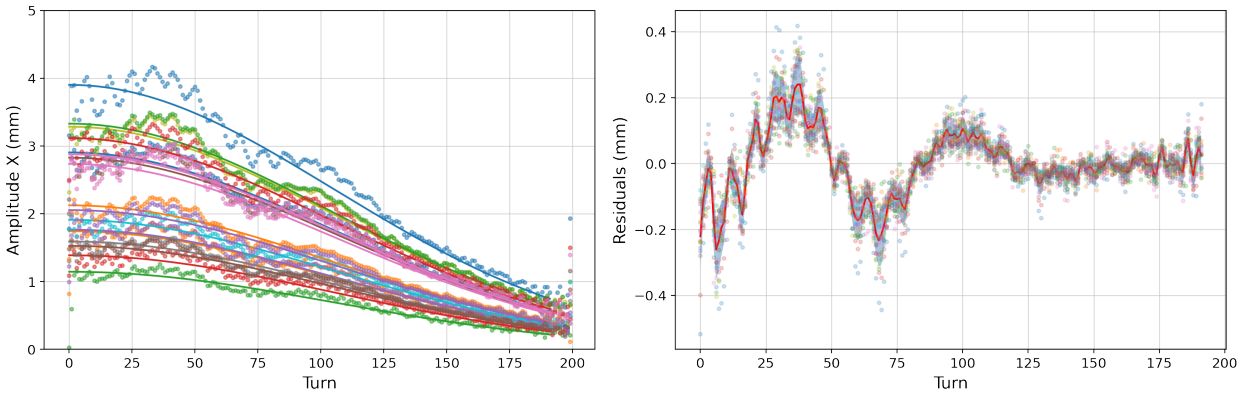

Figure 6.17: Decoherence fit in X plane for QI kick at $t = 0.25$ and 1.3/1.6mm IOR amplitude.

Application of phase space algorithms to recovered data showed good consistency between both simple pair and the more advanced methods. Results for same A2R-A3R-B1R-B2R-C1R region as in simulations are shown in Figure 6.19, with best pair being B1R-B2R and second best the B1R-A2R. Note how momentum from the second pair (in red) matches well in y/p_y plane and yet is stretched in p_x plane. Inspection of phase advances predicts that pair to have good recovery quality. The issues is instead in the low signal amplitude due

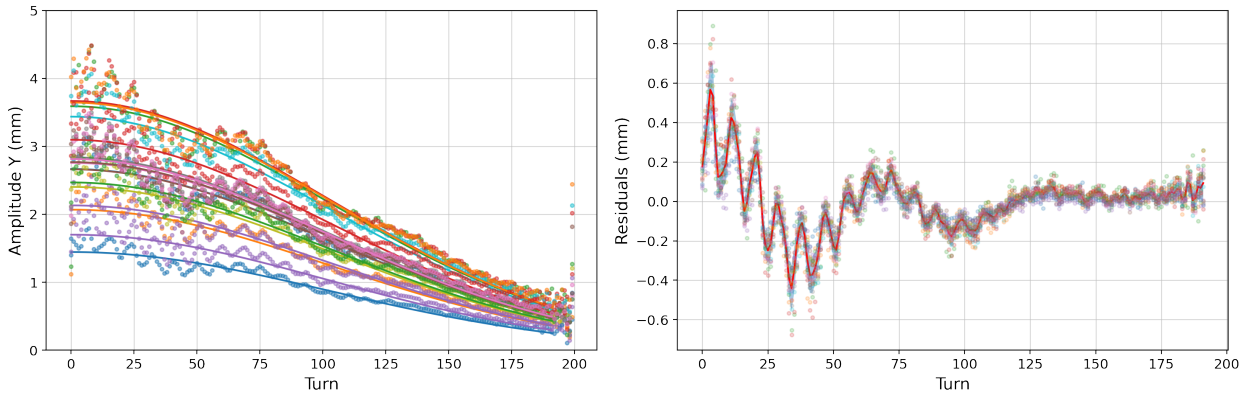

Figure 6.18: Decoherence fit in Y plane for QI kick at $t = 0.25$ and 1.3/1.6mm IOR amplitude.

to small β_x at A2R. The observed distortion suggests that optics model has a large relative discrepancy at this location, and hence a strong effect on the recovered momentum.

Inspection of other mostly-linear regions, such as E-straight (bottom long section of IOTA), showed similar situation - optics systematics dominated the quality of momentum recovery, with analytic-based weights not penalizing the marginal BPM pairs sufficiently. Addition of model systematics to the covariance did not improve performance, sometimes even degrading it. This suggested a mismatch of model and lattice, not surprising given other hints of model imperfections.

Based on above observations, algorithms were changed to more aggressively remove any pairs less than 20 degrees away from $n\pi$ and with too small signal amplitudes. Phase uncertainty estimates were revised, in some cases reaching 0.03. The resulting invariant computation is shown in Figure 6.20 for the B1R-B2R pair as the most reliable one.

There is decent agreement between expected and observed jitter minimum, but it should be noted that this is the ideal case of just a drift. Computations at other BPM locations yield minima $\pm 50\%$ of nominal value. The problem lies in significant impact of any systematics - broad minimum of the jitter function makes it susceptible to spurious signals, and only in cases of very good optics and clean data does the result fully agree with theory.

Overall, phase space recovery algorithms performed very well and produced consistent

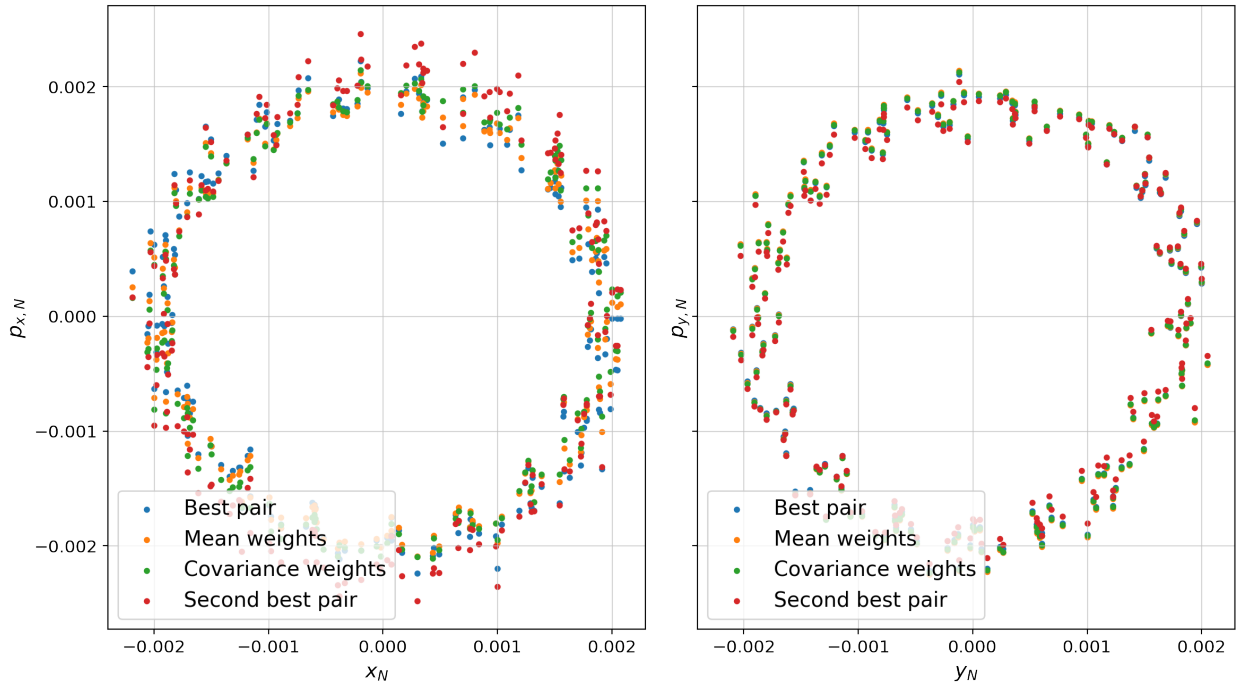

Figure 6.19: Phase space recovery with various methods for QI kick at $t = 0.25$ and 1.3/1.6mm IOR amplitude.

momentum data in terms of suppressing statistical noise. Performance of invariant recovery was dominated by experimental systematics, especially discrepancy between model or fitted optics and the actual experimental one. Using only known good regions that were well tuned, especially BR/BL drifts, allowed for reasonable but not perfect verification of integrability.

Resonances

During run 1, behavior of QI system near 1/4 resonance was explored - lattice was tuned to 0.255 and bunch kicked, pushing the tune over the resonance. Formation of four stable resonant islands was observed with lifetime of several minutes, as shown in Figure 6.21. The distance between islands and beam core would scale with the current in the octupoles. While no quantitative measurements were done, it was a very instructive experience to observe the interplay of nonlinear beam dynamics in practice. Hopefully future studies will aim to explore this regime, and even try inject into one of the islands.

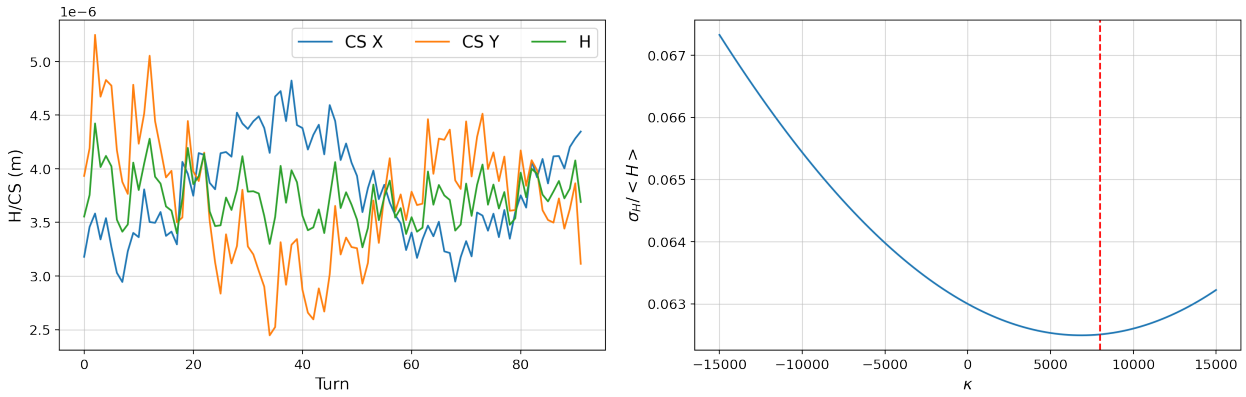

Figure 6.20: Invariants and their jitter for QI kick at $t = 0.25$ and 1.3/1.6mm IOR amplitude.

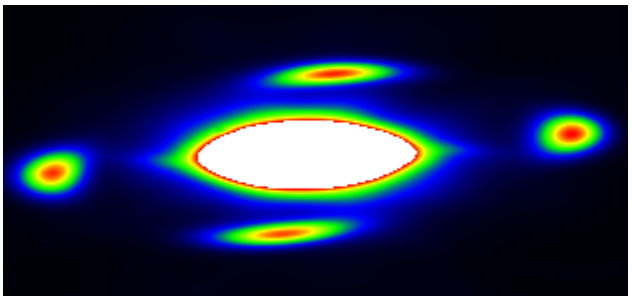

Figure 6.21: Resonant islands after kick near 1/4 resonance.

6.2.4 Results

Using similar procedure to that shown above and copious amounts of automation, QI datasets were analyzed to extract the tune and phase space figures of merit. For a quantitative comparison, a performance threshold is required - in simulations, the task was straightforward. In case of no IBS, or roughly same current, kicks could also be compared fairly. Unfortunately, this was not the case - time limitations forced data collection with only occasional reinjection, spanning a wide range of beam sizes and currents (3.0mA to 0.8mA). Combined with kicker variability, no two oscillations were alike, as can be seen in Fig. 6.22. The kicker variability problem was dealt with by fitting all BPM amplitudes by model optics to extract action estimate $\langle J \rangle$. Current effects however were difficult to compensate since exact distribution changes with current were not known. As such, the presented results do not make any quantitative absolute DA claims. Current dependence was compensated qualitatively - more

beam losses were permitted at higher current kicks, and if possible configuration comparison is done for kicks at same amplitude and similar current. If that is not possible, a threshold of 50% beam loss or any abnormal resonant signal was used.

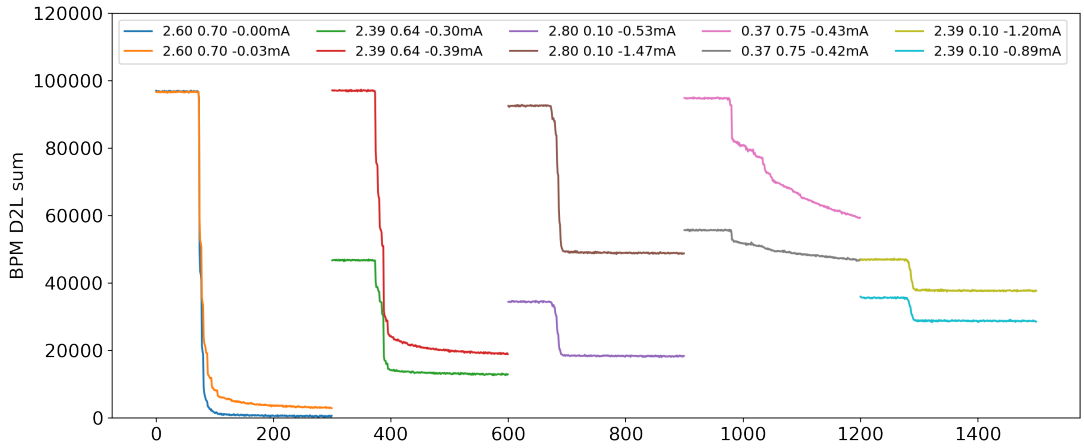

Figure 6.22: Beam current after pairs of identical kicks, showing variability of losses. Labels denote H kick, V kick, and remaining current respectively.

Nominal configuration

Nominal configuration was tested at several strengths. Simulations suggest that increasing QI current will produce slightly larger detuning for the corrected chromaticity configurations, whereas if octupole nonlinearity dominated, this would remain constant. Results of datasets at 0.75A, 1.0A, and 1.25A with full chromaticity correction are shown in Fig. 6.23 and 6.24. Fitting the detuning slopes along V line (i.e. J_y) yielded values in good agreement with detuning strength scaling (3/4, 4/4, 5/4 relative strength), but the absolute values of dQ_x/dJ_y were slightly lower than those expected from just octupoles (table 6.5), indicating additional sextupolar detuning contributions. Agreement for dQ_y/dJ_y was better but also not exact. Along V line, only the 1.0A and 1.25A sets reached the maximum detuning of 0.311. Keeping in mind the previously discussed caveat about kick variability, other kick

directions were also checked, and for both diagonal and horizontal directions 1.25A dataset had significantly larger maximum detuning. For the vertical arms, the equal results for 1.0A and 1.25A are likely due to the strong resonance and small available DA limit in that direction. Overall, QI system detuning behavior vs current was consistent with simulations, and a maximum tune spread of $\Delta Q_x/\Delta Q_y = 0.032/0.036 \pm 0.001$ was achieved.

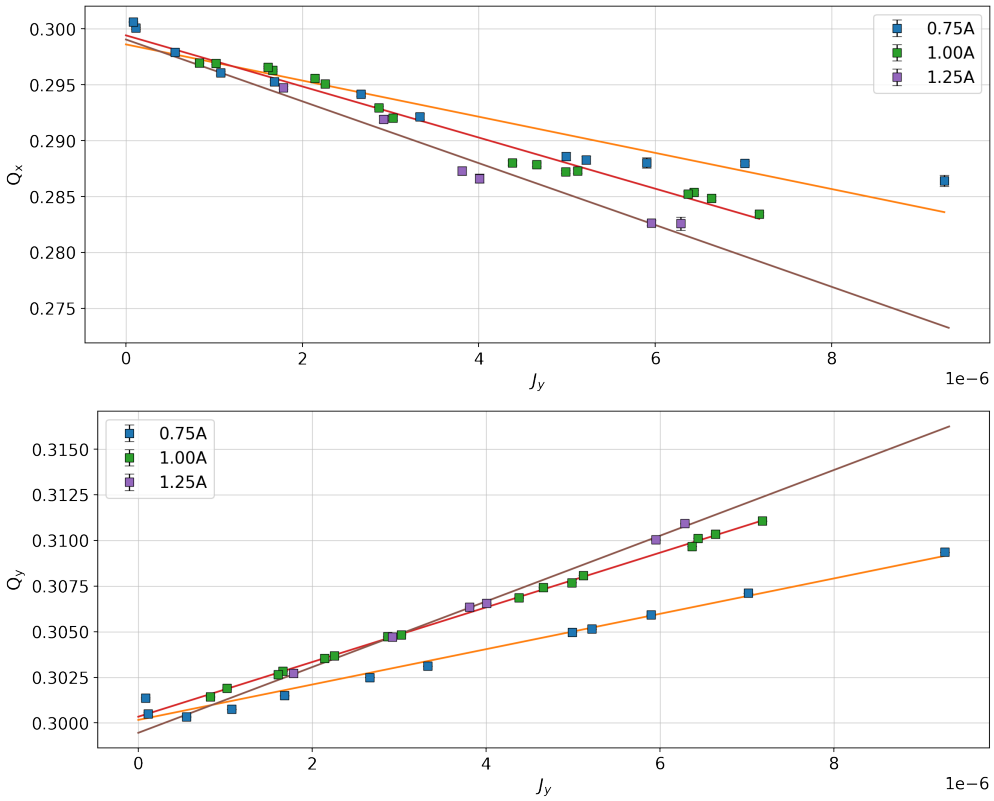

Figure 6.23: Detuning fit of three QI datasets with varying insert strengths.

t-strength	dQ_x/dJ_y theory	dQ_x/dJ_y exp.	dQ_y/dJ_y theory	dQ_y/dJ_y exp.
0.187 (0.75A)	-2255	-1996 ± 134	1127	1044 ± 44
0.250 (1.0A)	-3006	-2651 ± 188	1503	1505 ± 17
0.312 (1.25A)	-3758	-3657 ± 466	1879	1799 ± 31

Table 6.5: Quadratic detuning term measurement for various QI currents.

As mentioned in discussion of sextupoles effects, it is of interest to fit simulation FMA detuning data to check if the slope matches that expected from NIO + sextupole contri-

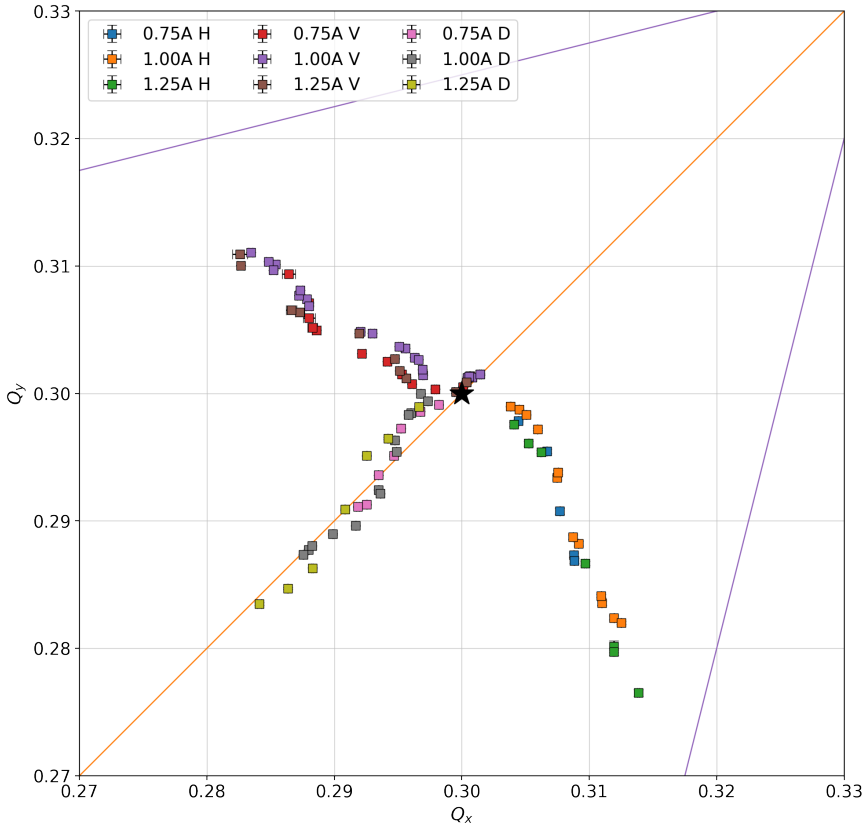

Figure 6.24: FMA of three nominal lattice QI datasets with varying insert strengths.

butions. Three simulation datasets at natural, -5, and 0 chromaticity were analyzed and plotted along with the data in Figure 6.25. From the linear best fit, best match for the data was located between -5 and 0, and not at the fully corrected detuning. This yet again confirms the anomalous chromaticity measurements, and also suggests that whatever the source is, it has lower detuning strength than an equivalent correction would at sextupole locations.

Perturbations

One of the best sampled perturbations (not for any particular reason) ended up being the phase advance in x, with 3 measurements outside and 3 inside the drift. The results for the +0.001, +0.003, +0.010 advance inside the drift are shown in Fig. 6.27. Working point shift

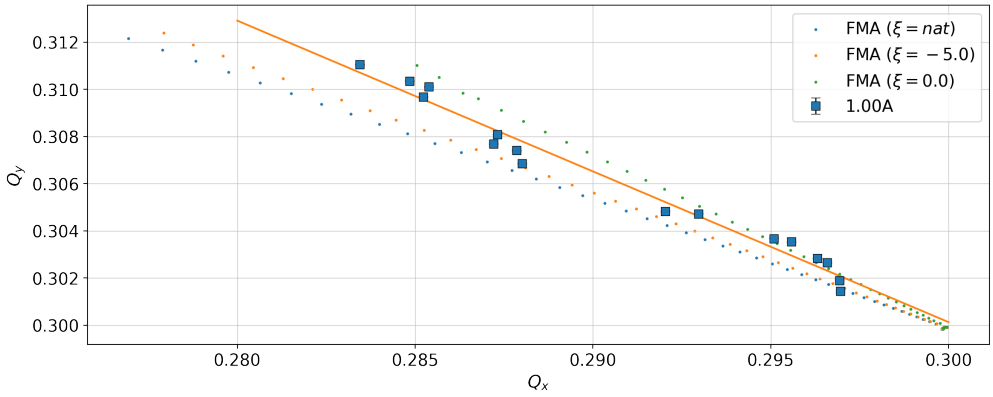

Figure 6.25: One branch of nominal 1.0A FMA along with three simulation datasets. Linear fit of experimental data indicates a mismatch with expected $\xi = 0$ line.

is evident in the changing fit y-intercept, meaning knobs were applied correctly. Note a small Q_y shift for the +0.010 perturbation, which suggests the knobs used were reaching their limit of linearity. In terms of detuning slopes, while one of +0.010 shift is slightly lower, consistent with expected theoretical decrease (1503 to 1411), no statistically significant differences were found for +0.003 and +0.001 measurements.

In terms of dynamic aperture, for the +0.010 case, all diagonal kicks beyond medium amplitudes (i.e. 1.94/2.08 H/V) exhibited large beam losses, and got excluded. This was not observed at +0.003 and +0.001 configurations. Inspection of simulation results hints at the answer - the frequency map degrades asymmetrically, with highest impact for the diagonal middle sector, where a deep inclusion separated part of the DA as an island. Overall, results show detuning and DA performance within the measurements uncertainty of the nominal configuration for up to +0.003 perturbations, with +0.010 causing a degradation of 15% along V line and nearly 30% along the diagonal. These are consistent with model.

Another interesting 'perturbation' was running the insert with a flat current distribution but same overall detuning as the QI configuration. FMA results initially indicated little if any performance degradation (Figure 6.28), which was surprising. However, closer signal inspection showed that beam survival was significantly lower if DCCT signal was considered several seconds after the kick instead of BPM sum signal. Corresponding resonant behavior

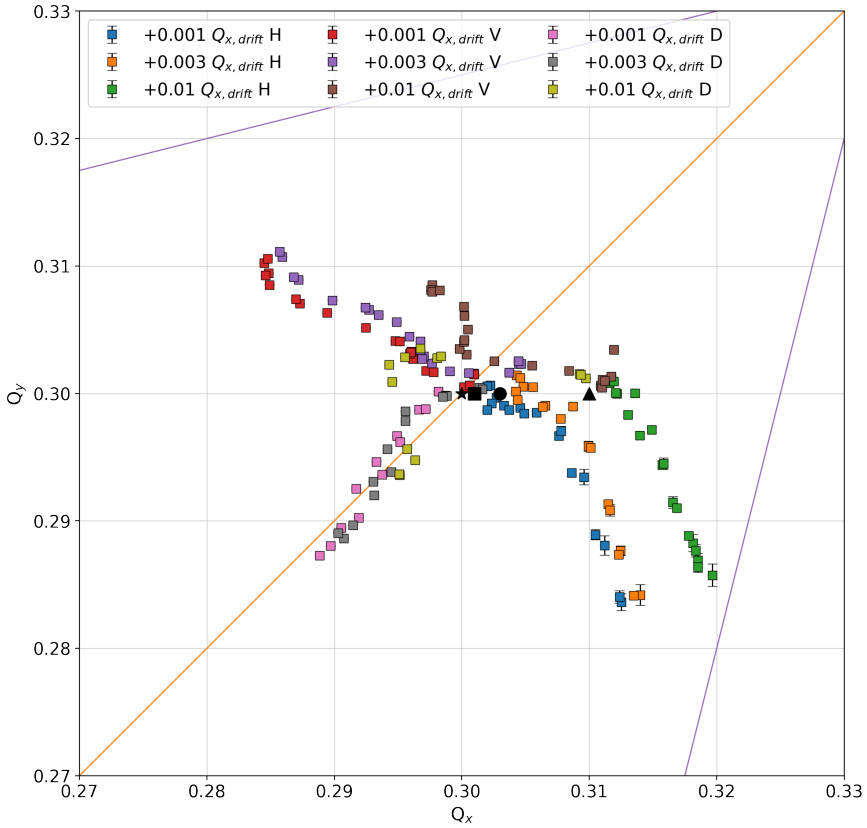

Figure 6.26: FMA of three QI@1.0A datasets with varying $\Delta Q_{x,drift}$.

was observed in TBT data, whereas no such signals were seen with QI current profile. This demonstrates how QI system is more beneficial in terms of nonlinear beam dynamics degradation.

Results of some of the other perturbations scans are summarized in Table 6.6. For the configurations not mentioned in the table, no changes were observed or data quality was not sufficient to determine the effects. In general, no performance drop over 20% was observed for any of the perturbations except for the largest of optics ones, which is a great result. Consistent with simulations, QI system was highly robust to various errors.

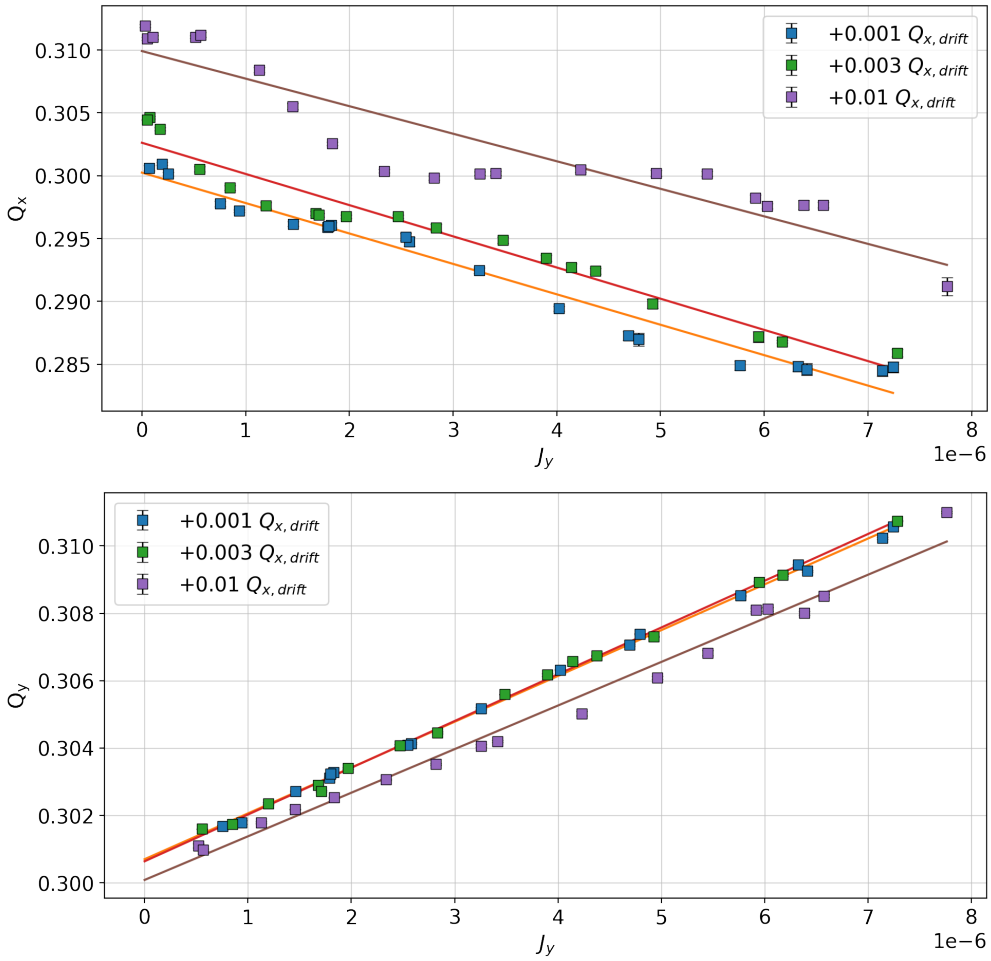

Figure 6.27: Detuning fit of three QI@1.0A datasets with varying $\Delta Q_{x,drift}$.

Invariants

Momentum recovery of both nominal and perturbed systems was attempted using the modified procedure with aggressive weighting described previously, but analysis did not yield statistically significant differences. It is likely that lattice optics drifts between shifts and other systematics dominated the analysis. As an easier case, analysis of kicks from a non-integrable flat arrangement was performed, and in this case a significant difference in invariant jitter was observed. Insofar as possible, a comparison was made with kicks at same current and same analysis parameters, and without any resonant capture. Jitter results showed approximately $\sigma_H / \langle H \rangle = 7.2\% \pm 0.8\%$ for the flat case and $\sigma_H / \langle H \rangle = 4.3\% \pm 0.6\%$ for comparable

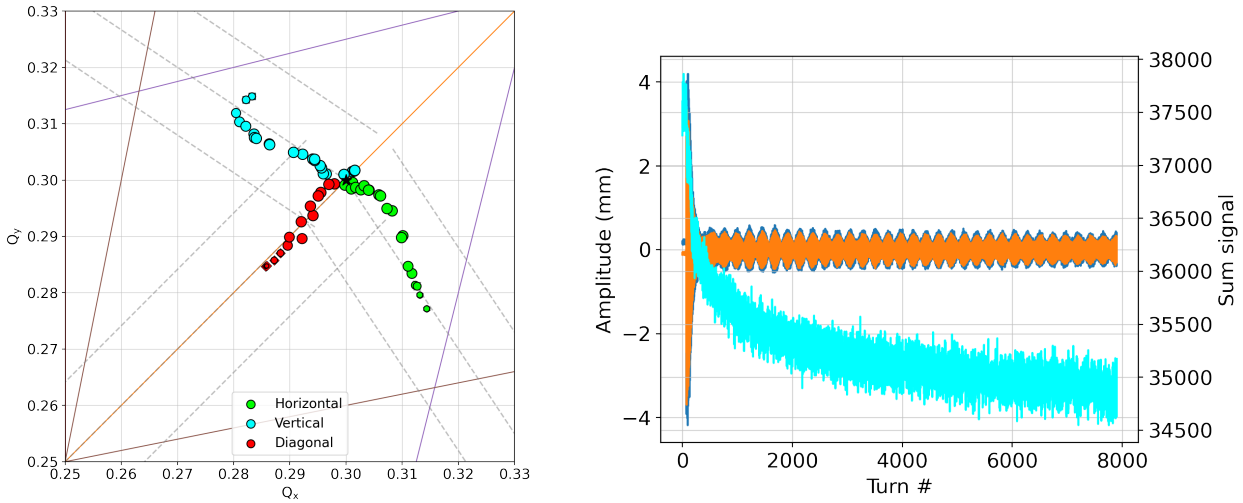

Figure 6.28: FMA and an example of resonant TBT signal for octupole flat current configuration. Most points with any current loss exhibit some degree of resonant signals.

Perturbation	$\Delta Q_{x,max}$	$\Delta Q_{y,max}$	DA	Notes
Current @ -1.0A	n/a	n/a	decreased	inverted DA
Current profile +0.01	+0.003	+0.003	NE	-
Current profile -0.01	-0.002	-0.002	NE	-
β_x^*/β_y^*	NE	NE	NE	optics asymmetry
Phase drift y +0.01	-0.004	-0.004	diagonal dec.	-
Phase ring x +0.01	-0.004	-0.002	diagonal dec.	-

Table 6.6: Impact of perturbations on QI system. NE stands for no observable effect compared to experimental uncertainties.

QI system once all BPM data was combined, while jitters of the CS invariants were approximately the same. Both smear values were higher than simulation results, but the advantage of QI system was clear and statistically significant.

Overall, invariant analysis produced qualitative claims of integrability, but further studies of the systematic errors and model improvements are needed for a quantitative model comparison of perturbed QI configurations.

6.3 DN measurements

6.3.1 Commissioning

Design and hardware of DN insert was presented in section 3.4. Unlike the 'adventure' of QI insert, no issues were encountered during either mechanical or beam-based measurements, with orbit accuracy after correction (Fig. 6.29) consistent with the 50 um prediction. Manual magnet calibration was done by turning them on individually and measuring the tune change of the ring, with resulting coefficients stored in the DN ramping routines inside pyIOTA. From these quadrupole values, and several checkpoints, a sextupole ramp was also derived so as to keep chromaticity zeroed at all DN currents. This has significantly improved beam survival when passing $Q_x = 1/3$, and produced some beautiful resonant islands, but there was a lot more room for optimization if the magnets could be set faster than control system limit of 1Hz. When measuring perturbed configurations, the procedure was to first ramp on best possible path and then apply lattice distortions once at desired t-strength. There is a small error from using same knobs as the QI system for what is essentially a different lattice, but design of special ones for each t value was infeasible.

6.3.2 Collected data summary

Because of lower usability of DN data, fewer kick sequences were acquired but they still covered a large parameter space, as detailed in table 6.7. About 2000 kicks were collected overall, many of them in near nominal configurations except for different ramp, sextupole, and kick directions settings. Because of the steep time cost in reinjecting the beam after each loss, conservative scan limits were typically picked and scans interrupted if they kept losing current, resulting in the sometimes asymmetric scan grids.

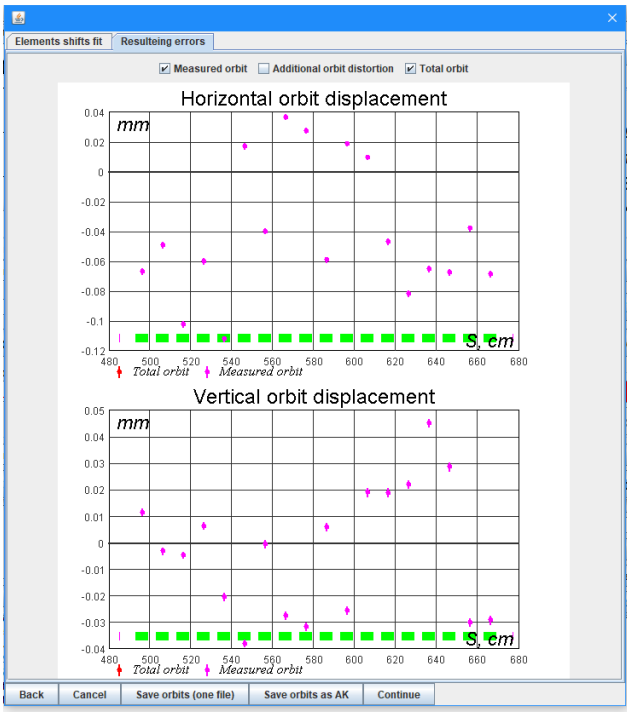

Figure 6.29: Orbit through DN magnet as measured by LOCO.

Configuration	Nominal value	Perturbation values
Nominal	N/A	N/A
Phase advance drift x	0.30	+0.01, +0.03,
Phase advance ring x	5.00	+0.01, +0.03
Phase advance ring y	5.00	+0.01
β_x^*	0.9m (middle)	+10cm along s
Strength	t=0.3	t=0.218, 0.363, 0.420, 0.5, ...
Current profile phase	mu=0.3	0.31, 0.29
Dispersion x	0.0	+10cm
Equal chromaticity	0/0	-5/-5 @ t=0.363
Low sextupoles	0/0	-5/-7 @ t=0.218, 0.363, 0.420

Table 6.7: Summary of DN configurations explored during run 2.

t-strength	Detuning H w/o loss	Detuning V w/o loss
0.146	0.010/0.025	N/A (resonance)
0.218	0.003/0.020	0.023/0.023
0.363	0.007/0.025	0.019/0.025
0.420	No data	0.030/0.050
0.490	No data	0.020/0.055 (small losses)

Table 6.8: Summary of DN maximum detuning results.

6.3.3 Results

Nominal configuration

One distinct advantage of the DN magnet is lack of complications with interplay of tune and coupling - the split tunes are clear and easy to distinguish, making for a simple NAFF window size optimization. Considering that decoherence wipes the signal in under a 100 turns at higher t values, using around 50-70 seemed to work well.

Results of nominal configurations for several t values are shown in Fig. 6.30. On all plots, the blue line denotes the small amplitude detuning expected from the quadrupole contributions, with black star the expected working point of the particular dataset. With increasing t-strength, the gap between expected and observed small tunes grows linearly, indicative of a small calibration error for magnet gradients. Each configuration has a slightly different tune footprint that is affected by the nearby resonance lines. This is especially evident for $t = 0.146$, where the vertical kick sequence hits 1/3 resonance and diagonal one the 1/4 - both resonances were strong enough to prevent getting the beam kicked past it. However, the horizontal direction with its larger negative Q_y detuning was accessible. Similarly, both $t = 0.42$ and $t = 0.49$ datasets had issues with sufficient horizontal dynamic aperture - their scans were focused on vertical kicks instead. The maximum detuning results are summarized in table 6.8.

As with QI, it is of interest to extract the action dependence, but linear tune shift presents

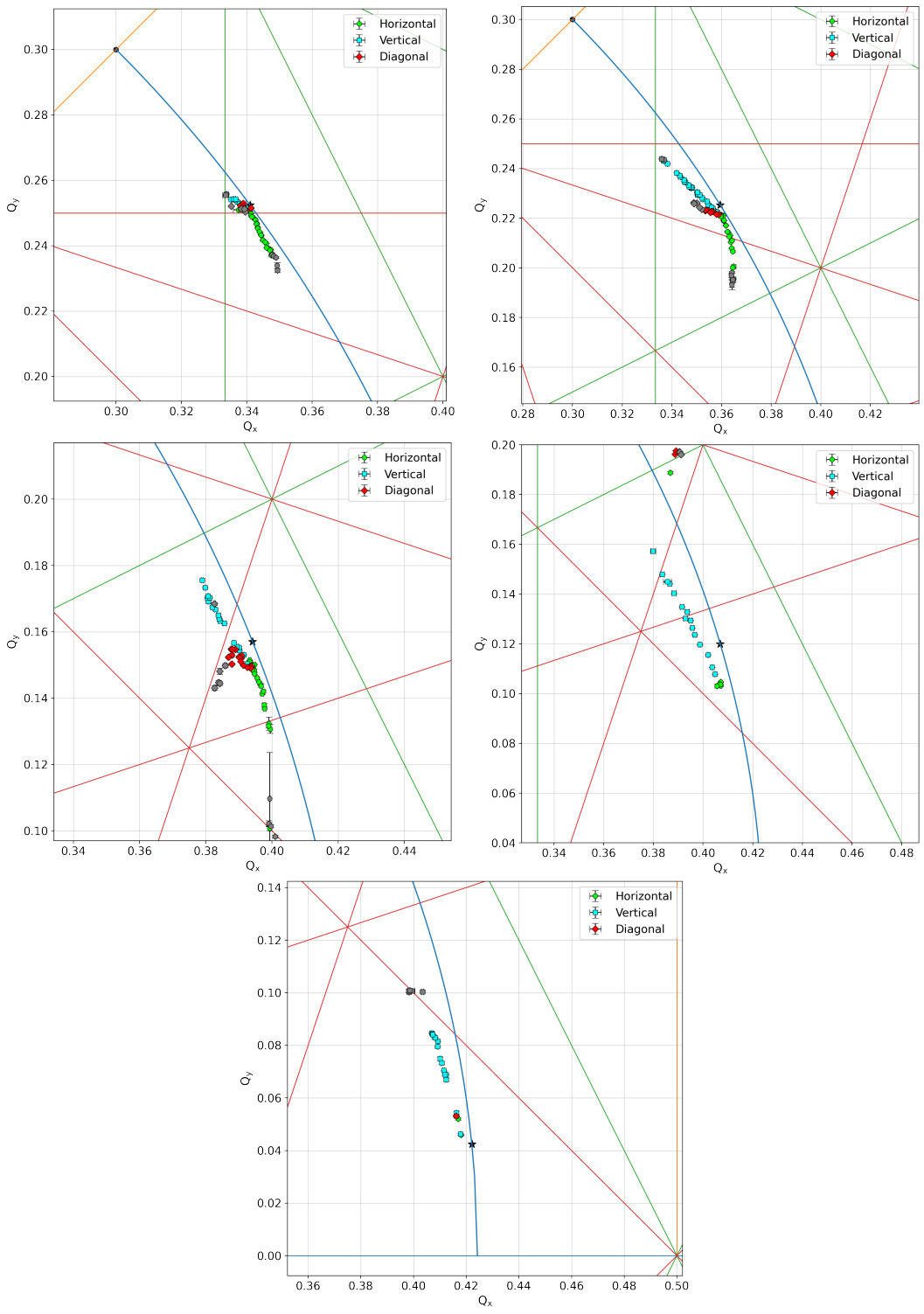

Figure 6.30: DN magnet detuning measurements at increasing t-strengths (see 6.8).

t-strength	dQ_x/dJ_y theory	dQ_x/dJ_y exp.	dQ_y/dJ_y theory	dQ_y/dJ_y exp.
0.218	-2920	-2945 ± 56	2332	2827 ± 49
0.363	-6373	-5819 ± 223	8020	8933 ± 230
0.420	-9368	-9822 ± 625	15 965	$15\,349 \pm 766$
0.490	$-31\,041$	$-23\,698 \pm 1800$	161 676	$135\,337 \pm 7925$

Table 6.9: DN quadratic detuning term measurements along vertical kick line.

a problem in that the measurements need to be fitted to a perturbed lattice (with DN contributions). The disagreement between expected and observed working points however suggests that using model DN optics would produce systematic errors. There was insufficient time to collect LOCO data with DN magnet on (also due to lifetime issues), and TBT optics analysis of small amplitude kicks did not identify any strong outliers. Calibration and correction of DN optics is definitely a good future project, given complex interplay of orbit distortion, chromaticity correction, and the necessary precision. Unfortunately no time was available to perform this during run 2. Instead, a simple t-strength correction was done to move model tune (along blue line) as close as possible to the observed value, and remaining optics systematics accepted as unavoidable. Results for the four datasets with clear vertical branches are presented in Figure 6.31. Unlike QI insert, the change in detuning with strength is not proportional to t, and even $\Delta Q_x/\Delta Q_y$ ratio varies from near unity at low t to 3.5 at high t. This behavior is consistent with tune footprint simulations. The detuning term values are compared to expected quadratic term contributions in Table 6.9, and show a good agreement for both dQ_x/dJ_y and dQ_y/dJ_y with exception of the highest strength $t = 0.49$ results. The discrepancy is likely due to the theoretical value not accounting for higher order terms in the DN potential.

Perturbations

Perturbation studies were performed similarly to QI ones, but significant performance degradation was quickly encountered. A representative set of $t = 0.363$ data with $+0.003$ $Q_{x,ring}$

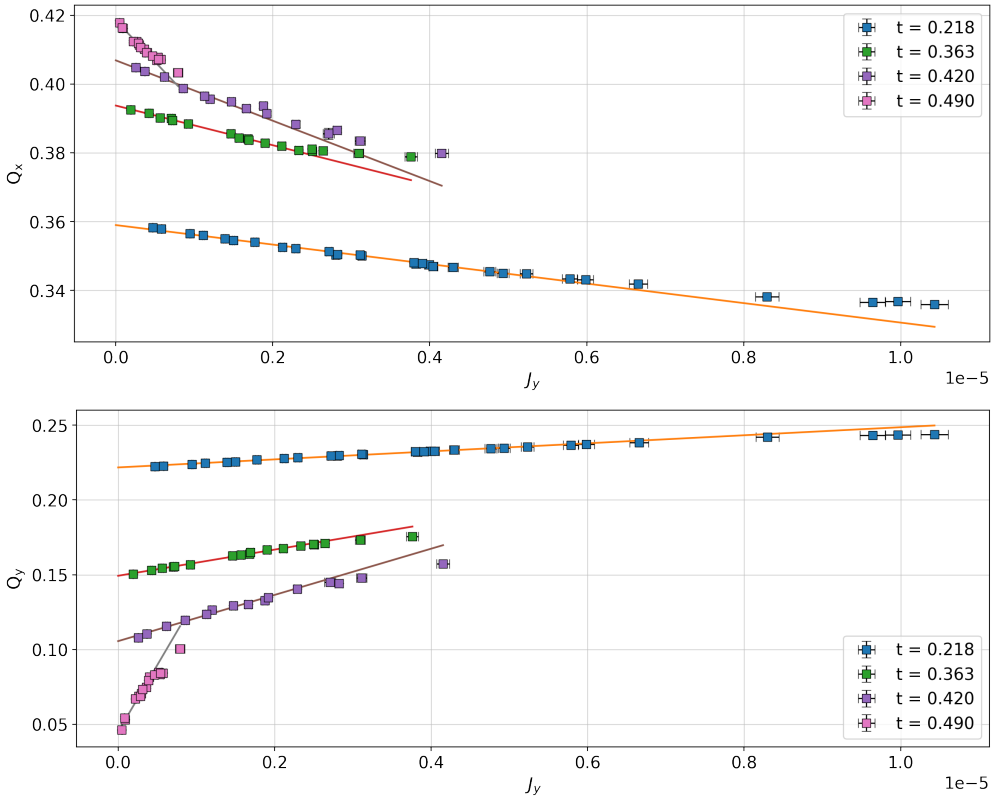

Figure 6.31: Danilov-Nagaitsev detuning with amplitude first order fits.

and +0.003 $Q_{x,drift}$ phase advances is shown in Figure 6.32. No clear reason for such fast falloff could be identified, but it is suspected that the knob set used for perturbations deviated too far from the real machine optics, causing significantly stronger errors than expected. However, this result also highlights the importance of linear optics for DN insert and justifies the order of magnitude tighter tolerances as compared to the QI system.

Phase space

With the operational parameters of run 2, diagonal kick signal decoherence was very quick. The corresponding typical kick envelope fits are shown in figures 6.33 and 6.34. For the stronger diagonal kicks of interest, only 20-30 turns were resolvable in the Y plane. Such low number of turns combined with optical errors resulted in insufficient data quality to attempt quantitative phase space recovery. Evidence of optics mismatch can be observed in the tilt

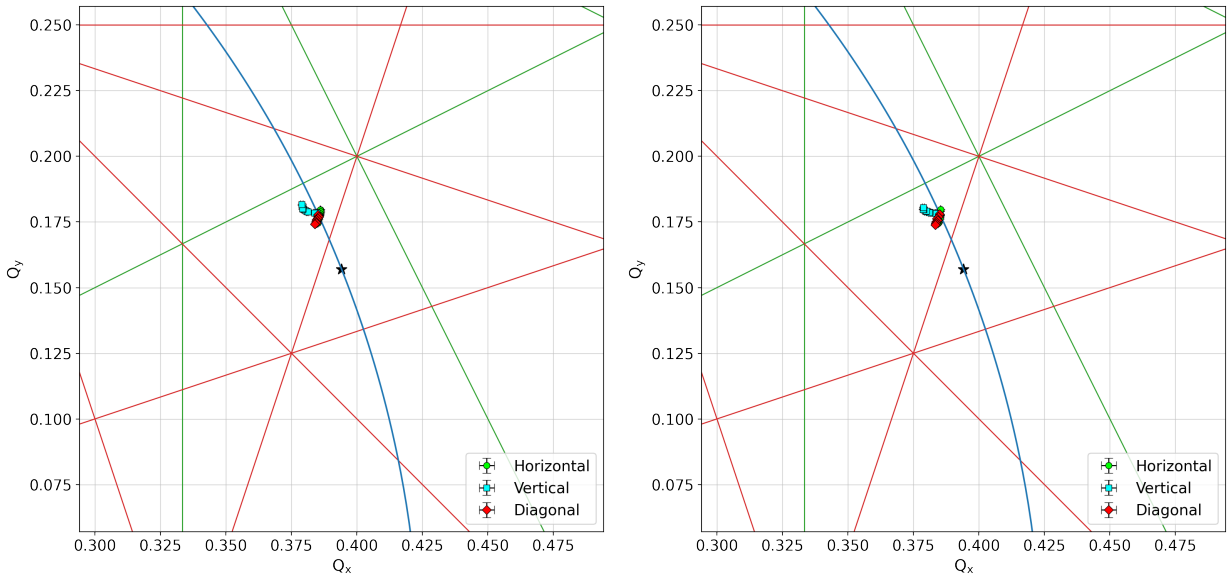

Figure 6.32: Tune perturbations of the DN magnet. Left - +0.003 x phase advance in the ring. Right - +0.003 x phase advance in the insert.

of the phase space ellipse shown in Figure 6.35, where a single BPM pair measurement across the drift (B1L-B2L) was used. For ideal reconstruction, no tilt of the ellipse would be expected after normalization.

Integer crossing and two-orbit splitting

One of the more exotic thing to come out of DN studies was successful crossing of the integer resonance at $t = 0.5$ (experimentally at $t = 0.51$). This resulted in only minor beam losses, and produced some fascinating beam profiles shown in Fig. 6.36. The distance between islands was measured and grew with increasing t-strength consistent with theoretical predictions [127]. Any attempts to kick the beam results in fast losses with little usable data. Nonetheless, the presence of this exotic configuration indicated a correct implementation of the DN Hamiltonian.

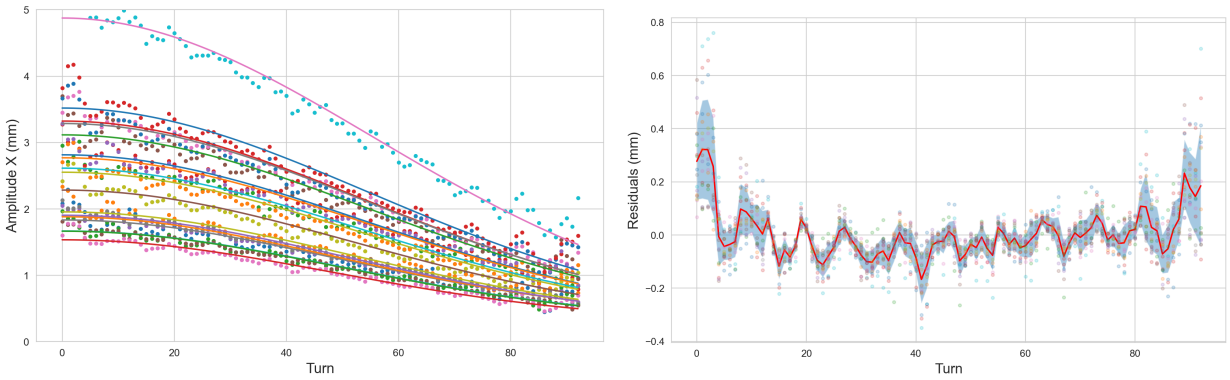

Figure 6.33: Decoherence fit in X plane for DN kick at $t = 0.25$ and diagonal X/Y of 1.9kV.

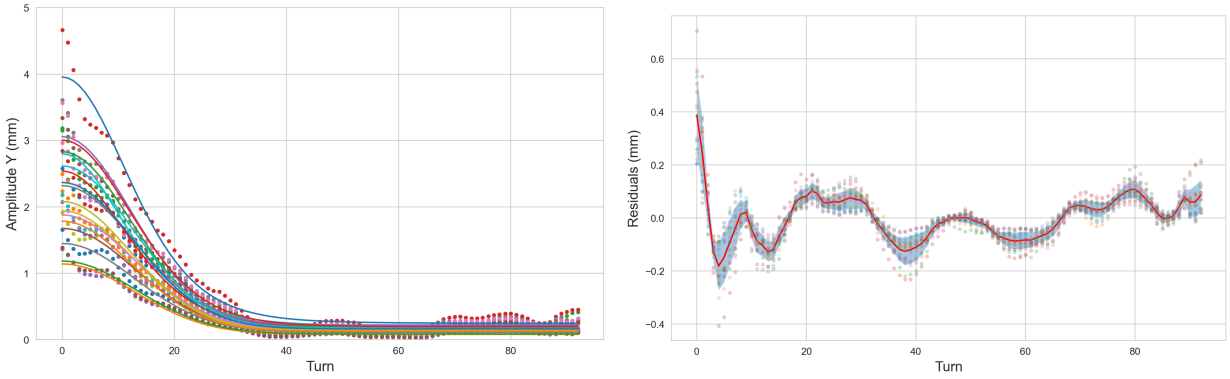

Figure 6.34: Decoherence fit in Y plane for DN kick at $t = 0.25$ and diagonal X/Y of 1.9kV.

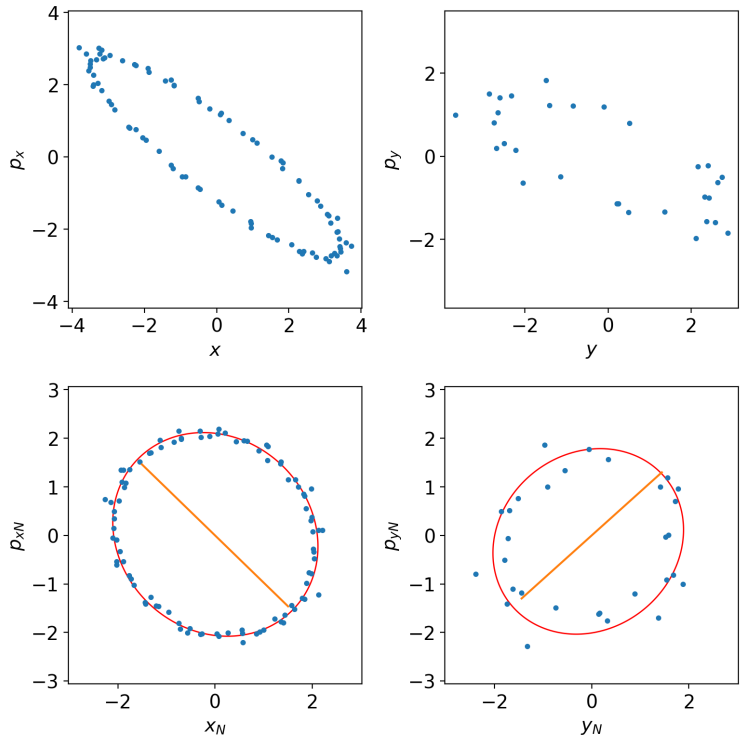

Figure 6.35: Standard and normalized phase space coordinates with a least squares ellipse fit. Orange line denotes the semi-major axis, and ideally should be vertical for normalized coordinates.

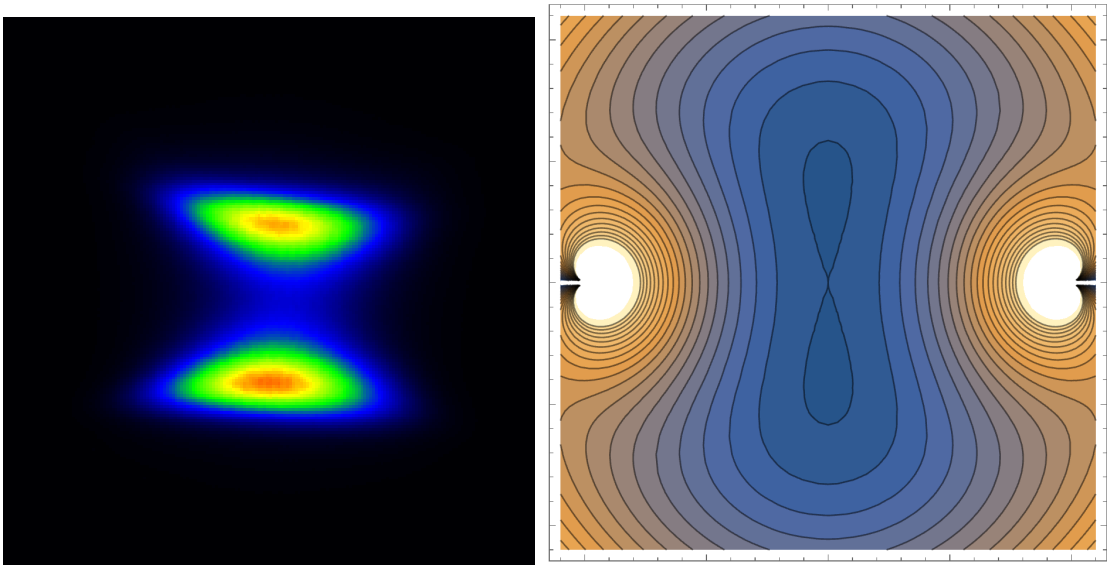

(a) SLM M3R image (b) Potential contours

Figure 6.36: Two stable orbit topology of DN magnet.

CHAPTER 7

CONCLUSIONS AND FUTURE WORK

7.1 Summary

This dissertation has explored with simulations and experimentally a novel class of integrable nonlinear systems that have the potential for strong suppression of collective beam instabilities without degradation of beam dynamics. If implementable, NIO could enable a new generation of higher energy and intensity particle accelerators. However, these system require a careful and robust implementation of both the insert and the rest of the ring. Overall, scientific goals of IOTA NIO phase I have been met - single particle dynamics of integrable systems was measured and matched simulations, with good QI robustness to perturbations and strong DN detuning. Much of the groundwork for direct instability studies with protons was established.

7.1.1 Quasi-integrable insert

Majority of experimental work has focused on exploring the quasi-integrable system with a single invariant of motion, driven by expected better system robustness and slower signal decoherence. Measurements of detuning with amplitude demonstrated a maximum tune spread of $\Delta Q_x/\Delta Q_y = 0.032/0.036 \pm 0.001$ for configuration with full chromaticity correction, consistent with the model and predicted DA reduction due to sextupoles. Various linear optics and QI potential perturbations were applied, with QI system retaining high performance ($> 90\%$) detuning for all realistic errors. Certain extreme configurations like $+0.01\ Q_{x,insert}$ significantly degraded performance in some kick directions without much effect in others. Quantitative comparison of quadratic amplitude detuning with action showed good agreement with theory - changes in current increased detuning linearly, while changes in working point did not change it (within margin of error). Dynamic aperture size was

consistent with simulations. Comparison of tune footprint slopes with model suggested a match at partially corrected chromaticity of ~ 3, consistent with observation of anomalously low natural horizontal chromaticity. Comparison with benchmark flat configuration demonstrated better beam dynamics of QI, with former exhibiting significant resonant losses that were not observed in any of nominal QI configurations. Phase space recovery indicated a better conservation of the nonlinear Hamiltonian, but smear levels were higher than expected and analysis accuracy was limited by signal recovery systematics. Overall, QI system demonstrated remarkable resilience to perturbations and behavior consistent with simulation predictions.

7.1.2 Danilov-Nagaitsev insert

DN magnet was studied with methods similar to the QI system, but accounting for the linear lattice distortions. Because of extremely fast decoherence in 20-50 turns and optics model uncertainties, phase space data was not sufficient for a quantitative analysis. Detuning measurements showed remarkable agreement with theory except at the strongest of probed settings. Maximum detuning of $\Delta Q_y = 0.058 \pm 0.0007$ was observed along a single kick direction, and overall achievable tune spread was predicted to be $\Delta Q_y = 0.12 \pm 0.001$. Lattice perturbations degraded DN performance, with large decrease in maximum observed tunes. Overall, DN system behavior was consistent with the model, showing large detuning in nominal configuration but also sensitivity to perturbations.

7.1.3 Simulation and software tools

In support of the main NIO research project, a number of software tools were developed, establishing a unified simulation and analysis framework for various beam dynamics algorithms. As far as we know, it is the only such research oriented Python codebase (though doubtless many grad students end up with a similar pile of scripts that is never released).

It is my hope to continue its development, integrating tools both from within and outside of accelerator physics community, enabling faster and more unified approach to accelerator research and development.

7.2 Future work

Although much progress has been made, there are many gaps remaining, both experimental and theoretical. In terms of single particle dynamics, collected dataset lacks high fidelity kicks at the original design parameters. IOTA is currently in run 3, with 150MeV commissioning being one of the goals. When achieved, it would create a whole host of opportunities. For instance, it would enable new methods for performance tuning, such as ML-inspired Bayesian optimization. While not reported in this thesis, several algorithm have been attempted in run 2 but did not beat manual results because of lattice drifts and low figure of merit resolution. With the ability to extensively tune and optimize the lattice at higher energy, exciting beam dynamics topics become accessible - studying particle motion near the stochastic boundary layer, comparison of smear dependence with analytic predictions near various resonances, high resolution resonance driving term measurements, and many others. More importantly, this would mean fully achieving the design DN magnet lattice accuracy and conclusively demonstrating its integrability.

Another avenue to pursue further are instability studies driven by an anti-damper system [128], where the advantages of electron beams can be retained and instability thresholds probed simultaneously. A permanent anti-damper upgrade and installation of a separate AC dipole would allow for collection of many thousand of TBT turns, as is done at LHC and other large machines, enabling a leap in optics accuracy. Combined with relatively large amount of beam time availability, this would yield extremely detailed nonlinear beam dynamics/RDT results and a better understanding of inherent IOTA nonlinearities.

With the proton injector also coming online for run 4, IOTA is on track to become

a unique hybrid single-particle/collective dynamics research facility, and to perform direct instability suppression demonstrations at the required precision and repeatability. As a very biased participant with potential delusions of grandeur, I hope current and upcoming NIO results over next few years will provide a convincing case for building a production NIO ring. Until then however, stay calm and keep kicking.

APPENDIX A

IOTA HARDWARE AND COMMISSIONING

Modern accelerators contain a vast number of devices for beam control and diagnostics. This appendix describes the instrumentation used for NIO studies, and the commissioning process.

A.1 Beam position monitors

IOTA ring is equipped with a custom system of 21 capacitive button BPMs designed by the Fermilab accelerator division instrumentation department [129]. A picture of one of IOTA BPMs is shown in Fig. A.1. Capacitive BPMs are a non-destructive diagnostic for measuring bunch transverse centroid position. They work by detecting image charges induced by bunch passage, whereby the differential signal on opposite sides is proportional to bunch displacement from central axis.

For large amplitude excursions, simple signal difference formula no longer holds and result becomes nonlinear. Based on extensive calibration with a wire source, a 2D 7th order polynomial fit grid is applied to raw position data to compensate [130], as well as a difference/sum fit [131]. Many other effects can also impact BPM operation - bunch length, shape, and current, coupled power supply and mains noise, and others. These are expected to be second order compared to nonlinearities. Since IOTA NIO team was not directly involved in BPM design, we had no knowledge of all low level detail and relied on experimental benchmarking to determine final performance.

A.1.1 Run 2 commissioning

BPM system was commissioned extensively in run 2, measuring noise and linearity in orbit and TBT modes. Sample signal during a corrector toggling sequence is shown in figure A.2.

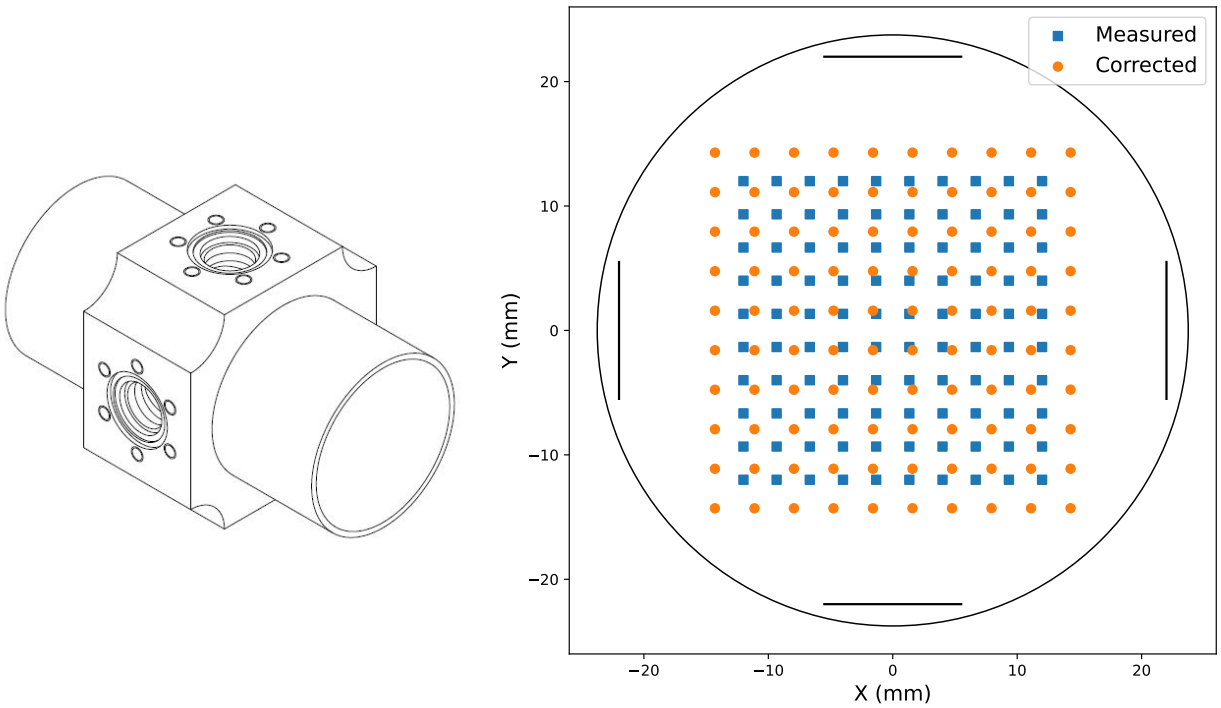

Figure A.1: IOTA BPM system. Left - CAD model of standard housing with 4 button feedthrough holes. Right - nonlinear correction map performed internally by the DAQ system.

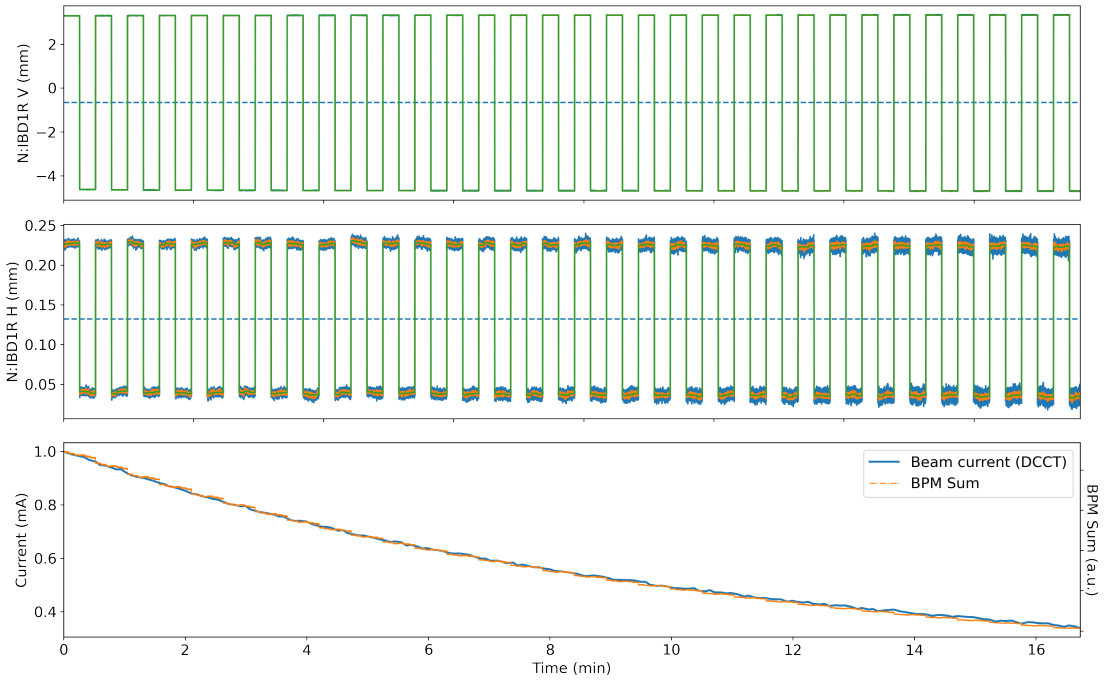

Figure A.2: Output of a single BPM for repeating closed orbit changes.

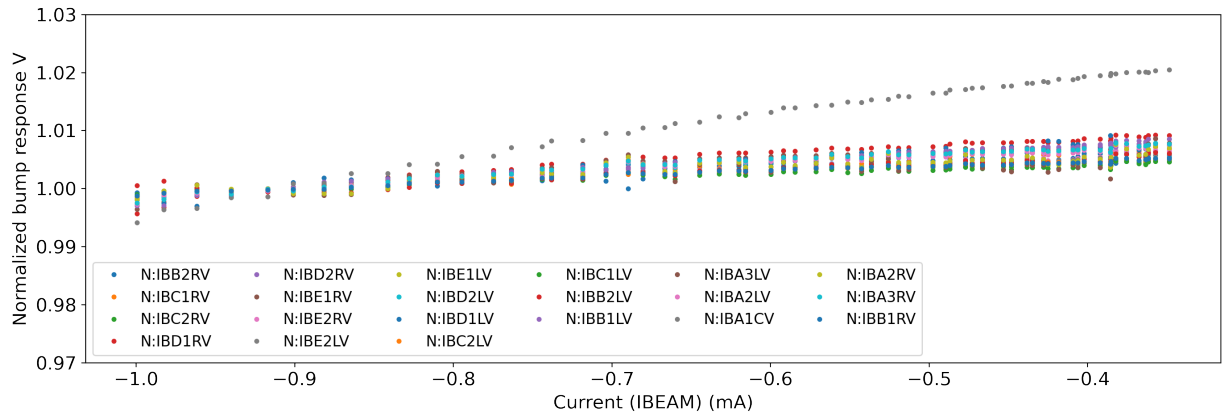

Figure A.3: Response nonlinearity to closed orbit distortions. BPM A1C outlier is expected.

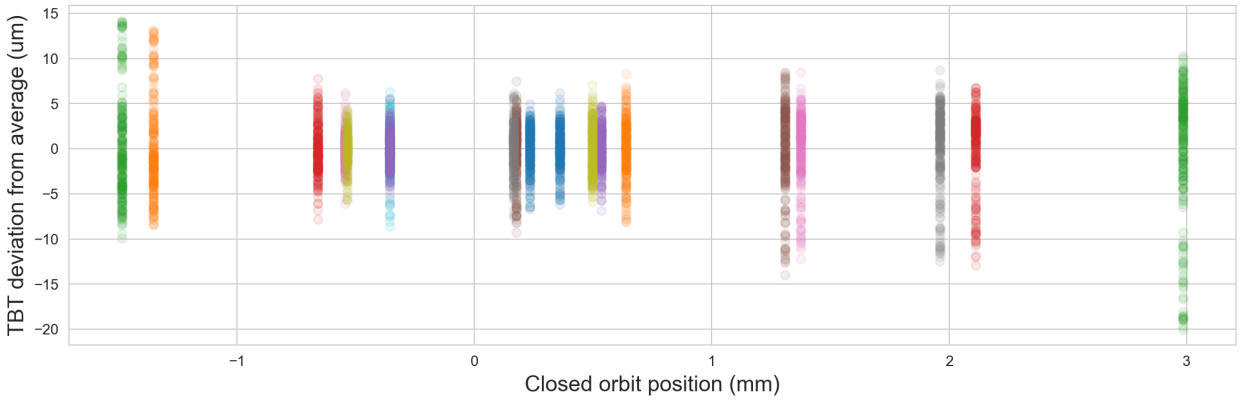

Figure A.4: BPM linearity inferred from mean shift of closed orbit with current.

The corresponding response linearity results are plotted in figure A.3. Note that A1C outlier is expected, since that is a special large button BPM, and is not used in data analysis.

After the BPM system damage, linearity was checked again indirectly from the TBT noise test data. Results are shown in figure A.4

A.2 Synchrotron radiation monitors

In addition to electrostatic BPMs, special vacuum chambers with window ports were installed on all 8 dipoles, allowing for extraction and measurement of synchrotron radiation. I have led

the prototype development and initial assembly of this 'synchrotron light monitor' (SLM) system in collaboration with A. Romanov and significant help from J. Santucci and rest of IOTA team [132, 133]. This section will present SLM system design and operational performance.

Hardware

Hardware design was done with standard CAD tools SolidWorks and Siemens NX, based on available 3D models of IOTA components. The design goals were to make a cost-effective system that could be manufactured using rapid prototyping techniques - commercial off the shelf parts, 3D printing, bulk computer numerical control (CNC) ordering. This would allow for SLM to be deployed and maintained internally by the IOTA team. In retrospect, this approach proved very fruitful as many other experiments have been able to take advantage of our system for their data acquisition while having the expert right with them in the control room. In terms of general design, a simple optical imaging path was implemented with 1 centrally located achromatic focusing lens with an iris, allowing for 1:1 imaging of radiation sources inside the dipoles. As detector, a commercial BlackFly BFLY-PGE-23S6M-C monochromatic camera on a set of linear stages was used. A diagram of this is given in Fig. A.5.

Prototype development was done on a spare bending dipole with a simulated light source, demonstrating good performance and auto-focus capabilities (Fig. A.6). System was installed in stages throughout run 1, and played a crucial role in achieving first turn and initial orbit in IOTA.

Software

In alignment with hardware design philosophy, it was decided to develop an in-house software architecture isolated from the main controls network. I have performed initial design of the

Raspberry Pi network, their software, control PCBs for motorizing the stages, and designed the data acquisition system network/hardware architecture (Fig. A.7). For camera readout, 'BPMServer' software written by A. Romanov was used (Fig. A.8), and readout integrated with other BPM systems for optics tuning purposes. Since then, many of the elements have been improved further by A. Romanov and others, with myself providing technical support of the DAQ infrastructure and being a user.

Applications

SLM systems has found a variety of unexpected and exciting uses beyond simple beam profile monitors. For example, single electron injection was established and could be observed on the cameras for long 0.5s integration times. Pi-mode synchrotron radiation was observed with a polarizing filter, allowing for emittance estimates below nominal resolution limit. SLM was also improved by various collaborators with new photo-multiplier detectors, single photon avalanche diodes, and other instrumentation, as can be seen in Fig. A.9.

A.3 Auxiliary hardware

Beyond the primary diagnostics, many devices were used to manipulate and measure beam properties of relevance for NIO experiments.

A.3.1 Kickers

To create beam excitation to any point within physical aperture, IOTA is equipped with a perpendicular set of traveling wave electrostatic kickers. The vertical kicker also serves to place the bunch onto the closed orbit as part of the on-axis injection system. In run 1, only vertical kicker was controllable, with fixed small horizontal excitation. In run 2, both systems were configurable, allowing for significantly better parameter space exploration.

Parameter	Max error
Voltage (max)	$\pm 25\,\mathrm{kV}$
E-field on axis	$11.5\,\mathrm{kV/cm}$
Pulse length	$< 100\mathrm{ns}$
Plate length (H/V)	58cm/105cm
Jitter	$< 5\%$ (run 2 measurement)
Linearity	$< 2\%$ (run 2 measurement)

Table A.1: IOTA kicker parameters.

Kicker specifications are summarized in table A.1, with further design description given in [134, 135]. While significant kick magnitude jitter was observed, it was not consistent or experimentally critical, since actual amplitudes could be recovered from beam motion measurements. In results of Chapter 6, kicks are labeled by nominal voltage divided by 6, which matches control system conventions. Kicker imparted angle θ can be calculated as

$$\theta = \arctan\left[\frac{El}{p\beta}\right] \tag{A.1}$$

where p is particle momentum in eV/c, E the electric field, l kicker length, and β the relativistic factor. For small deviations like those used in IOTA ($< 5\,\mathrm{mrad}$), small angle approximation holds and $V_{kick} \propto \theta \propto J$. Corresponding maximum oscillation amplitude elsewhere in the ring is given by Eq. 2.62.

A.3.2 Wall current monitor

IOTA wall current monitor (WCM) is a ceramic pipe element which measures beam longitudinal profile and intensity using a shunt resistor between the two sides. It was originally developed for EMMA [136]. For NIO, WCM was not used directly, but in other studies it was a key component for measuring bunch length and emittance. The derived beam parameters of these studies were then used in NIO simulations.

A.3.3 Direct-Current Current Transformer

While BPM and WCM systems can provide measurements of beam current, their signal processing is not optimized for this. Direct-Current Current Transformer (DCCT) is the primary tool for current measurement - its principle of operation is quite complex, and is described in [137]. In IOTA, Bergoz MPCT-RH-113 model was used, with nominal specifications of 10 uA resolution and 100 uA minimum current. In NIO studies, DCCT was the primary tool for high resolution beam current measurements.

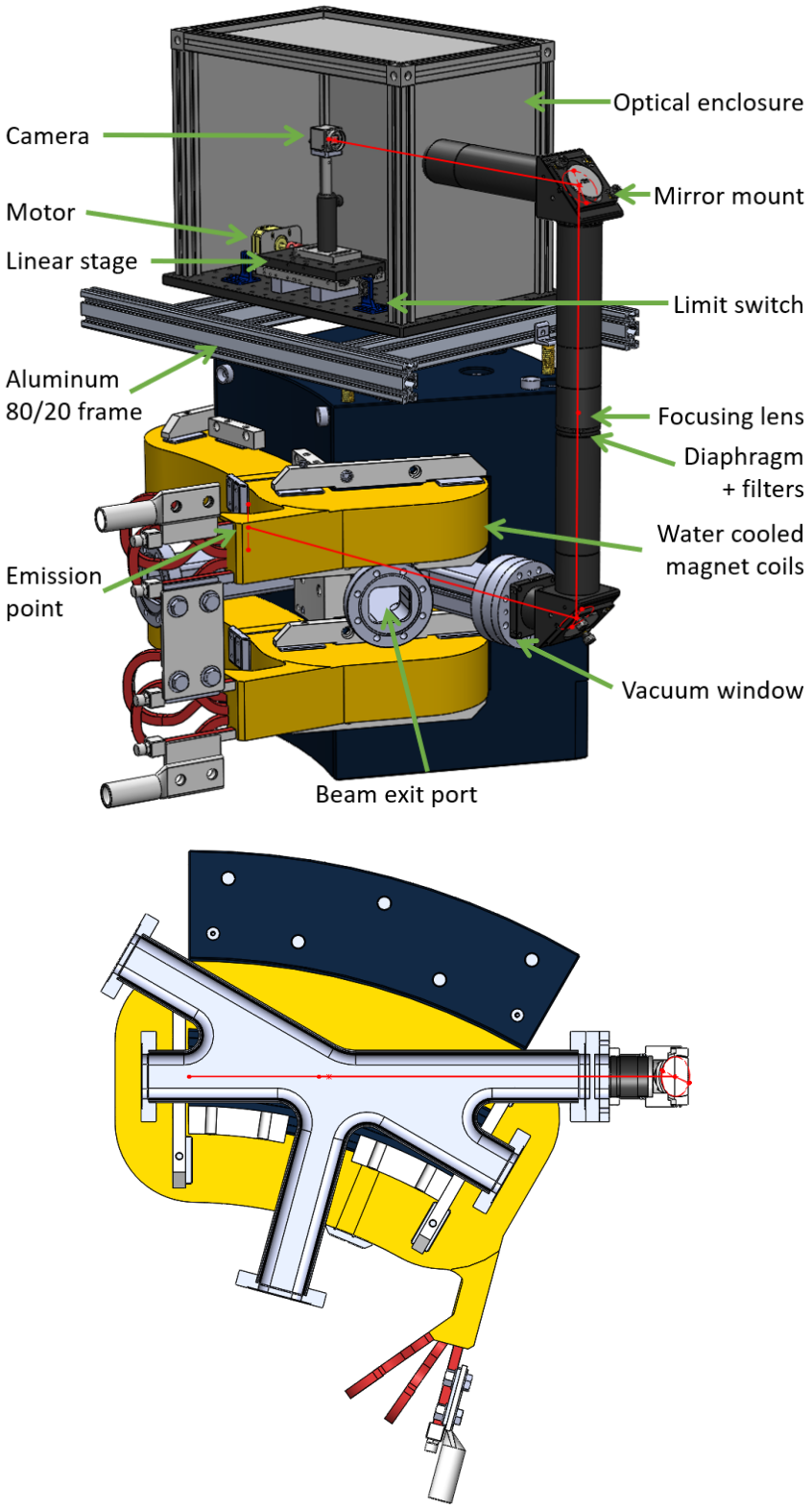

Figure A.5: CAD model of SR station on top of a 30 degree dipole magnet. (a) Overall 3D model. b) Top-down view from the optical light emission point for the vacuum window

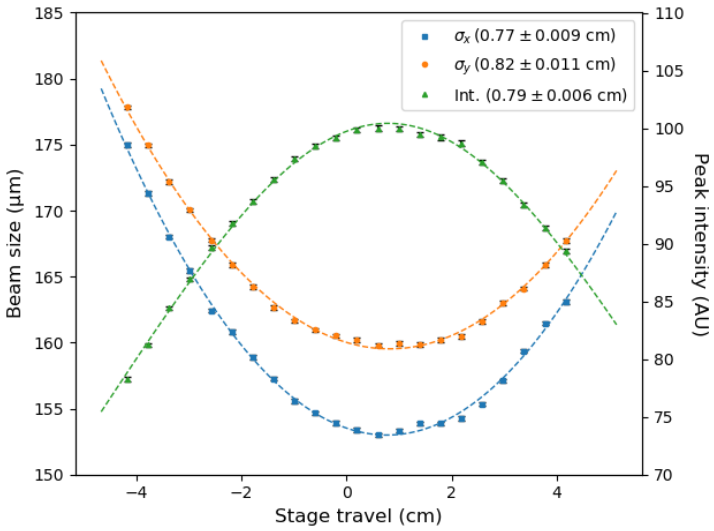

(a) Simulated beam source size as function of stage position.

(b) Prototype test stand on a 60 degree spare dipole.

Figure A.6: SLM prototype development.

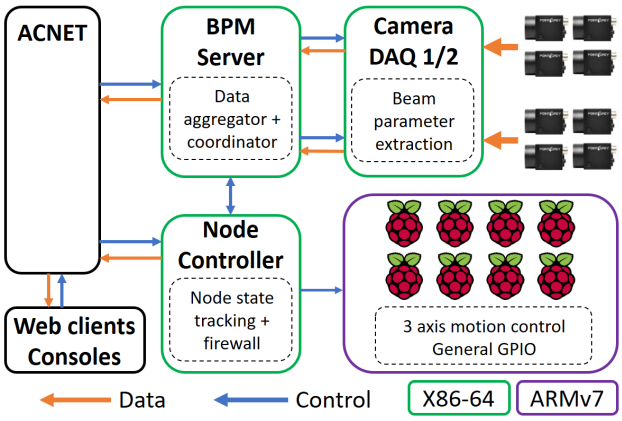

Figure A.7: SLM software architecture block diagram.

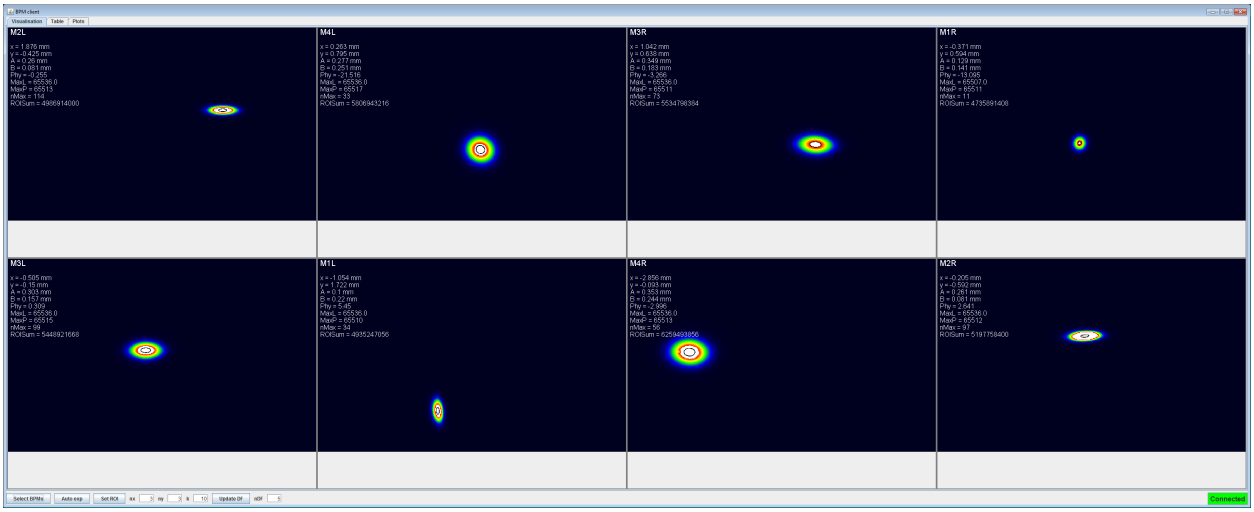

Figure A.8: All 8 cameras observing an electron beam on closed orbit.

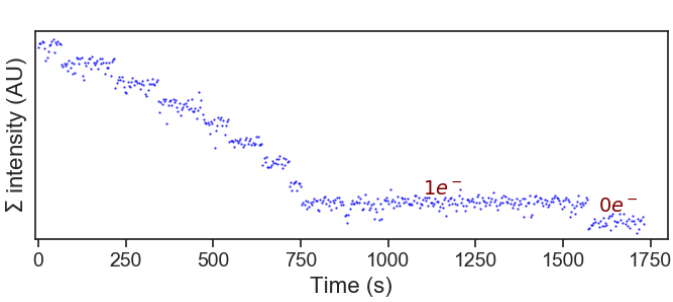

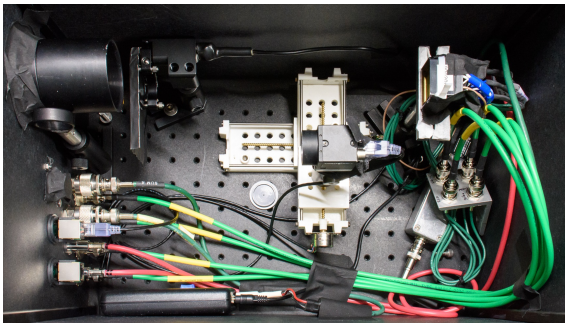

Figure A.9: SLM applications. Left - observation of single electron in IOTA ring. Image by A. Romanov/Fermilab. Right - an experimental station packed full of additional equipment. Image by G. Stancari/Fermilab.

A.4 QI insert

This sections describes some of the commissioning activities done with QI insert.

A.4.1 Laser tracker

Based on cylinder magnet fit done by the alignment crew, element positions in BL coordinate system were computed. Results were summarized previously in chapter 6. Detailed plots of longitudinal and transverse offsets are shown in figures A.11 and A.10.

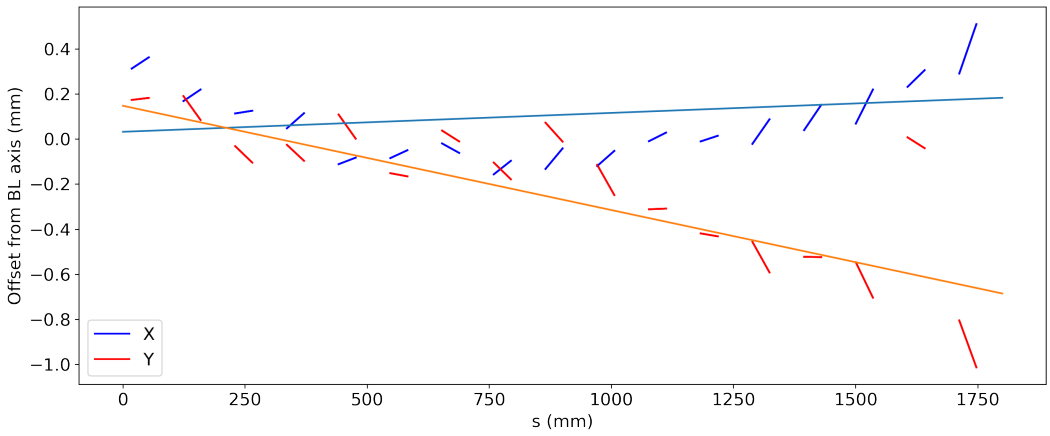

Figure A.10: Transverse laser tracker alignment data. The line slope denotes the connection between magnet (cylinder fit) faces. It is proportional to the yaw/pitch of the magnet.

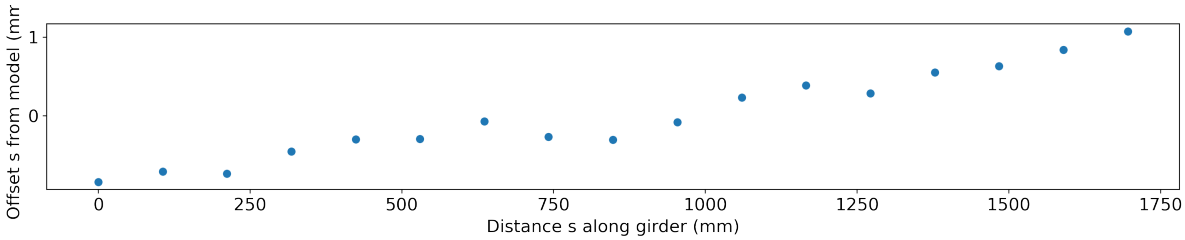

Figure A.11: Longitudinal relative offset laser tracker data.

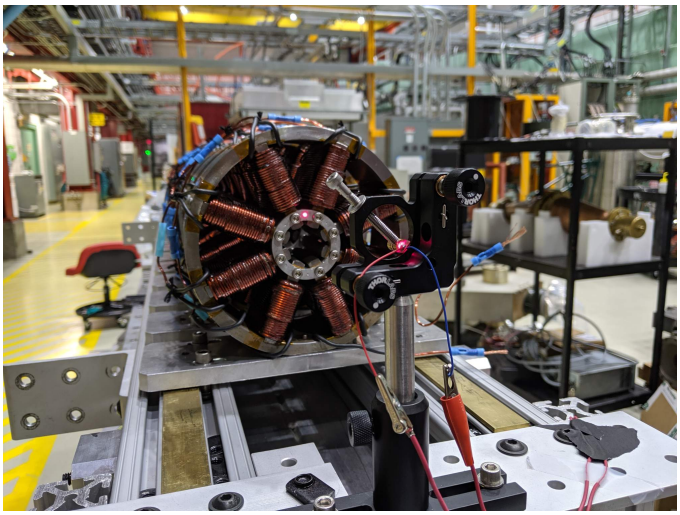

(a) Initial alignment device.

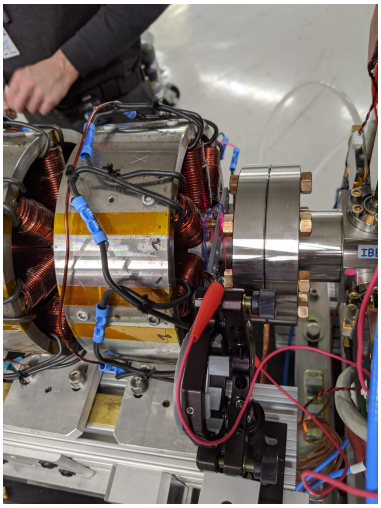

(b) In-place realignment.

Figure A.12: Laser alignment contraptions.

A.4.2 Pinhole alignment

Laser pinholes were used as both the primary alignment method and the in-place realignment method during run 2 after manual position adjustments disturbed the insert. The images of these processes are given in figure A.12b

A.4.3 Beam-based alignment

Beam-based methods showed significantly larger misalignments than that predicted by the mechanical constraints. Results after QI installation and in the final measurement configuration are shown in figure A.13b. The reason for such significant errors and corresponding disagreement of alignment methods is not known.

A.4.4 Electrical testing

In an attempt to debug the situation, several sanity check tests were performed. Because the magnets could not be removed from the beampipe, these had to be done in place and were time-limited. First, resistance across magnets was tested as well as voltage drop when pow-

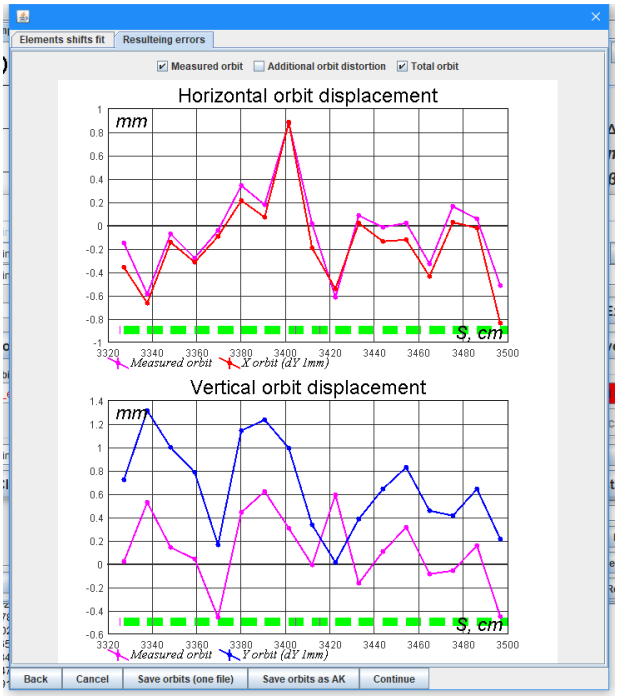

(a) Beam-based octupole alignment before any modifications.

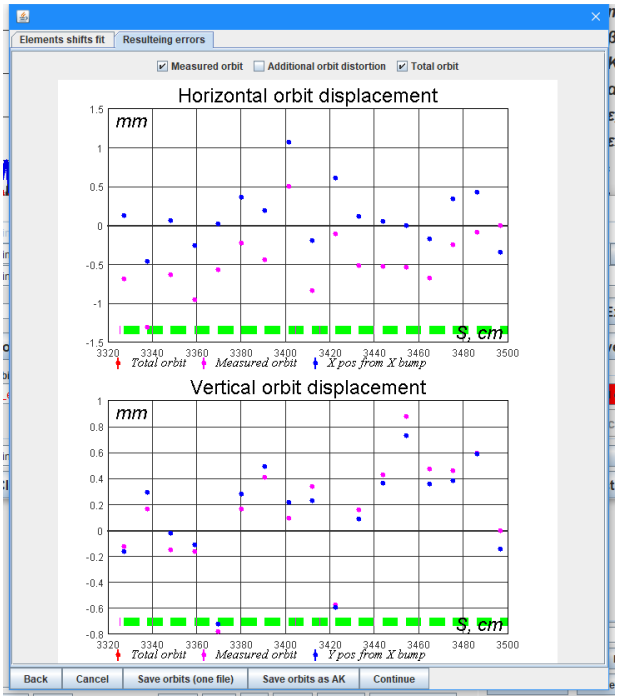

(b) Beam-based data after adjustments and laser realignment.

Figure A.13: Alignment measurements of QI insert with 6dsim. Offset of two lines signifies measurements done before/after orbit shift, with expected response of just a linear shift for all elements in questions.

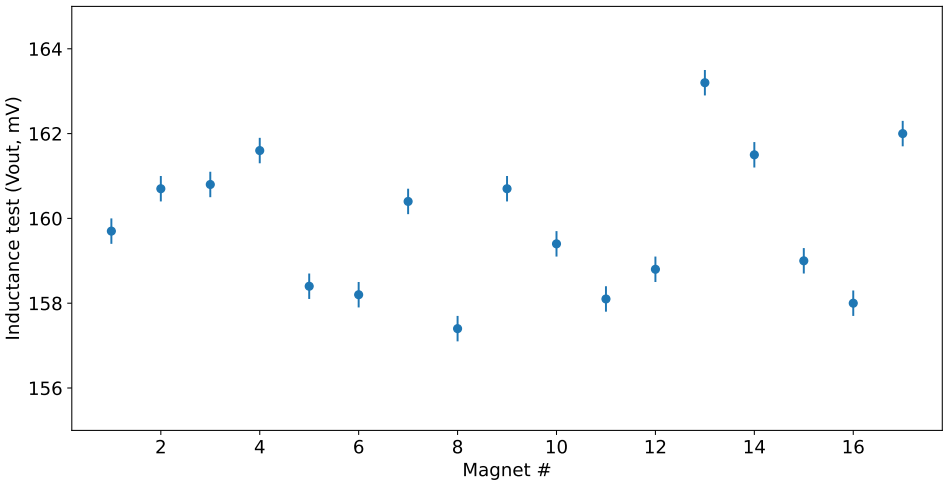

Figure A.14: Inductance measurement data. A short has reference value of 673mV.

ered, the latter being $905\,\mathrm{mV} \pm 20\,\mathrm{mV}$ across all magnets. Voltage measurements performed in 2021 by M. Obrycki also found no notable deviations.

A more sensitive method was devised to measure magnet inductance by forming an LR circuit consisting of a magnet, 8kHz 1V sine wave source, and a 5 Ohm resistor. Since inductance scales with the square of the number of coil turns, it was hoped a coil to coil internal short or another electrical issue would stand out. However, as can be seen in data of Fig. A.14, no outliers were detected.

APPENDIX B

SIMULATION AND ANALYSIS SOFTWARE

Accelerator physics relies heavily on accurate numerical simulation tools. This appendix describes the features and our experience with codes used for NIO studies. It also gives an overview of the features of our custom pyIOTA framework.

B.1 Simulation codes

B.1.1 Elegant

Elegant (ELEctron GEneration And Tracking) [138] is a 6D tracking code written in C, maintained by ANL in support of the Advanced Photon Source. It is one of the two most popular codes used by the light source community, the other being MATLAB-based AT. Elegant has symplectic integrators up to 6th order for a variety of elements, is capable of fast tracking and optimization, and supports HPC-scale computation via message passing interface (MPI).

Among its disadvantages is the coordinate system convention, which is $(x, x', y, y', s, \delta)$, also known as '$s$-based' (same as the theory presented in chapter 2). For consideration of Hamiltonian mechanics, it is preferable to work in (x, p_x) canonical coordinates, but the conversions are straightforward and are done internally before any symplectic integration steps. Moreover given $\gamma >> 1$ of IOTA, the two systems are very close numerically, and can be used interchangeably.

In this thesis, elegant was the primary code used for all dynamic aperture and other tracking studies. Because of cumbersome lattice and task file formats that have limited to no scripting ability, a wrapper was written in Python to generate input files on the fly, and later became part of pyIOTA framework.

B.1.2 MAD-X

MAD-X (Methodical Accelerator Design - 10) [139] is the most recent of the MAD family of codes, maintained by CERN. It is optimized for lattice design and nonlinear single-particle beam dynamics studies. One of its key features is integration with PTC (Polymorphic Tracking Code) library [140], which enables normal form analysis and nonlinear tracking with arbitrary accuracy (at the cost of performance). Without PTC, only a few thick elements have symplectic integrators, with most others pre-sliced into thin 'drift-kick' slices.

MAD-X has a highly flexible Turing-complete scripting language, and comes with various Python bindings for reading/writing files (`tfs-pandas`) and controlling the simulation (`cpymad`). As for disadvantages, since it is used primarily for high-energy hadron machines like LHC, there is little support for complicated edge fields, 3D field maps, or undulators. Also, it is single-threaded and has inflexible I/O, making large-scale tracking infeasible.

B.1.3 LIFETRAC

LIFETRAC [141] is a FORTRAN code developed by D. Shatilov for studying equilibrium particle distribution in lepton colliders, and later extended to non-equilibrium distributions and single particle tracking. Its key use has been in studying beam-beam effects, with extensive contributions to the design and benchmarking of LHC, FCC, and other machines. While it only supports thin elements, the overall tracking performance is very high. It also has an integrated FMA visualization tool. LIFETRAC was used by NIO team during early stages of conceptual ring design and evaluation.

B.1.4 6DSim

6DSim is a linear optics and tracking code developed by A. Romanov as his custom all in one optics correction toolbox [142]. A unique feature of 6dsim is a fully integrated GUI, allowing for use by non-experts and speeding up standard workflows. In our research 6DSim

was used for experimental lattice optics commissioning.

B.1.5 OCELOT

OCELOT is a pure Python code developed at EuXFEL for simulation and optimization of free electron lasers [143]. It provides standard optics calculation tools, and matrix based tracking up to second order. There are also several collective effects available, including space charge and coherent synchrotron radiation. Unfortunately, being optimized for single pass linac tracking, its ring performance was poor, and no symplectic integrators were available. Since the analysis code of this thesis is written predominantly in Python, it was inherently advantageous to have a native Python tracking code (no outside script files, all calculations can be done in same process, no code compilation). As such, OCELOT was modified and extended [144] to become the core optics engine for all other analyses.

B.2 pyIOTA

Control and coordination of all of the above tools required a large amount of glue and boilerplate scripting. To avoid it becoming an unmaintainable mess, we eventually decided to produce a single unified framework with all the bells and whistles of a modern software package. It is called pyIOTA, is open-source, is written in Python/C, and integrates accelerator simulation, analysis and control [145]. A large part of it functions as a wrapper and glue code around simulation and equipment control libraries. Its capabilities include backend-agnostic device control layer for reading actual machine data from Fermilab ACNET control network, built-in beam dynamics simulation through modified/extended OCELOT and custom code, task and script file generation and file I/O for elegant and MAD-X, lattice and data conversion between various codes, cluster simulation job management, and all of the analysis code and algorithms used in this thesis. Currently, it has over 23,000 lines of codes and is extensively commented, something sorely lacking in other accelerator libraries.

BIBLIOGRAPHY

[1] P. Bryant, "A Brief history and review of accelerators", in CERN Accelerator School: Course on General Accelerator Physics (1992).

[2] A. Sessler and E. Wilson, *Engines of Discovery: A Century of Particle Accelerators Revised and Expanded Edition* (World Scientific, Apr. 2014).

[3] E. D. Courant and H. S. Snyder, "Theory of the alternating-gradient synchrotron", Annals of Physics **3**, 10.1016/0003-4916(58)90012-5 (1958).

[4] V. Shiltsev and F. Zimmermann, "Modern and future colliders", Reviews of Modern Physics **93**, 10.1103/RevModPhys.93.015006 (2021).

[5] S. Y. Lee, *Accelerator physics*, 3rd ed. (World Scientific, 2012).

[6] A. Wolski, *Beam Dynamics in High Energy Particle Accelerators* (Imperial College Press, Apr. 2014).

[7] G. W. Hill, "On the part of the motion of the lunar perigee which is a function of the mean motions of the sun and moon", Acta Mathematica **8**, 10.1007/BF02417081 (1900).

[8] A. W. Chao and K. H. Mess, *Handbook of Accelerator Physics and Engineering* (World Scientific, 2013).

[9] S. Rexford and B. Erdelyi, "Numerical discretization of completely integrable nonlinear Hamiltonian systems", Physical Review Accelerators and Beams **21**, 10.1103/PhysRevAccelBeams.21.114601 (2018).

[10] V. A. Lebedev and S. A. Bogacz, "Betatron motion with coupling of horizontal and vertical degrees of freedom", Journal of Instrumentation **5**, 10.1088/1748-0221/5/10/P10010 (2010).

[11] H. Goldstein, C. P. Poole, and J. L. Safko, *Classical mechanics*, 3. ed., [Nachdr.] (Addison Wesley, San Francisco Munich, 2008), 638 pp.

[12] C. A. Lindstrøm and E. Adli, "Design of general apochromatic drift-quadrupole beam lines", Physical Review Accelerators and Beams **19**, 10.1103/PhysRevAccelBeams.19.071002 (2016).

[13] J. Tückmantel, *Synchrotron Radiation Damping in LHC and Longitudinal Bunch Shape*, LHC-Project-Report-819 (June 16, 2005).

[14] J. D. Bjorken and S. K. Mtingwa, "Intrabeam scattering", Particle Accelerators **13** (1983).

[15] K. Kubo, S. K. Mtingwa, and A. Wolski, "Intrabeam scattering formulas for high energy beams", Physical Review Special Topics - Accelerators and Beams **8**, 10.1103/PhysRevSTAB.8.081001 (2005).

[16] N. N. Nekhoroshev, "Behavior of Hamiltonian systems close to integrable", Functional Analysis and Its Applications **5**, 10.1007/BF01086753 (1971).

[17] S. Barbieri, *On the algebraic properties of exponentially stable integrable hamiltonian systems*, (Nov. 19, 2020) http://arxiv.org/abs/2011.09731.

[18] *USPAS Lectures (Lecture 24 - Collective instabilities)*, (2001) https://www.classe.cornell.edu/~dugan/USPAS/Lect24.pdf.

[19] A. Bazzani, G. Servizi, G. Turchetti, and E. Todesco, *A normal form approach to the theory of nonlinear betatronic motion*, CERN-94-02 (CERN, 1994).

[20] R. Tomas, "Direct Measurement of Resonance Driving Terms in the Super Proton Synchrotron (SPS) of CERN using Beam Position Monitors", Ph.D. (Valencia U., 2003).

[21] N. Merminga and K.-Y. Ng, "Analytical expressions for the smear due to nonlinear multipoles", in Proceedings of the 1989 IEEE Particle Accelerator Conference, . 'Accelerator Science and Technology (1989).

[22] W. Herr, *Mathematical and Numerical Methods for Non-linear Beam Dynamics*, (June 16, 2020) http://arxiv.org/abs/2006.09052.

[23] R. D. Ruth, "Single particle dynamics and nonlinear resonances in circular accelerators", in Lecture Notes in Physics (1986).

[24] R. Tomás, M. Aiba, A. Franchi, and U. Iriso, "Review of linear optics measurement and correction for charged particle accelerators", Physical Review Accelerators and Beams **20**, 10.1103/PhysRevAccelBeams.20.054801 (2017).

[25] R. Baartman, "Betatron resonances with space charge", in AIP Conference Proceedings, Vol. 448 (1998).

[26] K. Ito, H. Okamoto, Y. Tokashiki, and K. Fukushima, "Coherent resonance stop bands in alternating gradient beam transport", Physical Review Accelerators and Beams **20**, 10.1103/PhysRevAccelBeams.20.064201 (2017).

[27] L. Landau, "On the vibrations of the electronic plasma", Journal of physics / Academy of Sciences of the USSR **10** (1946).

[28] V. Kornilov and O. Boine-Frankenheim, "Coherent Instability Thresholds and Dynamic Aperture with Octupoles and Nonlinear Space-Charge in the SIS100 Synchrotron", in Proceedings of IPAC 2010 (2010).

[29] J. Gareyte, J. P. Koutchouk, and F. Ruggiero, *Landau Damping, Dynamic Aperture and Octupoles in LHC*, LHC Project Report 91 (1997).

[30] W. Herr, *CERN Accelerator School: Advanced Accelerator Physics*, arXiv:1601.07311 (CERN, Jan. 27, 2016).

[31] E. Métral and F. Ruggiero, *Stability diagrams for Landau damping with two-dimensional betatron tune spread from both octupoles and non-linear space charge*, CERN-AB-2004-025 (2004).

[32] S. D. Webb, D. L. Bruhwiler, D. T. Abell, A. Sishlo, V. Danilov, S. Nagaitsev, A. Valishev, K. Danilov, and J. R. Cary, *Effects of Nonlinear Decoherence on Halo Formation*, (Aug. 7, 2013) http://arxiv.org/abs/1205.7083.

[33] V. Kornilov, "Landau Damping part 2" (CERN Accelerator School), 2017.

[34] S. D. Webb, D. L. Bruhwiler, D. T. Abell, V. Danilov, S. Nagaitsev, A. Valishev, K. Danilov, and J. R. Cary, "Suppressing Transverse Beam Halo with Nonlinear Magnetic Fields", TBD (2012).

[35] C. Montag, J. Kewisch, D. Trbojevic, and F. Schmidt, "Overcoming a fast transverse instability by means of octupole-induced tune spread in the Relativistic Heavy Ion Collider", Physical Review Special Topics - Accelerators and Beams **5**, 10.1103/PhysRevSTAB.5.084401 (2002).

[36] V. Danilov, "Practical solutions for nonlinear accelerator lattice with stable nearly regular motion", Physical Review Special Topics - Accelerators and Beams **11**, 10.1103/PhysRevSTAB.11.114001 (2008).

[37] V. Danilov and S. Nagaitsev, "Nonlinear accelerator lattices with one and two analytic invariants", Physical Review Special Topics - Accelerators and Beams **13**, 10.1103/PhysRevSTAB.13.084002 (2010).

[38] R. Conte, M. Musette, and C. Verhoeven, "Explicit integration of the Hénon-Heiles Hamiltonians", Journal of Nonlinear Mathematical Physics **12**, 10.2991/jnmp.2005.12.s1.18 (2005).

[39] L. Gupta, Y. K. Kim, S. Baturin, and S. Nagaitsev, "Study of Integrable and Quasi-Integrable Sextupole Lattice", in Proceedings, 10th International Particle Accelerator Conference (IPAC2019) : Melbourne, Australia, 19-24 May, 2019 (2019).

[40] M. Henon and C. Heiles, "The applicability of the third integral of motion: Some numerical experiments", The Astronomical Journal **69**, 10.1086/109234 (1964).

[41] S. Antipov, S. Nagaitsev, and A. Valishev, "Single-particle dynamics in a nonlinear accelerator lattice: attaining a large tune spread with octupoles in IOTA", Journal of Instrumentation **12**, 10.1088/1748-0221/12/04/P04008 (2017).

[42] R. G. Smirnov, *The classical Bertrand-Darboux problem*, (May 7, 2006) http://arxiv.org/abs/math-ph/0604038.

[43] C. Mitchell, *Complex Representation of Potentials and Fields for the Nonlinear Magnetic Insert of the Integrable Optics Test Accelerator*, (July 31, 2019) http://arxiv.org/abs/1908.00036.

[44] C. E. Mitchell, R. D. Ryne, and K. Hwang, "Bifurcation analysis of nonlinear Hamiltonian dynamics in the Fermilab Integrable Optics Test Accelerator", Physical Review Accelerators and Beams **23**, 10.1103/PhysRevAccelBeams.23.064002 (2020).

[45] S. D. Webb, D. L. Bruhwiler, A. Valishev, S. N. Nagaitsev, and V. V. Danilov, *Chromatic and Dispersive Effects in Nonlinear Integrable Optics*, (May 18, 2015) http://arxiv.org/abs/1504.05981.

[46] S. Webb, N. Cook, and J. Eldred, "Averaged invariants in storage rings with synchrotron motion", Journal of Instrumentation **15**, 10.1088/1748-0221/15/12/P12032 (2020).

[47] A. Valishev, "Possible Experiments With an Electron Storage Ring at NML", Future Directions for Accel. R&D at Fermilab, 2009.

[48] A. Valishev, "IOTA - A Brief Parametric Profile", Focused Workshop on Scientific Opportunities in IOTA, Apr. 28–29, 2015.

[49] M. J. Syphers and S. Chattopadhyay, "Landscape of Future Accelerators at the Energy and Intensity Frontier", Proceedings of Science (2016).

[50] J. Eldred and A. Valishev, *Integrable RCS as a proposed replacement for Fermilab Booster*, (2017) `http://arxiv.org/abs/1703.00952`.

[51] J. Eldred, V. Lebedev, and A. Valishev, "Rapid-Cycling Synchrotron for Multi-Megawatt Proton Facility at Fermilab", Journal of Instrumentation **14**, `10.1088/1748-0221/14/07/P07021` (2019).

[52] G. Kafka, "Lattice design of the integrable optics test accelerator and optical stochastic cooling experiment at Fermilab", Ph.D. (Illinois Institute of Technology, United States – Illinois, 2015).

[53] S. Antipov, "Injection Design for IOTA", 2014.

[54] A. Romanov, *IOTA ring enegy*, E-mail, 2020.

[55] V. Lebedev, I. Lobach, A. Romanov, and A. Valishev, *Report on Single and Multiple Intrabeam Scattering Measurements in IOTA Ring in Fermilab*, FERMILAB-TM-2750-AD, Beams-doc-8837, 1764146 (2020).

[56] M. Borland, V. Sajaev, L. Emery, and A. Xiao, *Multi-objective direct optimization of dynamic acceptance and lifetime for potential upgrades of the Advanced Photon Source.* ANL/APS/LS-319 (Aug. 24, 2010).

[57] A. Romanov, "IOTA Optics Update: Flexibility for Experiments", FAST/IOTA Scientific Program Meeting 2017, 2017.

[58] A. Romanov, G. Kafka, S. Nagaitsev, and A. Valishev, "Lattice Correction Modeling for Fermilab IOTA Ring", in Proceedings of 5th Int. Particle Accelerator Conf. (IPAC'14), Dresden, Germany, June 15-20, 2014 (July 2014).

[59] *NSLS-II Conceptual Design Report - Lattice and Accelerator Physics* (2006).

[60] M. Borland, L. Emery, R. Lindberg, V. Sajaev, Y.-P. Sun, and A. Xiao, "Overview of Lattice Design and Evaluation for the APS Upgrade", ICFA Beam Dynamics Newsletter **71** (2017).

[61] S. Antipov, *Design of octupole channel for IOTA*, Internal report (2015).

[62] S. Antipov, K. Carlson, R. Castellotti, A. Valishev, and S. Wesseln, "Design of Octupole Channel for Integrable Optics Test Accelerator", in Proceedings of 7th Int. Particle Accelerator Conf. (IPAC'16), Busan, Korea, May 8-13, 2016 (June 2016).

[63] L. Walckiers, "Magnetic measurement with coils and wires", CERN Document Server, `10.5170/CERN-2010-004.357` (2011).

[64] F. H. O'Shea, R. B. Agustsson, A. Y. Murokh, and E. Spranza, "Measurement of Non-Linear Insert Magnets", in (2013).

[65] F. H. O'Shea, R. Agustsson, R. Technologies, S. St, S. Monica, D. W. Martin, J. D. McNevin, R. Systems, S. St, and S. Monica, "Non-linear Magnetic Inserts for the Integrable Optics Test Accelerator", in (2015).

[66] F. H. O'Shea, R. B. Agustsson, P. S. Chang, and Y. C. Chen, "Non-Linear Inserts for the IOTA Ring", in (2017).

[67] C. Mitchell, F. O'Shea, and R. Ryne, "Accurate Modeling of Fringe Field Effects on Nonlinear Integrable Optics in IOTA", in Proceedings of the 9th Int. Particle Accelerator Conf. (2018).

[68] G. Le Bec, J. Chavanne, and C. Penel, "Stretched wire measurement of multipole accelerator magnets", Physical Review Special Topics - Accelerators and Beams **15**, 10.1103/PhysRevSTAB.15.022401 (2012).

[69] J. DiMarco and J. Krzywinski, *MTF Single Stretched Wire System*, MTF-96-0001 (1996).

[70] R. Jones, "Measuring Tune, Chromaticity and Coupling", (2018).

[71] A. Boccardi, *First Results from the LHC BBQ Tune and Chromaticity Systems* (2009).

[72] R. Bartolini, A. Bazzani, M. Giovannozzi, W. Scandale, and E. Todesco, *Tune evaluation in simulations and experiments* (1996).

[73] Ç. Candan, "A Method For Fine Resolution Frequency Estimation From Three DFT Samples", IEEE Signal Processing Letters **18**, 10.1109/LSP.2011.2136378 (2011).

[74] M. Gasior and J. L. Gonzalez, *Improving FFT Frequency Measurement Resolution by Parabolic and Gaussian Interpolation*, AB-Note-2004-021 (2004).

[75] J. Laskar, C. Froeschlé, and A. Celletti, "The measure of chaos by the numerical analysis of the fundamental frequencies. Application to the standard mapping", Physica D: Nonlinear Phenomena **56**, 10.1016/0167-2789(92)90028-L (1992).

[76] P. Zisopoulos, Y. Papaphilippou, and J. Laskar, "Refined betatron tune measurements by mixing beam position data", Physical Review Accelerators and Beams **22**, 10.1103/PhysRevAccelBeams.22.071002 (2019).

[77] R. Bartolini, A. Bazzani, M. Giovannozzi, W. Scandale, and E. Todesco, "Algorithms for a Precise Determination of the Betatron Tune", in Particle accelerator. Proceedings, 5th European Conference, EPAC 96, Sitges, Spain, June 10-14, 1996. Vol. 1-3 (1996).

[78] Y. Alexahin, E. Gianfelice-Wendt, and W. Marsh, *Tune Evaluation From Phased BPM Turn-By-Turn Data*, (Feb. 7, 2012) http://arxiv.org/abs/1202.1507.

[79] R. Tomás, M. Bai, R. Calaga, W. Fischer, A. Franchi, and G. Rumolo, "Measurement of global and local resonance terms", Physical Review Special Topics - Accelerators and Beams **8**, 10.1103/PhysRevSTAB.8.024001 (2005).

[80] R. Meller, *Decoherence of Kicked Beams*, SSC-N-360 (1987).

[81] I. C. Hsu, "The Decoherence And Recoherence Of The Betatron Oscillation signal And An application", Part. Accel. **34** (1990).

[82] S. Y. Lee, *Decoherence of Kicked Beams II*, SSCL-N-749 (1991).

[83] L. Nadolski, "Application de l'Analyse en Fréquence à l'Etude de la Dynamique des Sources de Lumière", Theses (Université Paris Sud - Paris XI, July 2001).

[84] J. Shi and S. Ohnuma, "Decoherence and recoherence of beam in phase space", in Proceedings of International Conference on Particle Accelerators (1993).

[85] G. Rumolo and R. Tomas, "Decoherence of a longitudinally kicked beam with chromaticity", Nuclear Instruments and Methods in Physics Research Section A: Accelerators, Spectrometers, Detectors and Associated Equipment **528**, 10.1016/j.nima.2004.03.206 (2004).

[86] C. S. Edmonds, J. Gratus, K. M. Hock, S. Machida, B. D. Muratori, R. G. Torromé, and A. Wolski, "Reconstruction of lattice parameters and beam momentum distribution from turn-by-turn beam position monitor readings in circular accelerators", Physical Review Special Topics - Accelerators and Beams **17**, 10.1103/PhysRevSTAB.17.054401 (2014).

[87] M. Carla, A. Alekou, H. Bartosik, and L. R. Carver, *Beam-based measurement of the skew-sextupolar component of the radio frequency field of a HL-LHC-type crab-cavity.* CERN-ACC-NOTE-2020-0024 (2020).

[88] L. Dovlatyan, "Study and Mitigation of Transverse Resonances with Space Charge Effects at the University of Maryland Electron Ring", Ph.D. (University of Maryland, College Park, 2020).

[89] P. Castro, "Luminosity and beta function measurement at the electron-positron collider ring LEP" (CERN, 1996).

[90] R. Miyamoto, S. E. Kopp, A. Jansson, and M. J. Syphers, "Parametrization of the driven betatron oscillation", Physical Review Special Topics - Accelerators and Beams **11**, 10.1103/PhysRevSTAB.11.084002 (2008).

[91] J. Safranek, "Experimental determination of storage ring optics using orbit response measurements", Nuclear Instruments and Methods in Physics Research Section A: Accelerators, Spectrometers, Detectors and Associated Equipment **388**, 10.1016/S0168-9002(97)00309-4 (1997).

[92] A. Franchi, *Error analysis of linear optics measurements via turn-by-turn beam position data in circular accelerators*, (Apr. 17, 2018) http://arxiv.org/abs/1603.00281.

[93] A. Langner and R. Tomás, "Optics measurement algorithms and error analysis for the proton energy frontier", Physical Review Special Topics - Accelerators and Beams **18**, 10.1103/PhysRevSTAB.18.031002 (2015).

[94] A. Wegscheider, A. Langner, R. Tomás, and A. Franchi, "Analytical N beam position monitor method", Physical Review Accelerators and Beams **20**, 10.1103/PhysRevAccelBeams.20.111002 (2017).

[95] P. Castro, J. Borer, A. Burns, G. Morpurgo, and R. Schmidt, "Betatron function measurement at LEP using the BOM 1000 turns facility", in Proceedings of International Conference on Particle Accelerators (1993).

[96] C.-X. Wang, "Model independent analysis of beam centroid dynamics in accelerators", Ph.D. (Stanford University, Aug. 2000).

[97] C.-x. Wang, V. Sajaev, and C.-Y. Yao, "Phase advance and $\ensuremath{\beta}$ function measurements using model-independent analysis", Physical Review Special Topics - Accelerators and Beams **6**, 10.1103/PhysRevSTAB.6.104001 (2003).

[98] X. Pang, "Independent component analysis for beam measurement", Ph.D. (Indiana University, United States – Indiana, 2010).

[99] X. Pang and S. Y. Lee, "Independent component analysis for beam measurements", Journal of Applied Physics **106**, 10.1063/1.3226858 (2009).

[100] A. V. Petrenko, A. A. Valishev, and V. A. Lebedev, "Model-independent analysis of the Fermilab Tevatron turn-by-turn beam position monitor measurements", Physical Review Special Topics - Accelerators and Beams **14**, 10.1103/PhysRevSTAB.14.092801 (2011).

[101] M. Giovannozzi, W. Scandale, and E. Todesco, "Dynamic aperture extrapolation in the presence of tune modulation", Physical Review E **57**, 10.1103/PhysRevE.57.3432 (1998).

[102] A. Bazzani, M. Giovannozzi, and E. H. Maclean, "Analysis of the non-linear beam dynamics at top energy for the CERN Large Hadron Collider by means of a diffusion model", The European Physical Journal Plus **135**, 10.1140/epjp/s13360-020-00123-2 (2020).

[103] E. H. Maclean, M. Giovannozzi, and R. B. Appleby, "Innovative method to measure the extent of the stable phase-space region of proton synchrotrons", Physical Review Accelerators and Beams **22**, 10.1103/PhysRevAccelBeams.22.034002 (2019).

[104] E. Todesco and M. Giovannozzi, "Dynamic aperture estimates and phase-space distortions in nonlinear betatron motion", Physical Review E **53**, 10.1103/PhysRevE.53.4067 (1996).

[105] K. Ruisard, "Design of a Nonlinear Quasi-Integrable Lattice for Demonstration of Resonance Suppression at the University of Maryland Electron Ring", Ph.D. (University of Maryland, College Park, 2018).

[106] J. Laskar and D. Robin, *Application of frequency map analysis to the ALS*, LBL-38241; CONF-9510138-6 (1996).

[107] J. Laskar, "The chaotic motion of the solar system: A numerical estimate of the size of the chaotic zones", Icarus **88**, 10.1016/0019-1035(90)90084-M (1990).

[108] E. Maclean, F. Carlier, L. Malina, J. M. Coello de Portugal, R. Tomás, M. Giovannozzi, P. Skowroński, T. Persson, and A. Garcia-Tabares, "New Methods for Measurement of Nonlinear Errors in LHC Experimental IRs and Their Application in the HL-LHC", in Proceedings of the 8th International Particle Accelerator Conference, CERN-ACC-2017-166 (2017).

[109] D. Shatilov, E. Levichev, E. Simonov, and M. Zobov, "Application of frequency map analysis to beam-beam effects study in crab waist collision scheme", Physical Review Special Topics - Accelerators and Beams **14**, 10.1103/PhysRevSTAB.14.014001 (2011).

[110] Y. Papaphilippou, "Detecting chaos in particle accelerators through the frequency map analysis method", Chaos: An Interdisciplinary Journal of Nonlinear Science **24**, 10.1063/1.4884495 (2014).

[111] J. Laskar, *Frequency map analysis and quasiperiodic decompositions*, (June 27, 2003) http://arxiv.org/abs/math/0305364.

[112] S. D. Webb, D. T. Abell, D. L. Bruhwiler, and J. R. Cary, "Simulating High-Intensity Proton Beams in Nonlinear Lattices with PyORBIT", (2012).

[113] S. S. Baturin, *Hamiltonian preserving nonlinear optics*, (Mar. 18, 2020) http://arxiv.org/abs/1908.03520.

[114] H. S. Xu, W. H. Huang, C. X. Tang, and S. Y. Lee, "Intrinsic nonlinear effects of dipole magnets in small rings", Physical Review Accelerators and Beams **19**, 10.1103/PhysRevAccelBeams.19.064001 (2016).

[115] H. S. Xu, W. H. Huang, C. X. Tang, and S. Y. Lee, "Design of a 4.8-m ring for inverse Compton scattering x-ray source", Physical Review Special Topics - Accelerators and Beams **17**, 10.1103/PhysRevSTAB.17.070101 (2014).

[116] T. Arion, W. Eberhardt, J. Feikes, A. Gottwald, P. Goslawski, A. Hoehl, H. Kaser, M. Kolbe, J. Li, C. Lupulescu, M. Richter, M. Ries, F. Roth, M. Ruprecht, T. Tydecks, and G. Wüstefeld, "Transverse resonance island buckets for synchrotron-radiation based electron time-of-flight spectroscopy", Review of Scientific Instruments **89**, 10.1063/1.5046923 (2018).

[117] L. R. Carver, X. Buffat, K. Li, E. Métral, and M. Schenk, "Transverse beam instabilities in the presence of linear coupling in the Large Hadron Collider", Physical Review Accelerators and Beams **21**, 10.1103/PhysRevAccelBeams.21.044401 (2018).

[118] M. Hofer and R. Tomás, "Effect of local linear coupling on linear and nonlinear observables in circular accelerators", Physical Review Accelerators and Beams **23**, 10.1103/PhysRevAccelBeams.23.094001 (2020).

[119] C.-x. Wang, "Untangling mixed modes in model-independent analysis of beam dynamics in circular accelerators", Physical Review Special Topics - Accelerators and Beams **7**, 10.1103/PhysRevSTAB.7.114001 (2004).

[120] *Fermilab FAST/IOTA ELog*, https://www-bd.fnal.gov/Elog/?orLogName=FAST.

[121] A. Valishev, "IOTA/FAST: Status, First Run and Outlook", IOTA/FAST Run 1 Retreat, 2019.

[122] A. Valishev and A. Romanov, "IOTA Commissioning and Operations", IOTA/FAST Run 2 Retreat, 2020.

[123] A. Valishev, "Introduction to Nonlinear Integrable Optics Experiments", FAST/IOTA Collaboration Meeting 2020, 2020.

[124] N. Eddy, "IOTA BPM Discussion", IOTA/FAST Run 1 Retreat, 2019.

[125] E. H. Maclean, R. Tomás, F. S. Carlier, M. S. Camillocci, J. W. Dilly, J. Coello de Portugal, E. Fol, K. Fuchsberger, A. Garcia-Tabares Valdivieso, M. Giovannozzi, M. Hofer, L. Malina, T. H. B. Persson, P. K. Skowronski, and A. Wegscheider, "New approach to LHC optics commissioning for the nonlinear era", Physical Review Accelerators and Beams **22**, 10.1103/PhysRevAccelBeams.22.061004 (2019).

[126] V. Lebedev, I. Lobach, A. Romanov, and A. Valishev, *Report on Single and Multiple Intrabeam Scattering Measurements in IOTA Ring in Fermilab*, FERMILAB-TM-2750-AD, Beams-doc-8837 (2020).

[127] S. Szustkowski, "Nonlinear Integrable Optics Beam Dynamics Experiment and Diagnostics", Ph.D. (Northern Illinois University, United States – Illinois, 2020), 106 pp.

[128] N. Eddy, "Experiment: Instability Thresholds with Octupole Channel (NIOLD)", FAST/IOTA Collaboration Meeting 2020, 2020.

[129] N. Eddy, D. R. Broemmelsiek, K. Carlson, D. J. Crawford, J. Diamond, D. R. Edstrom, B. Fellenz, M. A. Ibrahim, J. Jarvis, V. Lebedev, S. Nagaitsev, J. Ruan, J. K. Santucci, A. Semenov, V. Shiltsev, G. Stancari, A. Valishev, D. Voy, A. Warner, N. Kuklev, I. Lobach, and S. Szustkowski, "Beam Instrumentation at the Fermilab IOTA Ring", in Proceedings, 8th International Beam Instrumentation Conference, IBIC2019 : Malmö, Sweden, September 8-12, 2019 (2019).

[130] N. Eddy, *IOTA BPM information*, E-mail, 2021.

[131] A. Reiter, R. Singh, and O. Chorniy, "Statistical Treatment of Beam Position Monitor Data", Nuclear Instruments and Methods in Physics Research Section A: Accelerators, Spectrometers, Detectors and Associated Equipment **890**, 10.1016/j.nima.2018.02.046 (2018).

[132] N. Kuklev, Y.-K. Kim, and A. Romanov, "Synchrotron Radiation Beam Diagnostics for the Integrable Optics Test Accelerator", in Proceedings, 9th International Particle Accelerator Conference (IPAC 2018) : Vancouver, BC Canada, April 29-May 4, 2018 (June 2018).

[133] N. Kuklev, J. Jarvis, Y.-K. Kim, A. Romanov, J. Santucci, and G. Stancari, "Synchrotron Radiation Beam Diagnostics at IOTA - Commissioning Performance and Upgrade Efforts", in Proceedings, 10th International Particle Accelerator Conference (IPAC2019) : Melbourne, Australia, 19-24 May, 2019 (June 2019).

[134] S. Antipov, "IOTA Kickers", 2014.

[135] S. A. Antipov, A. Didenko, V. Lebedev, and A. Valishev, "Stripline kicker for integrable optics test accelerator", (2016).

[136] R. J. Smith, M. Dufau, C. Hill, J. K. Jones, A. Kalinin, L. Ma, P. A. McIntosh, B. D. Muratori, and B. J. A. Shepherd, "The EMMA Accelerator, A Diagnostic Systems Overview", (2011).

[137] D. Brandt, *CAS - CERN Accelerator School: Beam Diagnostics*, CERN-2009-005 (CERN, 2009).

[138] M. Borland, *ELEGANT: A flexible SDDS-compliant code for accelerator simulation*, LS-287, 761286 (Aug. 18, 2000).

[139] *MAD - Methodical Accelerator Design*, `http://mad.web.cern.ch/mad/`.

[140] F. Schmidt, E. Forest, and E. McIntosh, *Introduction to the polymorphic tracking code: Fibre bundles, polymorphic Taylor types and Exact tracking*, CERN-SL-2002-044-AP (July 24, 2002).

[141] D. Shatilov, Y. Alexahin, V. Lebedev, and A. Valishev, "Lifetrac Code for the Weak-Strong Simulation of the Beam-Beam Effects in Tevatron", in Proceedings of the 2005 Particle Accelerator Conference (May 2005).

[142] A. Romanov, D. Edstrom Jr., F. A. Emanov, I. A. Koop, E. A. Perevedentsev, Y. A. Rogovsky, D. B. Shwartz, and A. Valishev, *Correction of magnetic optics and beam trajectory using LOCO based algorithm with expanded experimental data sets*, (Mar. 28, 2017) `http://arxiv.org/abs/1703.09757`.

[143] S. I. Tomin and X. Eu, "OCELOT as a Framework for Beam Dynamics Simulations of X-Ray Sources", in Free Electron Lasers (2017).

[144] N. Kuklev, *Nikitakuklev/ocelot*, `https://github.com/nikitakuklev/ocelot`.

[145] N. Kuklev, *Nikitakuklev/pyIOTA*, `https://github.com/nikitakuklev/pyIOTA`.